EFFECT OF CONTROLLING TOROIDAL FIELD TOPOLOGY IN A SIMPLE TOROIDAL PLASMA: AN EXPERIMENTAL STUDY

By

Umesh Kumar

PHYS06201204005

Institute for Plasma Research, Gandhinagar

A thesis submitted to the
Board of Studies in Physical Sciences

In partial fulfillment of requirements
for the Degree of

DOCTOR OF PHILOSOPHY

of

HOMI BHABHA NATIONAL INSTITUTE

July 2018

Homi Bhabha National Institute

Recommendations of the Viva Voce Committee

As members of the Viva Voce Committee, we certify that we have read the dissertation prepared by **Umesh Kumar** entitled " EFFECT OF CONTROLLING TOROIDAL FIELD TOPOLOGY IN A SIMPLE TOROIDAL PLASMA: AN EXPERIMENTAL STUDY " and recommend that it may be accepted as fulfilling the thesis requirement for the award of Degree of Doctor of Philosophy.

-- **Date :** 17/ 01/ 2019

Chairman : Prof. Prabal K. Chattopadhyay

-- **Date :** 17/ 01/ 2019

Guide/ Convener : Prof. Rajaraman Ganesh

-- **Date :** 17/ 01/ 2019

Examiner : Prof. Ashish Ganguli

Ghosh

-- **Date :** 17/ 01/ 2019

Member : Dr. Joydeep Ghosh

Raju

-- **Date :** 17/ 01/ 2019

Member : Dr. Daniel Raju

-- **Date :** 17/ 01/ 2019

Member : Prof. Y. C. Saxena

Final approval and acceptance of this thesis is contingent upon the candidate's submission of the final copies of the thesis to HBNI.

I hereby certify that I have read this thesis prepared under my direction and recommend that it may be accepted as fulfilling the thesis requirement.

Date : 17/ 01/ 2019

Place: IPR, Gandhinagar

Prof. Rajaraman Ganesh

Guide

STATEMENT BY AUTHOR

This dissertation has been submitted in partial fulfillment of requirements for an advanced degree at Homi Bhabha National Institute (HBNI) and is deposited in the Library to be made available to borrowers under rules of the HBNI.

Brief quotations from this dissertation are allowable without special permission, provided that accurate acknowledgement of source is made. Requests for permission for extended quotation from or reproduction of this manuscript in whole or in part may be granted by the Competent Authority of HBNI when in his or her judgment the proposed use of the material is in the interests of scholarship. In all other instances, however, permission must be obtained from the author.

Umesh Kumar

Umesh Kumar

DECLARATION

I, hereby declare that the investigation presented in the thesis has been carried out by me. The work is original and has not been submitted earlier as a whole or in part for a degree / diploma at this or any other Institution / University.

Umesh Kumar

Umesh Kumar

List of Publications arising from the Thesis

Journal:

1. **A simple experimental method to determine magnetic field topology in toroidal plasma devices**

   Shekar G. Thatipamula Umesh Kumar, R. Ganesh, Y. C. Saxena, and D. Raju. *Rev. Sci. Instrum* **86**, 033504, (2015).

2. **Effect of magnetic field topology on quasi-stationary equilibrium, fluctuations, and flows in a simple toroidal device**

   Umesh Kumar, Shekar G Thatipamula, R. Ganesh, Y. C. Saxena, and D. Raju *Phys. of Plasmas* **23**, 102301, (2016).

3. **Observation of high frequency Geodesic Acoustic-like Mode in a Simple Toroidal Plasma**

   Umesh Kumar, R. Ganesh, K. Sathyanaryana and Y. C. Saxena, *Under review, (2018).*

4. **Effect of parallel connection length on the properties of a low temperature plasma confined in a simple magnetized torus**

   Umesh Kumar, R. Ganesh, Y. C. Saxena, Shekar G Thatipamula and D. Raju, *Under review (2018).*

5. **Effect of a small yet finite component of vertical magnetic field on electron cyclotron resonance produced plasma characteristics in a simple magnetized torus**

   Umesh Kumar, R. Ganesh, K. Sathyanaryana and Y. C. Saxena, *to be submitted, (2019).*

6. **Effect of net poloidal flow on particle confinement time in a simple magnetized torus using two different sources**

   Umesh Kumar, R. Ganesh, K. Sathyanaryana and Y. C. Saxena, Shekar G Thatipamula and D. Raju, *to be submitted, (2019).*

7. **Role of poloidal flow on plasma characteristics in a simple magnetized torus using two sources: A comparative study**
   Umesh Kumar, R. Ganesh, K. Sathyanaryana, Y. C. Saxena, Shekar G Thatipamula and D. Raju, *to be submitted, (2019).*

Conferences/ Schools:

International Participation:

1. "Role of Radial Electric Field on the Particle Confinement in a Simple Toroidal Device."
   19th International Congress on Plasma Physics (ICPP-2018), 4th June-8th June, 2018, Vancouver, Canada.

2. "Role of poloidal flows on particle confinement in a simple toroidal device: an experimental study ."
   59th Annual Meeting of the APS- Division of Plasma Physics (APS-DPP, 2018), 23rd Oct.-27th Oct., 2017, Wisconsin, USA.

3. "Role of magnetic field topology in particle confinement in simple toroidal device."
   44th European Physical Society Conference on Plasma Physics (EPS-2017), 26th-30th June, 2017, Belfast, Northern Ireland, UK.

4. "Parallel connection length and flow-fluctuation cycle in simple toroidal device."
   10th Asia Plasma and Fusion Association Conference (APFA-2015), 14th-18th Dec., 2015, Gandhinagar, India.

5. "Experimental study of role of magnetic field topology on fluctuation and flows in simple toroidal device"
   7th International conference on the Frontiers of Plasma Physics and Technology (FPPT-7), 13th-17th April, 2015, Kochi, India.

National Participation:

1. *DST-SERC School on Tokamaks and Magnetized Plasma Fusion, 25th Feb. to 15th Mar., 2013*, IPR, Gandhinagar, Gujarat, India.

2. "Study of role of toroidal field topology on flow And fluctuation in a Simple Toroidal Device"
29th National Symposium on Plasma Science and Technology & International Conference on Plasma Science and Nanotechnology (Plasma-2014), 8th-11th Dec., 2014, Kottayam, Kerala, India.

3. *Hands-on School on Nonlinear Dynamics (HSND-2015), 16th-22nd Feb., 2015,* IPR, Gandhinagar, Gujarat, India.

Umesh Kumar

Umesh Kumar

Dedicated to

My family

ACKNOWLEDGEMENTS

I was fortunate enough to receive guidance, motivation and support from various people during my academic career at IPR. I would like to use this opportunity to acknowledge their support and express my gratitude to them.

At the very outset, I convey my deepest gratitude to my Thesis supervisor Prof. Rajaraman Ganesh. The structure of this very Thesis lies on the foundation of his ideas. Whenever his sentence started with *Umesh! if I were you...*, I knew something big is coming. In the end of almost every new physics idea, he used to say joyfully *karo yaar!*, that was a great motivation for me. It was very often that our discussion use to range from plasma physics to history to movies to politics to almost everything. His friendly, calm and spirited attitude throughout my PhD work has been the source of inspiration for me. I could not have imagined, having a better supervisor and guide for my PhD. Apart from plasma physics, I have learned several things from him, for example, being calm even in adverse situations, efficient management of time and hardworking attitude. I still wonder, how he manages, working very late at night ($\sim$ 3 am!) and still coming to the office on the very next day with full of energy and enthusiasm. His emphasis on the reading of good novels and watching movies to improve the grip on the language was really helpful for me. It is because of his never ending rigorous revisions of my Manuscripts and the present Thesis that my writing style has improved to a great deal. He is primarily responsible for my interest in the studies related to fluctuation-flow synergy and turbulence. However, I regret that I could not live up to his expectations to learn numerical technique despite my great deal of interest and his constant motivation. There were numerous occasions during my PhD, whenever I faced difficult and frustrating problems, he always provided moral support and adequate freedom. He was always available to support me in my personal problems as well. I deeply indebted to him and consider myself really fortunate to work under him.

I am immensely indebted to our ultimate *guru*, Prof. Y. C. Saxena, for his scrutiny of all the experimental activities. His immense knowledge and vast experience come out to be very helpful for me throughout my PhD. There were numerous occasions when an hour discussion with him solved those problems, which I was facing for weeks! He is always calm and composed, despite my several silly mistakes and vague questions.

It is my pleasure to thank Dr Shekar G. Thatipamula for introducing me to the very fine details of BETA experimental device. He further helped me to understand various technical and physical aspects of several diagnostics developed and used in BETA. I was fortunate enough to receive his support for the substantial time, otherwise, it would have been very difficult for me to operate and maintain the whole experimental set up by my own.

I would like to heartily thank Mr K. Sathynarayana for developing Microwave source for BETA, which was an essential part of the present Thesis. I was fortunate that he came back to IPR. Apart from developing Microwave source, he helped me at several occasion to overcome from various technical difficulties. I would also like to thank the support of Mr Deep Vadher, for his consistent support in operating and maintaining the experimental set up and his contribution in developing Microwave source is huge.

I would like to heartily thank Mr Sharvil Patel for performing coordinate measurement for the TF and VF coils using ECDS and ADITYA-U group for providing the ECDS equipment. I would also like to thank Mrs Richa Bandyopadhyay and Dr R. Srinivasan for performing the simulation to determine the 3-D topology of the toroidal field results. I am immensely thankful to Dr R. Srinivasan for various discussion on the toroidal field topology part, which increased my understanding, many folds.

It is my pleasure to thank my Doctoral committee members Prof. P. K. Chattopadhyay (Chairman), Dr Joydeep Ghosh, Dr D. Raju and Prof. Y. C. Saxena for carefully monitoring my progress and putting me on the correct path. I would like to thank Dr J. Ghosh for critically reviewing my Manuscripts and I am indebted to Dr D. Raju for teaching me various data analysis techniques.

I would like to thank the Academic committee members and the other faculties, who taught me during my course work, namely Prof. S. Mukherjee, Dr Mainak, Dr Kundu, Prof. P. K. Chattopadhyay, Dr D. Sharma, Dr Ramasubramanian, Dr S. Karkari, Dr A. K. Chattopadhyay, Prof. S. Sengupta, Dr Pintu, Dr J. Ghosh, Dr G. Ravi and many more.

There were several instances during the experimental or other activities, when I needed equipment or information. I always got warm support from my colleagues in the BETA lab, Basic lab and MEL lab, Awasthi, Pankaj, Amulya, Prabhakar, Ganguli, Aaron, Priya Vandana, Anitha, Ved Prakash, Surabhi, Pintu, Garima, Hari, Lavkesh, Manu, Yeole, Amit, Meenakshi, Pratibha, Raval, Yuvakiran, Siju, Ramasubramanian, Bhoomi, Hirel, Neeraj, Sonu. I would like to convey my sincere thanks to all of them.

I would like to sincerely thank the Electronics group members for helping me in numerous instances. I would like to thank Praveenlal ji, Abhijit, Priyadarshini ji for their support. I would like to thank Stores department, Purchase department, Workshop, Transport, Administration, Accounts, Canteen, Air and Water cooling section, Library, Computer Center for their support during my PhD.

I express my sincere thanks to the seniors and friends in the hostel for their unconditional support and company. My warm regards to Aswin, Soumen, Sayak, Aditya, Sanat, Kshitish, Deepak, Ujjwal, Manjit, Gurudatt, Vikram Sagar, Satya, Rameswar, Sushil, Pravesh, Vikram Dharodi, Veda Prakash, Rana, Rimza, Dushyant, Vara, Bibhu, Neeraj, Rupendra, Chandrasekhar, Mangilal, Vidhi, Akanksha, Deepa, Meghraj, Harish, Samir. I am especially grateful to Aswin, Kshitish, Deepak, Vikram Sagar, Sayak, Soumen and Aditya for their many helpful advice, discussions and suggestions. I am very thankful to my batchmates Bhumika, Sonu, Debraj, Arghya, Ratan, Narayan, Amit, Surbhi, Modhu and Ramkrishna Rane and my junior friends Prabhakar, Sagar, Chetan, Atul, Deepak Verma, Alam, Jervis, Sandeep, Pallavi, Minakshi, Harshita, Arun, Gaurav, Rupak, Shivam, Avnish, Subroto, Niraj, Srimanto, Dipshika, Garima, Nidhi, Swapnali, Ayushi, Devshree, Pawandeep, Satadal Das, Soumen De, Pradeep, Hariprasad, Sanjeev and Tanmay, Prince, Lavanya, Jagannath and other scholars and TTPs for taking me to grow with all of you together in the hostel, a delightful natural ambient inside the campus. I would like to thank Bhumika for her several suggestions and support. I would to sincerely thank my best friends at IPR, Sonu, Debraj and Ratan for all the laughter, enjoyment, late night outing and many more, without them my life would have become dull at IPR.

I was fortunate that my relatives live in Ahmedabad, I would like to thank my *Mama*, *Mami* and all my three cousins and their wives for providing me a homely environment away from home. I spent several weekends there and in the company of kids Rashmi, Girish, Arpit, Harshit and Ruchi, I forgot my work stress during my stay with them.

In the end, I would like to thank the most important people in my life, my family. I am greatly indebted to my parents, especially to my mother, for their unconditional love, support, motivation and everything in my life. They are the reason, whatever, I am today. I would like to thank my younger sister Sushma for her unconditional love and support and my younger brother Avdhesh for taking the responsibility of an elder son and because of his support, I could focus on PhD without worrying about my family. In the end, I would like to thank my beloved wife, Madhulika for her love and support. She always encouraged me to focus on my work.

Contents

SYNOPSIS

The current Thesis investigates the role of toroidal field topology on the flow, fluctuation, quasi-static equilibrium and particle confinement time in a simple magnetized torus (SMT) [1]. In an SMT, plasma is confined using an external, purely toroidal, magnetic field. As there is very little or no toroidal current in an SMT, magnetic rotational transform ceases to exist, leading to open, single particle orbits and consequent absence of single particle confinement. In the presence of a continuous ionizing source such as a hot cathode or an electron cyclotron resonance mechanism, magnetic drifts of particles create vertical charge separation leading to a residual vertical electric field, which in turn, transports the plasma outward along the major radius direction and eventual loss of plasma. A transit time or quasi-static equilibrium is achieved due to a weak balance between plasma source and radial losses, thus making the nature of plasma source to be a crucial component in determining the overall plasma properties . A poloidally continuous metal strip is used to minimize the residual vertical electric field [2, 3].

Magnetic confined hot plasmas in toroidal devices gained significant importance due to their potential to achieve controlled fusion. In spite of the remarkable advance in this field, transport of particles and energy have been found to be anomalous and pose challenges in further improving the plasma confinement. The source of anomalous transport is free energy due to cross-field density and temperature gradient driven instabilities. A clear understanding of these processes, therefore, is of paramount importance. However, complex magnetic scheme in Tokamaks set constraints to carry out experimental studies of individual instabilities and their role in ensuring transport. An SMT provides a relatively simple and well diagnosable test-bed for experimental plasma studies which are relevant for the weakly collisional Edge/SOL region of Tokamaks [4, 5], which is crucial to understand overall transport and L to H transition in Tokamaks.

In this experimental Thesis work, experiments were carried out in BETA, a simple magnetized torus at the Institute for Plasma Research, India, an attempt is made to address some of the following questions : (i) As minimizing the residual vertical field is crucial to the nature of quasi-static equilibrium, its mean density and temperature profiles, consequent low frequency fluctuations, turbulence and transport, can one use a relatively weak external magnetic field to create parallel connection lengths or pathways for electrons long the total field line direction so that the residual vertical field is minimized further? (ii) Is there a novel, yet simple way of experimentally determining the magnetic field line topology? (iii) If so, by varying the vertical magnetic field for a given toroidal field strength, can one experimentally determine the changes in the nature of plasma mean profiles, fluctuations and mean poloidal plasma flows. (iv) Are there special ratios of vertical to toroidal field strengths which significantly improve plasma confinement and why? (v) Does the nature of mean profiles, fluctuations and overall confinement, crucially dependent on the type of plasma source, for example, hot cathode-based source or electron cyclotron resonance-based source? These issues have been addressed in the current Thesis.

A more detailed description of the Thesis in terms of chapter-wise summaries is provided below:

Chapter-1: Introduction

The introductory first chapter of the Thesis outlines the motivation behind the study and defines the scope of the study. This chapter provides details of the SMT configuration and its significance in understanding the phenomenon related to Edge/SOL of the Tokamaks and details of the establishing equilibrium in an SMT. Theoretically, equilibrium cannot be established in a plasma confined by pure toroidal field, due to the radial loss of the plasma because of residual vertical electric field E_z created by the gradient and curvature of the toroidal magnetic field. As discussed earlier, E_z can be reduced by mounting a limiter, however by application of external vertical field (B_v) can further reduce the E_z [6]. Therefore, application of B_v can increase the particle confinement [6, 7] and may result in high plasma density. This chapter also provides a brief history of past work related with variation in toroidal field topology and its effect on plasma properties. The chapter also includes details as to why an SMT is important for studying the paradigm of flow and fluctuation and their role in establishing the quasi-static equilibrium. The chapter ends with a brief outline indicating the chapter-wise organization of the contents of the Thesis.

Chapter-2: Experimental system, diagnostics and plasma sources

The experimental system, BETA is described in detail along with the diagnostics developed and technical aspects of the measurements and two different kind of plasma sources. The major radius of BETA is 45 cm and minor radius is 15 cm. The toroidal field is generated by passing current through 16 toroidal field (TF) coils and the maximum field at the minor axis can reach up to 1 kG. The vertical field is generated by one set i.e, two vertical field (VF) coils. These VF coils are placed in Helmholtz coil configuration and the vertical distance from the center of the torus to each VF coil in 60 cm. The diagnostics developed and used are Mach probe, an array of Langmuir probe, triple Langmuir probe and emissive probe. The array of Langmuir probes simultaneously measures the density and potential time series at one particular radial location. The electron temperature and density (at another toroidal location) time series are measured using triple Langmuir probe. The plasma potential is measured using the hot emissive probe and net poloidal flow is measured using Mach probe. The plasma sources used are namely i) Hot cathode source and ii) Electron Cyclotron Resonance (ECR) source. The hot cathode source has an inherent zeroth order radial electric field and thus a strong compressible poloidal flow [8]. To address physics issues in the absence of poloidal flows or in the presence of weak poloidal flows, an Electron Cyclotron Resonance (ECR) based plasma source has been developed. Another interesting difference between Hot Cathode (HC) source and ECR plasma source is the start difference in the relative fractions of fast or energetic electrons [9]. The details of plasma production for these sources along with description of various diagnostics, vacuum system, magnetic field coils etc, are described in detail in this chapter.

Chapter-3: Experimental determination of toroidal field topology

In an ideal case, the toroidal field line is supposed to close on itself, however a relatively small vertical component of magnetic field may arise due to presence of uncompensated leads in toroidal field coils. Due to this field lines may not close on themselves and this facilitates along magnetic field pathways for electrons to minimize residual E_z as well as the response time to nullify/determine phase difference between density and potential fluctuations which is crucial to the nature of instabilities. Therefore determination of toroidal field topology is crucial to identify the nature of fluctuations in the plasma. The topology of toroidal magnetic field is determined by using a novel yet effective technique which involve a tiny plasma-beamlet produced by a tiny filament and a regular camera. The tiny filament is collimated using a collimating cylinder with holes of 1 mm on both sides of the cylinder. A camera is mounted to the 180^0 opposite of the source location, due to which drift due to gradient and curvature of the magnetic field are equal from both side of the source. Therefore any opening observed in field line is due to a vertical magnetic field. An inherent offset has been observed in toroidal field line, without charging the vertical field (VF) coil. It has been further observed that the offset in the field line can be corrected by the application of a particular external VF current for a fix value of toroidal magnetic field and it may open up in another direction by increasing VF current further. Furthermore, as the topology of the field line is determined, two sets of Langmuir probe, each containing two probe tips are mounted from the top separated toroidally by 90^0. It has been ensured that these probes are on the same field line by using tiny plasma beamlet. This helps in determining the minimum value of parallel wavenumber. The details of the tiny plasma beamlet source, offset and its correction and determination of parallel wavenumber studies are discussed in detail in this chapter. The experimental details and findings are published in [**S. G. Thatipamula, Umesh Kumar et al, Rev. Sci. Instrum. 86, 033504 (2015)**]. As discussed, nature of instabilities strongly depends on the path traverse by electrons along the magnetic field line. Therefore nature of quasi-static equilibrium, flow and fluctuation strongly depends on toroidal field topology, detailed study of which is discussed in subsequent chapter i.e, Ch-4.

Chapter-4: Role of parallel connection length on quasi-static equilibrium, flow and fluctuation in a simple toroidal device

Using the information from the Chapter-3, we found that the topology of the toroidal field line can be controlled by varying the external vertical magnetic field (B_v) or toroidal magnetic field (B_T) or both. It has also been observed that for some B_v and B_T ratios the toroidal field lines are nearly close on themselves, therefore, it makes several turns before hitting the limiter or wall. Similarly for some relatively high value of ratio, the field lines are widely opened and hit the limiter or wall in few turns. The parallel connection length can be estimated as, $L_c = 2\pi RN$, where R is the major radius of the vessel, N is the number of turns a field line makes before hitting the wall or limiter. As for few turns L_c is small, it helps in reducing the residual vertical electric field E_z created by the gradient and curvature drifts [6].

This chapter is divided into two parts, part-A and part-B, the details are provided as follows:-

Part-A: Effect of variation of external vertical field on equilibrium, flow and fluctuation using hot cathode source

In this part of experimental study the toroidal magnetic field B_T was kept fix at 220 G at the minor axis and external vertical field in varied. It has been observed that for $B_v \sim 1.0$ G, which corresponds to 12 A of VF current the field lines are almost closed and L_c is very large. Similarly for $B_v \sim 4.5$ G corresponds to 60 A VF current, the L_c is very small. It has been observed that the density on the inboard side increases for small L_c due to effective short circuiting of E_z. Several strong non-linear interaction between modes and between modes and background fluctuations are present, which further modifies the nature of fluctuation and resultant flows. It has also been observed that the L_c strongly controls the nature of fluctuation, net poloidal flow, instabilities and hence equilibrium. The net poloidal flow reduces on the inboard side for the small L_c value. The details of experimental measurement techniques, observations, error-estimation and conclusion are provided in this chapter. The major findings of this work is published in [**Umesh Kumar et al, Physics of Plasmas 23, 102301 (2016)**].

Part-B: Effect of simultaneous variation of external vertical field and toroidal field on equilibrium, flow and fluctuation using hot cathode

In this part of studies, B_T and B_v are varied simultaneously in fixed ratios and these ratios have been chosen on the basis of L_c length. Therefore, we have three different ratios (i) 0 A or inherent L_c, (ii) large L_c and (iii) small L_c. The toroidal field values at minor axis, used are 220 G, 330 G and 440 G and suitable values of B_v have been chosen for large L_c and small L_c for all three toroidal fields based on approach used in Ch-2. The experimental results confirms that for small L_c, density increases on inboard side and a high frequency broad band fluctuation exist. The nature of fluctuation, flow and equilibrium and similar for similar value of L_c. The details are provided in this chapter. A manuscript with the results of these experimental findings is [**Umesh Kumar et al to be submitted (2018)**].

In this present experimental study, there exist a strong net poloidal flow which controls of the nature of fluctuation and quasi-static equilibrium. Therefore to determine the role of poloidal flow, we require a plasma source which has very weak or negligible poloidal flow. Therefore an ECR plasma source is developed for this very purpose, the details of the experiments performed using ECR source and effect of toroidal field topology on ECR plasma characteristics are discussed in subsequent chapter, Ch-5.

Chapter-5: Role of parallel connection length on plasma properties of an electron cyclotron resonance plasma

The experimental studies mentioned in Ch-4 were conducted using a hot cathode produced plasma. However, plasma produced by hot cathode source has zeroth order radial electric field due to negative biasing of hot cathode with respect to the wall. The wall of the vessel is grounded and the bias voltage is around 70 V. This zeroth order electric field provide strong poloidal rotation to the plasma which in turn controls the nature of fluctuation and equilibrium. Therefore to study the role of poloidal flow on fluctuation and equilibrium a electron cyclotron resonance (ECR) source is developed, which has very weak zeroth order radial electric field and hence a very weak or negligible poloidal flow. Moreover, in hot cathode produced plasma the region of minor axis is populated with high energy electrons but ECR source does not have this problem. The ECR source has microwave frequency of 2.45$\pm$0.1 GHz, launched in "O" mode from the outboard side. The average launched power is around 1 kW. The toroidal field strength at the minor axis is 750 G, therefore ECR region lies around -6 cm on the inboard side. The secondary ionization in ECR plasma occurs due to upper hybrid resonance (UHR) and it has been observed that the location of UHR varies with L_c values. For large L_c values UHR lies close to minor axis and therefore density gradient is very weak and for small L_c values it lies close to limiter location on the outboard side, therefore a finite gradient in density exist. As discussed earlier E_z can be minimized by the application of B_v and it well evident for ECR plasma profiles. It has been observed that the density increases with decrease in L_c, which could be attributed to the effective short-circuiting of the E_z. The radial profile of electron temperature for each value of L_c peaks at -6 cm, which is the location of EC resonance. There exist a finite gradient in electron temperature for the case of large L_c cases and weak gradient in temperature for small L_c cases. The radial profile of plasma potential for each L_c has very weak gradient, therefore poloidal flow is very weak, which is evident from the net poloidal flow measurement from the Mach probe. The level of fluctuation for both density and potential is at most $20\% - 30\%$ and one or two modes exist in spectral analysis followed by background fluctuations. The detailed experimental study of role of L_c on plasma properties along with detailed discussion of equilibrium, fluctuation and flow are discussed in this chapter. A manuscript with the results of this experimental findings is [**Umesh Kumar et al to be submitted (2018)**].

As the plasma produced using ECR source has negligible poloidal flow and is free from high energy electron population. To determine the role of poloidal flow on fluctuation, equilibrium and particle confinement, a comparative experimental study has been performed by using two sources. The experimental conditions like working pressure, toroidal and vertical magnetic fields were kept same as far as possible. The details of the experiment and major results are described in chapter-6.

Chapter-6:- Comparative study and role of poloidal flow on equilibrium, fluctuations and particle confinement in a simple magnetized torus for two different sources

The role of L_c on plasma properties for hot cathode source is described in Ch-4 and for ECR source in Ch-5. However due to presence of strong poloidal rotation of plasma in hot cathode produced plasma, equilibrium and nature of fluctuation can be regulated. Therefore a comparative experimental study has been performed to study the role of poloidal flows. Therefore operating conditions like working pressure, toroidal and vertical magnetic field strengths have been kept same as much as possible for both the sources. The toroidal field used is 750 G at the minor axis for both the sources and L_c has been tried to keep the same for both the sources by application of same external vertical field. Various plasma properties like density, electron temperature, plasma potential, level of fluctuation, poloidal flows and particle confinement have been compared. It has been observed that the hot cathode produced plasma is 5-8 times more dense than ECR plasma due to low ionization efficiency in ECR plasma. The level of fluctuations are quite high in hot cathode produced plasma as compared to ECR plasma, moreover nature of fluctuations are also quite different for both the sources. The particle confinement time has been estimated using afterglow technique for both the sources. It has been observed that the nature of density fall is different for both the sources despite having same working pressure, toroidal and vertical magnetic field. However, it has been observed that the confinement time increases with decrease in L_c and it could be attributed to the fact that short L_c quickly reduced the E_z. The detailed comparative experimental studies along with role of poloidal flow on equilibrium, fluctuation and particle confinement have been discussed in this chapter. A manuscript with the results of this experimental findings is [**Umesh Kumar et al to be submitted (2018)**].

It was shown that controlling B_v in an ECR discharge has strong influence on the mean density and mean temperature profiles and hence different instabilities which were flute-like as well as drift-like were found to be unstable. The primary modes thus excited may also drive a secondary mode unstable.

In the next Chapter, we report on Geodesic Acoustic Mode which has a flute-like character driven unstable by a drift-interchange unstable mode for a particular choice of B_v using ECR plasma.

Chapter-7: Observations of Geodesic Acoustic-like mode in a simple toroidal device

Geodesic Acoustic Modes (GAMs) are pressure oscillations supported by plasma compressibility in a toroidal magnetic geometry where average geodesic curvature provides a restoring force. GAMs exhibit top bottom antisymmetry in density fluctuation and potential fluctuations are nearly independent of the poloidal angle. It implies density fluctuation exhibit m=1, n=0 symmetry and potential fluctuation exhibit m=0, n=0 symmetry, where m and n are poloidal and toroidal mode number respectively. The GAMs were first predicted as oscillating zonal flows [10] and are believed to regulate the turbulence in Tokamaks [11]. In this chapter we present a simple and surprising experimental observation of global, discrete, high frequency GAM-like mode in an SMT perhaps the first time. To measure the poloidal mode numbers two sets of Langmuir probes, each containing two pins have been mounted from top and bottom port and similarly two probes are mounted at same radial locations separated toroidally by 120^0. The observed GAM-like mode was found to be generated from the non-linear interaction of drift-interchange mode with itself and its frequency is found to be around three times that of theoretical GAM frequency for an SMT. The reason for this up-shift could be attributed to the interaction of GAM-like mode with background fluctuations [12]. The detailed experimental method to measure GAM-like characteristics, generation of the mode and reason for up-shift in the frequency is described in detail in this chapter. A manuscript containing detailed experimental study and major findings is [**Umesh Kumar et al, in communication (2018)**].

Chapter-8: Summary and conclusion

Chapter 8 is the concluding chapter of this Thesis and provides a chapter-wise summary of all the research problems addressed during the Thesis work. The chapter highlights the effects of parallel connection length L_c on equilibrium, flow, fluctuation and particle confinement in an SMT. It has been observed that flow significantly affects the nature of equilibrium and fluctuation, therefore, it role has been studied by performing a comparative studies for two different sources. It has been observed that the particle confinement increases for small L_c and thus the density. Further a high frequency, global, discrete, high frequency GAM-like mode has been observed in an SMT perhaps the first time. The chapter ends with highlights of future work based on the present Thesis.

List of Figures

List of Tables

1
Introduction

1.1 Simple magnetized toroidal plasma

Magnetically confined plasmas in a toroidal device have drawn significant attention due to their suitable candidature to achieve controlled thermonuclear fusion. Understanding plasma transport and confinement is a significant area of interest in devices like Tokamaks, Stellarators, Reverse field pinch devices (RFPs) to name a few. In spite of remarkable advances in last few decades, magnetically confined fusion is still a burning topic of research worldwide. One of the main issues is the physics of anomalous cross-field transport which are driven by cross-field drifts due to gradients in mean density and temperature profiles. Thus understanding the nature of cross-field instabilities is of paramount importance in understanding their effect on plasma confinement, which in turn affects the usefulness of the device. However, the complexity of the magnetic field geometry in Tokamaks set constraints to carry out experimental studies of the individual instabilities and their role in ensuing transport. A simple magnetized torus (SMT) provides an alternate facility to carry out fundamental plasma studies, particularly for weakly collisional Edge/SOL region of Tokamak.

A current-less simple toroidal device (STP) also known as simple magnetized toroidal device (SMT) [1] (terms used interchangeably throughout the Thesis) is one in which plasma is confined only by the application of toroidal magnetic field. The major difference between a Tokamak and a current-less toroidal device is the absence of a magnetic rotational transform in the SMT. Due to which, magnetic flux surfaces cease to exist in the SMT. Such devices provide a simple yet non-trivial alternative to carry out experimental studies of instabilities, fluctuations and transport [4, 5]. This configuration has been of long-standing interest to the plasma and fusion communities for two main reasons: First, it offers a simple and well-diagnosable testbed in which study of the basic physics of plasma instabilities and the associated transport of particles and energy becomes possible. Second, by virtue of its dimensionless parameters and magnetic geometry, it provides a simplified setting in which one may explore one of the most important topics in fusion research namely, the physics of turbulent transport in the edge region of magnetically confined fusion devices such as Tokamaks. Understanding edge-SOL physics in Tokamaks is an important issue because particles and heat transport across the edge region of these machines largely govern the fusion power output of the entire device.

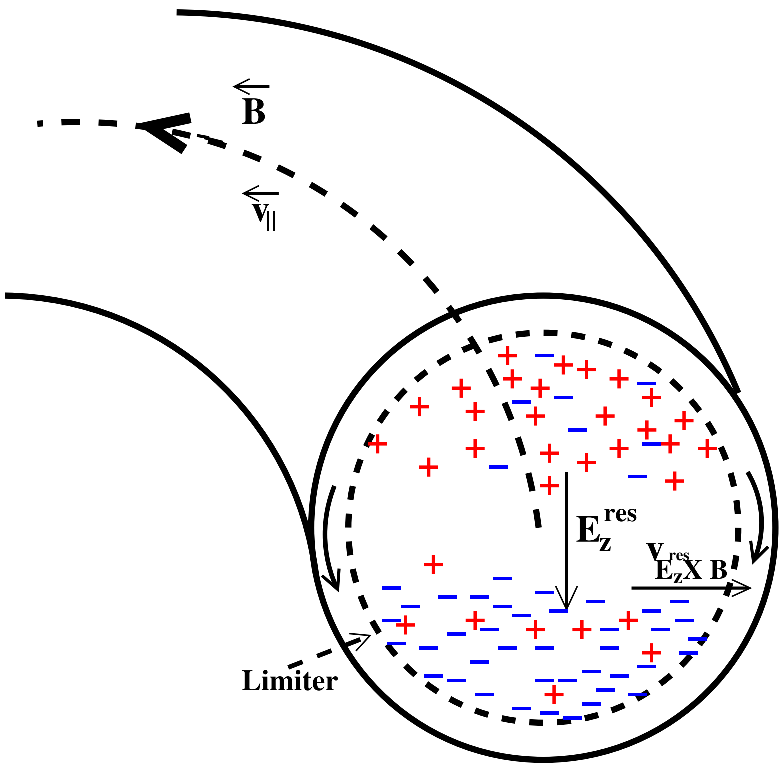

Figure 1.1: A schematic showing the loss of the plasma due to the residual vertical electric field, E_z^{res} in an SMT. The limiter shown helps in reducing E_z^{res}.

At a given collisionality, the motion of electrons is determined by the thermal speed of electrons, collisions and length of the path along the field line. Unlike a Tokamak, where single particle drift orbits are closed, as magnetic rotational transform is absent, drift orbits of charge particles in an SMT are open. The residual vertical electric field, E_z^{res} induced by charge separation due to gradient and curvature drifts drives a cross-field radial transport of the entire plasma due to $v_{E_z^{res}\times B}$ towards low field side as shown in Fig. 1.1. This loss can be minimized by mounting a poloidal continuous limiter [2, 3] as it helps in reducing E_z^{res}. In such cases, the charge flow is along the toroidal field into the limiter, and through the limiter transverse to the magnetic field and returning parallel to magnetic field [2]. In the following Section, let us discuss another methodology to reduce E_z^{res}.

1.2 Role of toroidal field topology

As the electrons traverse relatively faster along the magnetic field lines as compared to across the field lines, the addition of the external vertical magnetic field can facilitate the shortest or longest pathways $\bar{L}_c$ along magnetic field for electrons to minimize E_z^{res} [6]. The length of this pathway along magnetic field maybe defined as parallel connection length, $L_c = 2\pi R N_R$, where R is the local major radius of the torus and $N_R = N_R(R, Z)$ is the number of turns a toroidal field line makes before hitting the wall or limiter at a particular R. Therefore, when B_v is changed, at $Z = 0$ plane, L_c in principle would be a function of R and N_R. However, for simplicity, we propose to discuss in terms of $\bar{L}_c$ defined as $\bar{L}_c = 2\pi R_0 N$, where N is the mean number of toroidal turns before hitting the wall or limiter and R_0 is the major radius of the torus. The $\bar{L}_c$ controls two aspects in a toroidal plasma: (i) by determining E_z^{res}, $\bar{L}_c$ controls the outward radial transport of the plasma and thus controls the nature of quasi-static equilibrium. (ii) $\bar{L}_c$ determines the minimum parallel wavenumber i.e, $k_{||}^{min} = \frac{2\pi}{\bar{L}_c}$, thus controls the nature of instabilities or fluctuation.

The time in which electrons traverses the path $\bar{L}_c$ along toroidal magnetic field can be estimated as follows:

$$t_{\bar{L}_c} \approx \frac{\bar{L}_c^2}{\chi_{||e}} \approx \frac{\nu_{en}\bar{L}_c^2}{2v_{the}^2} \tag{1.1}$$

where $\chi_{||e}$ is electron thermal diffusivity, ν_{en} is electron neutral collision frequency and v_{the} is the electron thermal velocity. For a constant pressure and electron temperature, v_{the} and ν_{en} remains constant for all values of $\bar{L}_c$. Therefore for a given electron temperature (or v_{the}) and ν_{en}, electron travel time is smaller for shorter values of $\bar{L}_c$, resulting in effective minimization of E_z^{res}. Thus radially outward transport due to E_z^{res} can be expected to decrease for small $\bar{L}_c$ values and quasi-static equilibrium can be expected to improve. However, if electrons follow the path $\bar{L}_c$, what happens to the ions? Does it violate the assumption of quasi-neutrality locally? As charge separation due to gradient and curvature drifts violates charge neutrality, the motion of electrons to reduce E_z^{res}, helps conserve the quasi-neutrality. Moreover, if there is any violation of quasi-neutrality, an ambipolar electric field is generated to restore the same.

In experiments, there exist an inherent offset B_{off} in toroidal field lines which tends to open up the toroidal field line. This offset can be measured, details are provided in Chapter. 3. The minimum parallel wavenumber for open field lines is defined as:

$$k_{||}^{min} = \frac{2\pi}{\bar{L}_c} n_T \propto \left(\frac{B_{off} - \bar{B}_v}{B_T}\right) \tag{1.2}$$

where n_T is the toroidal mode number, B_{off} is the inherent offset in the toroidal field in the absence of applied vertical field, which leads to opening of toroidal field lines, B_T is the toroidal magnetic field strength, $\bar{B}_v =< B_v(R,Z) >_{(R,Z)}$. For convenience, we use B_v instead of $\bar{B}_v$ throughout. The B_{off} for each B_T can be determined using a method described in Chapter-3 and based on that, one can determine the values of B_v for which field lines are nearly closed or very large $\bar{L}_c$ and B_v for which field lines are widely opened or small $\bar{L}_c$. Eqn. 1.2 is valid only for open field lines (i.e., when $B_{off} \neq B_v$) and for perfectly closed field line, $N \sim 1$ and $\bar{L}_c = 2\pi R_0$. Therefore, from Eqn. 1.2, $k_{||}^{min}$ is given as $k_{||}^{min} = n_T/R_0$. On the other hand, when field line is "nearly closed", not perfectly, then field line makes several turns before hitting the wall or limiter, it forms a tight upward helix. For this case, N is very large and $\bar{L}_c$ would be the longest. Moreover, if field lines are so wide open that within a single turn, field line hits the wall or limiter, the $\bar{L}_c$ would be equal to the system size and may be considered shortest. However, in the latter case, it may be difficult to sustain a proper plasma discharge, if $t_{\bar{L}_c}$ is less than the ionization time. Hence by changing B_v and B_T, L_c changes and thus $k_{||}^{min}$ can be varied. As is well known, $k_{||}^{min}$ controls the nature of instabilities [7, 13, 14] and can be used to control as well as for the identification various instabilities. For example, for flute like instabilities $k_{||}^{min}$ is expected to be close to zero, whereas for drift like instabilities $k_{||}^{min} \neq 0$ [5, 15]. A transition from drift to interchange instabilities in an open magnetic field line configuration has been shown in TORPEX [16]. Experimental measurement of $k_{||}^{min}$ by directly measuring the magnetic field topology is shown in earlier works [7, 13, 17, 18].

As evident from Eqn. 1.1, E_z^{res} can be reduced by the application of external vertical field and hence can increase the confinement of the plasma [6]. In a work by Nakao et al, [6], the loss of the plasma due to E_z^{res} is estimated by equating toroidal drift to the vertical velocity of the electron. Therefore:

$$v_{E_z^{res}\times B} = \frac{T_e m_e \nu_{en}}{e^2 R_0 B_v^2} \tag{1.3}$$

However, for an inherent offset in toroidal field, Eqn. 1.3 modifies as follow:

$$v_{E_z^{res}\times B} = \frac{T_e m_e \nu_{en}}{e^2 R_0 (B_v - B_{off})^2} \tag{1.4}$$

and the confinement time is given as

$$\tau_C = \frac{a}{v_{E_z^{res}\times B}} \tag{1.5}$$

where a is the minor radius of the vacuum vessel. It can be inferred from Eqn. 1.4 and Eqn. 1.5, that for longer $\bar{L}_c$ values, one can expect rapid loss of the plasma and hence smaller confinement time. However, for shorter $\bar{L}_c$ values, loss of the plasma reduces due to a reduction in E_z^{res} and hence a increase in the confinement time [7]. Therefore by controlling the topology of the toroidal field one can control the loss of the plasma in an SMT.

However, while estimating the confinement time given in Eqn. 1.5, the effect due to the poloidal flows have not been taken into account. As we know, the presence of a substantial poloidal flow can control the nature of quasi-static equilibrium and fluctuation and hence confinement of the plasma [19].

Following the theoretical aspects of the role of the toroidal field topology on quasi-stationary equilibrium in an SMT, a brief review of some of the previous work related to study of the role of the magnetic field topology is given below.

1.3 Review of previous works related to toroidal field topology

Unlike a Tokamaks, a single particle trajectory is not closed in an SMT, therefore, a conventional plasma equilibrium does not exist. However quasi-stationary profiles of mean density and temperature in the presence of sources and sinks do get established. Similar to Tokamaks, inhomogeneity in mean density and temperature profiles lead to cross field instabilities and transport. Plasma instabilities drive transport while, at the same time, are believed to improve confinement via flow fluctuation cycle [8, 20]. While several currentless toroidal devices have reported the formation of 2-D quasi-stationary equilibrium [21] and nearly 1-D (variation along radial direction, nearly constant along Z) equilibria [5], the possible role of connection length in changing the equilibrium poloidal flow, the instabilities and their nonlinear interactions, the role of fluctuating poloidal flow etc. have not been fully explored.

Earlier in BLAAMANN [21] where the plasma source is a hot cathode discharge, it has been observed that if the magnitude of the vertical magnetic field B_v is larger than a critical value, fluctuation levels were found to be drastically reduced. The mean potential well depth was found to be substantially reduced for low values of B_v. Beyond a value of B_v more than a critical value, this potential well was found to disappear. Moreover, a numerical simulation performed for BLAAMANN shows that flute mode can sustain a substantial cross-field current, which is found to be an essential feature of the fluctuating plasma equilibrium. This further explains the experimental equilibrium and coherent flute mode structures have been observed in an SMT [22]. In another SMT with the hot cathode source, namely THORELLO, drift waves destabilization has been studied by evaluating wavenumber, frequency spectra and bicoherence coefficient of density fluctuation associated with drift wave propagation with an application of B_v [23]. Using the spectral analysis [24] and conditional sampling analysis, a study of waves and coherent structures in turbulent plasma [14] have been performed, which were similar to BLAAMANN [22].

A related study in HELIMAK [25], the presence of resistive drift wave turbulence has been confirmed by comparing the experimental measurement with analytical dispersion relation. These observed drift modes found to adjust themselves to have the longest parallel wavelength possible within the torus. However, as parallel connection length becomes larger, the parallel wavelength becomes shorter and the growth rate of the drift mode decreases. In another work in HELIMAK [18] itself, a 2-D numerical simulation indicates that the equilibrium plasma potential which produces sheared $E \times B$ flow is generated by the sheath effect at the ends of open field lines. For zero parallel wavenumber, this flow convects the interchange like fluctuations.

More recently, in TORPEX where the source plasma is based on electron cyclotron resonance [26], it has been observed that for low values of the external vertical field (B_v), drift mode dominates, which corresponds to a long parallel connection length. As soon as B_v was increased, a gradual transition from drift to interchange regime was observed [16]. Furthermore, a 3-D fluid simulation of interchange turbulence was shown to identify two turbulent regimes characterized by low and high confinements. This transition was found to be controlled by vertical magnetic field strength [27]. In another work, the role of parallel connection length in radial particle confinement [7] has been studied by varying B_v. It indicates maximum confinement for an optimum value of B_v, beyond this value the confinement, decreases again. Further, it has been shown that B_v is almost an ideal parameters, the variation of which can control various aspects in an SMT. The application of B_v can generate flows parallel to the magnetic field which is important for reducing the charge separation due to curvature and gradient drifts [28]. It has also shown that a strong drift-interchange instability propagates from a region of large gradients and unfavorable magnetic field curvature. This generates low frequency coherent wave with an almost same frequency almost all over the plasma cross-section [4]. More recently, radial particle transport from localized fluctuations and from radially propagating nonlocal structures or blob [29] have also been addressed. The existence of a critical pressure gradient to drive interchange instability is demonstrated and varying the neutral pressure of the Neon gas [15].

In these experiments, typically the equilibrium radial electric fields E_0 are such that $E_0 \times B \simeq 0.1c_s$ or less and is comparable to perturbed $E \times B$ flows, here c_s is the local sound speed.

In another simple magnetized torus, LATE, a vertical charge separation current in ECR plasma has been observed [30]. This vertical current has been confirmed by current collecting electrodes at the top and bottom of the vacuum vessel. It has been further shown that by the application B_v a toroidal current appears in addition to the vertical current, which fills up the plasma towards the low field side and helps in establishing a discharge [31].

In ACT-I toroidal device [32], the plasma produced and characterized by using different sources such as the Hot cathode, Microwave and lower hybrid ionization method. By using these sources, various experimental applications like lower hybrid wave current drive, ion Bernstein wave heating, parametric decay of lower hybrid waves and detection of density fluctuations associated with RF driven waves have been demonstrated.

Basic Experimental Toroidal Assemble (BETA) [33] is a simple magnetized torus (SMT) in which several experimental studies have been performed. These studies include experimentally simulating the characteristics of F-region of atmosphere [34] by comparing k-spectrum of density fluctuation in BETA with the F-region plasma. The radial outward propagation of low frequency electrostatic turbulence was observed, with the radial wavenumber comparable to the poloidal wavenumber [35]. A study with the hot cathode plasma source confirms the presence of slab nature in the vertical direction. Moreover, it was also observed that the flute-like coherent fluctuations were suppressed in the presence of a weak vertical magnetic field [5] and also confirms the existence of coherent fluctuations as the function of B_v. The toroidal length of BETA has been varied by mounting by putting end plates in the torus, which further controls the parallel wavenumber in BETA. It confirmed the presence of Rayleigh-Taylor instability and demonstrated the transport of fluctuations from the bad curvature region to good curvature region [36]. Detailed analytical studies of dispersion relations for various instabilities for BETA like parameters have been obtained [37] in order to identify the nature of instabilities. In more recent studies, it has been shown that the poloidal flow of plasma can be due to mean and fluctuating electric field and presence of flute like instabilities has been observed on high field side HFS as well as on low field side (LFS) [38]. A transition of fluctuations from coherent to turbulent mode regime has been observed with an increase in toroidal field strength [8]. It has also been found that poloidal flow increases with the decrease in ion mass [39]. Bursty nature is observed in BETA from time series of fluctuation induced poloidal flux. It has been demonstrated that the time series shows a strong non-Gaussian nature of the probability distribution function of fluctuation induced flux [40].

In all the above-mentioned work, detailed experimental work on the role of the zeroth order rotation of the plasma on quasi-stationary equilibrium and fluctuation with variation in mean parallel connection length was not attempted.

1.4 Motivation for the present Thesis

In spite of the various experimental and theoretical work described in Sec. 1.3, to the best of our knowledge, the role of the toroidal field topology on the quasi-stationary equilibrium, fluctuation, poloidal flow and confinement in a simple magnetized torus have not yet been completely resolved. On the basis of that, the present Thesis addresses the following aspects of an SMT in detail.

- As discussed earlier, in BETA, there exist an inherent offset in the toroidal field, due to which field lines do not close on themselves. So, can this inherent offset be determined experimentally using a simple yet effective method? Can this offset can be minimized or "nullified" by the application of an appropriate external vertical field? How can we experimentally determine the toroidal field topology and minimum parallel wavenumber?

- Can a relatively weak vertical component of magnetic field help in reducing the residual vertical electric field by providing a mean parallel connection length $\bar{L}_c$, along the toroidal field? How does $\bar{L}_c$ affects the quasi-stationary equilibrium, fluctuation, poloidal flow and confinement in an SMT?

- Does the nature of the plasma mean profiles, fluctuations and confinement crucially depend on the type of plasma source used?

- If mean plasma profiles depend on the location of the ionization and the type of source, hot cathode or ECR for different B_v values. Can this feature be used to study fundamental physics with application to Tokamak?

- How does the poloidal rotation of the plasma affect the particle confinement and equilibrium in an SMT?

1.5 Thesis outline

Rest of the Thesis is organized as follows. In **Chapter-2**, the experimental system, BETA, a simple magnetized torus in which all the experimental studies reported in the present Thesis has been carried out described in detail. The description also includes technical details of the toroidal and vertical magnetic field assembly along with the vacuum system of BETA. The technical aspects of the two different plasma sources have been described in detail along with the mode of operation and requirements for both the sources. Various diagnostics developed and deployed for the measurement of different plasma parameters, along with the details of measurement circuits, measurement principle and the possible sources of uncertainties have been described in detail.

The topology of the toroidal magnetic field is determined using a novel yet effective method, described in **Chapter-3**. The method involves the use of a tiny plasma beam-let produced by negatively biasing a hot tiny filament with respect to the vessel wall and using a regular camera. The inherent offset in the toroidal field line has been determined using this technique and a numerical simulation performed helps us to find out the reason for the opening of the toroidal field line. It has also been determined that the topology of the field line can be controlled by varying the vertical magnetic field. Moreover, with the help of the tiny plasma beam-let, two tips Langmuir probes have been aligned on the same field line at a different toroidal location to determine the minimum parallel wavenumber.

In **Chapter-4**, a detailed experimental study on the role of the toroidal field topology on the quasi-stationary equilibrium, fluctuation and flow has been discussed for the hot cathode source. From Chapter-3 results, we know that the topology of the toroidal field can be controlled by varying the external vertical magnetic field. Therefore, **Chapter-4** has been divided into three parts.

In Part-I, the external vertical magnetic field has been varied by varying the current in the vertical field (VF) coils for a fixed toroidal field strength of 220 G at the minor axis. The VF current has been varied gradually to understand the role of $\bar{L}_c$ on plasma properties. It has been found that for the VF current of 12 A, the field lines are nearly closed and $\bar{L}_c$ is very large. For the large value of $\bar{L}_c$, there exist few strong coherent modes accompanied by the large poloidal flows. However, for small $\bar{L}_c$ values, density on the inboard side increases with reduction in the poloidal flow on the inboard side close to the limiter and turbulent broadband can be observed in fluctuation spectrum.

In Part-II, both B_v and B_T are varied simultaneously in three fix ratios namely, large $\bar{L}_c$, intermediate $\bar{L}_c$ and small $\bar{L}_c$. It has been observed that the plasma density increases for shorter $\bar{L}_c$ and density profile is symmetric around its peak due to the reduction in E_z^{res}. Moreover for small $\bar{L}_c$ values net poloidal flow reduces close to the limiter on the inboard side, accompanied by broadband in the fluctuation spectrum. However, for large $\bar{L}_c$ values, there exists a strong poloidal flow, accompanied by a few coherent modes followed by the turbulent background fluctuation. The density is higher on the outboard side as compared to the inboard side, could be due to the radial plasma loss due to E_z^{res}.

In Part-III, the detailed discussion on the role of $\bar{L}_c$ on the particle confinement has been presented. The particle confinement is estimated for various values of B_v and for three different values of B_T using afterglow method. It has been observed that the confinement increases with an increase in VF current or a decrease in $\bar{L}_c$.

Therefore from **Chapter-4**, it can be confirmed that $\bar{L}_c$ strongly controls the nature of the quasi-stationary equilibrium, fluctuations, flows and confinement in a simple magnetized torus. The poloidal flow further controls the nature of the quasi-stationary equilibrium and fluctuation, hence to study the role of poloidal flows on the plasma properties, we developed a new plasma source. The details have been provided in the next Chapter.

In **Chapter-5**, experimental studies performed by producing plasma using a newly developed Microwave based ECR plasma source with the variation in B_v have been discussed. As the plasma produced by the ECR source has a very weak zeroth order radial electric field and hence a weaker poloidal flow as compared to the hot cathode produced plasma. Moreover, unlike the hot cathode plasma, ECR plasma is free from the presence of the high energy electrons. As the nature of plasma mean profiles depends on the location and type of the source, therefore, one can expect different plasma density and electron temperature. Due to which, the nature of fluctuation and turbulence, which further affect plasma properties will be different from hot cathode plasma. The plasma is produced by the injection of the Microwave of frequency around 2.45 GHz, with launched power $\sim$ 1 kW in "O" mode polarization from the low field side of the vacuum vessel.

As expected, the value of density increases for the shorter value of $\bar{L}_c$ could be due to the reduction of E_z^{res}. Moreover, the gradient in the density profile is very weak to generate R-T instability on the outboard side. However, a gradient in the electron temperature profile exists for the intermediate and large $\bar{L}_c$ values, which gets weaker for the shorter value of $\bar{L}_c$. Also, the transient nature of modes has been observed for large $\bar{L}_c$ values. The drift-interchange mode has been observed for small values of $\bar{L}_c$.

In **Chapter-6**, a comparative experimental study of plasma properties has been discussed for both the sources under similar experimental conditions namely B_T and neutral pressure with the variation in the toroidal field topology. Apart from the weaker poloidal flows in the ECR plasma as compared to the plasma produced by the hot cathode source, the plasma density in ECR plasma is found to be around 5-8 times less than that of the hot cathode plasma. Moreover, gradients in the plasma density profile for the ECR plasma is weaker to generate Rayleigh Taylor (R-T) instability, but R-T is unstable for the hot cathode plasma.

Furthermore, a comparative study of the particle confinement time for both the sources has been performed using the afterglow method to study the effect of the poloidal flow on the confinement in an SMT. The hot cathode plasma shows usual exponential fall of the density with two fall times known as fast and slow confinement time. The confinement time for hot cathode source increases with an increase in the VF current. However, for ECR plasma the initial fall of the density is found to follow the algebraic nature and subsequent fall is exponential. The confinement time for the ECR plasma increases with a decrease in $\bar{L}_c$. This is consistent with the Nakao's model [6] of the reduction of E_z^{res} with an increase in VF current or decrease in $\bar{L}_c$.

In **Chapter-7**, using ECR source and vertical field, the density and temperature profiles are modulated to obtain an unstable interchange mode. We reported a simple yet surprising experimental finding, perhaps the first time, of the observation of high frequency, discrete and global Geodesic Acoustic like (GAM-like) mode in a simple magnetized torus (SMT). The frequency of the observed mode is around three times higher than the theoretical GAM frequency. Moreover, for three different ion masses, the observed frequency of the GAM-like mode is found to scale linearly with $1/\sqrt{M_i}$, where M_i is the ion mass.

In **Chapter-8**, the conclusion of the various experimental findings and outcome of various analysis are presented. The present Thesis work demonstrates clearly, the experimental evidence of the role of toroidal field topology on the quasi-stationary equilibrium, flow-fluctuation synergy and on the particle confinement in an SMT. Moreover, the details of the experimental studies using two sources, to study the role of the poloidal rotation of the plasma on the plasma properties also discussed in detail. The present Thesis also reports the observation of high frequency, global, discrete Geodesic Acoustic-like Mode (GAM-like), perhaps the first time in a toroidal machine without any effective rotational transform.

Subsequently in Chapter-2, the experimental system, two different plasma sources, various plasma diagnostics have been described in detail.

2

Experimental setup, plasma sources and diagnostics

In this Chapter, a simple magnetized toroidal (SMT) plasma device, BETA is discussed, along with the details of the vacuum pumps, magnetic field assembly, plasma production methods or sources, diagnostics developed and used as well as measurements methods are discussed.

2.1 Device description

In this Section, the technical details of vacuum vessels, magnetic field assembly and supporting structure have been discussed as follows:-

2.1.1 Vacuum vessel

The device for Basic Experiments in Toroidal Assembly (BETA) [33] at Institute for Plasma Research (IPR), India is a toroidal device with the major radius of 45 cm and the minor radius of 15 cm is shown in Fig. 2.1(a). The co-ordinate system of BETA is shown in Fig. 2.1(b) and caption. The device was constructed around 1984 with the purpose of investigating basic physics of plasma in a toroidal geometry. The vacuum vessel of BETA consist of four separate quadrants made up of steel-304 stainless elbow, each quadrant having a circular cross-section and wall thickness of 6 mm. A toroidal electric break has been provided through proper insulation at one of the four joint quadrants. A poloidal conducting limiter

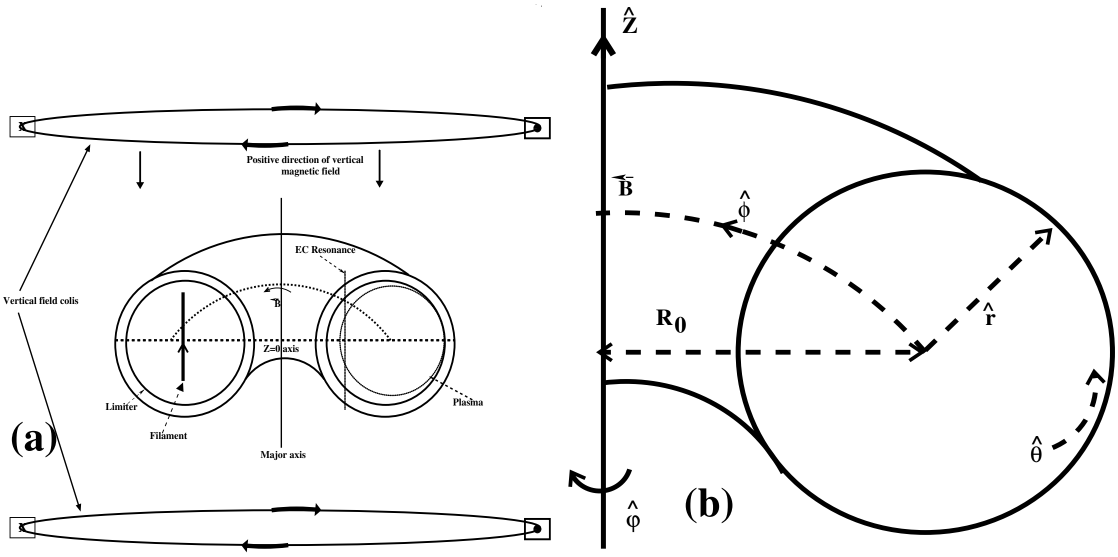

Figure 2.1: (a) A schematic showing BETA device and the location of its diagnostics. (b) The co-ordinate system of BETA. The cylindrical co-ordinates (R, φ, Z) and toroidal co-ordinates (r, θ, ϕ) are shown. The transformation from the cylindrical (R, φ, Z) to toroidal (r, θ, ϕ) co-ordinates can be given as $R = R_0 + rcos\theta$, $Z = rsin\theta$ and $\varphi = -\phi$. The direction of filament current is in $+Z$ direction as shown in (a). Throughout the present Thesis work, all the measurements have been performed radially on the $Z = 0$ plane, unless specified otherwise. The vertical magnetic field coils with the direction of the current which gives positive or downward vertical field are shown. Actual photo is shown in Fig. 2.2.

with open aperture of 18 cm is mounted at one particular toroidal location, 180^0 opposite to the hot cathode location discussed in Sec. 2.2.1. The limiter is made up of SS-304 and kept at the ground potential same as that of the vessel wall. The vacuum vessel has 12 radial ports of 15 cm inner diameter, on the outer wall and 20 ports each of inner diameter of 10 cm at the top and bottom of the vacuum vessel. The top of the vacuum vessel also has 8 ports of 5 cm inner diameter, with 2 ports at the center of each quadrant. A photograph of the actual BETA device along with its TF coils, VF coils, diffusion and rotary pump (one set) and supporting structure is shown in Fig. 2.2.

The vessel is pumped out to a desired base vacuum pressure by using two diffusion pumps through radial ports, diametrically opposite to each other. Each diffusion pump is a Diffstak Model-250 of Edwards make, with pumping speed of 2000 L/s. Each diffusion pump is backed by a rotary pump at the outlet, with a pumping speed of 40 $m^3/hour$. Base vacuum of 4×10^{-6} is achieved and the typical

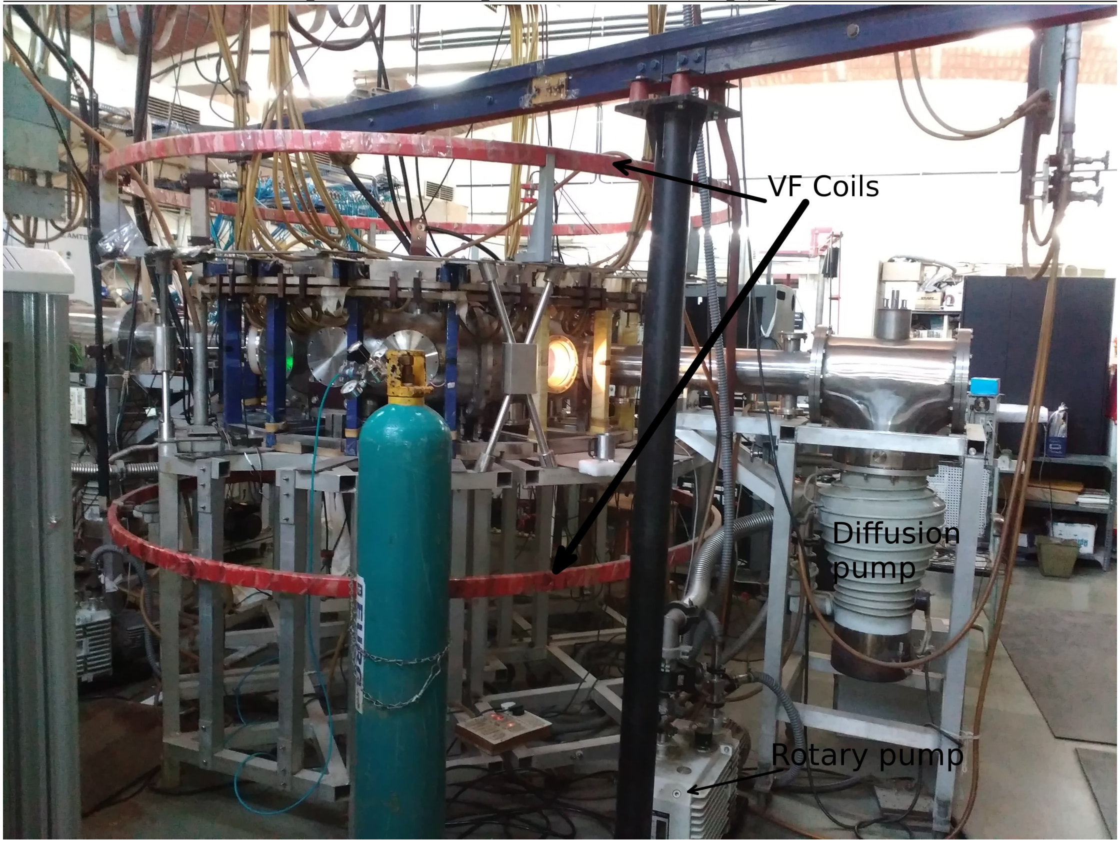

Figure 2.2: A photograph of the BETA, a simple magnetized torus along with its pumping system and magnetic field coils. The blue and yellow bars are the outer leg of TF coils and two red circles on top and bottom are the vertical field coils.

working pressure for most of the experiments presented in this Thesis is 1×10^{-4} torr.

2.1.2 Toroidal Magnetic field (TF) coils

The vacuum vessel is enclosed in a toroidal structure made up of 16 picture frame TF coils, centered at a toroidal radius of 50 cm. As the major radius of the vessel is 45 cm, it implies that the vacuum vessel is shifted inward radially by 5 cm. Each square picture frame coil has a side of 50 cm, with 3 turns made up of 5 cm wide and 1 cm thick copper bars, insulated from each other. These TF coils can provide a maximum magnetic field of 0.1 T at the major axis for the the typical duration of 5 s, by passing a DC current of 5 kA through TF coils. The heat generated in the TF coils due to the large current, is removed by a continuous chilled water circulation through the copper tubes brazed at the inner edge of the copper bars. The TF coils are charged using a high current DC power supply of rating 5 kA, 35 V for the typical duration of 5 s. As soon as the power supply gets triggered, large magnetic field oscillations in time due to the inductive load of the TF coils sets in, which gets stabilized after the typical duration of 250 ms as shown in Fig. 2.3. The plasma production and measurement starts after 500 ms of the power supply trigger. After the toroidal field is stabilized, a maximum ripple of 2% has been observed in TF coils on BETA on the outboard side close to the outer leg.

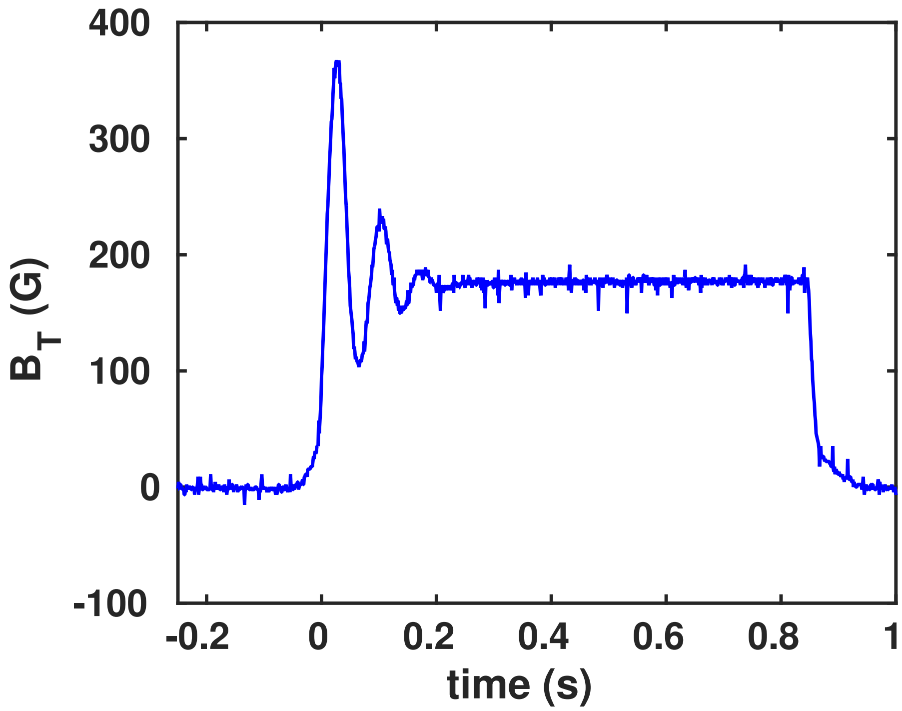

Figure 2.3: A variation of toroidal magnetic field strength with time, measured on the surface of the vacuum vessel from the outside. Therefore, the magnetic field strength after initial large fluctuations is around 180 G. Due to these large oscillations our measurement starts at around 0.5 s (or 500 ms). The small spikes visible on the stabilized part are due to the ripple in toroidal magnetic field, which are found to be around 2%. The frequency of the ripple is around 10 times smaller than the lowest plasma mode observed. The TF is switched off at around 800 ms, however, the duration of TF is larger than the plasma duration.

2.1.3 Vertical Magnetic field (VF) coils

A pair of circular coils is placed at 60 cm symmetrically above and below the major axis of the vacuum vessel as shown in Fig.2.1. Each coil has an inner diameter of 230 cm and is made up of 10 turns of the copper strips of 2.5 cm width and 0.3 cm thickness. As these coils are about 60 cm above and below the vacuum vessel with diameter around 2.5 times larger than the vacuum vessel major radius, therefore, the vertical magnetic field produced by these coils has a very weak dependence on radial (R) and vertical dimension (Z) of the torus inside the vacuum vessel. The current in the clockwise direction in VF coils produces vertically downward magnetic field i.e, in $-Z$ direction and this direction is taken as positive. By passing a current of around 60 A to VF coils (or 600 A$\times$turns), the VF coils provide around 4.5 G at the minor axis of the vessel.

In the present Thesis, VF coils have been charged for various currents for different values of vertical magnetic field. As will be discussed extensively, an application of vertical field controls the topology of the toroidal magnetic field, which further determines the nature of plasma properties, the details of which is provided in the later Chapters.

2.1.4 Supporting structure

The entire toroidal structure of BETA, including the experimental vessel and magnetic field coils, is supported by a set of aluminium stands and a buckling cylinder at the center. The supporting structure also provides flexibility to assemble or disassemble the quadrants and it can also withstand the mechanical forces generated while passing large currents in the TF coils. Each quadrant is supported by a separate supporting stand and one of the quadrants is fixed in its position as its stand bolted on the floor and other three quadrants are free to move by the wheels attached to their stands.

The buckling cylinder is placed on a table at the center of the toroidal system, supported by a separate aluminium stand. The TF coils are supported by stainless steel channels at the top and bottom legs and the buckling cylinder at the inner leg.

2.2 Plasma production using two different sources

For this Thesis in BETA, two different sources namely hot cathode and electron cyclotron resonance (ECR) sources have been used to produce plasma. In order to produce a pulse discharge of the toroidal plasma and to carry out the measurements, a sequence of TTL pulses with preset delays generated using a field programmable gate arrays (FPGA) pulse generator circuit is used. Using this circuit, the toroidal field coil power supply is triggered first because, as discussed in Sec. 2.1.2, TF is generated with few large oscillations followed by the steady state after 500 ms. While the toroidal field is steady after typical duration of 500 ms as shown in Fig. 2.3, the plasma sources are triggered. The details of each source with details of the plasma production is given in the following subsections.

2.2.1 Hot cathode source

In the hot cathode source, a pure Tungsten filament of 2 mm diameter and 20 cm length is heated by passing a current of around 142 A, which causes thermionic emission of electrons. The filament is mounted at the minor axis, at one particular toroidal location and is clamped through flexible supports made up of SS-304, suspended from top and bottom ports. The filament flanges are electrically isolated from the ports of the vacuum vessel using tight insulation between them. After toroidal field is stabilized, the hot cathode is biased in pulse mode for the typical duration of 800 ms after the source is triggered to -70 or -80 V with respect to the wall, which leads to the breakdown of the filled gas. The discharge current for all the studies in this Thesis involving hot cathode source is limited to 5 A. The diagnostics circuits and data acquisition are triggered with an approximate delay of 100 ms with respect to hot cathode bias to avoid initial rise of the discharge voltage. The bias of hot cathode with respect to the wall creates a potential well between the hot cathode and the wall, which further provide a strong zeroth order radial electric field, E_r, where r is the radial co-ordinate in toroidal geometry shown in Fig. 2.1(b). The $E_r \times B$ provides poloidal rotation to the plasma. This poloidal flow which is inherently sheared, in turn, stabilizes the quasi-static equilibrium and controls the fluctuations. The details have been provided in one of the previous work [38]. Also, there exist a radial (r) gradient in density as well. Therefore, due to the presence of density and potential gradients, the hot cathode produced plasma provides a suitable medium to carry out fluctuations studies in detail. The number density of the high energetic electron is estimated to be around 10^{14} m^{-3} for 10^{17} m^{-3} of plasma density [9]. It suggests high energetic electron density is around 0.1% of the plasma electron density. However, the presence of high energy electrons, particularly in the region around the minor axis, limits the study of equilibrium and fluctuations to the region away from the hot cathode source. As discussed, poloidal flow strongly influence the nature of quasi-static equilibrium and fluctuations. A detailed study of the role of weak vertical field on the poloidal flow, fluctuation etc, will be discussed in Chapter-4.

2.2.2 Electron Cyclotron Resonance (ECR) source

As discussed in Sec 2.2.1, the plasma produced by hot cathode has a strong zeroth order radial electric field in the the plasma and region around the minor axis is contaminated by the presence of high energy electrons. To facilitate studies where zeroth order radial electric field is not desirable, a simple pulsed Microwave based plasma source has been conceived which uses a commercially available Magnetron 2M107A. The frequency of the Microwave from the Magnetron is 2.45$\pm$0.1 GHz. For Electron Cyclotron Resonance (ECR) to occur within the vacuum vessel, the toroidal magnetic field should be $\sim$875 G. TF coils are charged such that within the radial domain of the vessel, the toroidal field strength at the major axis is 750 G, therefore EC resonance lies at -6 cm on the inboard side from the minor axis of the vacuum vessel. The schematic of the Microwave system is provided in Fig. 2.4. The Magnetron is coupled to the waveguide (WR-340) using a co-axial to waveguide exciter. A directional coupler with ports for the measurement of forward and reflected power is connected to the waveguide exciter. The forward and reflected ports of the directional coupler have a coupling of -40 dB with the flatness of the passband for both the ports is $\pm$1 dB. The Microwave power is launched from outboard side into the BETA vacuum vessel in “O” mode through a glass window ensuring vacuum compatibility and Microwave barrier window. Here “O” mode implies that the launched Microwave has similar dispersion relation as that of a unmagnetized plasma. In other words, it is plane polarized with Microwave electric field vector parallel to the toroidal magnetic field.

The schematic of the pulsed power supply to energize the Magnetron is shown in Fig. 2.5. For Microwave power to exit from the Magnetron source, the filament

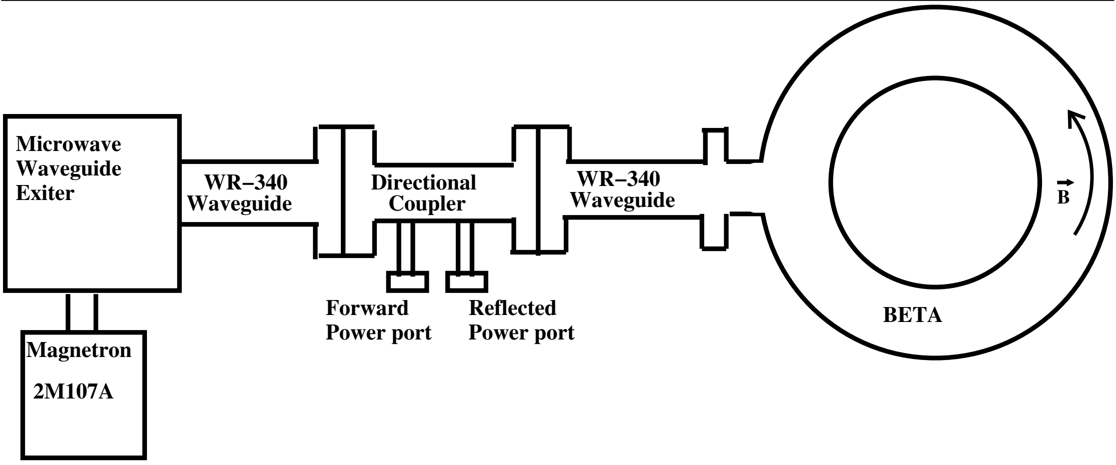

Figure 2.4: A schematic showing launching of Microwave power in BETA device. The Microwave is launched from the outboard side using a directional coupler and a WR-340 waveguide as shown in schematic.

of the Magnetron source is turned on and filament is kept "ON" for the entire experimental campaign. The filament is energized by a single phase, A.C. source from a transformer, with the current $\sim$ 9.4 A for 3.6 V. A high voltage bias pulse of $\sim$4.4 kV/1A is applied to the cathode of the Magnetron, which ensures the generation of Microwave from the Magnetron source. To avoid thermal run-away, a forced passive cooling is employed using a small table fan. A high voltage isolation transformer with adequate isolation feeds the A.C. power to the filament.

A master trigger turns on the power supply, that feeds the TF coils of the BETA described in Sec. 2.1.2. A delay of $\sim$500 ms between master trigger and a synchronization pulse generated from FPGA (Sec. 2.4) based pulse generator. The delay is chosen such that the toroidal field gets stabilized after initial large oscillations as shown in Fig. 2.3.

The switching electronics to the system are maintained on a high voltage deck and all the electrical power requirements to the electronics are supplied through a high voltage isolation transformer with adequate capacity.

The switching and control electronics initiates TTL voltage pulses which are opto-coupled using a Optocoupler. An Optocoupler, interconnects two separate electrical circuits by means of a light sensitive optical interface. The attached output of the electronic pulses drive two IGBT's (IRF-840) in totem pole configuration using a floating power supply of voltage values -200 V and +100 V. The configuration is such that the normal output of the totem pole is -200 V. The

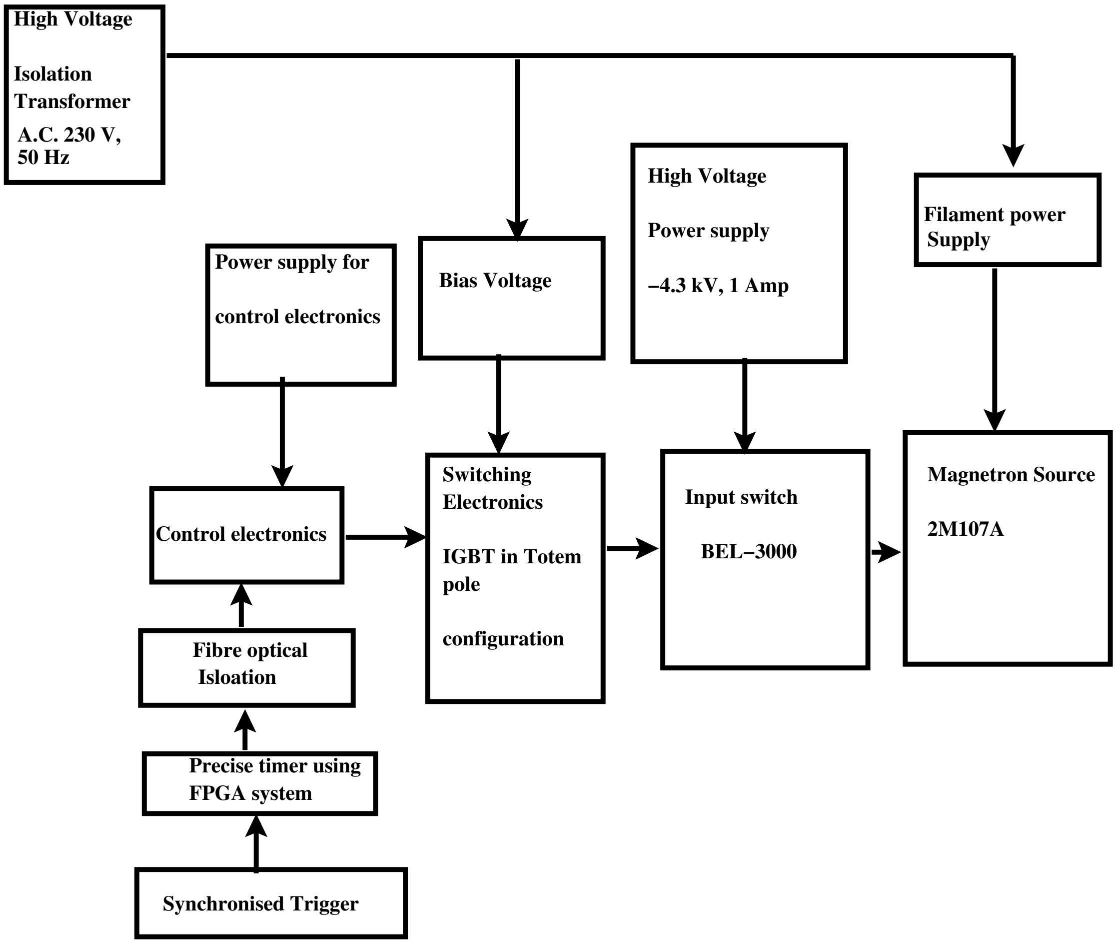

Figure 2.5: A schematic showing pulse power supply to energize the Magnetron. The Magnetron is triggered using the synchronized trigger circuit.

switching control electronics controls the output of the totem pole IGBT's to ensure cut-off (-200 V) prior/after a synchronization pulse. The term "totem pole" refers to stacking components together in series. The purpose of the totem pole configuration here is to supply adequate current to ensure that the output goes up to required high voltage when pulled up and to sink adequate current to guarantee that the output goes down to a required low voltage when pulled down.

A Triode is used as a switch in the current application. The filament to the triode is powered by a single phase, A.C. 26 A, 3.3 V rated transformer. The transformer is connected to a high voltage isolation transformer with adequate capacity. The Triode tube BEL-3000 is used as a high voltage pulsed switch. The cathode of the filament is connected to a high voltage output i.e, -4.4 kV/1 A. The anode of the triode is connected to 100 kΩ and 100 W load resistor and connected to the ground. The effective circuit diagram is shown in Fig. 2.6.

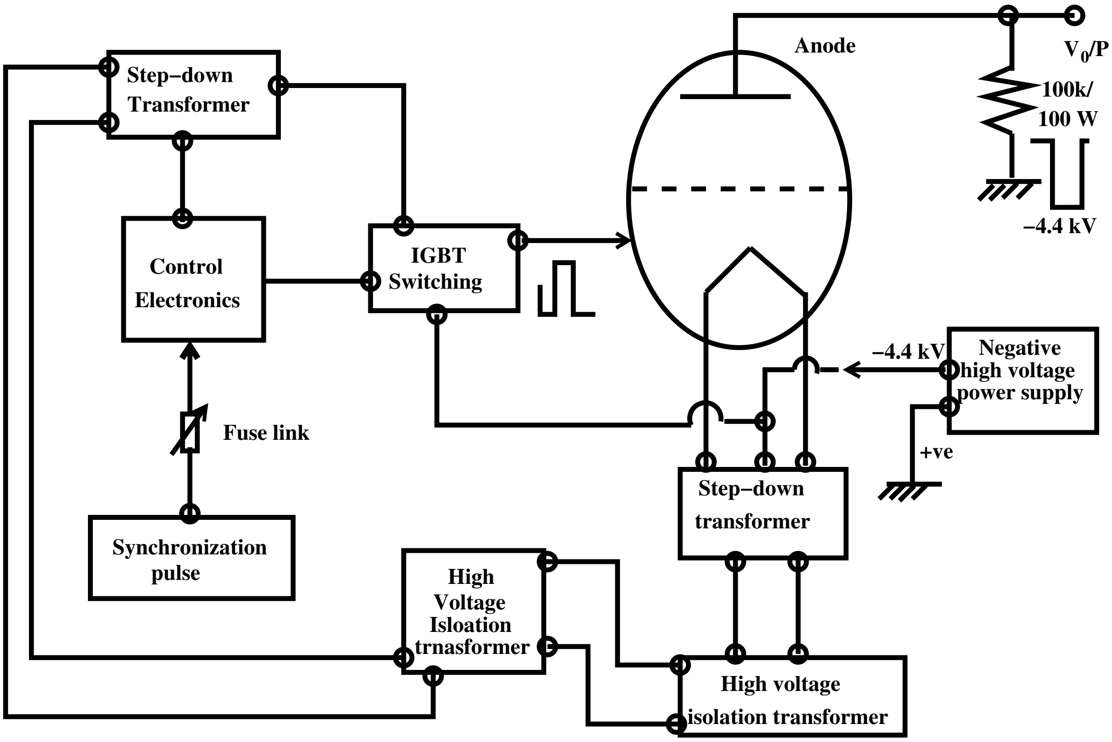

Figure 2.6: A schematic of the circuit diagram of the switching circuit in totem pole configuration. The term "totem pole" refers to stacking components together in series.

The control grid of the triode is maintained at a cut-off voltage of ∼-200 V. This voltage is available to the control grid from the totem pole output of the IGBT's, when the synchronization pulse is applied from the FPGA system, the totem pole voltage goes positive to +100 V. This voltage is available on the control grid of the triode. The triode switches "ON" and the output voltage across the load resistor is ∼-4.4 kV, for a duration set in the FPGA system, which is connected to the Magnetron source. As the conditions for the Microwave power are satisfied, the Magnetron delivers Microwave power for the duration set in the FPGA system. The viewgraph shown in Fig. 2.7 shows the typical traces of the pulsed voltage applied to the Magnetron on channel-1 (yellow), along with forward power on channel-2 (cyan), reflected power on channel-3 (magenta) and ion saturation current corresponding to plasma density measured from a single Langmuir probe on channel-4 (green). We have measured the injected power and the reflected power using suitable detectors, providing the estimate of launched Microwave power. However, there is no estimate of the power coupled to the plasma, as the required detectors are not available. The required measurements will be attempted in the future (details are discussed in Chapter-8).

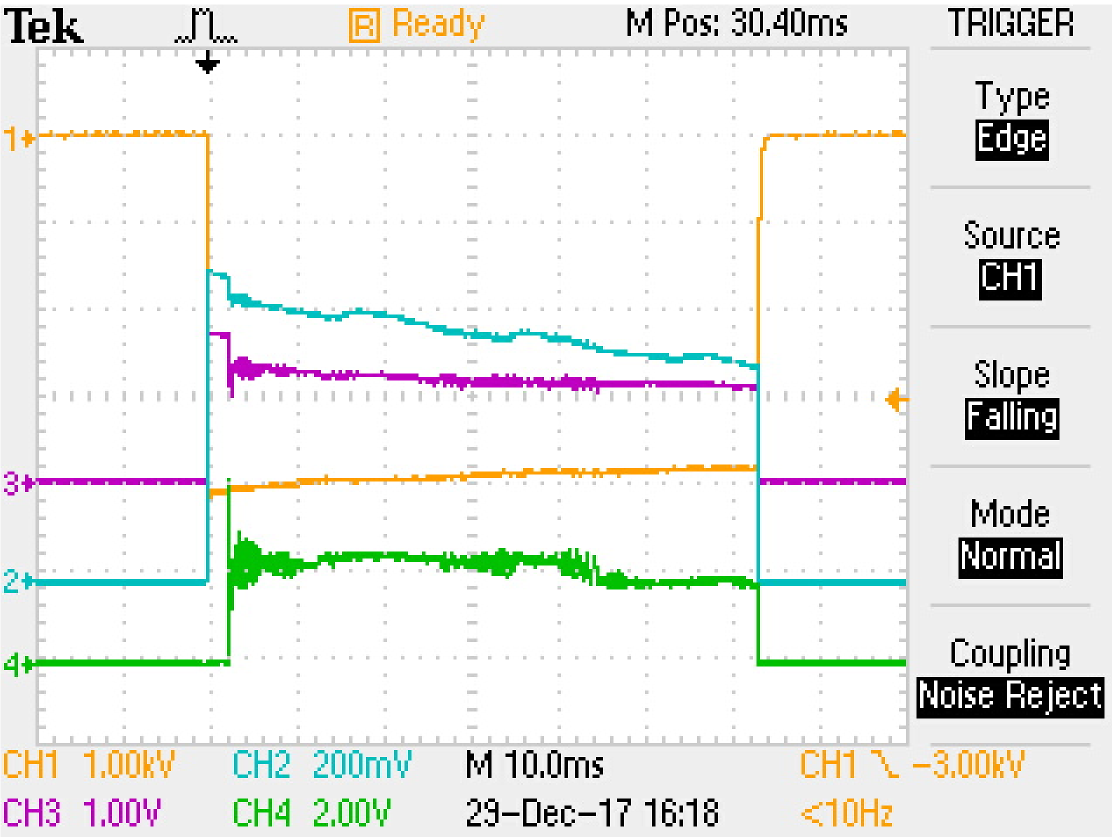

Figure 2.7: A viewgraph showing typical traces of negative pulse voltage applied to Magnetron on channel-1 (yellow), forward power on channel-2 (cyan), reflected power on channel-3 (magenta) and ion saturation current measured from a single Langmuir probe on channel-4 (green). After the proper calibration, the averaged forwarded power is measured to be around 1 kW and reflected power is around 0.25 kW.

In the present Section, we discussed method to produce plasma in BETA using two different plasma sources. The details of the diagnostics used for the measurement of various plasma properties for both the sources are discussed in Sec. 2.3.

2.3 Diagnostics

In BETA Langmuir probe-based diagnostics has been used to measure various plasma parameters. The Langmuir probe (LP) is probably the simplest plasma diagnostics known as it consists of putting a wire into the plasma. However, it is an intrusive diagnostic. The dimension of the wire should be chosen in such a way that it should **in principle NOT** perturb the plasma or alter plasma properties. The Langmuir probe is easy to fabricate but difficult to understand and interpret. Various probe based diagnostics can be used for the measurement of mean and fluctuation of plasma parameters in low temperature plasmas (approximately a few electron volts). Langmuir probes have the advantage in obtaining local measurements of plasma properties. The probe diagnostics used in this Thesis work consist of cold collecting probes and hot emissive probes. The cold collecting probes used are single and triple Langmuir probes, an array of Langmuir probes and Mach probe.

2.3.1 Single Langmuir probe

Probe construction and theory

The single Langmuir probes (SLPs) used in BETA are made up of cylindrical Tungsten wire of 1 mm diameter, 4 mm length. The probes are inserted from radial ports of the vacuum vessel and probe tips are always perpendicular to the toroidal magnetic field. The probe is mounted through ceramic holder with thin ceramic sleeves shielding, to reduce shadowing effect of bulk material close to probe collecting surface. An array of SLPs (Sec. 2.3.3) with specific probe separation has been used for measurements. The entire probe assembly is mounted on a radially movable SS shaft.

When immersed in plasma, Langmuir probe collects current I_{pr} which depends on the applied voltage V_{pr}. Therefore, varying the voltage V_{pr} over a wide range provides a $I_{pr} - V_{pr}$ characteristics of LP, ranging from ion saturation current to electron saturation current. Assuming the plasma to be quasi-neutral, negligible ion temperature and assuming that electrons satisfy a Boltzmann distribution function, the I-V characteristics is as follow [41]:

$$I_{pr} = 0.5Aen_0\sqrt{\frac{T_e}{m_e}}\exp[e(V_{pr} - \phi_p)/T_e] \tag{2.1}$$

where A is the effective probe collection area, n_0 is the plasma density, T_e is electron temperature, ϕ_p is plasma potential and m_e is electron mass. As the probe has been mounted on the vessel from one of the radial ports, the probe tip is always perpendicular to the toroidal magnetic field B_T, therefore, Eqn. 2.1 is valid as far as $V_{pr} < \phi_p$ or the ion Larmor radius is larger than the probe radius.

As shown in Fig. 2.8(a), the $I_{pr} - V_{pr}$ curve has three regions. First region is the ion saturation current I_{sat} region, where $V_{pr} << \phi_p$. For these V_{pr} values, all the electrons get repelled and LP collects ion current I_i only. If the V_{pr} increase gradually, LP starts collecting electron current I_e as well and at a particular value when $I_i \approx I_e$, the corresponding voltage is called floating potential ϕ_f. For sufficiently large and negative applied voltage, $V_{pr} << \phi_f$, the current should ideally be independent of V_{pr} and is known as ion saturation current I_{sat} given by

$$I_{sat} \approx 0.5Aen_0\sqrt{\frac{T_e}{M_i}} \tag{2.2}$$

where M_i is the ion mass. However in actual practice due to Child-Langmuir law, the I_{sat} increases with increase in V_{pr} due to increase in sheath thickness [41]. Therefore, plasma density can be obtained from ion saturation current as follows:

$$n_0 = \frac{2I_{sat}}{eAc_s} \tag{2.3}$$

where $c_s = \sqrt{T_e/M_i}$. By increasing V_p further to the range of $\phi_f < V_{pr} < \phi_p$, there is second region of $I_{pr} - V_{pr}$ known as transition region or exponential region, which is given by the Eqn. 2.1. This exponential part of $I_{pr} - V_{pr}$ curve, when plotted semi-logarithmically versus V_p, should be a straight line if the electrons are Maxwellian. The electron temperature can be determined by the inverse of the slope of this straight line.

As soon as $V_p > \phi_p$, the electron saturation part of I-V curve begins. Theoretically, there exist an electron saturation region, however experimentally obtained curve does not have well defined electron saturation and a weak “knee” correspond-

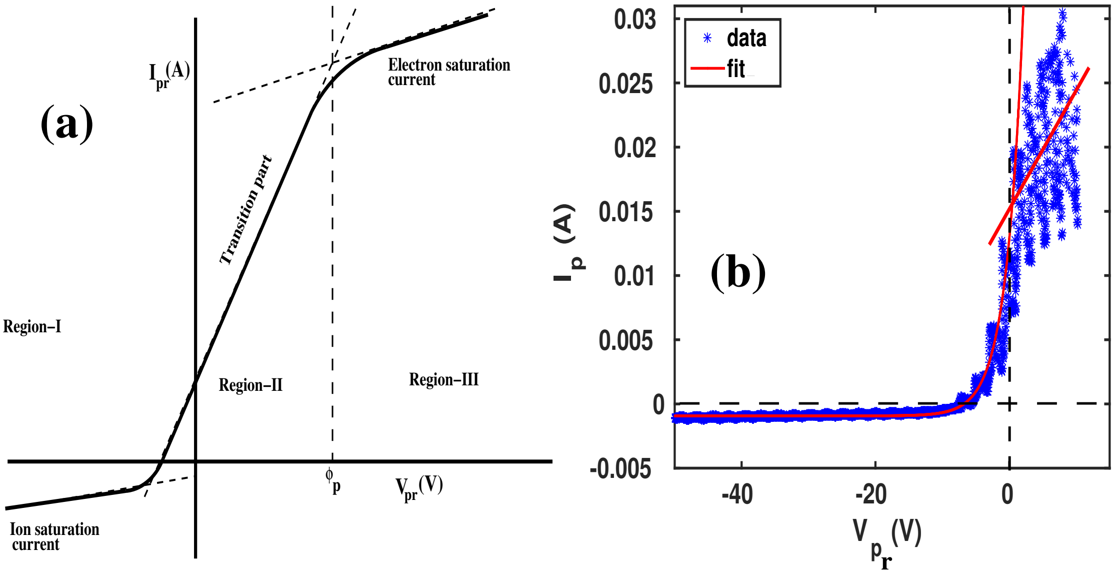

Figure 2.8: (a) A typical theoretical $I_{pr} - V_{pr}$ curve of a single Langmuir probe, showing ion saturation region, transition region and electron saturation region. (b) Experimentally obtained I-V characteristics averaged over 40 cycles, along with fits for $B_T = 220$ G, at outboard side. The exponential curve is fitted with red curve, which fits the ion saturation and transition region of I-V and the second red straight line fits is in the electron saturation regime. The intersection point of exponential and straight fit determine the plasma potential.

ing to plasma potential is present. But I-V curve in magnetized plasma neither has well defined "knee" nor electron saturation. Therefore, as discussed earlier, the Langmuir works well for $V_p < \phi_p$. Hence to obtain time variation of plasma parameters various diagnostics have been used, which are discussed in subsequent section.

Signal electronics for SLP measurements

To sweep voltage to generate I-V characteristics curve, a sawtooth wave generator has been used. The circuit diagram of sawtooth wave generator is shown in Fig. 2.9. As the typical floating potential for the hot cathode plasma varies in the range of -5 V to -35 V and the plasma potential is typically around 2 V, therefore, typical range of sweep voltage is -60 V to +20 V. The sweep period is 10 ms repeatedly swept across the probe for 40 cycles. The sweep across LP provide an average value of n_0, T_e, ϕ_f and an approximate ϕ_p. However, Langmuir probes may need to be compensated while using in a time varying field like in capacitive discharges as the plasma potential and T_e part of $I_p - V_p$ also oscillates with the same frequency, resulting in higher electron temperature than the actual T_e. However, for Microwave discharge of frequency 2.45 GHz, therefore the oscillations are much faster than the measurement time. Therefore, the compensation of Langmuir probes is not needed [42]. Therefore, these diagnostics can be used for the measurements in an ECR plasma without any hassle.

In order to obtain the time variation of above said parameters as a function of time, the following measurement techniques are used.

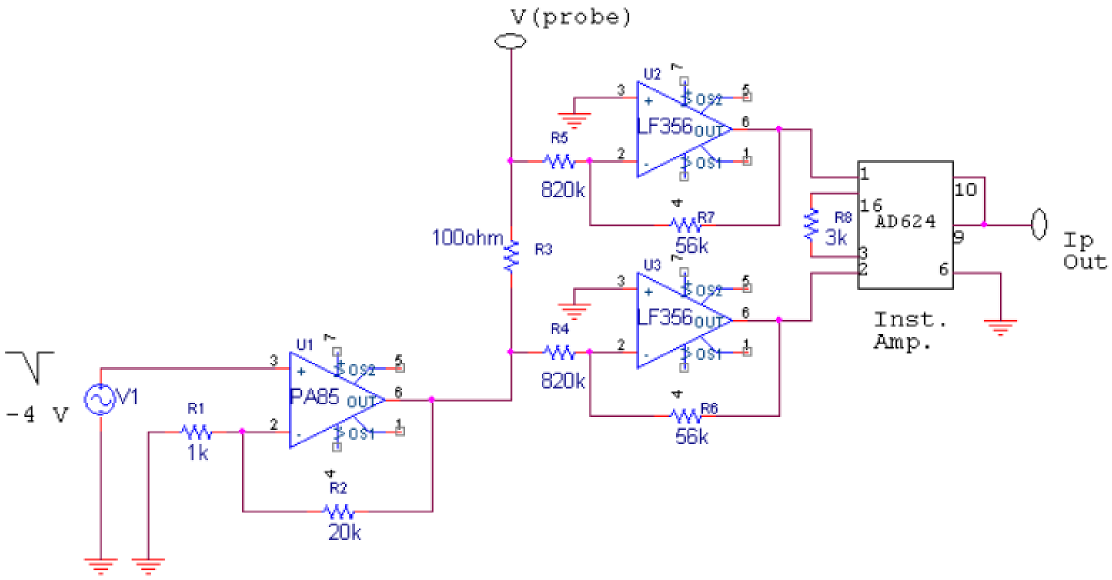

Figure 2.9: Circuit diagram of the sawtooth wave generator used to sweep voltage across the single Langmuir probe to obtain full I-V characteristics. The figure is taken from T. S. Goud Thesis, IPR (2012) [19] with permission.

To measure I_{sat} as a function of time, without sweeping voltage across the probe, a sufficient fixed negative bias ($V_p < \phi_f - 3T_e/e$) is applied across the probe. In our case the bias voltage for hot cathode produced plasma is typically -40 to -50 V and for ECR plasma the bias voltage is around -30 V applied using a current to voltage (I to V) converter circuit. The I to V circuit shown in Fig. 2.10 is made using op-amp OPA454, which has a common voltage rating of 100 V. The circuit consist of two parts, first parts provides a negative bias to the probe and provides an output voltage, which is the sum of bias voltage and the voltage proportional to the probe current. The differential amplifier at the second stage subtract the bias voltage from the first stage output and provides voltage proportional to probe current. The time series of I_{sat} obtained using I to V converter provides mean and fluctuation in the density.

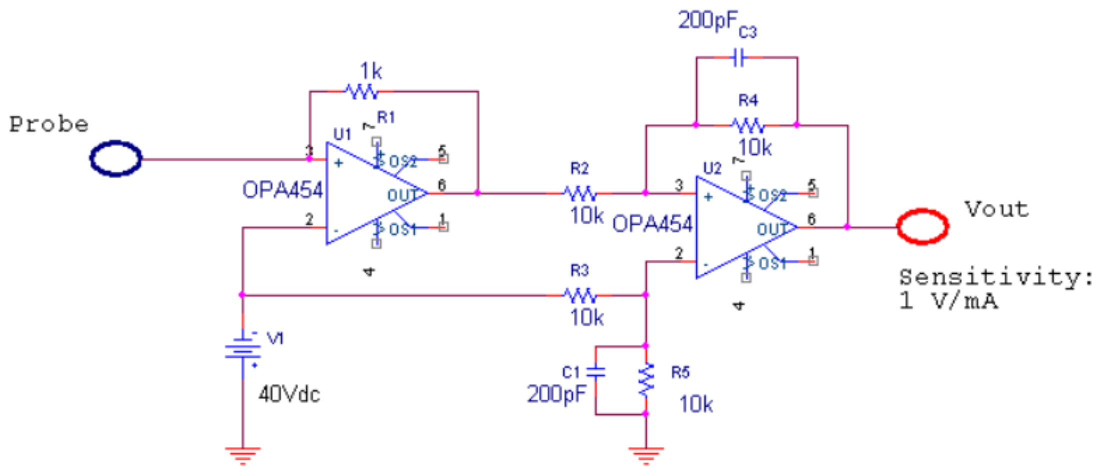

Figure 2.10: Circuit diagram of the I to V circuit used for the measurement of ion saturation current. The figure is taken from T. S. Goud Thesis, IPR (2012) [19] with permission.

Similarly, time series of floating potential can also be obtained using the voltage follower circuit shown in Fig. 2.11. The voltage follower circuit is made up by using a high common-mode voltage a PA85 operational amplifier as a buffer. The measurable voltage range for floating potential is $\phi_f \sim$ 0 to -100 V, which is attenuated by a factor of 20, before acquiring using the data acquisition system.

As discussed earlier, T_e can be determined by taking the inverse of the slope of the semi-logarithmic plot of the transition region of $I - V$ curve of the Langmuir probe. Time series of T_e is measured directly using triple Langmuir probe described in Sec. 2.3.2.

2.3.2 Triple Langmuir probe

Probe construction

Triple Langmuir probe (TLP) directly provide instantaneous values of electron temperature and ion saturation current since the probe operates at a fixed bias and no voltage sweep is required. Earlier it has been observed that the measure-

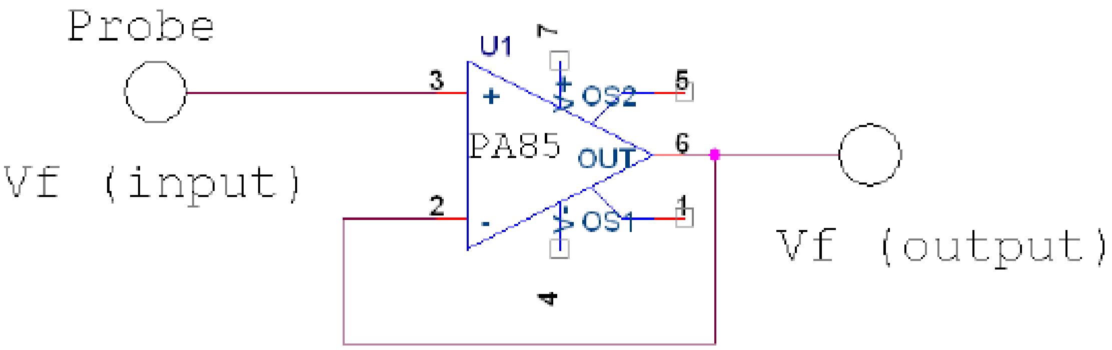

Figure 2.11: Circuit diagram of the voltage follower circuit used to measure time series of floating potential. The figure is taken from T. S. Goud Thesis, IPR (2012) [19] with permission.

ment of electron temperature from single Langmuir probe shows spuriously high values when the voltage scan value exceeds the floating potential [43]. A TLP operates close to floating potential region of I-V characteristics, with one of the probes exceeding floating potential, ϕ_f by only a small voltage, which is a measure of electron temperature T_e. The TLP used for simultaneous measurement of T_e and I_{sat} consist of three tungsten tips, each of diameter 1 mm and length around 3 mm, mounted on a cuboid ceramic block. The whole probe assembly is mounted through an SS metal shaft which can move throughout the radial location at $Z = 0$ plane. The TLP is mounted in such a way that is perpendicular to the toroidal magnetic field.

Signal electronics for TLP measurements

The measurement scheme adopted for TLP is such that one of three probes is floating and other two probes are biased with respect to each other. All the measurements were recorded with respect to the vessel ground. Since the probes have a direct reference through plasma, therefore, the biasing circuit has different "ground", which provide isolation to the measurements. The electrical schematic is provided in Fig. 2.12. The probes are labeled as 1 - floating tip, 2 and 3 biased and 2 is relatively positive. The bias between probes 2 and 3 (V_{23}) has to be sufficiently enough ($V_{23} > 3T_e/e$), so that probe -3 draws only ion saturation current. Therefore a fixed bias of 12 to 24 V is applied between two probes using batteries.

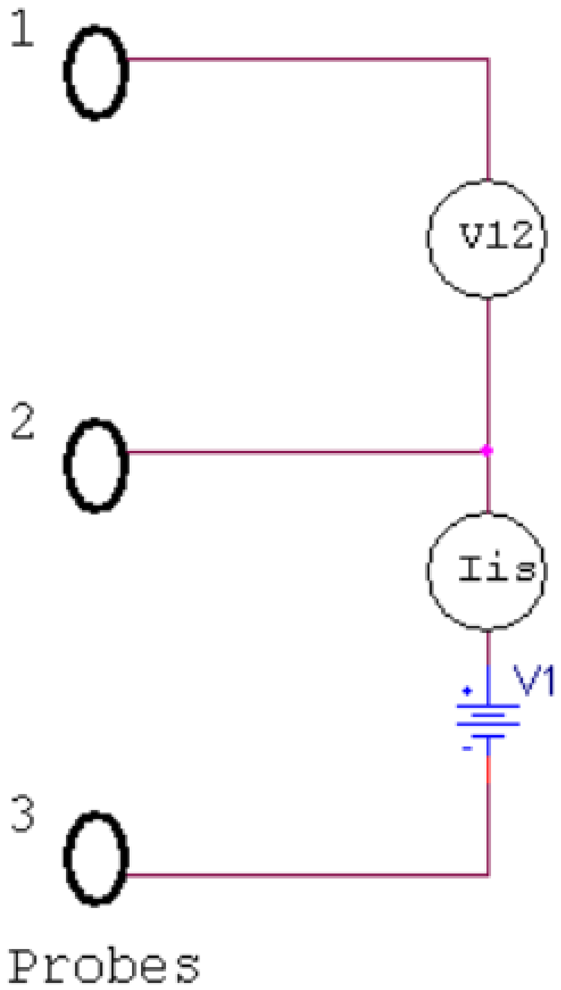

Figure 2.12: Schematic method employed for TLP measurements. '1', '2' and '3' are the numbers labeled for three probes.

The circuit diagram of used for TLP measurements is shown in Fig. 2.13. It can be observed that the circuit has two parts, the first part provides a direct measurement of T_e time series and the second part provides time series of I_{sat} by measuring the voltage drop V_R across 100 Ω resistance. The first part is further divided into two parts, one which determines the probe-1 floating potential using buffer circuit and the second part provides difference voltage (V_{12}) of probe-1 and probe-2 (positively biased probe). Both the quantities (V_{12} and V_R) are obtained using analog isolation amplifier.

As shown in Fig. 2.12, probe-2 is biased positively with respect to probe-3 and probe-1 is kept floating. The current flowing in all these probes is given as follows:

$$I_1 = I_{1e} \exp(-\frac{V_1}{T_e}) + I_{1i} \tag{2.4}$$

$$I_2 = -I_{2e} \exp(-\frac{V_2}{T_e}) - I_{2i} \tag{2.5}$$

$$I_3 = I_{3e} \exp(-\frac{V_3}{T_e}) + I_{3i} \tag{2.6}$$

where I_1, I_2 and I_3 are the current flowing through the probes 1, 2 and 3, respectively, and the negative and positive signs represent electron and ion current collection. V_1, V_2 and V_3 are the potentials at the respective probe tips. As probe-2 and 3 are biased with respect to each other, the current flowing through them remains the same, i.e. $I_2 = I_3$, using this condition and rearranging Eqns. 2.4, 2.4 and 2.4, we obtain

$$\frac{I_1 + I_2}{I_3 + I_2} = \frac{[I_{1e} \exp(-\frac{V_2}{T_e}) + I_{1i}] - [I_{2e} \exp(-\frac{V_2}{T_e}) + I_{2i}]}{[I_{3e} \exp(-\frac{V_3}{T_e}) + I_{3i}] - [I_{2e} \exp(-\frac{V_2}{T_e}) + I_{2i}]} \tag{2.7}$$

Assuming all the probes are of equal dimension and they collect equal electron and ion saturation currents i.e. $I_{1e} = I_{2e} = I_{3e}$ and $I_{1i} = I_{2i} = I_{3i}$. Furthermore, as probe-1 is floating, it means $I_1 = 0$. Hence Eqn. 2.7 reduces to

$$\frac{1 - \exp(-\frac{V_{12}}{T_e})}{1 - \exp(-\frac{V_{32}}{T_e})} = \frac{1}{2} \tag{2.8}$$

where $V_{12} = (V_1 - V_2)$ and $V_{32} = (V_3 - V_2)$. When $V_{23} > V_{12}$, the temperature can be estimated as follow.

$$T_e = \frac{-V_{12}}{\ln(1/2)} = \frac{V_{12}}{0.693} \tag{2.9}$$

Hence, T_e is estimated from V_{12}. The above mentioned circuit can measure T_e in the range of 0.2 eV to 30 eV.

In similar low temperature toroidal devices, it has been found experimentally that the electron temperature fluctuations [44] are less than 1%. Hence, in this Thesis work, the effect of temperature fluctuations have been considered negligible. In order to accurately obtain electron temperature fluctuations, it is well known that even the capacitative pickup of the TLP has to be taken care of in the mea-

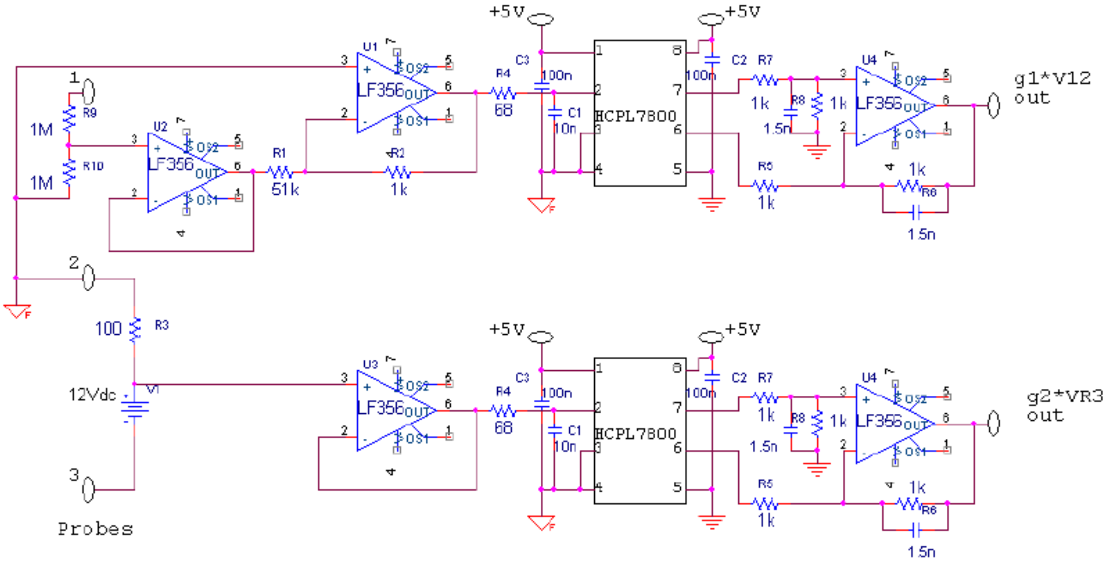

Figure 2.13: The circuit diagram of used to measure directly T_e and I_{sat} from triple Langmuir probe. The first part of the circuit provides T_e and the second part provides I_{sat}. The figure is taken from T. S. Goud Thesis, IPR (2012).

suring circuits. More on this will be discussed in Chapter 8 in the future scope Section.

2.3.3 Radial array of Langmuir probes

A linear array of four single Langmuir probes is used to determine the density (n_0) and floating potential (ϕ_f) time series simultaneously. The radial separation between consecutive probe tips is 5 mm, length of each tip is around 4 mm and probe tips are aligned vertically. The probe array is aligned along the major radius in the horizontal mid-plane of the torus. The ion saturation current and floating potential time series are measured using the I to V converter circuit shown in Fig. 2.10 and voltage follower circuit is shown in Fig. 2.11 respectively. The important application of this diagnostics is in the estimation of fluctuation induced poloidal flux which will be discussed in Chapter 4.

2.3.4 Mach probe

Mach probe provides a direct measurement of the plasma flow velocity, which is based on the principle of the asymmetry in the particle flux in upstream and downstream direction, when a flow exists. Several theoretical models exist to estimate the flow velocity using fluid [45–47] and kinetic [48] approaches.

The Mach probe used in this Thesis for estimating net poloidal flow in BETA consist of two circular metallic collection surfaces. Theoretically, the separation of two probe surfaces should be as small as possible to accurately measure the local flow, however, due to experimental constraints, the separation between the probe surfaces is finite and which define the size of the ceramic block, in which probe is mounted. In our case, the block is cylindrical in shape with length and diameter of 10 mm. The probe surfaces are placed at the depth of 2 mm into the ceramic block for convenience, however measurement of net flow depends on the complexity of the length of the ceramic block and depth of the probe surfaces but details are not well known. The entire probe assembly has been mounted on an SS shaft, which can move radially at $Z = 0$ plane and mounted on the vacuum vessel perpendicular to the magnetic field. The schematic view of the Mach probe is shown in Fig. 2.14

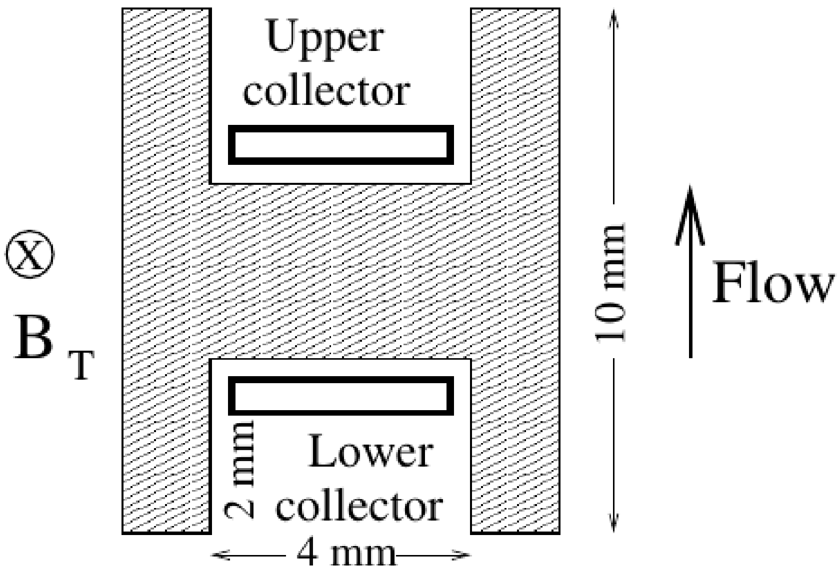

Figure 2.14: Schematic view of Mach probe used for net poloidal flow measurements at $Z = 0$ plane. Upper and lower collectors diameters are shown to be 4 mm, however, it has been reduced to 2 mm for $B_T > 440$ G, such that probe radius $r_P < r_{Li}$, where r_{Li} is the ion Larmor radius. The figure is taken from T. S. Goud Thesis, IPR (2012) [19] with permission.

The model used for net flow measurements in BETA is based on magnetic field symmetry arguments to eliminate the magnetic field dependence [49]. The cylindrical axis of Mach probe is usually aligned perpendicular to the toroidal field direction and difference of ion saturation currents of two collecting surfaces provides net poloidal flow, at $Z = 0$ plane. The net poloidal flow is estimated from the following equation,

$$\frac{v_{net}}{c_s} = \frac{1}{\alpha} \frac{I_{is,0}(upstream) - I_{is,0}(downstream)}{I_{is,0}(upstream) + I_{is,0}(downstream)} \tag{2.10}$$

where c_s is the local ion acoustic velocity and α is a calibration factor, may be accurately obtained by using a "known flow". The calibration factor α is estimation and description of possible uncertainties in flow measurement are described in detail in Chapter-4.

Though the derivation of net flow is based on elimination of magnetic field effects, the method is applicable for the condition $r_{L_i}/r_P > 1$, where r_{L_i} is ion Larmor radius and r_P is probe radius [49]. Therefore, two separate Mach probes with different open aperture for ion collections have been used for $B_T \leq 440$ G and for $B_T > 440$ G. The open aperture of Mach probe used for lower fields is around 4 mm and for the higher field values Mach probe with 2 mm open aperture has been used such that the ions should be unmagnetized with respect to the probe. To measure the poloidal flow, ion saturation current has been collected on both the side of the Mach probe using the I to V converter circuit shown in Fig. 2.10 and appropriate gain has been used to amplify the probe signal using signal conditioning circuits discussed in Sec .2.4. The net poloidal flow is calculated using the Eqn .2.10, throughout the radial location at $Z = 0$ plane. To check the area asymmetry in two collecting surfaces, the ion saturation current is collected on both the surfaces. Let us say probe-1 is collecting upstream and probe-2 is collecting downstream current then the probe is rotated by 180^o, such that probe-1 now collects downstream current and probe-2 upstream. Ideally speaking, if the area of both the probes is same, then the upstream or downstream current collected by either probe should be same, therefore, a difference of the upstream or downstream current collected by probe-1 and probe-2 provides area asymmetry in the Mach probe. The other uncertainties in the measurement include an error in estimating α, uncertainty in ion saturation current measurement and statistical variation over various shots, the details of these are provided in Chapter 4.

2.3.5 Emissive probe

As discussed in Sec. 2.3.1, theoretically plasma potential can be determined by sweeping the voltage across the Langmuir probe and "knee" around (see Fig. 2.8) the electron saturation region determines the plasma potential. However, during experimental measurements particularly in a magnetized plasma, electron saturation does not occur and the "knee" cannot be easily determined and values obtained are erroneous.

Using the fact that the probe will emit below the plasma potential, but not above it, a direct measurement of ϕ_p is possible using hot Langmuir probe or better known as the emissive probe [50]. Following methods can be used to accomplish this task [50], (i) separation technique, (ii) inflection point method and (iii) floating point with large emission. In order to obtain plasma potential using separation method, the probe could be heated to a point just below emission and by shorting part of the circuit with a button, one can temporarily increase the temperature, so that the emission increases. The lowest potential at which the collected current was same for the non-emitting and emitting cases was taken to the plasma potential [50]. However, considering space charge, this method was found to be not suitable for measurements. The space charge formed around the hot probe restrict electrons motion towards plasma and hence obtained measurements may not be accurate. The inflection point method is based on obtaining the full $I-V$ characteristics of the emissive probe with finite emission and in the limit of zero emission approaches, the plasma potential. In our present method we have used the floating point with large emission method which is based on the fact that as emission increases, the floating potential of an emissive probe approaches the plasma potential [51]. However, as in this method, the probe has to be heated to the level of maximum emission and emitted electrons form a space charge around the emissive probe. Emissive probes are known to work best for densities in the range $10^5 - 10^{12}\ cm^3$ and space charge effects are known to be insignificant for magnetic fields when the average electron Larmor radius $\bar{\rho}_{Le}$ is larger than the probe radius r_{pr} [50–52]. As discussed, maximum toroidal field used in our measurement is around 750 G at the minor axis, which corresponds to averaged electron Larmor radius $\bar{\rho}_{Le} \simeq 0.1$ mm, therefore we have chosen $r_{pr} \simeq 0.0625$ mm, shown in Fig. 2.15 and thus space

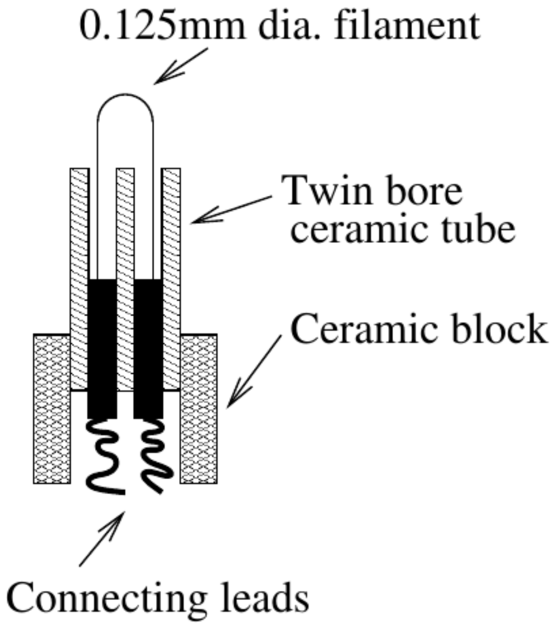

Figure 2.15: Schematic view of emissive probe used for direct measurements of plasma potential at $Z = 0$ plane. The figure is taken from T. S. Goud Thesis, IPR (2012) [19] with permission.

charge effects would not dominate. Hence, the only major source of error is of the order $\frac{T_w}{e}$ where T_w is the temperature of the heated probe [52].

A schematic view of the emissive probe is provided in Fig. 2.15. The emissive probe loop is heated by passing 2.5 A of DC current across its terminals with an isolated DC power supply. Typically 3-5 V potential drop is observed across at the heating DC supply, depending upon the contact resistance of emissive probe connections. Therefore, measurements have been performed across a potential divider applied between two terminals using voltage follower circuit shown in Fig. 2.11.

2.4 Signal conditioning and data acquisition

The data acquired from experiments is analog voltage over a wide range of voltages from various probe circuits discussed in previous sections. However, the digitizers used can work in the range of ±10 V with a 14-bit resolution. Therefore, before putting the analog signal to digitizers, it is required to amplify or attenuate the signal depending on the signal output from the probe circuits. Moreover, the characteristics plasma fluctuation which is reflected in the measured parameters do vary in a wide frequency range; depending on the sampling frequency of the digitizers. Thus analog bandwidth of the signal is determined according to Nyquist criteria to avoid aliasing effect. These tasks have been accomplished using suitably designed signal conditioning cards which consist of analog circuits.

For experimental measurements in BETA, two different kinds of signal conditioning cards have been utilized and are labeled as type-1 and type-2. Type-1 has pre-amplification of the signal, with a varying gain factor. Type-2 has pre-attenuation over a varying range. The dominant plasma fluctuations are expected to be of low frequency nature and substantially lower than the 35 kHz. In the present work, we focus on the study of low frequency phenomenon and use a low pass filter of 35 kHz in signal conditioning cards for measurements which terminates all the higher frequencies without eliminating any frequency of interest. Multiple signal conditioning cards are stacked in an aluminium chasis which is mounted on the diagnostics rack adjacent to the vacuum vessel. Suitable isolation is provided from the chasis ground, to avoid possible ground loops. The signal conditioning cards are connected to vessel ground. The analog signal obtained from these cards are digitized using a 14-bit PXI based NI-6133 data acquisition system. the digitizers have a simultaneous sampling with a maximum sampling rate of 2.5 MS/s, a maximum voltage range of ± 10 V and a deep on board memory of 16 MS. The trigger for the Data acquisition is a TTL pulse from FPGA based circuit.

So, in the series of events for producing plasma and acquiring the data, first a master trigger turns on the TF power supply of the BETA. Due to an initial large fluctuations in toroidal field as shown in Fig. 2.3 a delay of around 250 ms is set up between FPGA pulse system and the master trigger. For hot cathode discharge, the discharge voltage is triggered by the FPGA after the mentioned delay, followed by a trigger to electronics circuits, signal conditioning card and the data acquisition system. Similarly for ECR discharge, after a delay of around 500 ms after the master trigger, the ECR pulse, circuits, signal conditioning and the data acquisition are triggered simultaneously.

In summary, in this Chapter, the details of the experimental apparatus including the vacuum vessel, vacuum pumps and other subsystems are described in detail. This Chapter also covered, details of plasma production using two different sources, various diagnostics and their applicability are discussed. In the next Chapter, we will use these tools to determine the topology of the toroidal magnetic field.

3

Determination of toroidal magnetic field topology

3.1 Introduction

As discussed in Chapter-1, unlike a Tokamak, the single particle drift orbits are open in an SMT. The vertical residual electric field E_z^{res} created due to the charge separation due to gradient and curvature of the toroidal field drives a cross-field radial outward transport of the plasma due to $E_z^{res} \times B$. As discussed in Sec. 1.2, an application of the external vertical field, B_v controls the topology of the toroidal field. The topology of the toroidal field further controls the nature of the quasi-static equilibrium by providing a mean parallel pathway $\bar{L}_c$ along the toroidal field line for charges. The time required to reduce E_z^{res} depends on $\bar{L}_c$ is given in Eqn. 1.1. As B_v controls the topology and hence $\bar{L}_c$, therefore by varying B_v, one can vary $\bar{L}_c$ from very small value to a very large value. Therefore from Eqn. 1.1, it can be observed that minimization of E_z^{res} can be efficient for shorter values of $\bar{L}_c$. The reduction of E_z^{res} further helps in increasing the confinement time in a toroidal device [6], as indicated in Eqn. 1.5, the confinement increases with a decrease in $\bar{L}_c$ [7]. Moreover, from Eqn. 1.2, it can be observed that the topology of the toroidal field also controls the minimum parallel wavenumber, which further controls the nature of instabilities and fluctuations in the plasma. Hence, the topology of the toroidal field controls important aspects of toroidal plasma which include quasi-static equilibrium, fluctuations and confinement. Therefore, determination and proper understanding of the toroidal field topology is required to understand various plasma phenomenon in an SMT.

Moreover, in the magnetized fusion plasma devices, the topology of the magnetic field is known to play a key role in producing and confining the plasma. For example, a proper understanding of the magnetic flux surfaces and error fields often help in improving the performance of the fusion device. In the past, to determine the topology of the toroidal field lines, use of electron beam to trace the magnetic field lines has remained a popular technique to date [53]. For example, in an advanced toroidal facility (ATF) Torsatron, the electrons launched from an electron gun were intercepted repeatedly by a high transparency fluorescent screen during their successive toroidal transits, generating an image of magnetic flux surface [53]. The magnetic field mapping measurements using fluorescent screen technique on the Compact Helical System (CHS) Torsatron and the computational analysis revealed the existence of islands due to the ambient error fields from external magnetized structures. An improved method of measurements for magnetic surface cross sections was demonstrated, replacing the fluorescent screen with a fluorescent rod, on WEGA stellarator [54]. Application of the fluorescent rod technique on the Wendelstein 7-AS stellarator allowed the identification of islands in the vacuum magnetic field, before starting the plasma experiments [55]. The existence of closed nested flux surfaces was established with vacuum magnetic field line mapping using the fluorescent rod technique as well as the excitation of the background neutrals at much higher pressures in H-1 Heliac [56] and the Columbia Non-neutral Torus (CNT) [57]. Estimation of magnetic field errors using saddle loops was demonstrated on TCV tokamak (Tokamak a Configuration Variable) [58]. The parallel wave dynamics were investigated by aligning the probes toroidally to characterize the drift-wave turbulence in torsatron TJ-K [59] and WEGA stellarator [60].

In this Chapter, the topology of open toroidal field lines in an SMT, BETA is determined using a simple yet novel method based on the use of a tiny plasma beam-let. Using a tiny plasma beam-let and two toroidally separated probes shown in Fig. 3.4, accurate alignment of probes has been demonstrated, facilitating the measurements of minimum parallel wavenumber $k_{||}^{min} = \frac{2\pi}{\bar{L}_c}$, where $\bar{L}_c$ is the average parallel magnetic connection length.

3.2 Measurement of magnetic field line pitch using imaging method

Under ideal condition with zero vertical magnetic field, the toroidal magnetic field lines would close on themselves. With a finite vertical magnetic field, however, the toroidal magnetic field lines execute helical path vertically. On passing external current in the vertical field coils, the pitch of the vertical magnetic helix can be varied in a range making the toroidal magnetic field lines nearly closed to widely opened. As evident through the results in this Section, in reality, error magnetic fields are always resulting in the non-ideal toroidal field, even when the vertical field coils are not energized. For our problem, it is independent to experimentally determine this error or offset. In the present experiments, a tiny filament made up of pure tungsten wire of 0.125 mm diameter was mounted on a ceramic block using a thin twin-bore ceramic tube with a total wire length of ≈6 mm exposed to the surrounding. The ceramic block is fixed on a stainless-steel shaft movable radially. The tiny filament was positioned on the major radius R = 0.48 m through the radial port of BETA. The usual plasma sources mentioned in Sec. 2.2 were kept turned-off during these experiments, hence does not affect the measurements when the tiny filament alone was used as the plasma source. The neutral argon pressure was kept at 3×10^{-4} Torr and the toroidal magnetic field was set at 220 G at the minor axis. On passing 2.5 A current through the tiny filament and biasing negatively 70 V with respect to the vessel at ground potential, a discharge current of few tens of milliamperes was measured. A thin visible ring of plasma was found to spread both sides of the filament implying to illuminate the toroidal magnetic field lines. A glass flange was mounted on the radial port 180^o away toroidally from the tiny filament, to serve as view-port, to make quantitative observations of the pitch of the helix. A digital camera was mounted in front of the view-port to acquire gray-scale-still images of 3456×2592 pixels, capturing the illuminated regions. The camera was aligned using an aluminum stand outside the toroid so that the center of the radial port coincides with the center of the image. To avoid stray light from the surroundings, the camera was covered with a thick dark cloth enclosing the entire radial port. For spatial calibration, before the vacuum vessel was closed for experiments, a long metal scale has been suspended through the supports at the top and bottom ports so that scale lies on the major radius R =

0.48 m. Image of the scale was obtained using the same pixel setting of the camera and analyzed using MATLAB; each pixel was found to be 0.144 mm high.

As the energetic electrons were accelerated both sides of the tiny filament ionizing the neutral atoms in the vicinity of their trajectory, distinctly intense regions of light (appear as nearly horizontal lines at the view-port) were found. A profile of intensity versus pixels along the vertical direction for zero current in the vertical field coils is shown in Fig. 3.1.

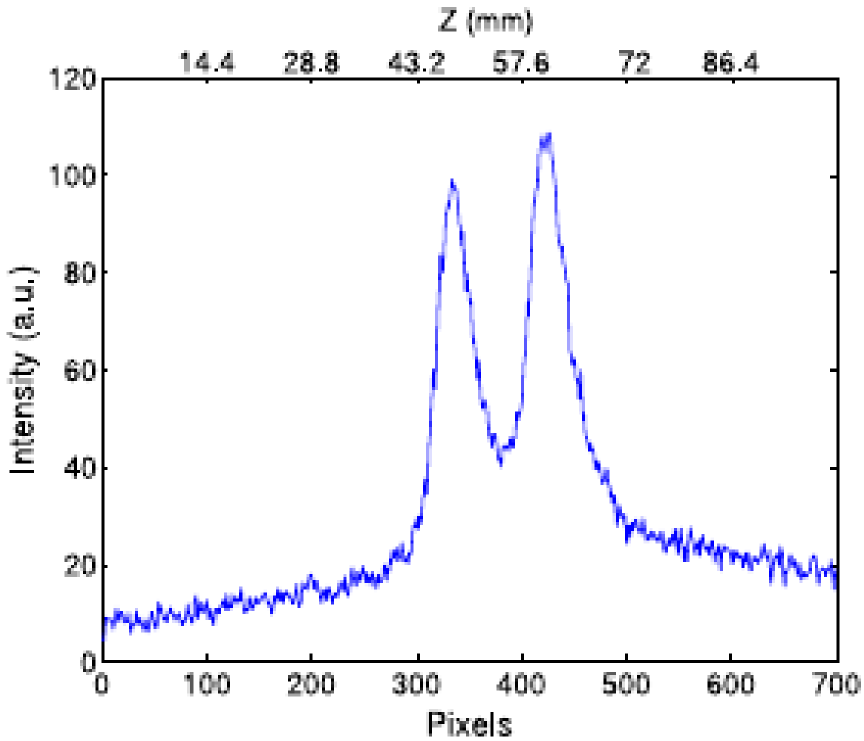

Figure 3.1: Intensity versus pixels on vertical line, corresponding to zero current in the vertical field coils, to determine the spacing between the intense lines. The spatial separation between the intense lines can be seen on the top horizontal axis.

As the observations were made at a location 180^o away toroidally from the tiny filament, the energetic electrons will be traversing equal path lengths which should account for equal amounts of drifts downward due to magnetic field gradient and curvature, both sides. As the contribution from electron-drift is nullified at the location of view-port, the measured distance between the peaks of two intense lines (l) is, therefore, due to the actual vertical spacing or pitch of magnetic field lines; thus this case is unlike the measurements using a single electron beam launched

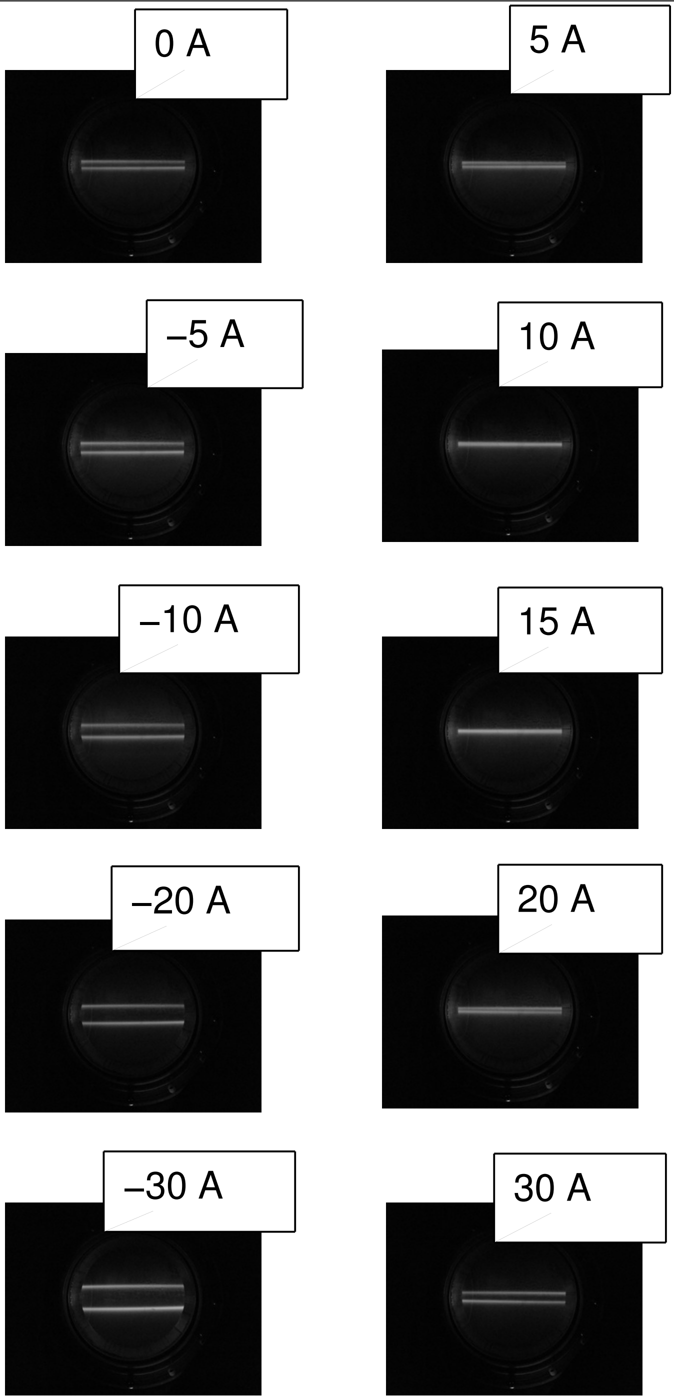

Figure 3.2: Images showing the variations in spacing between the intense lines with varying currents in the vertical field coils. The intense lines appear to overlap for I_{VF} = 10 A and 15 A.

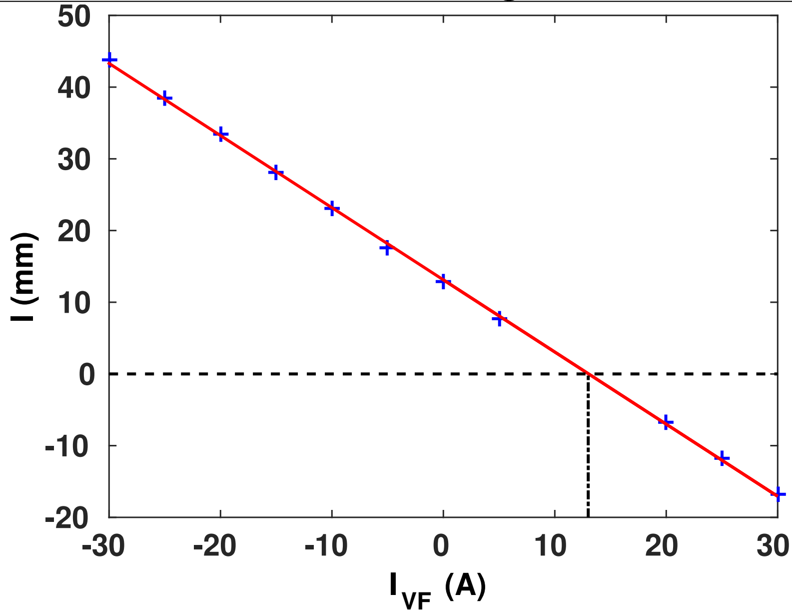

Figure 3.3: Pitch of the magnetic field lines (l) versus current in the vertical field coils (I_{VF}). The intercept on the horizontal axis is close to 13 A.

using an electron gun. Applying discrete values of current in the vertical field coils, images with illuminated lines were obtained through the radial view-port for both directions of the current in the vertical field coils as shown in Fig. 3.2. The distance between the two intense lines (l) is plotted as a function of the applied current in the vertical field coils (I_{VF}) as shown in Fig. 3.3. In this plot, the data points for 10 A and 15 A are not shown due to the merger of the intensity peaks in this range. The distance versus current in the vertical field coils exhibits a linear relation. Fitting a straight line to the data points shows that magnetic field lines would be closing on themselves at 13 A of the current in the vertical field coils in the clockwise direction from top-view; the toroidal magnetic field at the minor axis was 220 G in the anticlockwise direction from top-view. These intense lines were used for achieving the alignment of the two Langmuir probes on the same magnetic field lines as described in Sec. 3.3.

3.3 Two Langmuir probe-alignment using a tiny filament as plasma source

Two Langmuir probes tips mounted from the top ports of BETA were used for demonstrating probe alignment and measurement of minimum parallel wavenumber. A schematic of the positions of the tiny filament and the two probe tips from top view is shown in Fig. 3.4. As described in this Section, each probe tip was moved to align with the same bundle of magnetic field lines which were intercepting with the tiny filament source, thereby demonstrating a set of dimensional parameters for which both probes will be aligned precisely. For convenience, the two probe tips were named: the probe tip mounted 180^o away from the tiny filament was referred as Probe-1 and the probe tip toroidally midway between Probe-1 and the tiny filament was referred as Probe-2. The method of alignment is described as follows.

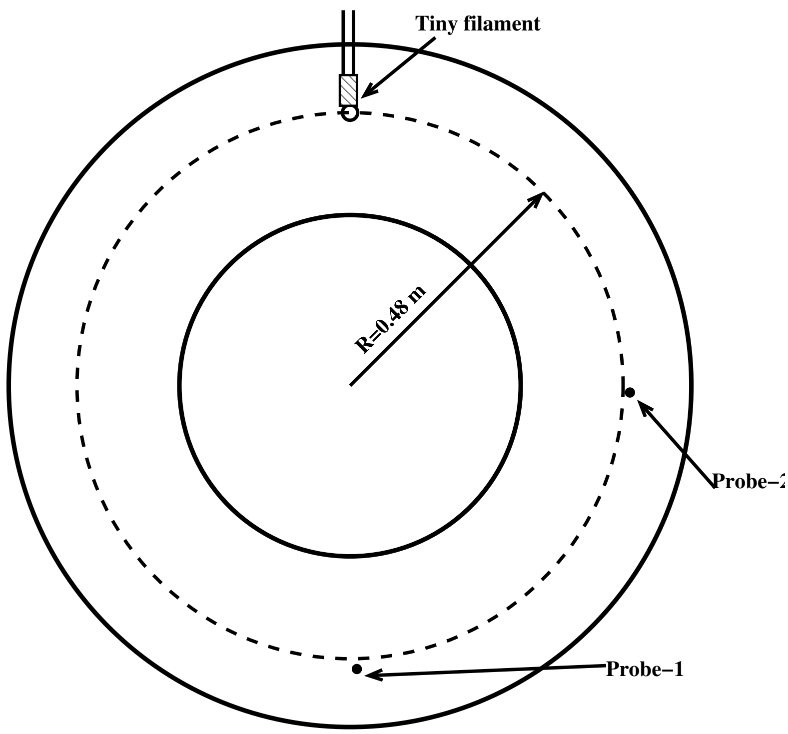

Figure 3.4: Schematic top view of the positions of the tiny filament and two probe-tips at zero reference position. Only the probe-tips used in the present experiment are shown.

The tiny filament source was positioned at R = 0.48 m. It was shown in

Sec. 3.2 that this filament acts as a localized plasma source. All the operating conditions were similar to those used in Sec. 3.2, except for the current in the vertical field coils, for obtaining discharge with the tiny filament. Three discrete values of current in the vertical field coils were chosen for which probe alignment was achieved in each case: 0 A, 12 A clockwise, and 60 A anti-clockwise from top-view. From the plot of $l - I_{VF}$ shown in Fig. 3.3, l varies from a negligibly small value at 12 A clockwise to 12.8 mm at 0 A; the projected value of l at 60 A anticlockwise is 73 mm. In each case, while scanning with Probe-1, Probe-2 was kept high from the intense line to avoid possible shadowing or perturbation effects and vice versa.

Initially, the height of Probe-1 was adjusted so that only the probe-tip intercepts the intense line; the width of the intense line was found comparable to the length of the probe-tip. A reference mark on the probe shaft was made so that the height of the probe from the bottom of the vessel can be measured and noted. After adjusting the height of Probe-1, it was rotated around the vertical axis with respect to the reference position 10^o each time and the mean floating potential was acquired on the oscilloscope. The zero reference for the angular position was chosen such that the probe-tip used for measurements lies relatively close towards the outer wall which on rotation by 180^o moves relatively close towards inner wall. The purpose of the probe rotation was to trace for a possible dip in the mean floating potential profile. After the scan with Probe-1 had been completed, Probe-2 was aligned vertically and scanned for potential dip similarly. This process of scanning with Probe-1 and Probe-2 was performed for three values of current in the vertical field coils. The corresponding heights of vertical alignment for two probe-tips were noted, which were used later for probe-alignment during regular plasma experiments as described in the Sec. 3.4. The plots of mean floating potential are shown in Fig. 3.5.

As the probe-tip rotates on a circle of radius 2.5 mm with an angular displacement of 10^o each time, the maximum displacement perpendicular to the magnetic field lines would be $\approx$0.43 mm, moving from 80^o to 90^o position, which is less than the probe-tip diameter. The spatial location of the potential dip will, therefore, be determined with a spatial resolution better than the probe-tip diameter. From Fig. 3.5, it is found that in all the cases, potential dip typically lies in a range of $60^o - 80^o$. These observations imply that in the above angular range, the two-

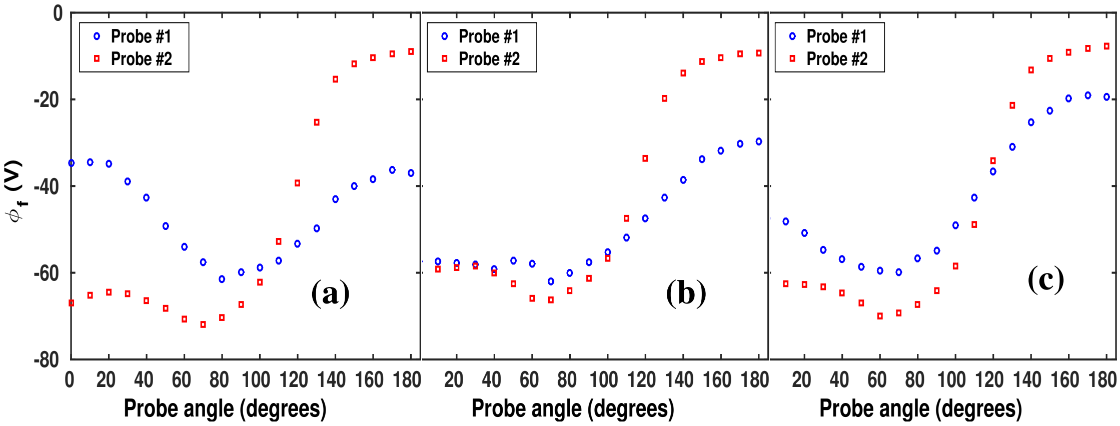

Figure 3.5: Mean floating potential indicating occurrence of dip at the intermediate angular positions for I_{VF} = (a) 0 A, (b) 12 A clockwise, and (c) 60 A anticlockwise.

probe tips were aligned with the potential well and hence the magnetic field lines through it, therefore, the probe-tips would be aligned with respect to each other. As shown in Sec. 3.4, using measurements with these probes in the regular plasma discharges, the probe alignment will be confirmed further using other parameters and the corresponding wavenumber will be estimated.

3.4 Minimum parallel wavenumber estimation using Langmuir probes

Demonstration of alignment of two probe-tips on same magnetic field lines is shown in Sec. 3.3, by aligning each of them with respect to a fixed tiny filament through the potential well. For the set of measurements shown in this section, Probe-2 was fixed at 70^o with respect to the same zero reference, and Probe-1 was rotated as described in Sec. 3.3. The Probe-1 rotation was performed in steps of 10^o each time, except in the angular range 40^o to 100^o where 5^o was used instead for better angular resolution. The tiny filament was moved out into the limiter shadow, and the vertical filament at R = 0.45 m was turned ON for producing regular plasma discharges. The floating potential was measured simultaneously on Probe-1 and Probe-2 and acquired three values of current in the vertical field coils used were same as described in Sec. 3.3. The probes were adjusted to corresponding heights for each value of the current in the vertical field coils, as noted in Sec. 3.3. The demonstration of the probe alignment and estimation of the corresponding wavenumber are described in the following. Let x_1, x_2 denote the time series data of the floating potential with zero mean values for Probe-1 and Probe-2, respectively; $X_1(\omega)$ and $X_2(\omega)$ denote the respective discrete Fourier coefficients, corresponding to frequency ω. The auto-power spectrum is defined as $P_{ii} = X_i(\omega)X_i(\omega)^*$, where i = 1 or 2 and X_i^* is the corresponding complex conjugate. The cross-power spectrum is defined as $P_{12}(\omega) = X_1(\omega)X_2(\omega)^*$. Coherence between the fluctuations at two locations represented by x_1 and x_2 is given by $\gamma = |P_{12}|/((P_{11}(\omega))^{1/2}(P_{22}(\omega))^{1/2})$, and the cross-phase $\theta(\omega)$ is given by the complex argument of P_{12}. The minimum parallel wavenumber is given by $\theta(\omega)/\Delta x$, where Δx is the probe separation along the magnetic field line in the present case. For each value of the current in the vertical field coils, measurements were conducted with multiple discharges (4 shots) at each angular position of Probe-1, keeping the position of Probe-2 fixed. The simultaneously acquired data of floating potential on two probe-tips were analyzed using Fourier analysis described above. Each time series was divided into 78 number of bins of 1024 samples each. Coherence and cross-phase were estimated between the time series corresponding to Probe-1 and Probe-2. Strong peaks at low-frequencies (few kHz) were found in the cross-power spectra in all three cases, often dominated by one or two peaks. Typical absolute cross-power spectra are shown in Fig. 3.6

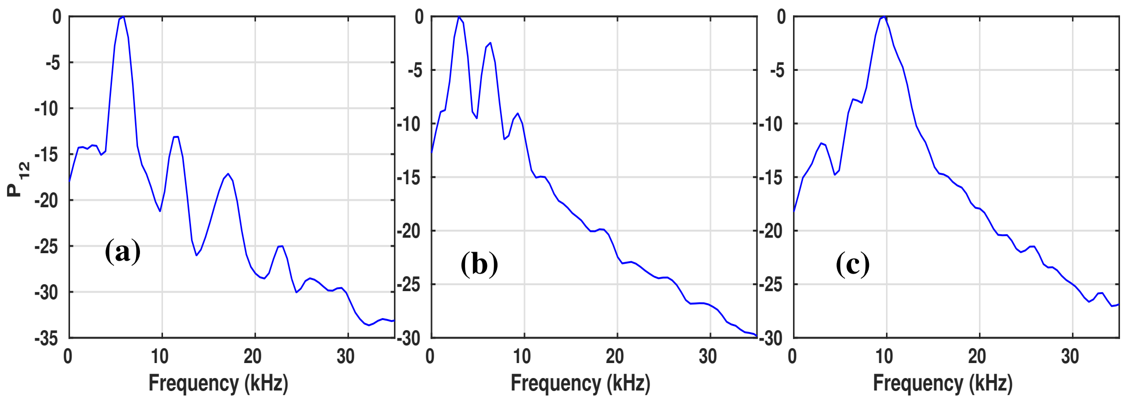

Figure 3.6: Absolute cross-power spectra for I_{VF} = (a) 0 A, (b) 12 A clockwise and (c) 60 A anticlockwise.

Coherence and cross-phase corresponding to the dominant frequency in each case, viz., 9.4 kHz for 60 A anticlockwise, 5.9 kHz for 0 A, 2.9 kHz for 12 A clockwise, were estimated for which the error bars were constructed from the multiple discharges. Coherence profiles are shown in Fig. 3.7

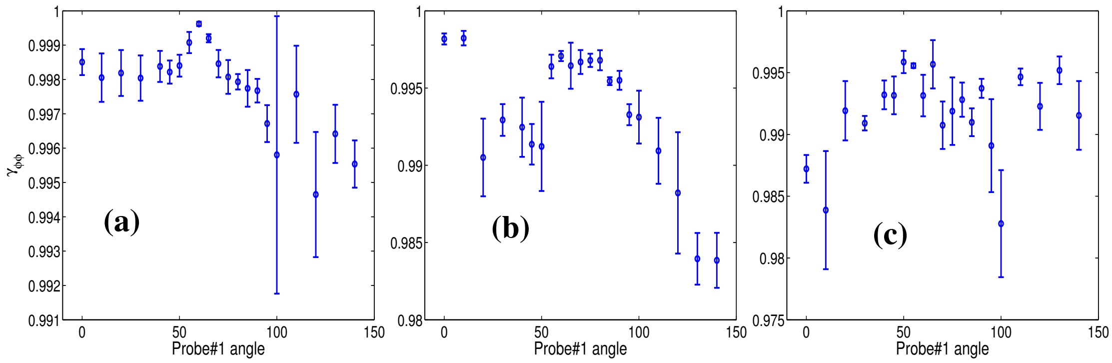

Figure 3.7: Coherence between the two probe-tips for the dominant frequency peak of potential fluctuations for I_{VF} = (a) 0 A, (b) 12 A clockwise and (c) 60 A anticlockwise.

The minimum parallel wavenumber was estimated from the cross-phase between two probe-tips, using the same time series data, corresponding to the position with maximum coherence. This method has been used as a tool to achieve probe-alignment along the same magnetic field lines in similar toroidal devices; [13, 61] however, the coherence profiles were used to confirm the probe-alignment demonstrated in the present work. The coherence profiles were found to be either broad or slowly varying in all three cases close to 60^o, probably due to a high spatial resolution of measurements chosen as compared to the probe diameter. Keeping this in view, full profiles of cross-phase were estimated in all the three cases; however, the main focus has to be in the neighborhood of the coherence maximum in each case. The cross-phase profiles are shown in Fig. 3.8.

The finite $k_{||}$ modes can occur predominantly with mode number equal to 1, resulting in $k_{||} \sim 1/NR$, as reported for similar toroidal devices; [13] here, $N \sim 2a/l$ is the number of toroidal turns the magnetic field lines execute inside the torus, a denotes either the inner radius of the limiter or the minor radius of the torus and R is the major radius of the region of interest, which is 0.48 m in the present measurements. The distance between Probe-1 and Probe-2 is given by $\Delta x (= \pi R/2) = 0.75m$. For 0 A current in the vertical field coils, $l = 12.8$ mm and $2a = 180$ mm result in $N = 14.1$ considering the inner diameter of the limiter, for which $k_{||} \sim 0.15\ m^1$. The corresponding cross-phase is $\theta = k_{||} \times \Delta x = 0.036\pi$. The observed θ in experiments as shown in Fig. 3.8 corresponding to maximum

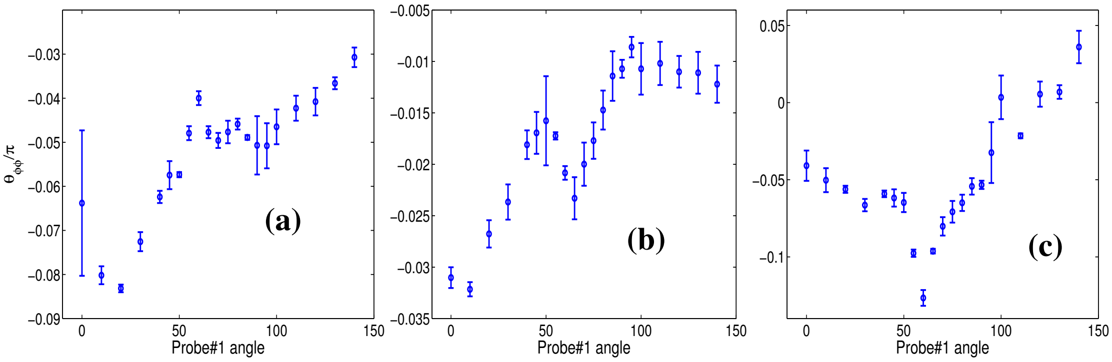

Figure 3.8: Cross-phase between the two probe-tips for the dominant frequency peak of potential fluctuations for I_{VF} = (a) 0 A, (b) 12 A clockwise and (c) 60 A anticlockwise.

coherence is $\sim 0.04\pi$ which is close to the analytical calculation above. In the case of 60 A anti-clockwise, $l = 73$ mm and $2a = 300$ mm result in $N = 4.11$ for which $k_{||} \sim 0.51\ m^1$, considering the diameter of the poloidal cross-section of the vessel rather than taking limiter dimensions. The calculated phase difference with same probe separation is 0.12π, which is close to the value 0.13π estimated from the experimental observations as shown in Fig. 3.8. The observed variation in the case of 60 A anti-clockwise can be due to larger pitch (73 mm) of the magnetic field lines as compared to the limiter width (50 mm), which could lead to the existence of finite number of magnetic field lines hitting the bottom and/or top of the vessel without intercepting the limiter. In the case of 12 A clockwise current in the vertical field coils, field lines would be nearly closed leading to large N and relatively small $k_{||}$, implying a small phase difference. From Fig. 3.8, the magnitude of the phase difference is found to be $< 0.025\pi$ and varying continuously in the region corresponding to the broad peak in the coherence profile. Using the similar approach, $N \sim 180$ for 12 A clockwise VF current. A clear comparison of measured phase difference with the analytical calculation could not be demonstrated in this case. Through the above measurements and calculations, the fluctuations are found to possess finite parallel wavelength, at least in two cases: $I_{VF} = 0$ A and $I_{VF} = 60$ A anticlockwise.

As discussed in Sec. 1.2, the mean parallel connection length is given as $\bar{L}_c = 2\pi R N_R$ where R is the local major radius of the torus and N_R is the number of turns a toroidal field line makes before hitting the wall or limiter at a particular R.

For the present measurements, $R = 0.48$ m and N_R varies from 4 to 180. For 12 A clockwise current, where field lines are nearly closed on themselves, $N_R \sim 180$, therefore, $\bar{L}_c = 2\pi * 0.48 * 180 \approx 540$ m. Similarly for 60 A anticlockwise VF current, $N_R \sim 4$ and hence $\bar{L}_c = 2\pi * 0.48 * 4 \approx 12$ m and 0 A VF current is a intermediate case with $\bar{L}_c \approx 42$ m.

As discussed an inherent vertical offset in the toroidal field line can result even without charging the VF coils, due to which a field line does not close on itself. In order to determine the possible cause of this vertical offset, a numerical simulation has been performed using a EEFI code [62] using the measured TF and VF co-ordinates of BETA (see Appendix. A), details of which is provided in Sec. 3.5.

3.5 Numerical simulation to determine the cause of opening of toroidal field lines

As discussed in Sec. 3.2, possible misalignment in the toroidal field coils can introduce error magnetic fields, resulting in an non-ideal toroidal field, even when the vertical field coils are not energized. In this section, we will try to find out the possible reason for the opening of toroidal field line. The possible geometrical misalignment of TF coils and presence of uncompensated leads in the TF coils may lead to opening up of the toroidal field lines. To this end, a 3-D numerical simulation using EFFI code [62] has been performed with inputs of actual coordinates of TF coils measured using a metrology instrument named as electronics co-ordinates displacement sensor (ECDS). The principle of working of ECDS is the measurement of distance with a modulated microwave or infrared carrier signal, generated by a small solid-state emitter within the instrument optical path, and reflected by a prism reflector or the object under survey. The modulation pattern in the returning signal is read and interpreted by the on-board computer in the total station. The distance is determined by emitting and receiving multiple frequencies, and determining the integer number of wavelengths to the target for each frequency. In short, given the co-ordinate of the instrument position and bearing of a backward station the co-ordinates of any other point can be computed. The angular accuracy of ECDS varies from 1" to 20", instrumental error is ± 10 mm to ± 2 mm and error due to the length of the measurement varies from ± 10 mm to ± 2 mm per kilometer. The actual data of TF and VF coils co-ordinates measurement

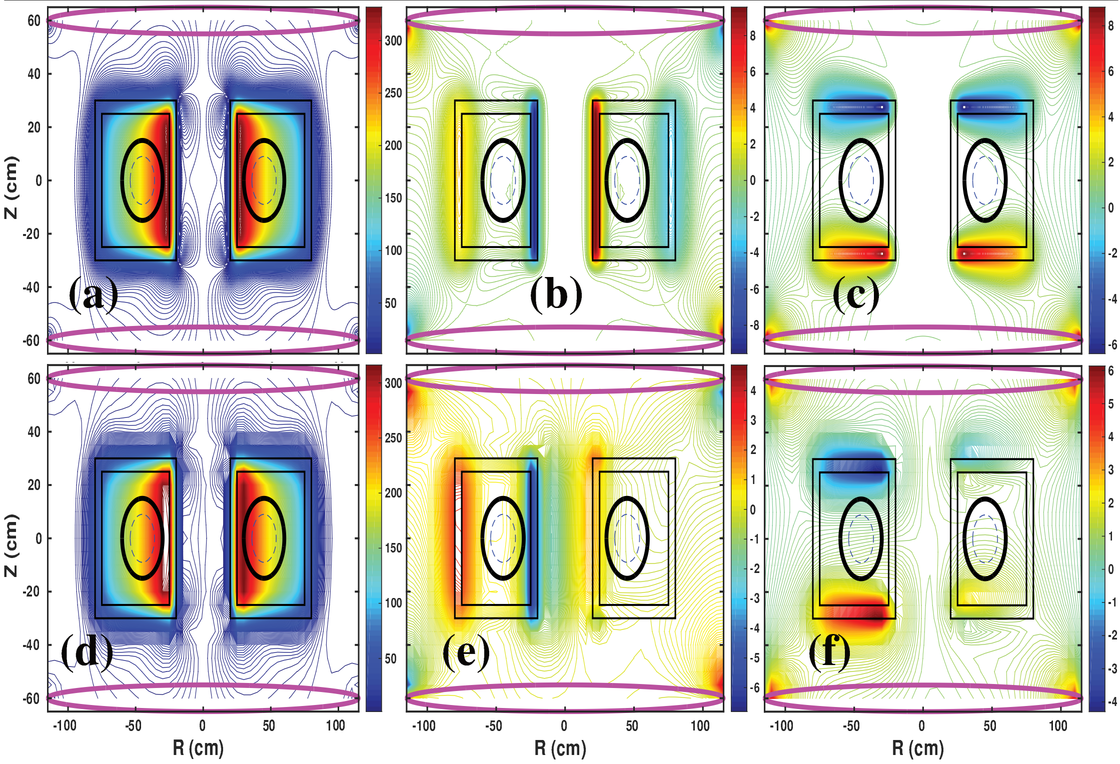

Figure 3.9: Contour plots of (a) toroidal magnetic field, (b) radial component of field, B_r, (c) vertical component of the field, B_v for the ideal case, and (d) toroidal magnetic field, (e) radial component of the field and (f) vertical component of the field for the actual co-ordinates of TF coils (see Appendix. A) for BETA for an external VF current of 12 A. The magnetic field data is obtained using the EFFI simulation for the ideal and the actual cases. The black squares in each subplot represent the TF coils, magenta rings on the top and bottom represent VF coils. The bigger solid circles represent, the BETA vacuum vessel and dotted circles represent the plasma radius limited due to the limiter. It can be observed that, despite the misalignment in the TF coils no significant difference exists between ideal (upper plots) and actual (bottom plots) cases.

using ECDS is shown in Appendix. A.

The EFFI code calculates the electromagnetic field and vector potential in coil systems of arbitrary geometry. The coils are made from circular arc and/or straight segments of rectangular cross-section conductor. EFFI can also calculate magnetic flux lines, magnetic force, and inductance. The methods used for the calculations are based on a combination of analytical and numerical integration of the Biot-Savart law for a volume distribution of current. These methods yield accurate field values inside and outside the conductor [62]. The inputs for the

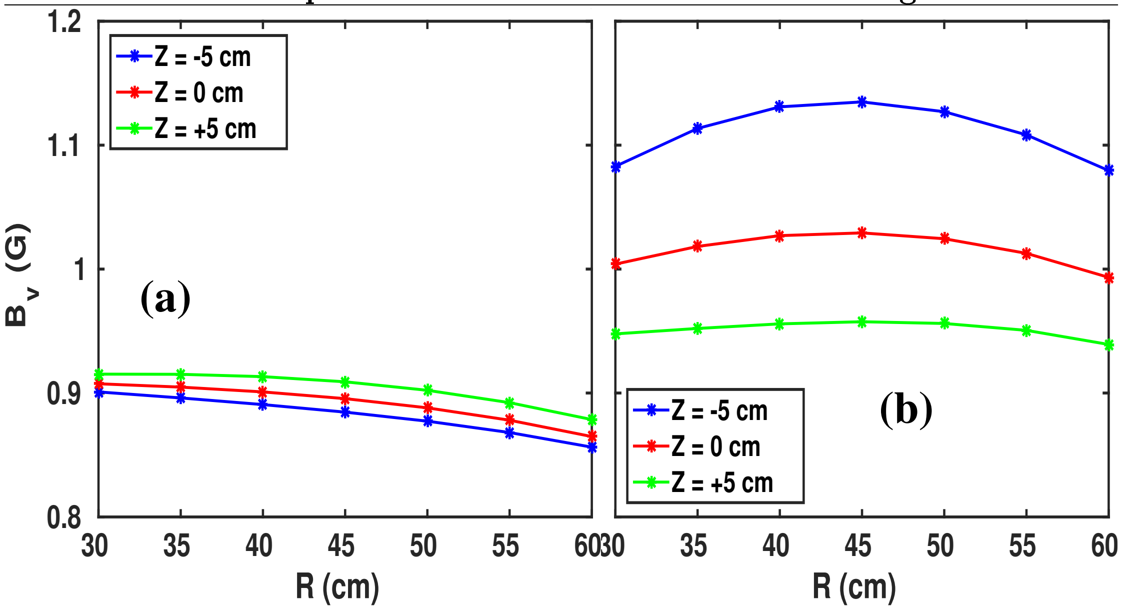

Figure 3.10: Radial profile of vertical magnetic field B_v; (a) an ideal TF locations and (b) the actual TF locations at different different vertical distance Z for the case when VF coils are charged to 12 A current. It can be observed that for the ideal case shown in (a) has very weak dependency on Z as compared to the actual case (b).

simulation is the actual co-ordinates of all the 16 TF coils determined using a ECDS instrument, which provides all the possible geometrical misalignment of TF coils. The contour plots shown in Fig. 3.9 shows total toroidal field, the radial component of the toroidal field and the vertical component of the toroidal field for the ideal case and the actual case for VF current of 12 A, obtained using the simulation. The ideal case implies considering that no misalignment in the TF coils is present. The contours of toroidal field (B_T), radial component of the magnetic field (B_r) and the vertical component of the field (B_v) shown in Fig. 3.9(a), (b) and (c) respectively, does not differ much with the counterparts of actual case shown in Fig. 3.9(d), (e) and (f). Though there are no significant differences are visible between the ideal and actual values profiles shown in contour plot in Fig. 3.9, however, to observe finer differences, the radial profiles of B_v has been shown in Fig. 3.10 at different Z planes for VF current of 12 A. It can be observed that for the ideal case the variation of B_v with Z is relatively weaker as compared to the actual case. However, for the actual case, the variation of B_v with Z is around 10%, which can be considered to be very weak. Moreover, the radial variation of

B_v is not significant for both the ideal case as well as for the actual case.

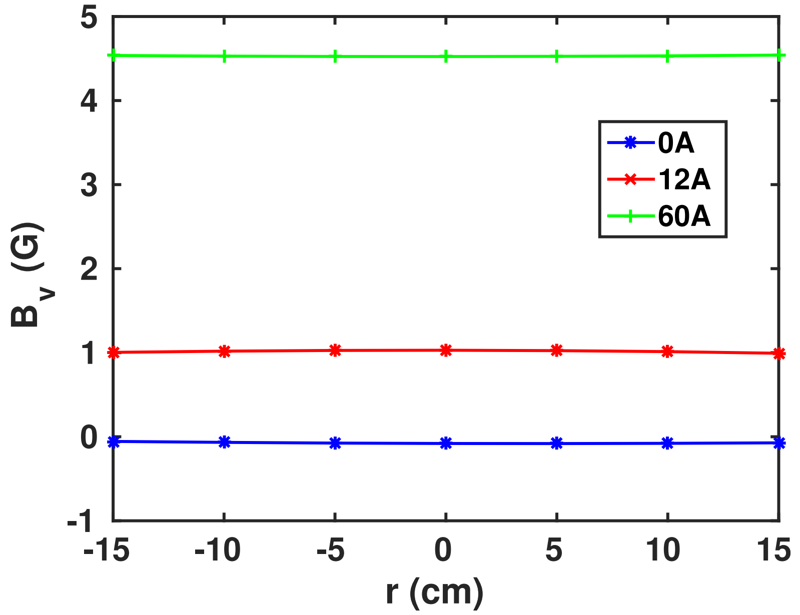

Figure 3.11: Radial profile of vertical magnetic field, B_v for different values of I_{VF} for the actual locations of TF coils. It can be clearly observed that for 0 A, VF current the inherent offset is very small, close to zero, which implies field lines cannot be opened by the misalignment of TF coils. Moreover, it can also be observed that the radial variation of B_v is very weak.

Similarly the radial variation of B_v for different VF current for the actual co-ordinates is shown in Fig. 3.11. The presence of the inherent B_v may open up the toroidal field line. However, it can be observed that the value of offset vertical magnetic field is negligibly small and hence field lines cannot be opened by the misalignment of the TF coils, which is evident from Fig. 3.12(a), that the field line is closed on itself. But experiment described above clearly indicate that there exists an inherent offset in toroidal field lines even when the VF coils are uncharged. It implies the opening of the toroidal field line even without charging VF coils could be due to the uncompensated leads present in TF coils, which provide a vertical component of magnetic field.

Irrespective of the offset in toroidal field, Fig. 3.12(b) and (c) confirm that the topology of the toroidal field can be controlled by the application of an external vertical field. For a small value of the external vertical field, the toroidal field opens up marginally and forms a small pitched vertical helix as shown in Fig. 3.12(b) but with an increase in external vertical field, the pitch of the helix increases and

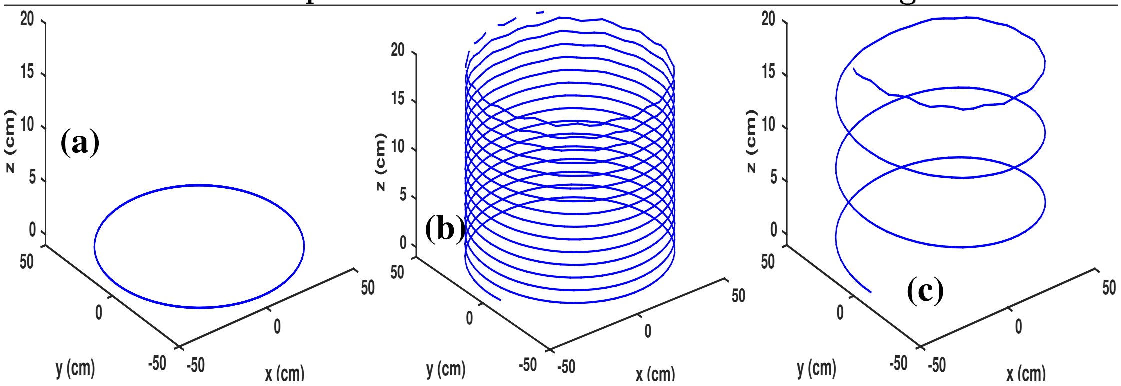

Figure 3.12: The topology of the toroidal field in Cartesian co-ordinates for actual TF coils locations simulated using EFFI code for VF currents of (a) 0 A or uncharged VF coils, (b) 12 A and (c) 60 A. It can be observed that for 0 A case, the field lines closes on itself despite the geometrical misalignment in the TF coils. However field line does open up by the application of an external vertical field as shown in (b) and (c), if the applied vertical field is small, the field lines are opened marginally (or $\bar{L}_c$ is relatively large) and on further increasing VF current, the field line opens up widely (or $\bar{L}_c$ is relatively small).

field line opens up further as shown in Fig. 3.12(c).

3.6 Summary

The topology of the toroidal field line is experimentally determined using a novel yet effective method, which involves a tiny filament and a regular camera. The measurements provide an inherent vertical offset in the toroidal field line, without charging the VF coils and the offset for $B_T = 220$ G, is found to be around 1 G. As discussed, the offset could be due to two possible reasons namely (i) geometrical misalignment of the TF coils and (ii) presence of uncompensated leads in the TF coils. A simulation of the toroidal field line is performed using EEFI code using the actual physical coordinates of all 16 TF coils and 2 VF coils (see Appendix. A). As discussed in Sec. 3.5, the simulation results clearly show, the misalignment of the toroidal field coils does not provide any vertical component of the magnetic field and toroidal field lines are supposed to close on themselves. Therefore, the offset observed experimentally could only be attributed to the presence of uncompensated leads present in TF coils providing effective vertical component of the magnetic field B_{off}. Moreover, simulation results confirm that the topology of the toroidal field line can be controlled (i.e, opened and nearly closed) by the application of the external vertical field.

Moreover, a method of aligning two Langmuir probe-tips, using a localized plasma source, is demonstrated through this work which is an essential requirement to estimate the minimum parallel wavenumber or $\bar{L}_c$ precisely. First of all, two lines of intense light were produced at a view-port, using a tiny filament source 180^o away toroidally; the spacing between the lines was found to vary linearly with the current in the vertical field coils through the analysis of the images captured. The probe tips were aligned by vertical translation to coincide with the intense lines and rotation in the horizontal plane, for appropriately chosen three values of current in the vertical field coils. The probe-tip alignment was further confirmed from the coherence plots during the regular plasma discharges. From the cross-phase corresponding to maximum coherence, the minimum parallel wavenumber was estimated. The observed values were found in agreement with the analytical calculations for at least two values of current in the vertical field coils. Through this work, the use of a small plasma beam-let is demonstrated to be an effective method of revealing the toroidal magnetic field topology, over the techniques based on the use of an electron-gun. Major findings are summarized as follow:

- The topology of the toroidal field is experimentally determined using a simple yet effective method, by using a tiny plasma beam-let and a regular camera [63].
- An inherent offset in the toroidal field is observed, even without charging the VF coils and the inherent offset is determined to be around 1 G for B_T =220 G.
- It has been demonstrated that the topology of the toroidal field or $\bar{L}_c$ can be varied from very long ($N \sim 180$) to very small ($N \sim 4$) connection length by varying the VF current.
- To determine the minimum parallel wavenumber $k_{||}^{min} = \frac{2\pi}{\bar{L}_c}$, Langmuir probes mounted at the different toroidal location, aligned to the same toroidal field line by using the tiny plasma beam-let.
- $k_{||}^{min}$ has been determined experimentally for different VF currents and found to be in the agreement with the theoretical values.

- Further to determine the cause of the opening of the toroidal field line, the co-ordinates of TF coils is measured using ECDS equipment and these co-ordinates are used as input for performing a numerical simulation using EFFI code.

- The results of numerical simulation confirm that the misalignment of TF coils cannot result in opening up of a toroidal field line. Therefore, the observed opening is attributed to the presence of uncompensated leads in the TF coils.

In this Chapter, the topology of the toroidal field is determined using a novel and effective method. It has also been clearly shown that the topology can be controlled by the application of an external vertical field. In the Chapter. 4, a detailed experimental study of the role of toroidal field topology on quasi-stationary equilibrium, fluctuations and flow by varying the external vertical and toroidal field will be presented.

4

Effect of toroidal field topology on quasi-static equilibrium, fluctuation and flows in a hot cathode produced plasma

4.1 Introduction

In Chapter-3 the topology of the toroidal field is determined in a simple magnetized torus (SMT) using a tiny plasma beam-let and a regular camera. It has been confirmed that the topology of the toroidal field can be controlled by the application of the vertical field. As discussed in Chapter.-1, in an SMT, the absence of conventional magnetic rotational transform in our current less toroidal device implies the absence of single particle confinement and hence conventional stationary equilibrium does not exist. In other words, plasma is confined by the application of the toroidal field only and due to which vertical charge separation occurs in the plasma. This charge separation leads to the generation of a residual electric field, E_z^{res}, which causes the radial transport of the plasma via $E_z^{res} \times B$ drift. However, the topology of the toroidal field controls the nature of equilibrium and fluctuation by providing a parallel pathway, $\bar{L}_c$ to electrons to move along the toroidal field, which may effectively help reduce the residual vertical electrical field E_z^{res} for widely opened field lines. Moreover, this may also result in better ionization as the path traversed by the electrons has become shorter. It is suggested in the present Chapter that smaller $\bar{L}_c$ in establishing quasi-stationary profiles of mean density and temperature in the presence of sources and sinks. Similar to Tokamaks, inhomogeneity in mean density and temperature profiles leads to cross field instabilities and transport.

As discussed in Sec. 1.2, the mean parallel connection length $\bar{L}_c$ is defined as $\bar{L}_c = 2\pi R_0 N$, where N is the mean number of toroidal turns before hitting the wall or limiter and R_0 is the major radius of the torus. As discussed in Chapter.-1, the $\bar{L}_c$ controls two aspects in a toroidal plasma: (i) by determining E_z^{res} controls the outward radial transport of the plasma and thus controls the nature of quasi-static equilibrium. As evident from Eqn. 1.1, radial transport of plasma reduces for shorter $\bar{L}_c$ and quasi-static equilibrium improves. (ii) Determine the minimum parallel wavenumber as provided in Eqn. 1.2, thus controls the nature of instabilities or fluctuation.

In this Chapter, a detailed study of the role of toroidal field topology on quasi-static equilibrium, fluctuation and flows have been performed using hot cathode source (Sec. 2.2.1) in a simple magnetized torus, BETA. As can be observed from Eqn. 1.2, $\bar{L}_c \propto \frac{B_T}{B_{off}-B_v}$, which implies that $\bar{L}_c$ can be varied by varying B_v or B_T or simultaneously varying both. The inherent offset in the toroidal field, B_{off} has been determined in Chapter-3. As a detailed study of the variation of B_T without charging VF coils has already been performed in BETA [19]. Therefore, the present Chapter is divided into three parts, in the first part of the Chapter, the toroidal field strength has been kept fixed and the mean parallel connection length, $\bar{L}_c$ is varied by the application of vertical field only. In the second part, the toroidal and vertical magnetic field varied simultaneously in three fixed ratios which are, intermediate $\bar{L}_c$, large $\bar{L}_c$ and small $\bar{L}_c$. In Part-III, experimental measurements have been discussed estimate the particle confinement in an SMT and its dependence on the topology of the toroidal field.

Part I

Effect of variation of B_v on the hot cathode produced plasma properties for a fixed value of B_T

As discussed in Sec. 3.4, the topology of the toroidal field can be varied from very small values of $\bar{L}_c$ to very large $\bar{L}_c$ by varying B_v. Therefore, in Part-I of the present Chapter, we will present the details of the experimental studies performed by varying B_v to vary $\bar{L}_c$ for a fixed B_T.

4.2 Operating conditions

1. Base pressure $\sim 4 \times 10^{-6}$ torr
2. Filling gas: Argon
3. Working pressure $\sim 1 \times 10^{-4}$ torr
4. Filament current, $I_f \sim 142$ A
5. Hot cathode bias voltage, $V_d \sim$ -70 V
6. Discharge current, $I_d \sim 5$ A (operated at constant current mode)
7. $B_T \sim 220$ G
8. VF current (B_v) $\sim$ 0 A (0 G), 12 A (0.9 G), 20 A (1.5 G) and 60 A (4.5 G)

4.3 Measurement method

The measurement methods are similar to those described in Sec. 2.3, Langmuir probe has been used to measure mean density (n_0), mean floating potential (ϕ_f) and mean electron temperature (T_{e0}). Mean density is estimated from ion saturation current (I_{is}) measured using a triple Langmuir probe (TLP) by applying 12 V bias between the two probe tips and keeping third floating. TLP also gives simultaneous measurement of T_{e0} [64].

A radial array of four Langmuir probes described in Sec. 2.3.3, has been used to measure I_{is}, with a probe at a bias of -40 V with respect to the vessel in single Langmuir probe configuration. The floating potential ϕ_f is measured with high input impedance voltage follower circuit shown in Fig. 2.11. Four tips of radial array give the simultaneous measurements of density and potential fluctuation which can be used to measure fluctuation induced poloidal flux and also for spectral calculations.

A hot emissive probe described in Sec. 2.3.5 is used to directly measure the mean plasma potential (ϕ_0). The probe is heated slowly and floating potential is measured by the same high impedance voltage follower. The probe gets saturated with emission current at around 2.7 A where the probe is said to be floating at the plasma potential and hence the direct measurement of plasma potential becomes possible.

Mach probe described in Sec. 2.3.4 directly measures the net poloidal flow. A schematic is shown in Fig. 2.14. The probe has two similar metallic-collection surfaces on either side of the ceramic cylinder. To check the asymmetry in collection area ion saturation current has been measured by both the surfaces at one position for given orientation and then the probe is rotated by 180^0 so that the lower collector becomes upper and vice versa, after which the ion saturation current is measured again on both the collecting surfaces. On comparing the collection current, the area asymmetry was found to be in the range of $10\% - 15\%$, which provides uncertainties of $\pm 0.1 c_s$ in the net poloidal flow. For the poloidal flow measurements, the axis of the cylinder passing through the centers of two collection surfaces is aligned vertically. Ion saturation current is drawn on both the ends.

Measurements of floating potential are first obtained using high impedance voltage followers, attached to floating probes, with the frequency response of $\approx 100kHz$. For typical gradient scale lengths of mean quantities such as mean density expected in our device, the dominant plasma instabilities are at the diamagnetic frequency of few kHz and therefore is of low frequency in nature. Consequently, beyond 35 kHz no significant modes were found . In the present work, we focus on the study of low frequency phenomenon and use low pass filter of 35 kHz for measurements which terminates all the higher frequencies without eliminating any frequency of interest. A 14-bit PXI based data acquisition system has been used to acquire time series of all the above mentioned measurements with low pass filter of 35 kHz with 40000 data points each at the sampling rate of 200 kS/s, higher than twice the measurement bandwidth as required by Nyquist criteria.

4.4 Experimental plasma profiles

For these experiments performed in this Chapter, the discharge is struck between hot cathode and wall of the vacuum vessel, with respect to which filament is biased.

Plasma parameters	Values
Ion mass	39.95 amu
Toroidal magnetic field (B_T)	0.022 T
Ion Larmor radius (r_{Li})	9.4$\times10^{-3}$ m
Electron Larmor radius (r_{Le})	3.8$\times10^{-4}$ m
Electron Debye length (λ_{De})	5.2$\times10^{-5}$ m
Ion gyration frequency ($\omega_{ci}/2\pi$)	7.9$\times10^{3}$ s^{-1}
Electron gyration frequency ($\omega_{ce}/2\pi$)	5.7$\times10^{8}$ s^{-1}
Electron plasma frequency ($\omega_{pe}/2\pi$)	2.8$\times10^{9}$ s^{-1}
Ion plasma frequency ($\omega_{pi}/2\pi$)	1.1$\times10^{7}$ s^{-1}
Electron neutral frequency (ν_{en})	7.2$\times10^{5}$ s^{-1}

Table 4.1: The typical plasma parameters for Argon plasma at $B_T = 220G$. For the calculations mentioned, it is considered that $T_e \sim 3.0$ eV and $n_0 \approx 10^{17}\ m^{-3}$, which are typical of BETA. $T_i \sim 0.1$ eV is assumed.

At operating conditions described earlier a voltage pulse of - 70 V of the duration of 0.8 sec is applied to the filament, during which the breakdown occurs and plasma is produced. The discharge current is set at 5 A, however, the discharge voltage may vary for different plasma conditions. The energetic primary electron emitted from filament mounted at the minor axis form a vertically extended charge region or a ribbon around the hot cathode, which helps in initiation of discharge and its sustainment. It results in a quasi-neutral plasma filling through the vessel by the continuous ionization of filled Argon gas, except close to the hot cathode, where the presence of energetic electrons in a region of about 1.5 cm around the hot cathode makes the region non-neutral. The presence of energetic electrons around the minor axis has been experimentally demonstrated using an RFEA [9]. A detailed study of discharge conditions in BETA, the existence of fluctuations, poloidal flows and plasma spread in the radial domain of BETA have been shown earlier at a toroidal field strength of 220 G [38]. In all the above mentioned works, the VF coils were not charged and hence externally applied vertical field was zero as the motivation of the experiment was to study the effect of variation of B_T on plasma properties. However as discussed in Chapter-3, the inherent offset in the toroidal field was present. As mentioned above, the discharge voltage is expected to be different for different topology of the toroidal magnetic field. The discharge voltage for 0 A case is around -40 ± 1 V, for longer $\bar{L}_c$ i.e, for 12 A and 20 A case is around -45 ± 1 V and -43 ± 1 V respectively and for shorter $\bar{L}_c$, i.e, for 60 A, the discharge voltage is around -36 ± 1 V. Therefore, it can be observed that for a constant discharge current, the discharge voltage is lower for shorter $\bar{L}_c$.

As discussed in Sec. 3.4, the parallel mean connection length $\bar{L}_c$ and hence the nature of instabilities can be varied by controlling the current through VF coils shown in Fig. 2.1(b), passing the current in the clockwise direction in the VF coils as seen from the top. The resultant B_v which would be in -Z direction is considered as positive B_v as shown in Fig. 2.1(a) and vice versa. It has been observed from the experiments discussed in Chapter-3, that for a particular value of applied VF current in the clockwise direction, the offset in the toroidal field can be reduced, such that the field lines are nearly closed on themselves. Further increasing the VF current in the same direction, field lines open up in the opposite direction. Similarly applying VF current in the anti-clockwise direction will further increase the existing offset in the toroidal field. Therefore, by the application of the external vertical field one can control the topology. This can change $\bar{L}_c$ and hence the nature of plasma in an SMT. In the present work, we have applied 14 different values of the vertical magnetic field on the toroidal field of 220 G [from -52 A to 60 A]. Let us first consider 4 values of vertical field current viz., 0 A, 12 A, 20 A and 60 A in the clockwise direction which produces a vertical magnetic field component in the vertically downward direction (-Z direction). The reason for choosing these values is following: 0 A is the default case in which no vertical field is applied externally. As discussed earlier in Chapter.-3, an inherent opening of field lines could be attributed to the presence of uncompensated leads in TF coils in BETA which may lead to an offset in toroidal magnetic field given by B_{off}.

In Chapter-3, it has been shown that this offset may be corrected by applying a vertical magnetic field with values between 12 A and 20 A. It was also shown in Chapter-3 that field lines are nearly closed for 12 A (or ~ 0.9 G) and widely opened at 60 A such that in the former case the mean connection length $\bar{L}_c$ is very large with an estimated toroidal number of turns $N \sim 180$ and for latter case $\bar{L}_c$ is very small with $N \sim 6$ using the method described in Sec. 3.4. Hence, these two cases represent different regimes of operation. In a later section [Sec. 4.4.4], we present all the 14 different VF current value mean and fluctuation profiles measured at $Z = 0$ plane. As discussed earlier, we assume that these measurements at $Z = 0$ plane meaningfully reflect on the nature of the underlying problem.

4.4.1 Radial Plasma Profiles

Radial profile of mean density, $n_0(r)$, mean electron temperature, $T_{e0}(r)$ and mean floating potential, $\phi_{f0}(r)$ for four different representative values (for all 14 VF currents values will be discussed shortly) of vertical field is shown in Fig. 4.1(a), 4.1(b) and 4.1(c) respectively and Fig. 4.1(d) shows radial profile of mean plasma potential (ϕ_{p0}). The time series of each plasma parameter, ion saturation current I_{is}, electron temperature T_e, floating potential ϕ_f and plasma potential is obtained using concerned diagnostics and data acquisition system described in Chapter 2 and the mean of these time series gives the corresponding mean plasma parameters. The mean density (n_0) is estimated using the formula $n_0 = 2I_{is,0}/eAc_s$ where e is the electron charge, A is the probe area, $I_{is,0}$ is the measured ion saturation current from probe and $c_s = (K_B T_{e0}/M_i)^{1/2}$ is the ion acoustic velocity with ion mass M_i. Mean density does not vary significantly for the VF current values of 0 A, 12 A and 20 A, but increases on an average for 60 A case. The peak of density for all values of VF current coincides at the source region. The error-bars plotted here are obtained from four independent measurements at each radial location. As can be expected, in hot current filament based discharges such as ours, the region close to the minor axis can be contaminated by high energy primary electrons. It is well known that the presence of even a small fraction of fast electron may lead to difficulties in interpretation of data [65]. For example in BETA device, it has been shown that the primary fast electrons are present around the minor axis and a rough estimate of the number density of the residual fast electrons and its spread has been obtained [9]. The peak in the electron temperature shown in Fig. 4.1(b) and dip in floating potential Fig. 4.1(c) is believed to be due to the presence of residual high energy electrons [9]. Hence the experimentally obtained values of electron temperature using Langmuir probes close to the hot cathode location i.e., $\sim$1.5 cm on both sides of the filament, may be erroneous due to the presence of these fast primary electrons. The region between the vertical lines in Fig.4.1(b), indicates the region where presence of these high energy electrons cannot be ruled out and hence one should be wary of measured plasma properties in this region. Away from the source region, the electron temperature is comparable for all the VF values, however, at the minor axis, the peak of electron temperature differ for all VF values. Floating potential appears comparable for all the VF current values. The dip in plasma potential and floating potential coincides with the position of hot cathode indicating that in steady state, electrons emitted from filament results in effective negative charge at the minor axis. The gradient in (ϕ_{p0}) and (ϕ_{f0}) indicate the presence of a mean electric field directed from the wall to the minor axis. The gradient in plasma profiles acts as a source of free energy, giving rise to instabilities and consequent coherent and turbulent fluctuations.

The error-bars in plasma density shown in Fig. 4.1(a) are estimated from the uncertainties in ion saturation current, electron temperature, probe collection area and statistical variation between multiple shots. The contribution of each of them is discussed as follows. The ion saturation current is measured across a 1 kΩ resistance in which has a maximum tolerance of 10%, uncertainty in electron temperature arises from the asymmetric potential on three pins of Triple Langmuir probe. Error in collection area arises due to the thin sheath approximation, in which probe area is considered to be equal to sheath area under the condition that probe radius should be much larger than the electron Debye length. In our case, the probe radius is 0.5 mm and it is nearly 20 times of the electron Debye length as shown in Table. 4.3, hence, thin sheath approximation holds good. To estimate uncertainty due to the sheath correction for a cylindrical probe such as the one used here, with $3mm$ exposed length and $0.5mm$ diameter and with the axis of the probe perpendicular to the magnetic field. The thin sheath approximation is used which is valid when the probe radius is much larger than the electron Debye length. In our case probe radius is about 20 times the electron Debye length hence thin sheath approximation is valid. Hence uncertainty in collection area A is $\delta A/A \simeq x_s/a$ where x_s is the sheath thickness and a is the probe radius. Sheath thickness is given by [41]

$$\frac{x_s}{a} = 1.02\frac{\lambda_{De}}{a}\left(\frac{\ln(m_e/m_i)^{1/2}}{\sqrt{2}} - \frac{1}{\sqrt{2}}\right)^{1/2}\left(\frac{\ln(m_e/m_i)^{1/2}}{\sqrt{2}} + \sqrt{2}\right) \tag{4.1}$$

with m_e/m_i for Argon gas. The corrected sheath area A_s for a cylindrical probe is given as

$$A_s \approx A\left(1 + \frac{x_s}{a}\right) \tag{4.2}$$

Using Eqn. 4.1, maximum uncertainty due to sheath area was found to be around 20%. Thus the error in density measurements are found to be predominantly from uncertainty in sheath area and shot-to-shot variations. These uncer-

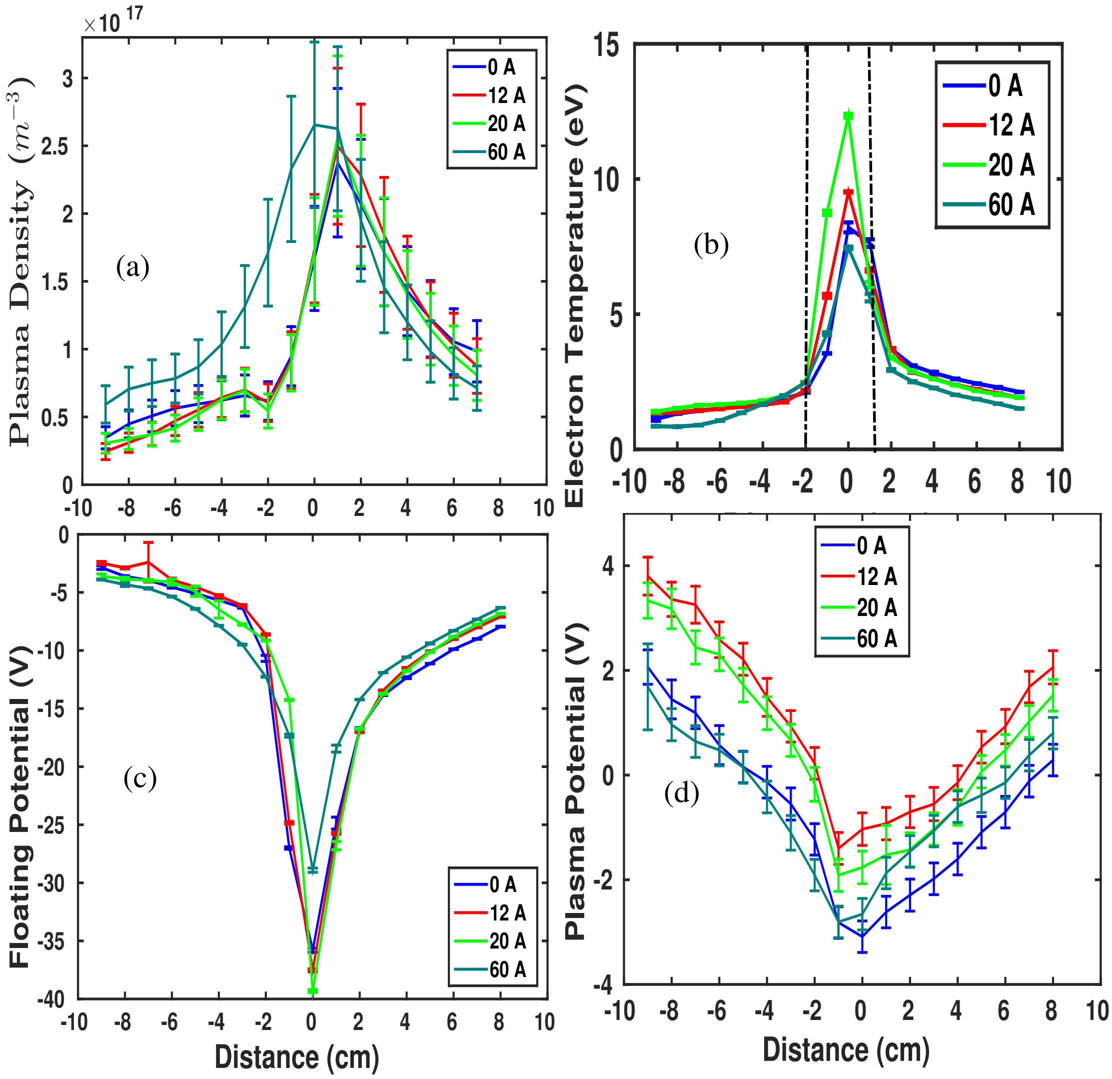

Figure 4.1: Radial profiles of (a) Mean density (b) Mean electron temperature (c) Mean floating potential and (d) Mean plasma potential. Profiles for all the parameter have been shown here for four different values of vertical field coil current. The dip in the floating potential and peak in electron temperature profile (region between vertical lines) around the minor axis is due to the presence of high energy electrons which makes this region more negative. Error-bars on density measurements are found to be predominantly from uncertainty in sheath area, uncertainty in ion saturation current and shot-to-shot variations, for details, see discussion around Eqn. 4.3

tainties have been cast as error-bars on density as follows:

$$\delta n_0/n_0 = \sqrt{\left(\frac{\delta I_{sat}}{I_{sat}}\right)^2 + \left(\frac{\delta A}{A}\right)^2 + \frac{1}{2}\left(\frac{\delta T_e}{T_e}\right)^2 + \left(\delta n_0/n_0\right)^2_{ss}} \qquad (4.3)$$

where $\left(\delta n/n\right)_{ss}$ is the error due to shot-to-shot variation. Plasma potential shown in Fig. 4.1(d) are measured using emissive probe using a floating potential method, as this method is found to be less erroneous [50, 52]. As discussed in Sec. 2.3.5, the only major source of error is of the order $\frac{kT_w}{e}$ where T_w is the temperature of the heated probe. For our emission currents, we estimate $\frac{kT_w}{e} \simeq 0.25$. So, the error-bars on plasma potential are resultant of T_w/e and shot to shot variation, using similar approach as shown in Eqn. 4.3.

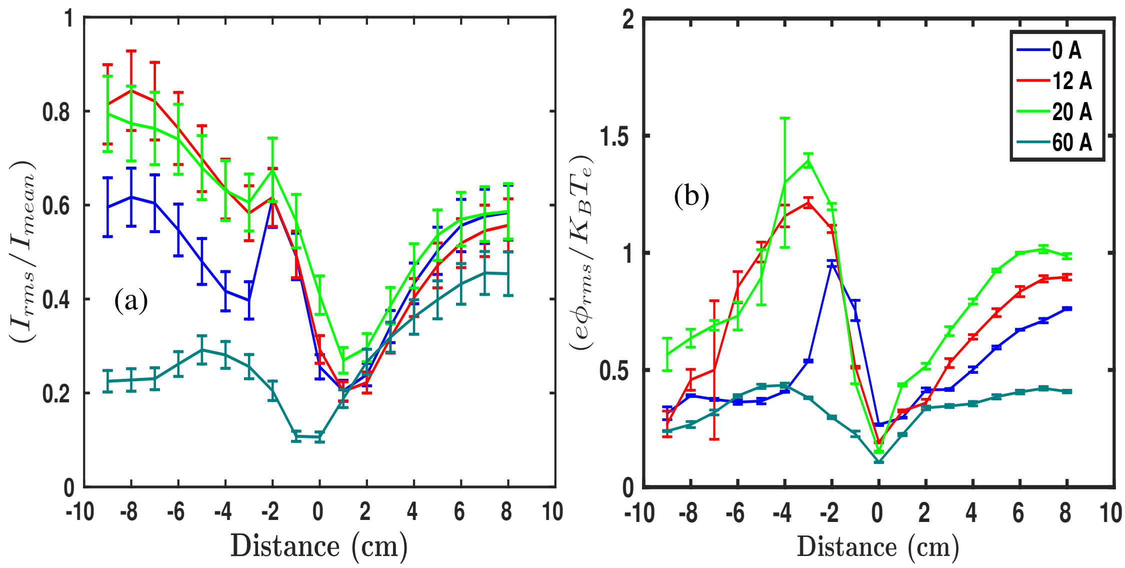

Figure 4.2: Radial profiles of relative "rms" fluctuations of (a) ion saturation current which are equivalent to the density fluctuations when the fluctuation in T_e is very small (b)floating potential normalized is to electron temperature. Profiles for both the parameter have been shown here for four different values of vertical field coil current. Error-bars on "rms" value of ion saturation current is due to uncertainty in ion saturation current measurements across $1k\Omega$.

The radial profile of relative "rms" fluctuation in ion saturation current and floating potential normalized to local mean electron temperature is shown in Fig. 4.2. Attempts have been made to measure relative fluctuation in electron temperature and were found to be insignificant (not shown here). Hence we assume that the relative fluctuation in I_{is} is equivalent to relative density fluctuation and relative fluctuation in floating potential represents the plasma potential fluctuation. Error-bars on "rms" value of ion saturation current is due to uncertainty in ion saturation current measurements across $1k\Omega$, as discussed above. On HFS as well as on LFS, relative fluctuation in both density and potential increases for 12 A and 20 A and reduces significantly for 60 A case. Since the fluctuations are found contribute to the poloidal flow, which further helps in sustaining the mean profiles [3, 38], a study with varying nature of fluctuations and consequent poloidal flows with varying $\bar{L}_c$ are reported in subsequent sections.

In this Section, we discussed the mean plasma parameters, in the next section [Sec. 4.4.2] we will address the nature of fluctuation.

4.4.2 Spectral Analysis

As described, there exists a substantial gradient in density profile, which may trigger various gradient driven instabilities in the plasma. These instabilities may further excite fluctuations in the plasma, in this Section, we shall attempt to characterize the nature of fluctuations and nonlinear interactions, if any.

4.4.2.1 Power Spectrum

We have characterized the nature of fluctuations and the possible turbulence by spectral analysis technique [8, 24]. The auto power spectra of density and potential are shown in Fig. 4.3. At 0 A VF current the dominant modes appear at around 6 kHz with several other modes but at higher values of VF currents shown here the dominant modes appears at around 2.5 kHz with very few other modes. On low field side (LFS) shown in Fig. 4.3(b) and 4.3(d) a broadband appears for 60 A VF current for both density and potential. Sampling frequency for data shown in Fig. 4.3 is 200 kHz, all these plots are blown up to 35 kHz.

The local wavenumber and frequency spectrum $S(k,\omega)$ of potential fluctuation is estimated using the measurement obtained from two vertically separated probe tips with separation of 4 mm.

$$S(k,\omega) = \frac{1}{M}\sum_{i=1}^{M} I_{[0,\Delta k)}[k - k^j(\omega)] \times \frac{1}{2}[P_{11}^j(\omega) + P_{22}^j(\omega)] \tag{4.4}$$

where

$$I_{[0,\Delta k)}[k - k^j(\omega)] = \begin{cases} 1, & \text{if } k \leq k^j(\omega) \leq k + \Delta k \\ 0, & \text{otherwise} \end{cases}$$

M is the number of records, $P_{11}^j(\omega)$ and $P_{22}^j(\omega)$ indicate auto power for frequency

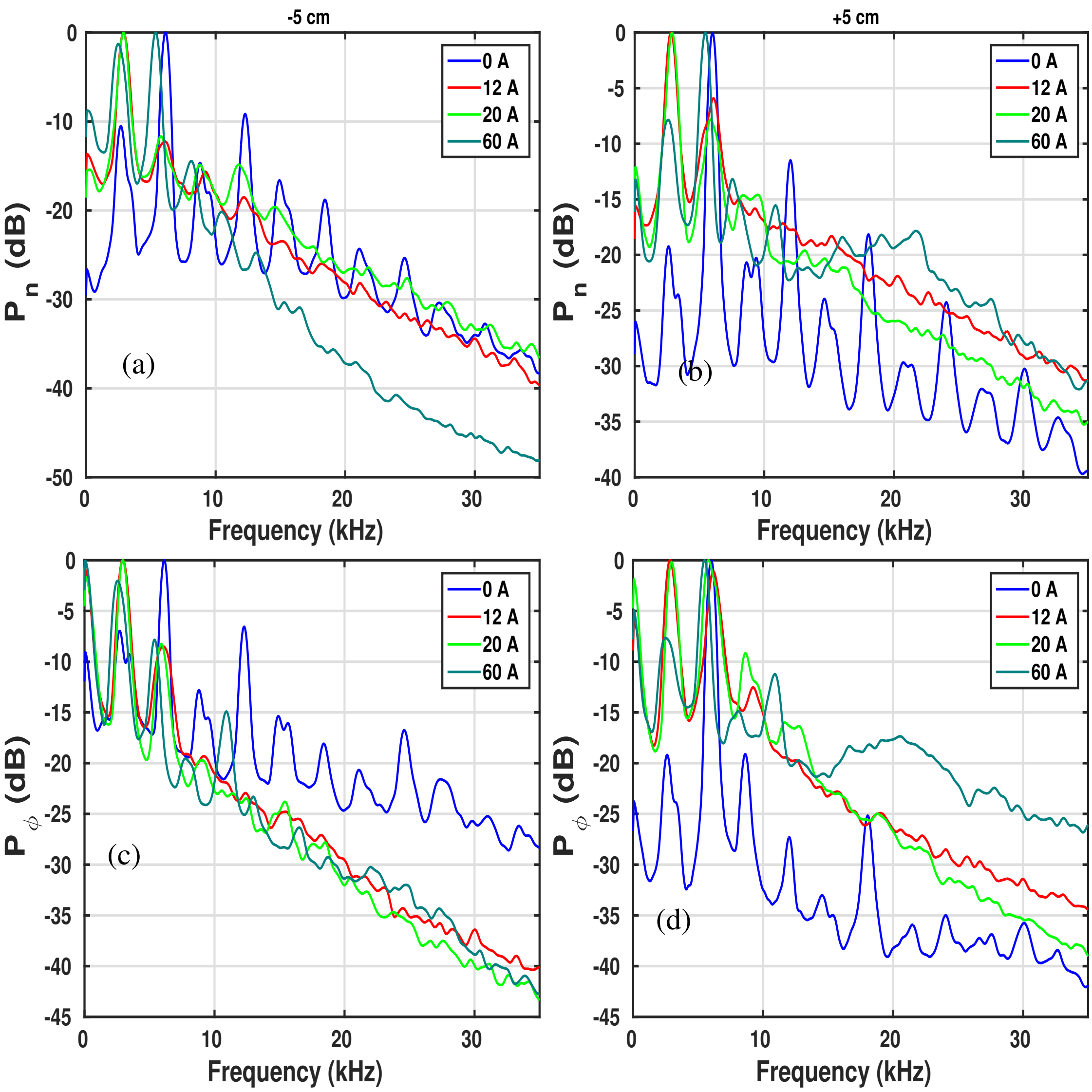

Figure 4.3: Auto power spectra for (a) density at -5 cm (b) density at +5 cm (c) potential at -5 cm (d) potential at +5 cm for four different values of vertical field coil current. Here it can be observed that the dominant frequency for 0 A is around 6 kHz, but for higher values, it is around 3 kHz and also at +5 cm for 60 A, a broad band for higher frequencies can be seen. Though sampling frequency is 200 kHz, but all these plots zoomed in to 35 kHz only.

ω for j^{th} record. The conditional spectrum is defined as

$$S(k|\omega) = \frac{S(k,\omega)}{\frac{1}{2}[P_{11}(\omega) + P_{22}(\omega)]} \tag{4.5}$$

where $P_{11}(\omega)$ and $P_{22}(\omega)$ are frequency spectral densities or auto power spectra for two time series. The first moment of the conditional spectrum is defined as

$$\bar{k}(\omega) = \sum_{m=-N_c/2+1}^{N_c/2} k_m S(k_m|\omega) \tag{4.6}$$

where $k_m = m\Delta k$, gives the average wavenumber. The range of wavenumber for given $\delta x = 4mm$ is -7.8$cm^{-1} \leq k_m \leq 7.8cm^{-1}$. For $N_c = 100$, $\Delta k \approx 0.16cm^{-1}$. Using $S(k,\omega)$, we can estimate the average vertical wavenumber k with very little error [24]. For example, for the present case, we have used M = 156 record each with 512 points to estimate $S(k,\omega)$, resulting in estimation error $1/M \approx 0.006$.

Contour plots of conditional spectrum $S(k|\omega)$ [Eq. 4.5] with embedded line showing vertical wavenumber (k_z or k_θ) estimated using Eq. 4.6 on both HFS as well as on LFS are shown in Fig. 4.4. It can be observed from Fig. 4.4 that the vertical wavenumber (k_z or k_θ) exactly follows conditional spectrum $S(k|\omega)$ and also for -5 cm for all VF currents, while k_z shows positive values, which shows wave propagation upwards and for +5 cm, it has negative values indicating the downward wave propagation. These are compatible with our net poloidal flow measurement shown in Fig. 4.9.

As we have determined the frequencies and wavenumbers of the various modes, however, it does not provide any information about the non-linear interaction among the modes. To this end, bispectrum analysis has been performed, which is discussed in Sec. 4.4.2.2.

4.4.2.2 Bispectral Analysis

The auto power spectrum shows the modes with corresponding frequencies, however, it cannot give any information about non-linear interaction present among these modes. In the bulk region of plasma, a large number of modes are present as shown in Fig. 4.3, hence these modes may interact non-linearly to generate new daughter modes or turbulence. The non-linear coupling of waves can be estimated using a well known three-wave interaction scheme [66], however, more than three mode interaction cannot be described by using bispectrum analysis.

The squared bicoherence $b(\omega_1, \omega_2)^2$ between two frequencies ω_1 and ω_2 is given as

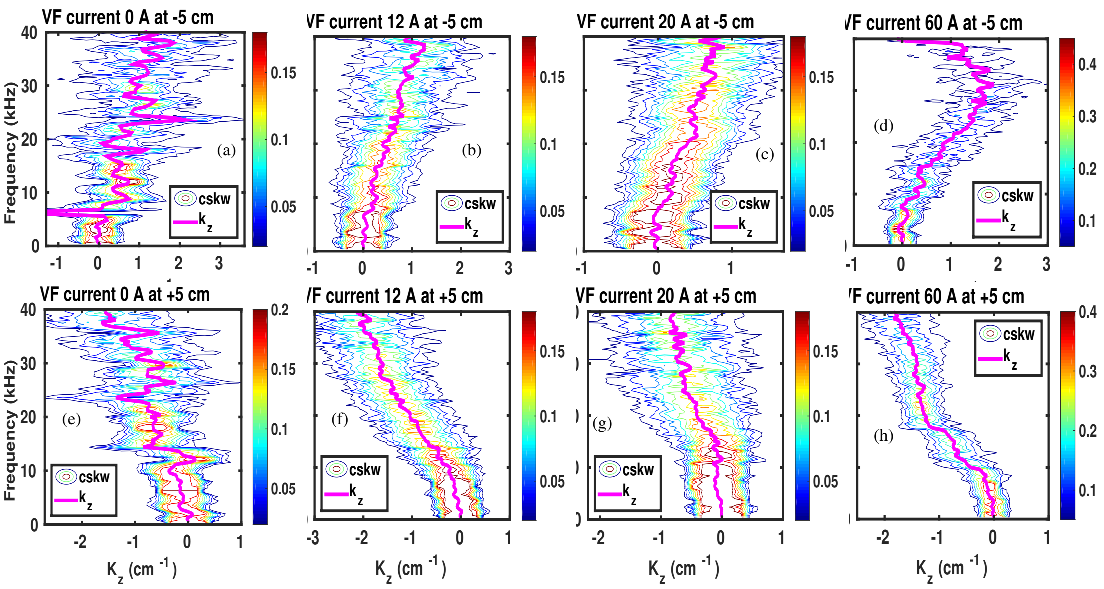

Figure 4.4: Contour plots of conditional spectrum $S(k|\omega)$ with embedded line showing vertical wavenumber (k_z or k_θ) for (a) VF current 0 A at -5 cm (b) VF current 12 A at -5 cm (c) VF current 20 A at -5 cm (d) VF current 60 A at -5 cm (e) VF current 0 A at +5 cm (f) VF current 12 A at +5 cm (g) VF current 20 A at +5 cm and (h) VF current 60 A at +5 cm.

$$b(\omega_1,\omega_2)^2 = \frac{|\frac{1}{M}\sum_{i=1}^{M} X_i(\omega_1)X_i(\omega_2)X_i^*(\omega_1+\omega_2)|}{(\frac{1}{M}\sum_{i=1}^{M}|X_i(\omega_1)X_i^*(\omega_2)|^2)(\frac{1}{M}\sum_{i=1}^{M}|X_i(\omega_1+\omega_2)|^2)} \tag{4.7}$$

where $X_i(\omega)$ represents the Fourier coefficient and $X_i(\omega)^*$ represents its complex conjugate for ω.

Bicoherence estimated in Eqn. 4.7 is expected to converge as the value of M increases. Here M is the number of realizations at a fixed frequency resolution. For estimating the convergence, the total bicoherence has been estimated, which is given as [67]

$$\Sigma b^2(\omega) = \lim_{M\to\infty} \Sigma b^2[\omega; M] \tag{4.8}$$

where b^2 is the estimated bicoherence.

The Fig. 4.5 shows the convergence of our bicoherence analysis for 4 values VF currents and their corresponding power spectrum of density fluctuation is also shown. It can be observed that the bicoherence obtained is highly convergent for

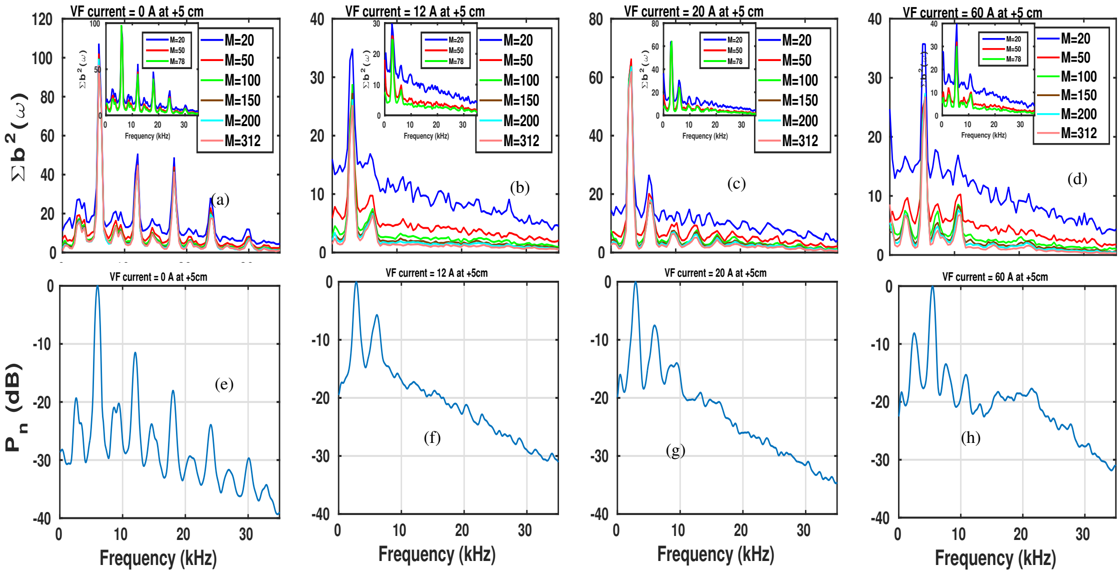

Figure 4.5: Total bicoherence for combined multiple shots and for single shot shown in inset of each total bicoherence plot in (a) for 0 A (c) for 12 A (e) for 20 A and (g) for 60 A VF currents and at +5 cm radial location. Corresponding power spectrum is shown in for (b) 0 A (d) 12 A (f) 20 A and (h) 60 A at + 5 cm radial location. It can be observed that the bicoherence shows reasonably good convergence for all VF currents.

all VF currents. Even for single shot data shown in the insets of the Fig. 4.6, shows good convergence for M = 20, 50 and 78. Fig. 4.6 shows bispectrum for rest of the values of VF currents with bispectrum zoomed in up to 40 kHz. As discussed earlier, due to the scale length of density inhomogeneity, the fluctuations are expected to be dominant in the range of 3-20 kHz. Our density and potential fluctuations and its bicoherence spectra clearly support our expectations. As can be understood, bicoherence spectrum indicates the strength of three mode non-linear interactions. The weakening of bicoherence amplitude with increasing values of B_v indicates the onset of broadband turbulence. This is seen to reflect in the fluctuation spectrum.

Here we have used M = 78 records each with 512 points to estimate $b(\omega_1, \omega_2)^2$, resulting in estimation error $1/M \approx 0.012$. The plot of bicoherence, $b(\omega_1, \omega_2)^2$ for I_{is} fluctuations at -5 cm and +5 cm are shown in Fig. 4.6. Fig. 4.6(a), 4.6(b), 4.6(c) and 4.6(d) shows bispectrum at -5 cm radial location and Fig. 4.6(e), 4.6(f), 4.6(g) and 4.6(h) shows bispectrum at +5 cm for 0 A, 12 A, 20 A and 60 A case respectively. $b(\omega_1, \omega_2)^2 \geq 0.9$ for 0 A case, but, it reduces to around 0.2

for 60 A case, implying that several mode coupling interactions are present for 0 A case which get suppressed for higher values of VF current. It can be concluded that for very large $\bar{L}_c$ values as in the case of 12 A and 20 A or very small $\bar{L}_c$ as in the case of 60 A, only few modes are present, subsequently the non-linear interaction among modes reduces and $b(\omega_1, \omega_2)^2$ is quite smaller than 1. Reduction in number of coherent modes for VF currents other than 0 A can be clearly seen in Fig. 4.3. Non-linear interactions are more dominant on +5 cm as compared to -5 cm location. For the case of long connection length, we speculate that the coherent low frequency peaks interact nonlinearly with low amplitude background turbulence [67] and produce the "horizontal line" in the corresponding bi-spectrum shown in Fig. 4.5.

These fluctuations and non-linear interaction among modes can lead to poloidal flow due to fluctuating component of radial electric field, as addressed in the subsequent section [Sec. 4.4.3].

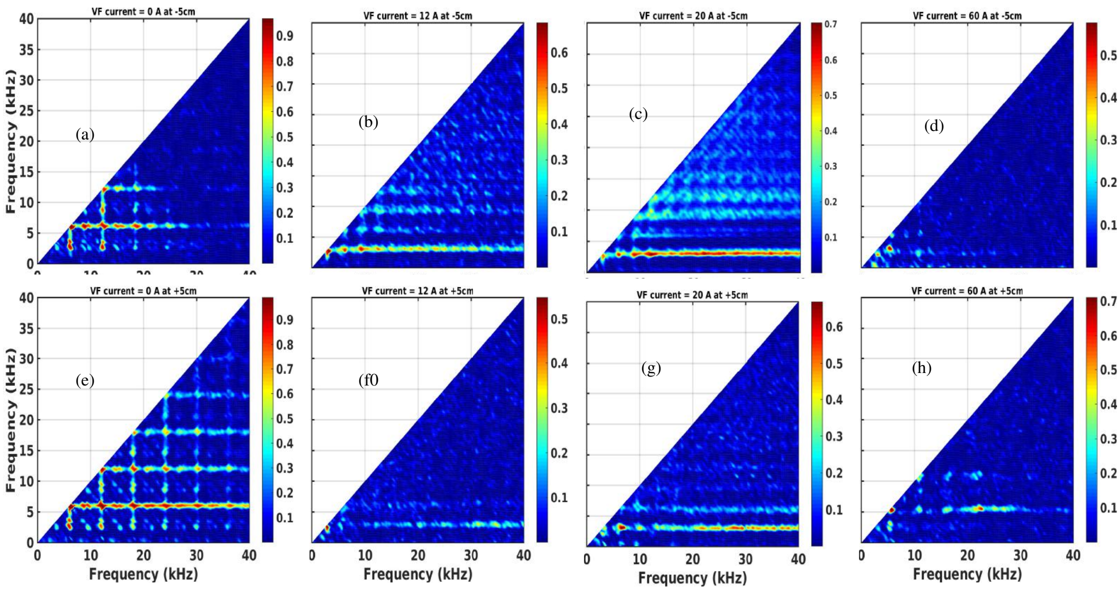

Figure 4.6: Bispectrum of I_{is} fluctuation for single shot for VF current of 0 A, 12 A, 20 A and 60 A at -5 cm and +5 cm. $b^2 > 0.9$ for 0 A and reduces further for higher currents. These plots are zoomed in up to 40 kHz.

4.4.3 Poloidal flows

As shown in Fig. 4.1(d), there exists substantial gradients in the plasma potential profiles, which indicates the presence of a strong zeroth order mean radial electric field, $E_r(r)$. Along with mean radial electric field, the fluctuating component of the radial electric field due to fluctuations in plasma properties is also present. The mean and fluctuating radial electric field provides a $E_r \times B_T$ rotation to the plasma. In this Section, one by one we will discuss the details of the mean as well as fluctuation driven flow along with their resultant net poloidal flow.

4.4.3.1 Mean Electric field driven flow

From the radial mean profile of plasma potential $\phi_p(r)$ obtained using an emissive probe, mean radial electric field E_r can be estimated by taking the spatial derivative of plasma potential radial profile. Here we have used fourth order central differencing method to estimate electric field in the bulk region and lower order differencing method to estimate electric field at the end points.

To estimate the error-bars in mean $E_r \times B$ velocity, the uncertainty in emissive probe measurements described in Sec. 4.4.1 has been used along with the uncertainty in probe positioning which is around 1 mm in each 1 cm and shot to shot variation in multiple shots. The maximum error due to emissive probe measurements are found to be around 20% and in the probe positioning error is around 10%. For fourth order central differencing method is of the fourth order of step-size, hence this error is very small and therefore neglected. The resultant of these errors provide error-bars for $v_{E_r \times B}$.

The hot cathode mounted at the minor axis is biased with a -70 V with respect to the grounded vessel wall. Thus electrons emitted have to execute a cross-field transport to reach the wall. In this process, a radial potential well is created between the vessel wall and hot cathode and it provides the radial electric field. Consistent with the above discussion, the direction of the mean electric field is found to be inward towards the minor axis, which provides a $E_r \times B$ rotation to the plasma in the poloidal direction, which is referred to as mean electric field driven poloidal flow ($v_{E_r \times B}$), shown in Fig. 4.7. The mean electric field driven flow is shown here for four different values of VF currents; it can be seen that for 0 A, 12 A and 20 A case the flow remains comparable on HFS as well as on LFS, except close to filament location i.e., -2 cm and -1 cm, but for 60 A case the value reduces on HFS.

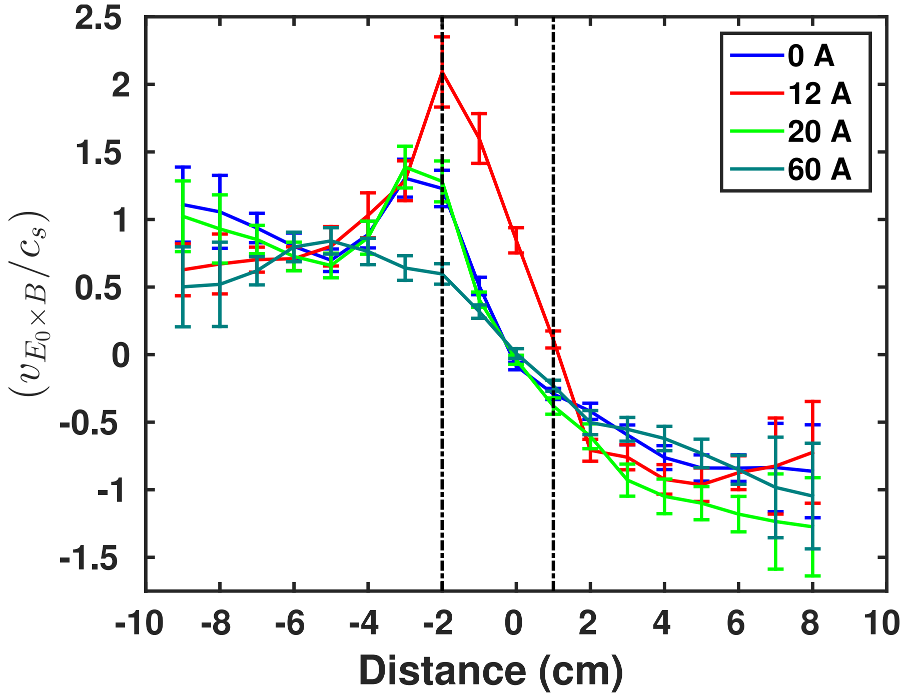

Figure 4.7: Mean electric field driven poloidal flow normalized to local ion acoustic velocity c_s, $(v_{E_r \times B})/c_s = (1/c_s)(E_r \times B)/B^2 = (1/c_s)(E_r/B)$. This flow is derived from plasma potential ϕ_p profile measured using an emissive probe. The central differencing method is used in deriving field E_r. The unusually high flow around -2 cm could be due to the presence of high energy electrons in this region.

4.4.3.2 Fluctuation driven flow

The mean radial electric field leads to a poloidal flow due to $E_r \times B$ drift as described in Sec. 4.4.3.1. Similarly, the fluctuating radial electric field can also lead to a finite fluctuation induced poloidal flux, depending upon the relative phase between density and potential fluctuations. In earlier work in BETA [38], this fluctuation induced poloidal flux has been found to play a vital role in the generation of self-consistent flow and effective rotational transform. Fluctuation driven flow is estimated using a radial array of Langmuir Probes described in Sec. 2.3.3, by measuring floating potential fluctuations on first two probes and measuring ion saturation current fluctuations and hence the density fluctuations on the third probe. Then using a digital spectral technique to estimate the flux [68]. In this method, the fluctuation induced flux is given as

$$\Gamma = < \tilde{n}\tilde{v} > = \frac{1}{B} < \tilde{n}\tilde{E} > = \frac{2}{B} Re \int_0^\infty P_{nE}(\omega) d\omega \tag{4.9}$$

where $\tilde{n}$, $\tilde{v}$ and $\tilde{E}$ are the fluctuating part of density, velocity and electric field respectively, B is the local magnetic field and P_{nE} is the cross power of density and electric field fluctuation and the factor of 2 comes because of symmetry properties of the cross power spectrum.

In most practical experimental situations, it is more convenient to measure potential fluctuation, $\tilde{\phi}$, rather than electric field fluctuations. As temperature fluctuations are very small, so $\tilde{\phi}_p \approx \tilde{\phi}_f$. Hence $\tilde{E} = -\nabla\tilde{\phi}_f$. So, relation between $P_{nE}(\omega)$ and $P_{n\phi}(\omega)$ can be expressed as

$$P_{nE} = -ik(\omega)P_{n\phi}(\omega) \tag{4.10}$$

Hence Eq. 4.9 gets modified as following

$$\Gamma = < \tilde{n}\tilde{v} > = \frac{1}{B} < \tilde{n}\tilde{E} > = -\frac{2}{B} Re \int_0^\infty ik(\omega) P_{n\phi}(\omega) d\omega \tag{4.11}$$

or,

$$\Gamma = < \tilde{n}\tilde{v} > = \frac{1}{B} < \tilde{n}\tilde{E} > = \frac{2}{B} \int_0^\infty k(\omega) Q_{n\phi}(\omega) d\omega \tag{4.12}$$

where $Q_{n\phi}(\omega)$ is the quad-spectrum between density and potential fluctuations, $Q_{n\phi(\omega)}$ is estimated from imaginary part of $P_{n\phi}$.

Then fluctuation induced velocity is given as

$$v_{fluc} = \frac{\Gamma}{< n >} \tag{4.13}$$

Fig. 4.8 shows the radial profile of Γ for four VF current values. To estimate the error-bars in fluctuation driven flux the uncertainty in density described in Sec. 4.4.1 is used along with the error in probe separation uncertainty ($\sim 10\%$) and statistical variation of multiple shots have been used. Close to the minor axis, Γ estimates are found to change by an order of magnitude, with a large peak or dip; subsequent check for typical radial wavelengths shows that the wavelength becomes comparable to the probe separation. The approximation of measuring $\tilde{n}$ and $\tilde{E}$ at a single point is, therefore, not valid. Hence Γ close to the minor axis is not reported. In the rest of the region, the radial wavelength is much larger than

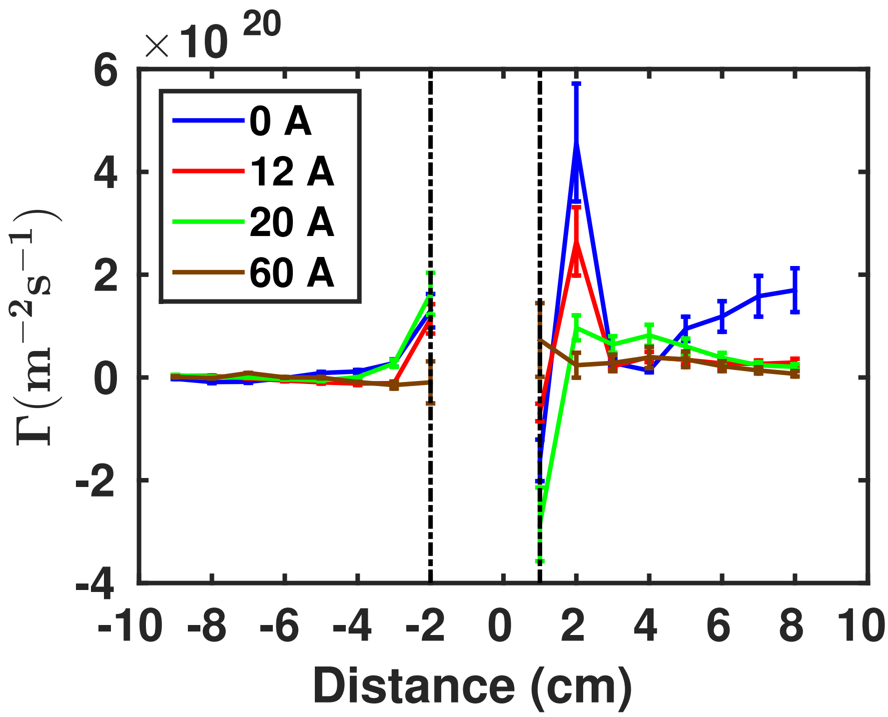

Figure 4.8: Radial profile of fluctuation induced flux, Γ for four values of VF coil current. It has been observed that around the minor axis, the wavelength becomes comparable or smaller than the radial probe separation of radial array diagnostic. Therefore, due to the short nature of wavelengths, measurements close to the minor axis (populated with high energy electrons) are not valid and not shown here.

the probe separation, hence Γ estimation is valid. For all VF values, Γ is found to be small on the HFS and significant only on LFS. With an increase in VF current, the value of Γ is reduced significantly.

In the present Chapter, one of our focuses is to obtain net poloidal flow estimates which are expected to comprise of mean poloidal flow and fluctuating poloidal flow. Poloidal particle flux is estimated from fluctuating components of density and radial electric field and averaging are performed in the range 0.4 KHz to 35 KHz. As the poloidal flow is sheared, (see Fig. 4.15) we believe that the poloidally propagating coherent structures may not contribute strongly as they may be localized and short lived. Thus in our case, the fluctuation induced poloidal flux is expected to be driven by local instabilities and the resultant phase difference between fluctuating density and electric field. Moreover, an estimation of the appropriate coherent structure timescale requires 2D measurements which is beyond the scope of the present work. More on this is described in Conclusions (Chapter-8).

4.4.3.3 Net Flow

Net flow measurement has been performed using the Mach probe described in Sec. 2.3.4. From the ion saturation current drawn at the two ends of the probe, the flow velocity can be calculated using the Eqn. 2.10 [49].

In Eqn. 2.10, α is the calibration factor and may be accurately obtained by using a “known flow”. Thus by measuring ion saturation currents for a “known flow”, α can be obtained with good accuracy. However, in our experiments, we identify radial locations where the fluctuation driven flow is close to zero (see Fig. 4.8). At these radial locations by considering that the $E \times B$ driven flow is shown in Fig. 4.7 to be the “known flow”, we obtain α from 4 (four) different radial locations where the fluctuation-driven flow is zero. The values of α's thus obtained are found to vary less than 20%, thus validating our methodology of calibration. The mean value of α used here is 0.7 throughout the net flow measurements.

Fig. 4.9 shows the radial profile of net poloidal flow measured using Mach probe for four value of VF current. The net flow for 0 A, 12 A and 20 A case is more on HFS than on LFS. However for 60 A case the flow gets reduced on HFS. The net poloidal flow profile with gradual variation in VF current is shown in Fig. 4.10, which confirms that the net poloidal flow reduces gradually on the inboard side close to the limiter with variation in VF current. Comparison of all the poloidal flows is shown in Fig. 4.11. The net poloidal flow differs from mean field driven flow throughout the radial profile: the difference is around 20% on HFS and around 60% on LFS. Assuming that error in the measurement of the electric field is around 10% - 15%, a flow also equal to the difference of net flow and mean field driven flow exist which is unaccountable by fluctuation driven flow also, the reason for which still unknown to us. As expected poloidal flows changes sign around the minor axis. For the 60 A case in which the field is widely opened, all the poloidal flows get reduced significantly on HFS and tend to zero on the extreme inboard side, close to the limiter.

To estimate the error-bars on net poloidal flow, we considered the area asymmetry on two probe surfaces of Mach probe which is around 10%, errors in calibrating the α, as discussed above, the maximum uncertainty is found to be around 20% and

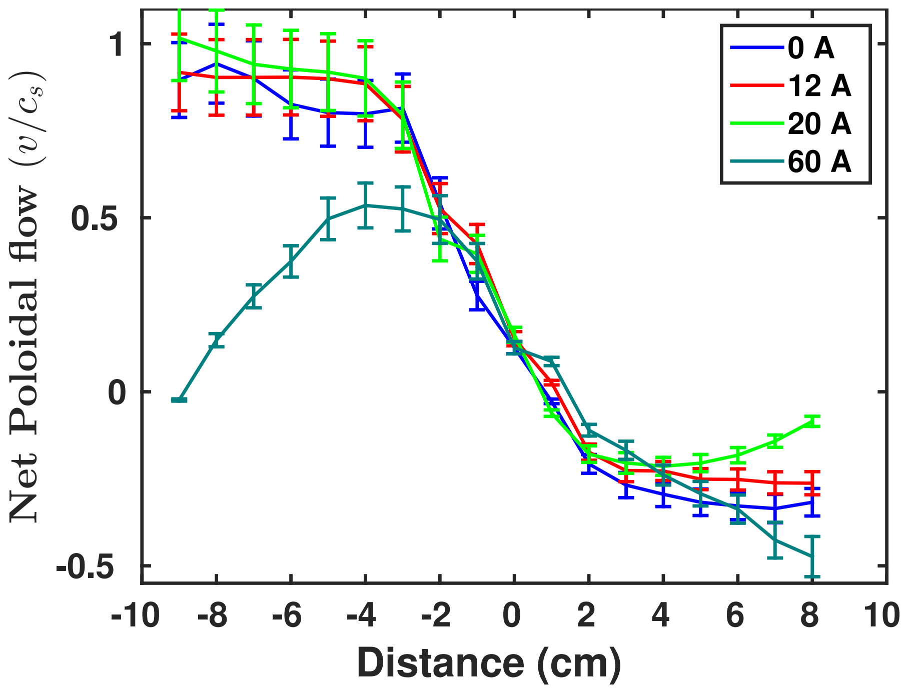

Figure 4.9: Radial profile of net poloidal flow measured using Mach probe for four values of VF coil current. The value of velocities are in Mach number as they are normalized with local acoustic speed. The net poloidal flow increase slightly for 12 A and 20 A case on HFS, but reduces to nearly zero for 60 A case.

shot to shot variation of multiple measurements has also been included. Resultant of these provides error-bars for net poloidal flows.

In Fig. 4.11, it can be seen that on HFS there is a significant difference between the mean $E_r \times B$ flow and net poloidal flow measured using Mach probe and this difference cannot be accounted by the fluctuation driven flow. However, on LFS this fluctuation driven flow qualitatively account for the difference between mean and net flow. Reason for this discrepancy has not been identified in the present Thesis and is to be addressed in future. A more detailed discussion is presented in Chapter-8.

4.4.4 Plasma profiles with gradual variation in VF current

In all the above Sections plasma profiles for 4 different value of VF current are shown, however measurement for 14 different VF current values were performed, which give a detailed picture of the effect of magnetic field topology on plasma mean parameters as well as on fluctuations. Here positive values of VF current

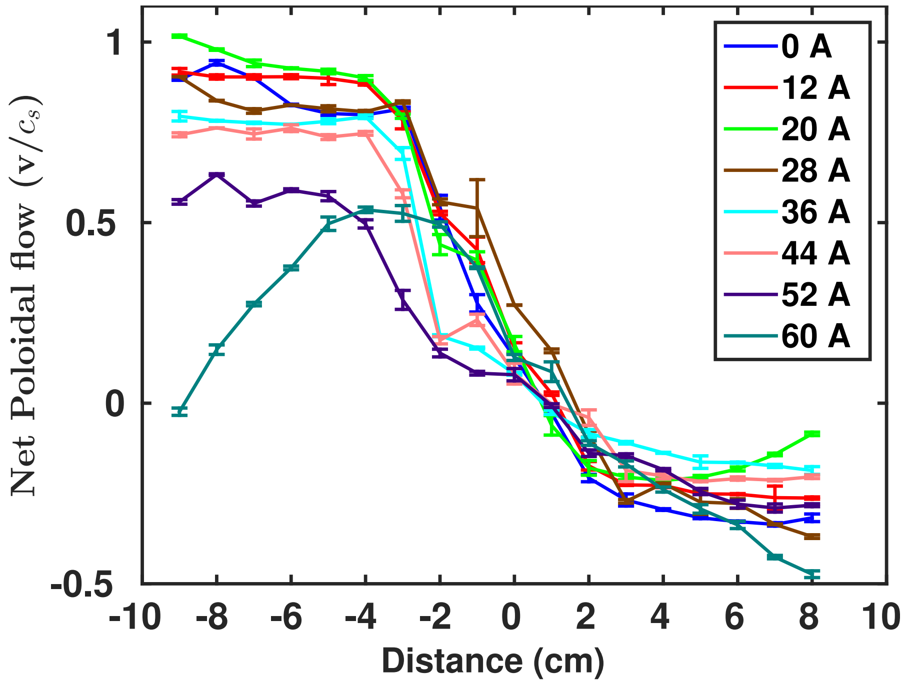

Figure 4.10: Effect of gradual variation of the VF current on the profile of net poloidal flow. It can be observed that the reduction of net flow on the inboard side close to the limiter is also gradual with variation in the VF current.

represents the clockwise direction of VF current from the top view and gives vertical magnetic field in the downward direction and similarly, negative values imply the anticlockwise direction of VF current and upward direction of the vertical magnetic field.

4.5 Radial mean profiles

Fig. 4.12 shows the radial variation of density, floating potential and plasma potential measured for 14 different VF current values, and it clearly shows that the mean parallel connection length $\bar{L}_c$ affects the mean profiles significantly. Again it can be seen that the peak in the densities and dip in the plasma and floating potential coincides around the minor axis, i.e., the source region. It can be seen that the density varies with VF current values non-monotonically, it increases for some values of VF currents like 60 A case and then decreases for some other values. Similar non-monotonic behavior can be observed for floating potential and plasma potential, however, the dip in both potentials coincides around the minor axis.

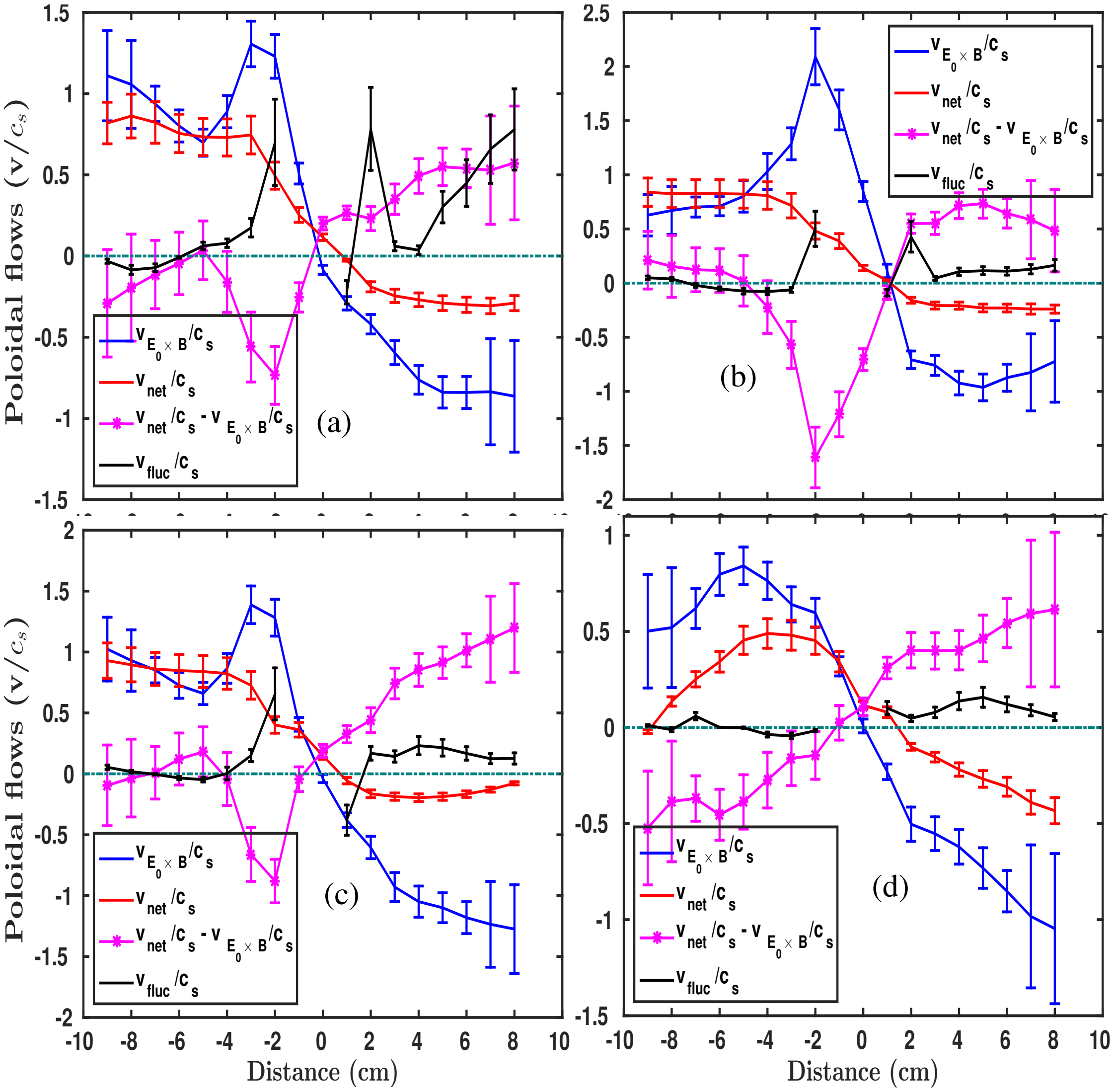

Figure 4.11: Comparison of all the component of Poloidal flows, viz., mean electric field driven flow, fluctuation field driven flow and net poloidal flow for VF current of (a) 0 A (b) 12 A (c) 20 A (d) 60 A. Curve for $(v_{net} - v_{E_r \times B})$ shows the expected contribution from the fluctuation driven flow, it confirms that the fluctuation driven flow cannot account for the difference between the mean flow and net flow.

4.5.0.1 Power Spectrum

From Fig. 4.13, it can be seen that the nature of fluctuations strongly depends on $\bar{L}_c$. For 0 A, 28 A, 36 A cases the spectrum shows the presence of several modes, but for other values, the higher modes get suppressed, moreover the fundamental modes changes with $\bar{L}_c$. On LFS broadband can be observed in frequency spectra,

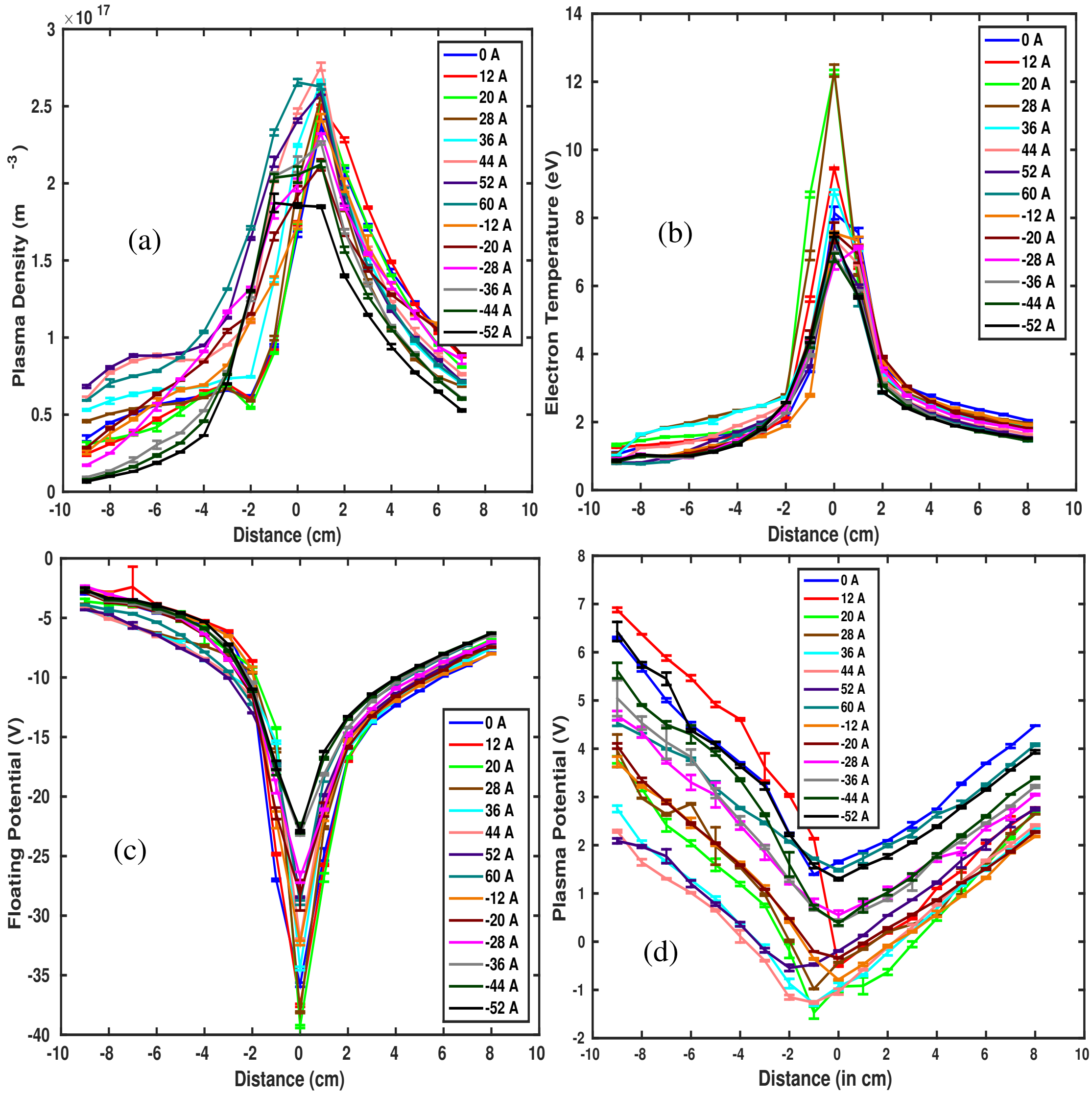

Figure 4.12: Radial mean profile of (a)Plasma density (b) Electron temperature (c) Floating potential (d) Plasma potential for 14 different values of VF current. It shows the gradual variation of plasma mean profiles with $\bar{L}_c$, it can be observed that the mean profiles are also controlled by $\bar{L}_c$.

which gradually becomes broader with the increase in VF current. It can be observed that in some cases where toroidal field lines are marginally opened and $\bar{L}_c$ is long enough to sustain fluctuations, several coherent modes are present, for nearly closed field lines (very long $\bar{L}_c$), only a few modes are present and higher modes get suppressed and for widely opened field line (very small $\bar{L}_c$) all modes are suppressed and a broadband frequency can be observed which could be due to

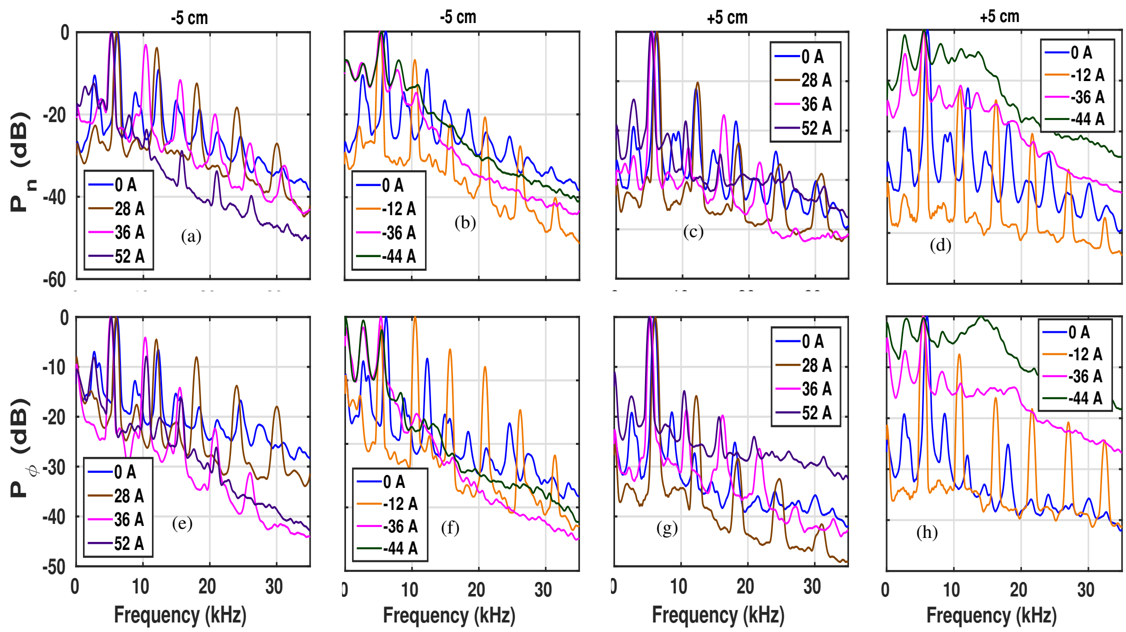

Figure 4.13: Power spectrum of density (a) at -5 cm for clockwise VF currents (b) at -5 cm for anti-clockwise VF currents (c) at +5 cm for clockwise VF currents (d) at +5 cm for clockwise VF currents. Power Spectrum of potential (e) at -5 cm for clockwise VF currents (f) at -5 cm for anti-clockwise VF currents (g) at +5 cm for clockwise VF currents (h) at +5 cm for clockwise VF currents . Here it can be observed that the for nearly closed field lines like for 12 A and 20 A, few modes are present, but for slightly opened field lines like 0 A, 28 A and 36 A several coherent modes are present and for widely opened lines broad band in frequency can be seen. Though sampling frequency is 200 kHz, all these plots blow up to 35 kHz only because above this frequency no significant modes are present. Power spectrum for 12 A, 20 A and 60 A is shown in Fig. 4.3 and data for 44A, -20 A, -28A and -52A VF values are available but not shown here to increase clarity of presentation.

turbulence.

4.5.0.2 Poloidal flows

Net poloidal flow estimation method using the Mach probe described in Sec. 4.4.3.3 for 4 values of VF currents, has also been applied for 14 values of VF currents which are shown in Fig. 4.14. The results show the effect of $\bar{L}_c$ on net poloidal flows, hence it confirms that the mean parallel connection length controls the nature of flows as well. For values from 40 A - 60 A clockwise case the net flow gradually reduce to zero on the inboard side, close to the limiter. This reduction of flow could be due to an effect of conducting wall [37], which become dominant for small $\bar{L}_c$. A detailed analysis is required to understand this issue. On comparing the Fig. 4.14(a) and Fig. 4.14(b), which shows net poloidal flow for clockwise and anticlockwise direction respectively shows that symmetry with the direction of VF current or topology of the magnetic field is not well behaved. For clockwise direction, on HFS flow reduces gradually and tends to zero on the extreme inboard side with increase in VF current but for the anticlockwise case the flow reduces with increase in VF current but does not become zero. Reason for this asymmetry, which is not yet understood, could be due to misalignment in the vertical field coils.

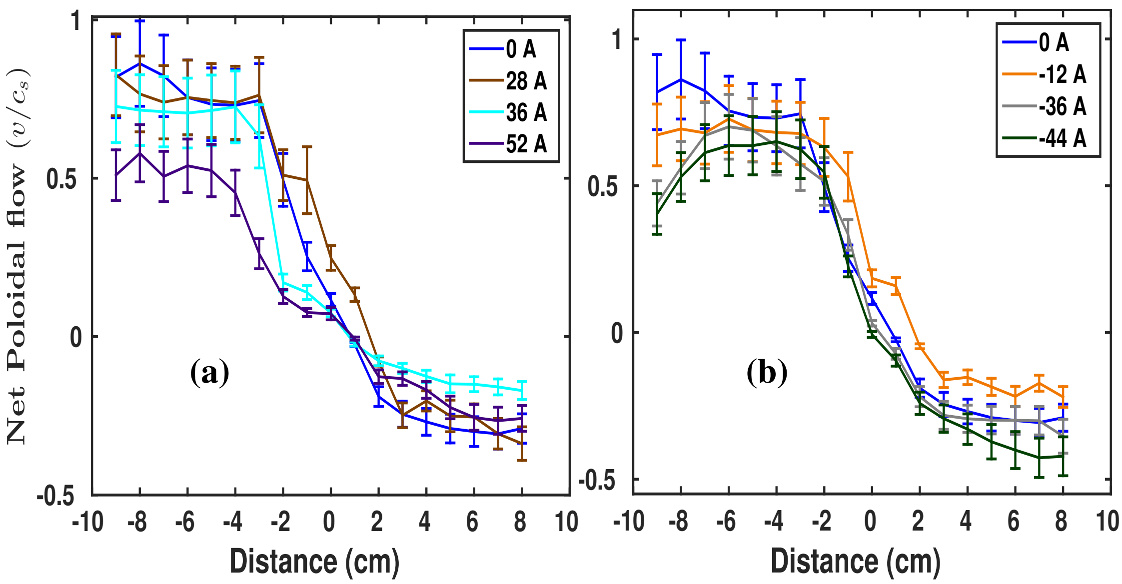

Figure 4.14: Net poloidal flow measured using Mach probe (a) for the clockwise direction of VF currents only indicated with positive values (b) for the anticlockwise direction of VF currents only indicated with negative values. It can be observed that for clockwise VF current values poloidal flow on HFS reduces gradually with VF current values, however for anticlockwise values flow reduces but symmetric with the clockwise case. It indicates that plasma properties are not symmetric with the direction of the topology of toroidal field. It is still not clear what causes this asymmetry. Net flow for 12 A, 20 A and 60 A is shown in Fig. 4.9 and data for 44 A, -20 A, -28 A and -52 A VF values are available but not shown here to increase clarity of presentation.

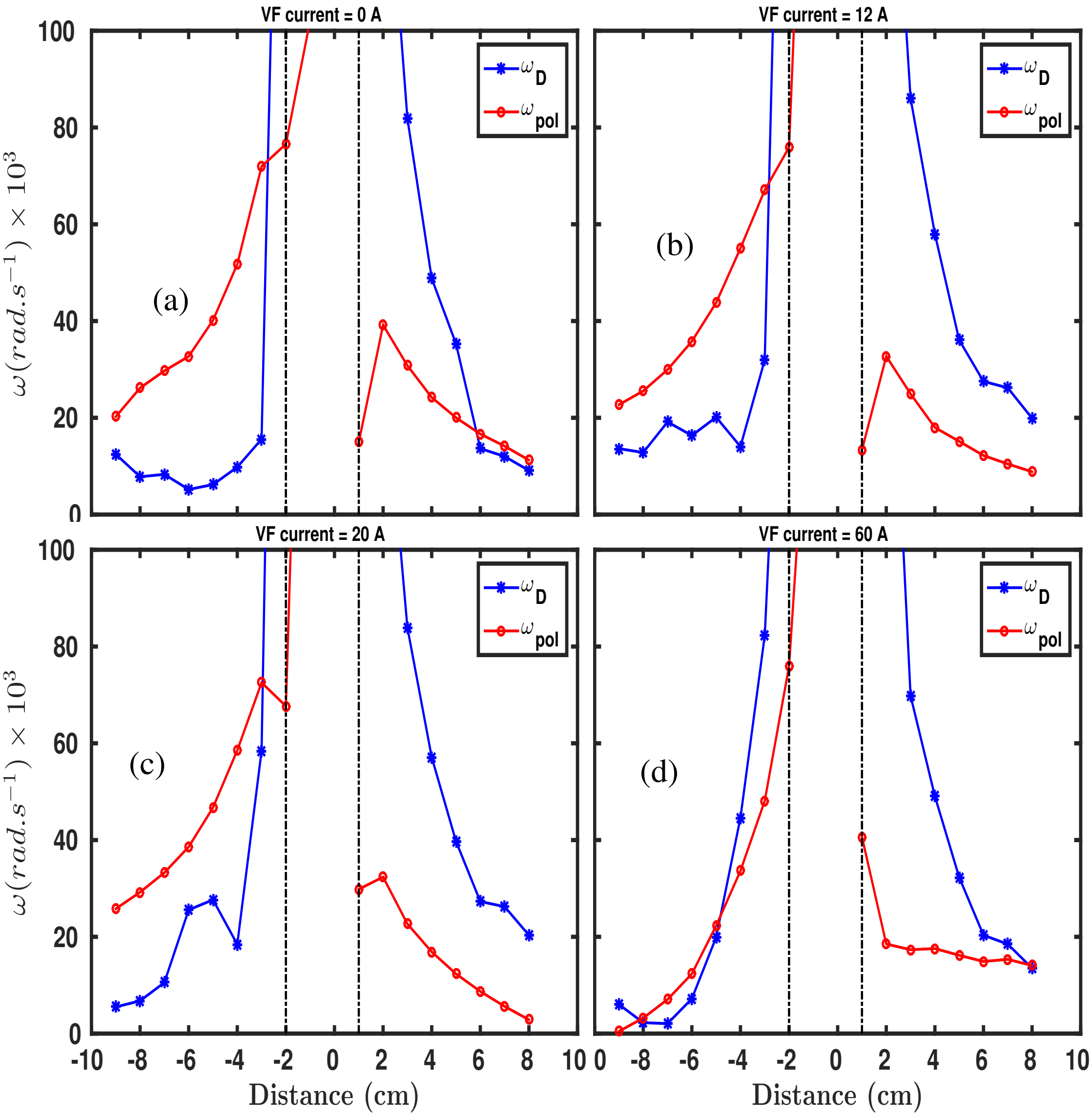

Figure 4.15: Radial comparison of diamagnetic angular velocity ω_D and angular velocity due to flow ω_{pol} for VF current of (a) 0 A (b) 12 A (c) 20 A and (d) 60 A. On HFS $\omega_D \ll \omega_{pol}$, which indicate the presence of velocity shear and shear driven instabilities are dominant here and on LFS $\omega_D > \omega_{pol}$, which implies that shear effects are not dominant here. The region between vertical lines in the above plots are populated with high energy electrons, hence the measurements may be erroneous.

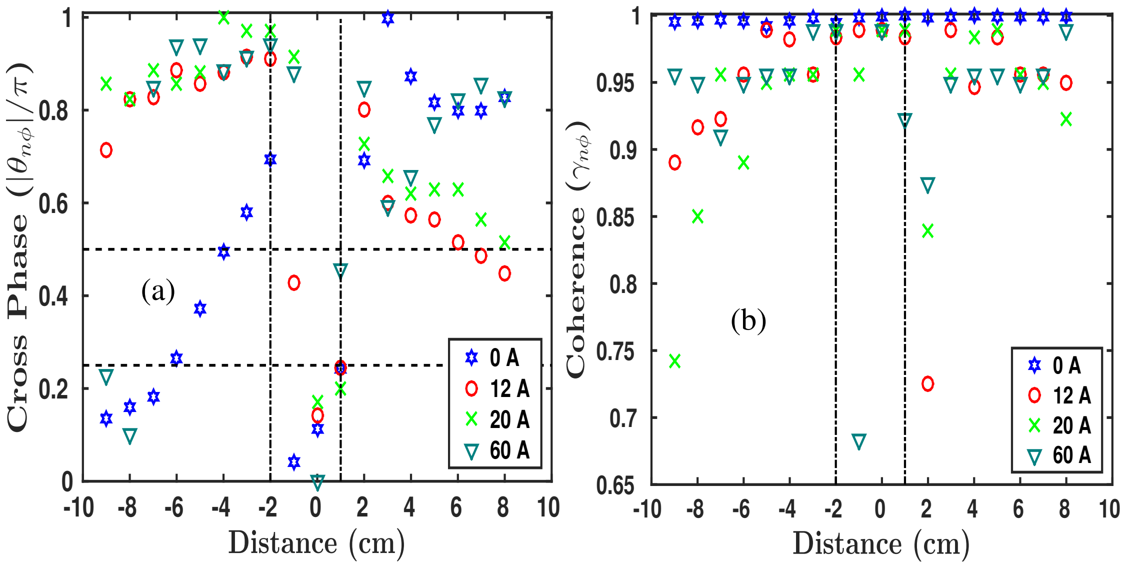

Figure 4.16: (a) Cross-phase normalized to π of density and potential fluctuations (b) Coherence between density and potential for four values of VF current of 0 A, 12 A, 20 A and 60 A. The measurements shown here are for dominant modes only. Here cross phase between density and potential is close to π on LFS which shows the presence of flute kind instabilities, but on HFS except 0 A all values are around π. Coherence for 0 A is almost 1 for the whole radial profile, but for other values, it ranges from 0.7 to 1. The region between vertical lines in above plots are populated with high energy electrons, hence the measurements may be erroneous. The region between horizontal lines in (a) signifies the different nature of instabilities for different $\theta_{n\phi}$, for example $0 < \theta_{n\phi} < 0.25\pi$ drift-like instabilities dominates, for $0.5 < \theta_{n\phi} < \pi$ flute-like instabilities may be present and intermediate values may indicate drift-interchange case.

4.6 Identification of instabilities

As described earlier, when the hot cathode is used as the plasma source, BETA is a device dominated by poloidal flows induced by equilibrium radial electric field, fluctuation-induced poloidal (or vertical flows) and connection length. Thus, BETA can be thought of as a device which is dominated by two major types of free energy sources. First one is the centrifugal force due to curvature on the LFS with an unfavourable density gradient, susceptible to Rayleigh-Taylor-like interchange instabilities and second is the class of poloidal velocity shear driven instabilities and can be categorized as Kelvin-Helmholtz-type interchange instabilities. In the absence of any measurable electron temperature fluctuations in BETA, the above

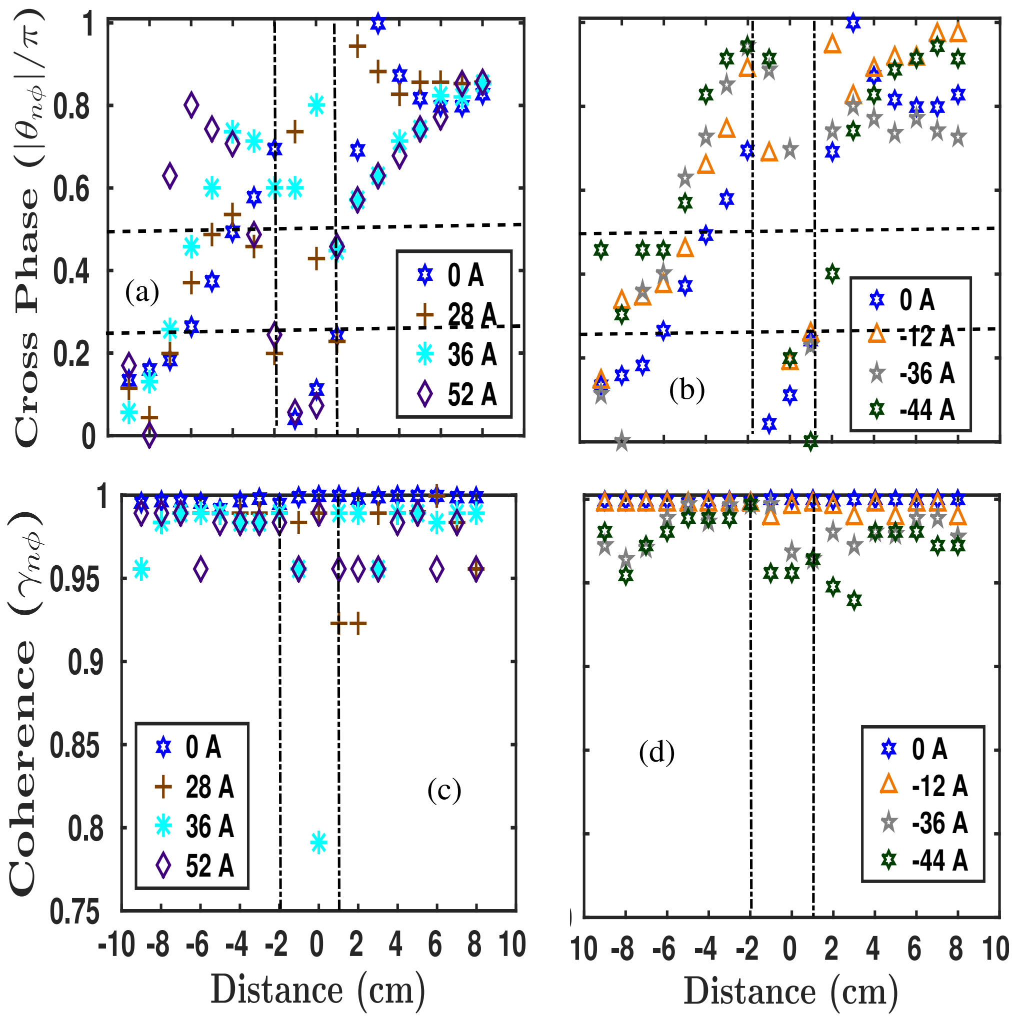

Figure 4.17: Cross-phase normalized to π of density and potential fluctuations for (a) the clockwise direction of VF currents (b) the anticlockwise direction of the current. Coherence between density and potential for (c) clockwise direction of VF currents (d) the anticlockwise direction of the current. The measurements shown here are for dominant modes only. Here also on LFS cross phase for almost all values of VF current is close to $\pm\pi$, but on HFS it changes with VF current. Coherence ranges from 0.2 to 1. The region between vertical lines in above plots is populated with high energy electrons, hence the measurements may be erroneous. The horizontal lines are shown in (a) and (b) signifies the different nature of instabilities for different $\theta_{n\phi}$, for example $0 < \theta_{n\phi} < 0.25\pi$ drift-like instabilities dominates, for $0.5 < \theta_{n\phi} < \pi$ flute-like instabilities may be present and intermediate values may indicate drift-interchange case. Cross-phase and coherence for 12 A, 20 and 60 A is shown in Fig. 4.16 and data for 44 A, -20 A, -28 A and -52 A VF values are available but not shown here to increase clarity of presentation.

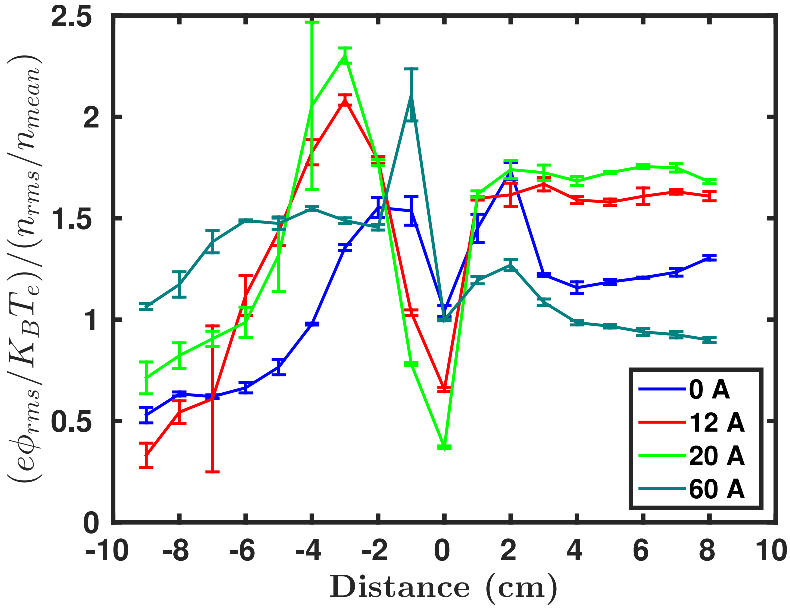

Figure 4.18: Radial profile of ratio of relative potential fluctuations to relative density fluctuations. On HFS for 0 A case the value ranges from 0.5 to 1, but for 12 A and 20 A case it goes from 0.2 to 2.2 which shows the presence of shear instabilities. On LFS for 0 A, 12 A and 20 A case the value is just above 1 which signifies the presence of flute kind of instabilities, for 60 A case it slightly less than 1.

said class of instabilities are found to be modified due to electron-neutral collisions, electron diffusivity controlled by T_e and parallel connection length $\bar{L}_c$ (or $k_{||}$) via application of external B_v leading to shear modified weak drift, drift-interchange and interchange modes.

In the following, we describe the methodology used and interpret our experimental measurements using measured cross-phase between fluctuations, cross-coherence and relative fluctuation strengths. In the past, in devices dominated by flows [69], measurements of cross-phase between fluctuations of density and potential, coherence between these two quantities and their relative strengths have been successful in predicting the nature of instabilities which in turn, point a finger at the source of the underlying free energy as described earlier. More recently, in other simple toroidal devices [16], the above said procedure was found to be inadequate to completely determine the nature and source of instabilities found. Motivated by the success of the cross-phase, coherence and relative fluctuations in flow-dominated devices in the past, we present in the following, our experimental

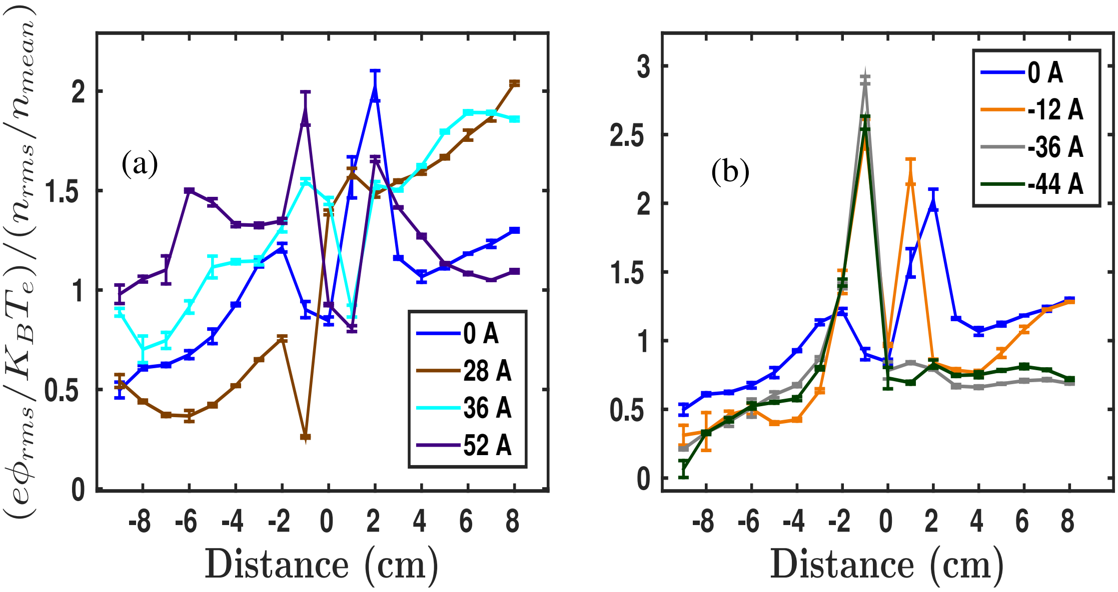

Figure 4.19: Radial profile of ratio of relative potential fluctuations to relative density fluctuations .On HFS for some VF current values it goes 3 which shows presence of shear instabilities. On LFS for some case the value is just above 1 which signifies presence of flute kind of instabilities, for other VF values the ratio is less than 1.

measurements and identify various instabilities which largely seem to corroborate well with simple linear stability based estimates.

For our neutral pressure of 1×10^{-4} Torr, magnetic field of 220G and average electron temperature of $T_e \sim 3eV[T_i \sim (T_e)/10^2]$, we find that $\nu_{en}/\omega_{ce}, \nu_{in}/\omega_{ci} \ll 1$, where ν_{en} and ν_{in} are the electron neutral and ion neutral collision frequencies respectively and ω_{ce}, ω_{ci} are gyration frequencies of electrons and ions. Hence we consider our plasma to be nearly collision-less. Similarly, electrons and ions are well magnetized as $\rho_{Le}/a, \rho_{Li}/a \ll 1$, where ρ_{Le} and ρ_{Li} are the Larmour radius of electron and ion respectively and a is the minor radius of the device. In the parallel direction, the physics is determined by parallel connection length $\bar{L}_c$, electron-neutral as well as ion neutral mean free paths and electron thermal diffusivity $\chi \sim 2v_{th,e}^2/\nu_{en}$. When the electric field and density gradient are in the plane but perpendicular to the ambient magnetic field, major instabilities are Simon-Hoh and Collision-less Simon-Hoh instabilities. As discussed, our plasma is collision-less hence conventional collisional Simon-Hoh [37] may be ruled out. For collision-less Simon-Hoh, arising due to the difference in finite Larmour radius (FLR) of electrons and ions, the theoretically estimated real frequencies are between electron and ion cyclotron frequencies. However, our observed frequencies are much smaller than both ion and electron cyclotron frequencies. Hence we eliminate collision-less Simon-Hoh instability as well. Determination of $k_{||}$ gives clear distinction between flute-like and drift-like instabilities [4, 16]. In the present work, we obtain the values of $k_{||}$ experimentally using the method suggested by Thatipamula et al [63]. Our values of $k_{||} = 2\pi/\bar{L}_c$ for 0 A, 12 A, 20 A and 60 A are 0.11 m^{-1} , 0.011 m^{-1} , 0.078 m^{-1} and 0.54 m^{-1} respectively at +3 cm and the number of toroidal turns toroidal field line makes before hitting the limiter or wall is given as 14, 182, 26 and 4 respectively.

In the Fig. 4.15, a comparison between angular diamagnetic velocity ω_D defined as $\omega_D = k_z(T_e/B)(1/L_n)$ and angular velocity due to poloidal flow ω_{pol}, for vertical or poloidal mode number, m=1 is defined as $\omega_{pol} = v_{pol}/r$ as measured at $Z =$ 0 plane have been shown as a function of radial variable. For spatial regions where ω_{pol} greater than ω_D, shear driven instabilities may be expected to dominate [69, 70]. For spatial regions where $\omega_{pol} < \omega_D$, interchange and/or diamagnetic drift related instabilities may be expected to dominate. With this preamble, in the following, let us try to identify the instabilities on LFS and HFS.

4.6.1 Instabilities on Low Field Side (LFS)

Low field side or LFS is the region where effective gravity due to curvature plus the poloidal centrifugal force and gradient in density are opposite to each other making it ideal for the occurrence and growth of Rayleigh-Taylor (R-T) type instability. For R-T instability, the cross phase between density and potential fluctuation should be between 0.5π and π [16] and $(e\tilde{\phi}/K_BT_e)/(\tilde{n}/n) \geq 1$ [23, 71]. In Fig. 4.16 and Fig. 4.17, the absolute value of experimentally obtained cross-phase between fluctuations in density and potential is shown as a function of the radial variable, for all values of B_v, along with its cross-coherence. It is evident that $\theta_{n\phi} > 0.5\pi$ for the LFS. Similarly, Fig. 4.18 and Fig. 4.19 shows $(e\tilde{\phi}/K_BT_e)/(\tilde{n}/n) \geq 1$ for the entire LFS for all VF currents. It is also consistent with the measured frequencies shown from Fig. 4.15 on LFS. It can be seen that the $\omega_D > \omega_{pol}$, therefore shear effects are not prominent on LFS. Hence one can attribute these observation to resultant of R-T instability [23, 71] and centrifugal instability [69]. In the presence of velocity shear, the real frequency of R-T mode is given as [37]:

$$\bar{\omega}_r = \frac{1}{2}[(\frac{2L_n}{R} - \frac{T_i}{T_e})\omega_D + \frac{1}{k_z}(V_{pol}^{//} - \frac{V_{pol}^{/}}{L_n})] \tag{4.14}$$

where $\bar{\omega}_r = \omega_{lab} - k_z v_{E_r \times B}/2\pi$ is the Doppler shifted real frequency, $V_{pol}^{/}, V_{pol}^{//}$ are the velocity shear and L_n is the density scale length. In our case $T_i/T_e \ll 1$ and considering $V_{pol}^{/} \approx \omega_{pol}$, $V_{pol}^{//} \approx 0$, then Eqn. 4.14 becomes

$$\frac{\bar{\omega}_r}{\omega_D} = \frac{1}{2}[\frac{2L_n}{R} - \frac{1}{k_z L_n}\frac{\omega_{pol}}{\omega_D}] \tag{4.15}$$

where $k_z = 16m^{-1}$, R=0.45 m, for LFS $L_n = 0.05 - 0.1m^{-1}$, then $L_n k_z \sim 1$ and $L_n/R \approx 0.15$ and also from Fig. 4.15, it can be observed that on LFS $\omega_{pol}/\omega_D \approx 0.15$, it implies that $\bar{\omega}_r/\omega_D \approx 0$. From experiments for 0 A VF current, $v_{E_r \times B} \approx 2200ms^{-1}$, $k_z \approx 16m^{-1}$ at +5 cm, $k_z v_{E_r \times B}/2\pi \approx 5.6kHz$, whereas observed lab frequency is 6 ± 0.4 kHz. Hence the observed frequency is believed to be Doppler shifted frequency itself. Therefore, our observations are consistent with our speculation that R-T instability is the most dominant instability on the LFS mildly corrected by velocity shear. We next turn to HFS.

4.6.2 Instabilities of High Field Side (HFS)

As discussed in Sec. 4.6.1, the LFS is prone to RT instability. Presence of poloidal flow brings in more flute-like character to the fluctuations on the LFS. Measurements of cross-phase, cross-coherence and ratio of potential to density fluctuations confirm this.

On the HFS, effective gravity and density gradients are in the same direction, which rules out RT-like flute instability for HFS. Fig. 4.9 and 4.14 suggest that the net poloidal flow measured strongly depends on the value of VF coil currents. For example, as VF values are increased from 12 A on either direction (meaning B_v up or down), the net flow on the HFS has a tendency to "turn around" towards inner limiter, thus providing conditions for Kelvin-Helmholtz like velocity shear driven instability. Consistently, Fig. 4.16 and Fig. 4.17 indicate 12 A and 20 A which have the longest connection lengths have $\theta_{n\phi}$ close to π. From Fig. 4.15, on the HFS, it can be observed that $\omega_{pol} \geq \omega_D$. Fig. 4.9 shows presence of large poloidal flows on HFS, which is the signature of velocity shear [69, 70] and this can give rise to shear-driven Kelvin-Helmholtz (K-H) instability [69].

For values of VF coil currents, where $\omega_{pol} \leq \omega_D$, nature of the instability appears to "mixed-mode", i.e., these modes appear to have characters of both weakly resistive-drift modes and velocity shear driven KH instability. Hence one can expect the presence of K-H instabilities on HFS for those values of VF currents for which $\omega_{pol} \geq \omega_D$ and drift/drift resistive instabilities for values of VF which show $\omega_{pol} \leq \omega_D$. Interestingly, for 60 A case, flow reduces to zero on extreme inboard side as shown in Fig. 4.9 and these points coincides with $\omega_{pol} < \omega_D$ in Fig. 4.15(a) and $\theta_{n\phi} \approx 0$ in Fig. 4.16(a), which are the signatures of drift or resistive drift instabilities. Hence one can conclude that as soon as velocity shear driven effect reduces, the drift instability dominates. For VF currents such as -12 A, 0 A, 28 A, 36 A, the value of $\theta_{n\phi} < 0.5$ in Fig. 4.16 and Fig. 4.17 along with $(e\tilde{\phi}/K_BT_e)/(\tilde{n}/n) < 1$, which indicate presence of drift instabilities for these values on HFS. For resistive drift instability, the Doppler shifted mode frequency [37] is $\bar{\omega} \ll \chi k_{||}^2$, and $\chi \sim 2v_{th,e}^2/\nu_{en}$. Let us find out $\bar{\omega}$ for 0 A case. The $k_{||}$ given earlier are at the minor axis of the BETA, for radial location of -9 cm or -8 cm, the $k_{||} \approx 0.198m^{-1}$, so $(\chi k_{||}^2)/(2\pi) \approx 6.4$ kHz and $\bar{\omega}/(2\pi) \approx 5.1$ kHz also $\theta_{n\phi} \sim 0.15\pi$ and $(e\tilde{\phi}/K_BT_e)/(\tilde{n}/n) < 1$, therefore, it may be confirmed that resistive-drift instability is present for 0 A case at extreme inboard side of HFS. However, for bulk region of HFS, where velocity shear is dominant $(\omega_{pol} > \omega_D)$ along with $\theta_{n\phi} < 0.25\pi$ and $(e\tilde{\phi}/K_BT_e)/(\tilde{n}/n) < 1$, drift-interchange instability may be present in this region. Similar estimate for VF current values of 28 A, 36 A and -12 A can be performed and they provide similar results. Hence one can comment that for these VF currents, resistive-drift and drift-interchange instabilities may be present on HFS Moreover, it can be predicted that there exist a strong correlation between mean parallel connection length $\bar{L}_c$ and the nature of instabilities.

4.7 Summary of Part-I

In a simple toroidal device, with a hot cathode as the plasma source, mean parallel connection length $\bar{L}_c$ has been controlled by varying the strength of the vertical component of the magnetic field. To begin with, we choose four values of VF current for which detailed discussion has been performed are the 0 A with the inherent opening of field line, 12 A and 20 A with field line is believed to be nearly closed in between these two values and 60 A for which the field line is widely opened. The direction of current for all these values is in the clockwise direction from the top view. Later the VF current values are changed in small steps in the clockwise and anticlockwise direction to get the more detailed picture of the role of $\bar{L}_c$ on flow and fluctuations in simple toroidal devices. For the clockwise direction of VF currents, the field line is found to be nearly closed for the values in between 12 A and 20 A [63]. On further increasing the vertical field coil current in same direction field lines get opened up. As can be expected on increasing VF current in the anticlockwise direction, the field lines get opened up in opposite direction.

As discussed earlier, the measurements reported in this work are along the radial direction on $Z = 0$ plane. We assume here that the measurements at $Z = 0$ meaningfully reflect the physics of the addressed problem. We believe that obtaining a 2-D profile of plasma will provide further insight into the problem and will be presented in a future communication.

Measured density profile shows that density scales up on HFS for 60 A case, but for other VF current, density remains comparable on HFS as well as on LFS. On LFS density for 60 A case is slightly lower than other VF current. Relative density and potential fluctuations increases for 12 A and 20 A case and reduced for 60 A case. Bispectral analysis also shows the presence of non-linear interaction among modes for 0 A case and value of $b^2 > 0.9$, but for higher values no significant non-linear interaction is present. Coherence measured for all VF current shows that for 0 A case the density and potential fluctuations are coherent for all radial locations, but as VF current increases the coherence decreases and it ranges from 0.65 to 1 at various locations.

Relative density and potential fluctuations increase for 12 A and 20 A case and reduced for 60 A case. In Sec. 4.6 various instabilities have been identified. It has been confirmed that on LFS the instabilities responsible for fluctuations are mainly R-T along with centrifugal instability for all VF currents. However, on HFS, nature of instabilities changes with variation in $\bar{L}_c$ and also strong poloidal flows present on HFS provides velocity shear, which gives rise to shear driven instabilities.

The effect of all these instabilities and turbulence can be seen in net poloidal flow, which shows strong dependence upon $\bar{L}_c$. On LFS poloidal flow does not vary much with $\bar{L}_c$, but on HFS a marginal increase in flow velocity within the error-bars can be seen for 12 A and 20 A case and flow reduces for 60 A case. Poloidal flows are strong on HFS and give rise to velocity shear, which leads to shear driven instabilities. So, it can be concluded that these flows significantly control the equilibrium and fluctuations.

On HFS for all values of VF current, there exist a difference between the net poloidal flow measured from Mach probe and mean $E_r \times B$ flow, in which E_r is estimated from the radial profile of plasma potential obtained from the emissive probe; fluctuation driven flow alone cannot account for this difference, however, on LFS it qualitatively accounts for the difference. A possible mechanism to explain this discrepancy is still unknown and will be addressed in future.

Main observations are as follows:

- It has been seen that $\bar{L}_c$ strongly affects the mean plasma parameters such as density, electron temperature, plasma potential and floating potentials. Density varies non-monotonically with $\bar{L}_c$ and strong dependence on $\bar{L}_c$ can be seen in plasma potential profiles.

- Nature of fluctuation changes significantly with $\bar{L}_c$, as it can be seen that for large $\bar{L}_c$, few modes are present and for very small $\bar{L}_c$ a broad band or turbulence can be seen, but for some cases where $\bar{L}_c$ is enough to sustain fluctuations, several coherent modes are present with strong non-linear interactions among them.

- Nature of flow also appears to be strongly affected by $\bar{L}_c$. For example, for very large $\bar{L}_c$ the increase in net poloidal flow and mean flow can be observed but for very small $\bar{L}_c$ both flows reduce significantly. Fluctuation driven flow also seems to be affected by $\bar{L}_c$, particularly on LFS.

- Equilibrium and fluctuation parameters are found to be affected strongly by poloidal flows and as nature of poloidal flows changes with $\bar{L}_c$ and it reflects in these properties.

- Poloidal flows generate velocity shear which can be confirmed by comparing angular velocity of poloidal flows to diamagnetic velocity in Fig. 4.15.

In this part of the Chapter, we discussed the role of mean parallel connection length, $\bar{L}_c$ on plasma properties by varying the external vertical field for a given

B_T. In the Part. II, a detailed study on the effect of $\bar{L}_c$ on plasma properties by simultaneously varying both B_T and B_v is discussed.

Part II

Effect of simultaneous variation of B_v and B_T on the hot cathode produced plasma properties

In Part-I of Chapter-4, we discussed the role of $\bar{L}_c$ on the plasma properties by varying B_v for a fixed value of B_T. However, from Eqn. 1.2, one can observe that $k_{||}^{min}$ and $\bar{L}_c$ can be varied by varying both B_v and B_T. Therefore, in this Part of the present Chapter, the experimental study of the role of varying $\bar{L}_c$ on plasma properties by simultaneous variation of B_v and B_T has been discussed in detail. For these, we have chosen three (B_v, B_T) pairs, which are large $\bar{L}_c$ for which field lines are almost closed on themselves, intermediate $\bar{L}_c$ due to the inherent opening of the toroidal field line and small $\bar{L}_c$ for widely opened field lines.

4.8 Operating condition

1. Base pressure $\sim 4 \times 10^{-6}$ torr
2. Filling gas: Argon
3. Working pressure $\sim 1\times10^{-4}$ torr
4. Filament current, $I_f \sim 142$ A
5. Discharge voltage, $V_d \sim$ -70 V
6. Discharge current, $I_d \sim 5$ A (operated at constant current mode)
7. B_T at the minor axis $\sim$ 220 G, 330 G and 440 G
8. VF current (B_v) $\sim$ 0 A (0 G), 12 A (0.9 G), 18 A (1.35 G), 24 A (1.8 G), 60 A (4.5 G), 90 A (6.75 G) and 120 A (9.0 G).

Plasma parameters	220 G	330 G	440 G
Ion Larmor radius (r_{Li})	9.4×10^{-2} m	6.3×10^{-2} m	4.7×10^{-2} m
Electron Larmor radius (r_{Le})	3.8×10^{-4} m	2.5×10^{-4} m	1.9×10^{-4} m
Ion gyration frequency ($\omega_{ci}/2\pi$)	7.9×10^{3} s^{-1}	1.2×10^{4} s^{-1}	1.6×10^{4} s^{-1}
Electron gyration frequency ($\omega_{ce}/2\pi$)	5.7×10^{8} s^{-1}	8.5×10^{8} s^{-1}	1.1×10^{9} s^{-1}

Table 4.2: The typical plasma parameters for Argon plasma for different B_T The rest of the plasma parameters are similar to the values shown in Tab. 4.3.

4.9 Experimental Results

As discussed in Sec. 4.4, the discharge is struck between hot cathode and wall of the vacuum vessel, with respect to which filament is biased. At operating conditions described earlier a discharge voltage pulse of -70 V of a duration of 0.8 sec is applied to the filament, during which the breakdown occurs and plasma is produced. The discharge current is set at 5 A. A detailed study of the role of mean parallel connection length, $\bar{L}_c$ on quasi-static equilibrium, fluctuation and poloidal flow has been already demonstrated in Part. I for a fixed toroidal field strength (B_T =220 G).

As evident from Eqn. 1.2, the $\bar{L}_c$ depends on the ratio of the B_v to the B_T. In the present work, three ratios of B_v/B_T will be presented to study the effect of $\bar{L}_c$. The chosen values of $\bar{L}_c$ are intermediate $\bar{L}_c$ (VF coils are not charged), large $\bar{L}_c$ (toroidal field lines are nearly closed on themselves and N is very large) and small $\bar{L}_c$ (toroidal field lines are widely opened and N is very small). As discussed earlier, we assume that these measurements at $Z = 0$ plane meaningfully reflect on the nature of the underlying problem.

4.9.1 Radial Plasma Profiles

Radial profiles of mean density, $n_0(r)$, are shown in Fig. 4.20 and Fig. 4.21 shows radial profiles of mean plasma potential (ϕ_{p0}). The time series of each plasma parameter, ion saturation current I_{is}, electron temperature T_e, floating potential ϕ_f and plasma potential is obtained using concerned diagnostics and data acquisition system described in Sec. 4.3 and the mean of these time series gives the corresponding mean plasma parameters. The mean density (n_0) is estimated using the formula $n_0 = 2I_{is,0}/eAc_s$ where e is the electron charge, A is the probe area, $I_{is,0}$ is the measured ion saturation current from probe and $c_s = (K_BT_{e0}/M_i)^{1/2}$ is the ion acoustic velocity with ion mass M_i.

The densities are shown in Fig. 4.20 increases monotonically with an increase in B_T for all $\bar{L}_c$. However, the gradient of densities is different for different $\bar{L}_c$. For intermediate $\bar{L}_c$ and large $\bar{L}_c$ cases, the density on High field side (HFS) is lower than the density on the Low Field Side (LFS), which is expected as curvature and gradient in B_T induce radial plasma transport. However, for small $\bar{L}_c$ value, the density profile is almost symmetric around its peak and densities values are comparable for HFS and LFS, which is interpreted to be an indication of the effective minimization of the residual E_z^{res}, created due to vertical charge separation [6]. It can be also observed that the nature of density gradient changes significantly with $\bar{L}_c$. For example for intermediate $\bar{L}_c$ or large $\bar{L}_c$ cases shown in Fig. 4.20(a) and Fig. 4.20(b), the density gradients are different on inboard and outboard sides, as on outboard side density gradient is steeper compared to inboard side. This also indicates that as the outboard side is a bad curvature region hence density gradient instabilities like Rayleigh-Taylor may dominate. However for small $\bar{L}_c$ case, the density gradient is almost similar on both side of the peak in density. Moreover, the magnitude of density for small $\bar{L}_c$ is more than that of intermediate $\bar{L}_c$ and large $\bar{L}_c$ cases, particularly on the inboard side. However, density gradient driven instabilities still dominate for the case of small $\bar{L}_c$, but overall loss of density due to gradient and curvature has been minimized. Plasma potentials for different $\bar{L}_c$ have been shown in Fig. 4.21, which indicate marginal change in the gradient with variation in $\bar{L}_c$. The spatial gradient in plasma potential provides a zeroth order radial electric field which further facilitates generation of poloidal flow, which has been discussed in detail in Sec. 4.9.3.

In Part. I, the uncertainty due to the sheath thickness has been used as the error in the density measurement. However, in this Part, the densities obtained using the sheath corrected probe area A_s instead of A [41] and therefore, the error-bars on density measurements are found to be predominantly from uncertainty in ion saturation current and shot-to-shot variations.

As discussed in earlier works [9], the region around the minor axis is contaminated with high energy electrons. Hence the experimentally obtained values of electron temperature (not shown) using Triple Langmuir probes close to the hot cathode location i.e., $\sim$1.5 cm on both side of the hot filament, may be erroneous due to the presence of fast primary electrons.

The radial profile of relative "rms" fluctuation in ion saturation current and floating potential normalized to local mean electron temperature shown in Fig. 4.22 and Fig. 4.23 respectively. Attempts have been made to measure relative fluctuation in electron temperature and were found to be insignificant (not shown here). Hence we assume that the relative fluctuation in I_{is} is equivalent to relative density fluctuation and relative fluctuation in floating potential represents the plasma potential fluctuation. The "rms" in density increases non-monotonically with B_T

[h!]

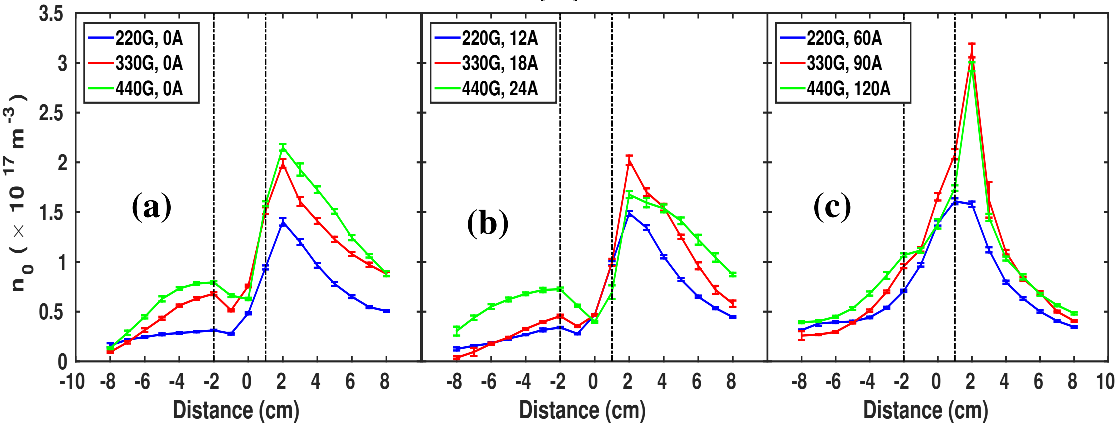

Figure 4.20: Radial profiles of Mean density for (a) intermediate $\bar{L}_c$ (b) large $\bar{L}_c$ and (c) small $\bar{L}_c$. For each case, the density increases monotonically with an increase in toroidal field B_T. (a) and (b) indicate more density on LFS as compared to HFS, but for (c) densities are comparable on both side. The vertical lines around the minor axis represent the region of high energy electrons.

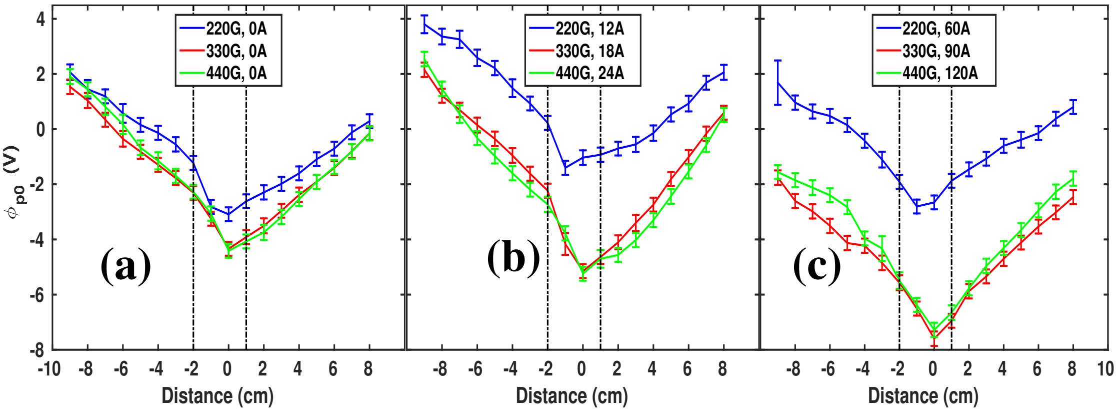

Figure 4.21: Radial profiles of plasma potential (a) intermediate $\bar{L}_c$ (b) large $\bar{L}_c$ and (c) small $\bar{L}_c$. Spatial gradient in plasma potential provides zeroth order radial electric field $E_r(r)$, which can provide a strong poloidal rotation to the plasma. The vertical lines around the minor axis represent the region of high energy electrons.

for intermediate $\bar{L}_c$ and large $\bar{L}_c$, and monotonically for small $\bar{L}_c$. The relative fluctuation in density reduces significantly for small $\bar{L}_c$ as shown in Fig. 4.22(c). Potential fluctuations normalized to electron temperature are shown in Fig. 4.23 for different $\bar{L}_c$, indicate that potential fluctuation is relatively high for intermediate $\bar{L}_c$ and large $\bar{L}_c$ as compared to small $\bar{L}_c$, particularly on the inboard side. The reduction in density and potential fluctuation for small $\bar{L}_c$ can be attributed to the reduction in E_z^{res}. Since the fluctuations can contribute to the poloidal flow, which further helps in sustaining the mean profiles [3, 38], a study with varying nature of fluctuations and consequent poloidal flows with varying $\bar{L}_c$ are reported in subsequent sections.

In this Section, we discussed the mean plasma parameters, in the next section [Sec. 4.4.2] we will address the nature of fluctuation.

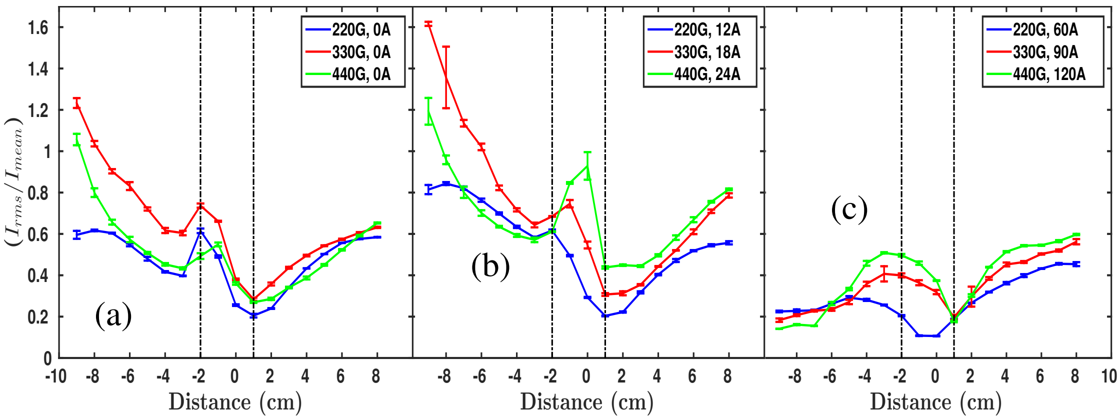

Figure 4.22: Radial profiles of relative "rms" fluctuations of ion saturation current which are equivalent to density fluctuations when fluctuation in T_e is very small for (a) intermediate $\bar{L}_c$ (b) Large $\bar{L}_c$ and (c) small $\bar{L}_c$.

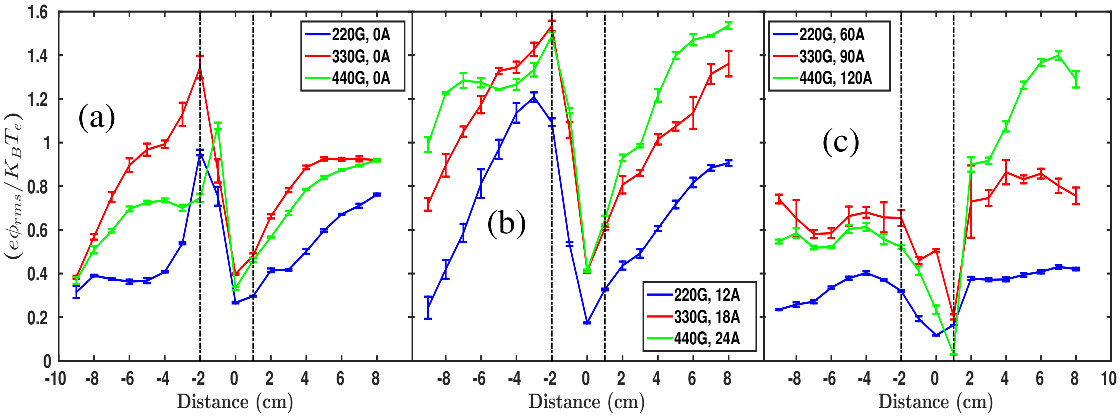

Figure 4.23: Radial profiles of relative "rms" fluctuations of floating potential which are equivalent to plasma potential fluctuations when fluctuation in T_e is very small for (a) intermediate $\bar{L}_c$ (b) Large $\bar{L}_c$ and (c) small $\bar{L}_c$.

4.9.2 Spectral Analysis

As discussed previously in Sec. 4.9.1, there exist reasonable gradients in n_0 and ϕ_0 for all values of $\bar{L}_c$, which leads to excitation of several density gradient and shear driven instabilities. These instabilities provide fluctuation in the plasma and these fluctuations can be characterized by different spectral analysis techniques described in current Section.

4.9.2.1 Power Spectrum

We have characterized the nature of fluctuations and turbulence by spectral analysis technique [8, 24]. The auto power spectra of density are shown in Fig. 4.24 for different values of $\bar{L}_c$. The intermediate $\bar{L}_c$ case is shown in Fig. 4.24(a), the large $\bar{L}_c$ case is shown in Fig. 4.24(b) and the small $\bar{L}_c$ case is shown in Fig. 4.24(c). The potential fluctuation (not shown) has similar spectrum as density fluctuation for all $\bar{L}_c$. For 220 G toroidal field and 0 A VF current (intermediate $\bar{L}_c$) the dominant mode appears at around 6 kHz with several other modes but as field value increases these modes disappear. This behavior is consistent with previous measurement [8], which shows a transition from coherent to the turbulent regime with an increase in toroidal field strength. For long $\bar{L}_c$, at most two dominant modes are present followed by high-frequency low amplitude turbulent fluctuation. On low field side (LFS) shown in Fig. 4.24(f) a broadband appears for small $\bar{L}_c$ for every value of B_T, the reason for this not yet known. Sampling frequency for data shown in Fig. 4.24 is 200 kHz, but all these plots are blown up to 35 kHz. Beyond the dominant modes there exist a turbulent fluctuation spectrum, which could be an indication of turbulence. Moreover, a broadband in small $\bar{L}_c$ case on the outboard side is shown in Fig. 4.24(f) could be due to the merger of several modes of frequencies beyond 10 kHz. As discussed earlier in Sec. 4.9.1, the outboard side is prone to instabilities due to density gradient and effective gravity due to curvature, like Rayleigh-Taylor (RT) instability. Moreover, inboard side may be prone to modified Simon Hoh (MSH), Kelvin-Helmholtz (KH) etc.

The local wavenumber and frequency spectrum $S(k, \omega)$ of potential fluctuation is estimated using the measurement obtained from two vertically separated probe tips with separation of 4 mm, described in Sec. 4.4.2.1.

Contour plots of conditional spectrum $S(k|\omega)$ [Eq. 4.5] with embedded line

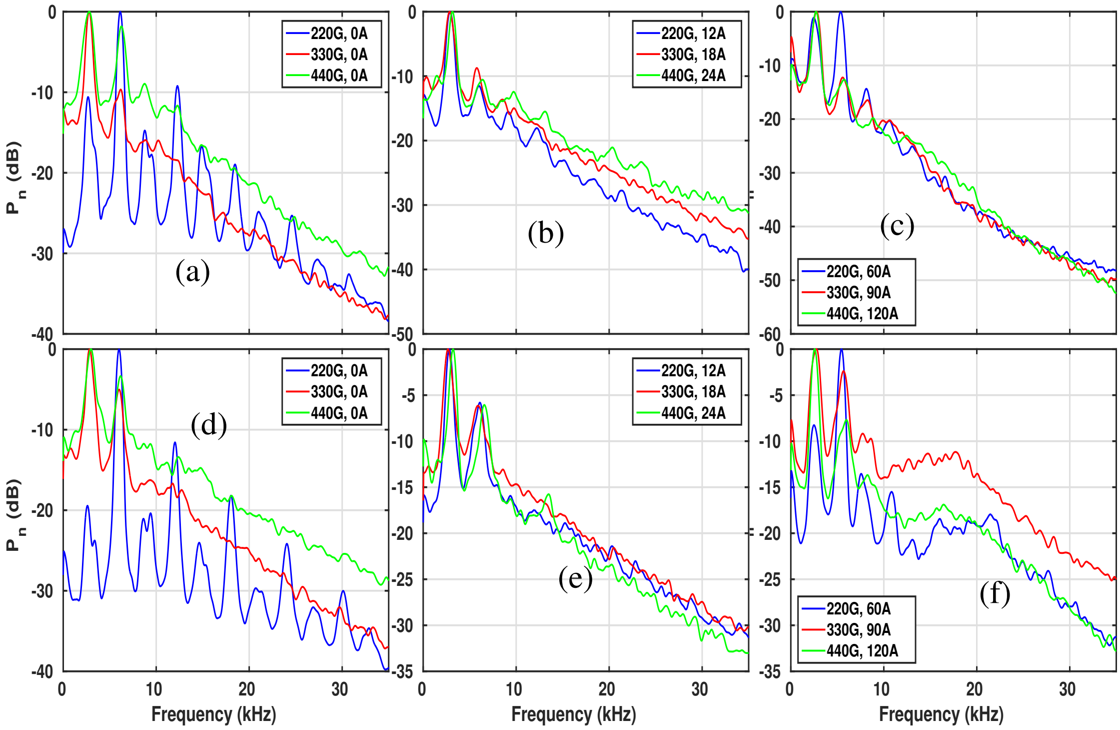

Figure 4.24: Auto power spectra of density fluctuation for (a) intermediate $\bar{L}_c$ at -5 cm (b) Large $\bar{L}_c$ at -5 cm (c) Small $\bar{L}_c$ at -5 cm (d) intermediate $\bar{L}_c$ at +5 cm (e) Large $\bar{L}_c$ at +5 cm (f) Small $\bar{L}_c$ at +5 cm. Here it can be observed that the dominant frequency ranges from 3-6 kHz and also at +5 cm for small $\bar{L}_c$ a broad band for higher frequencies can be seen for each B_T. Sampling frequency is 200 kHz. Due to low frequency nature, all these plots are shown up to 35 kHz.

showing vertical wavenumber (k_z or k_θ) estimated using Eq. 4.6 on both HFS as well as on LFS for small $\bar{L}_c$ values are shown in Fig. 4.25. It can be observed from Fig. 4.25 that the vertical wavenumber (k_z or k_θ) exactly follows conditional spectrum $S(k|\omega)$ and also for -5 cm for all VF currents, while k_z shows positive values, which shows wave propagation upwards and for +5 cm, it has negative values indicating the downward wave propagation. This is compatible for all values of $\bar{L}_c$, which are not shown here. These are also compatible with our net poloidal flows in Fig. 4.29.

4.9.2.2 Bispectral Analysis

The auto power spectrum discussed in the Sec. 4.9.2.1 shows the modes with corresponding frequencies. However, it cannot give any information about non-

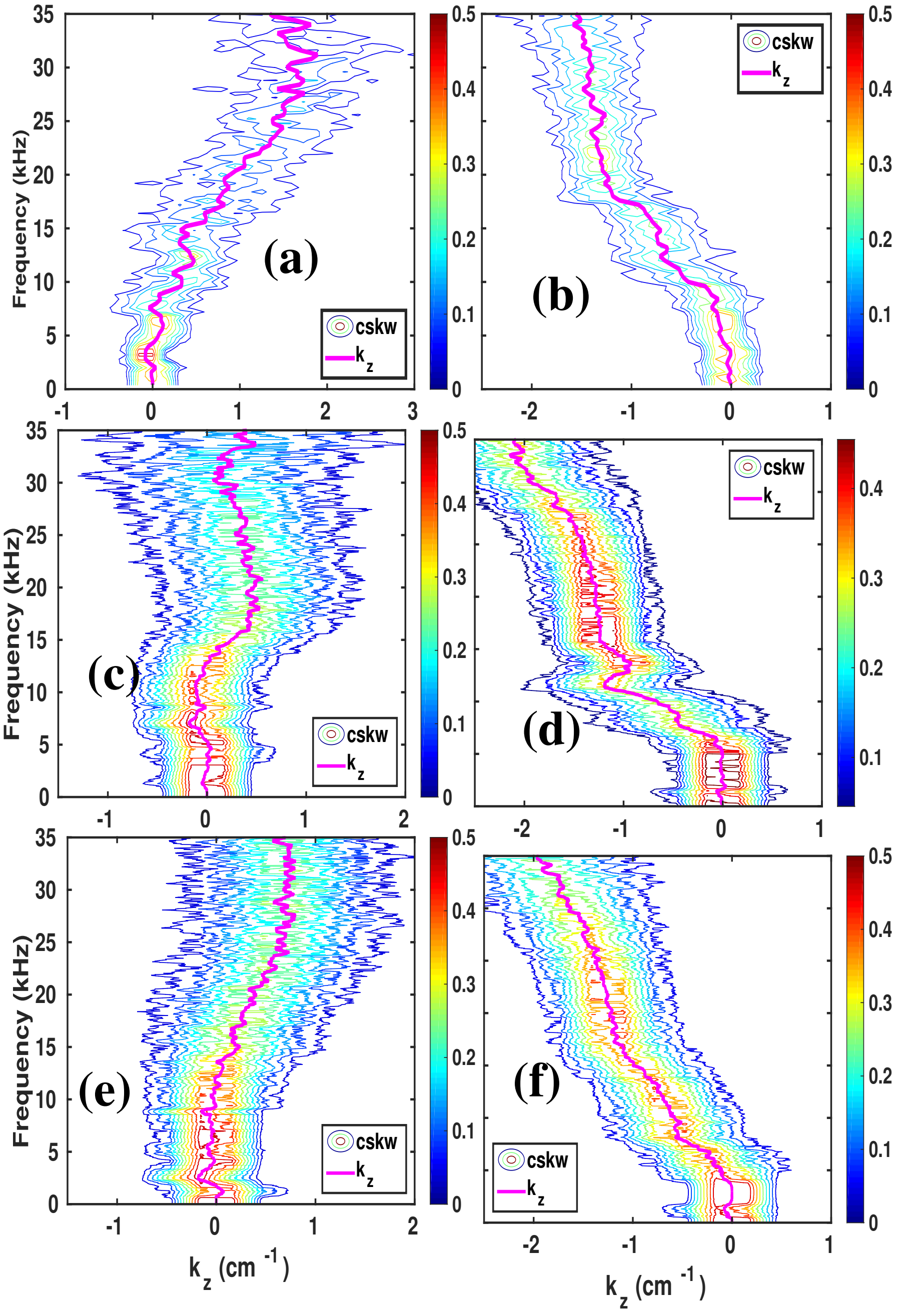

Figure 4.25: Contour plots of conditional spectrum $S(k|\omega)$ with embedded (magenta) line showing vertical wavenumber (k_z or k_θ) for small $\bar{L}_c$ for different B_T (a) 220 G, 60 A at -5 cm (b) 220 G, 60 A at +5 cm (c) 330 G, 90 A at -5 cm (d) 330 G, 90 A at +5 cm (e) 440 G, 120 A at -5 cm (f) 440 G, 120 A at +5 cm

linear interaction present among these modes. In the bulk region of plasma large number of modes are present, hence these modes may interact non-linearly to generate new daughter modes or turbulence. The non-linear coupling of waves can be estimated using a well known three wave interaction scheme [66] but more than three mode interaction cannot be described by using bispectrum analysis. The squared bicoherence $b(\omega_1, \omega_2)^2$ between two frequencies ω_1 and ω_2 is estimated using Eqn. 4.7

Bispectrum is found to highly convergent for all the cases using the method described previously in Sec. 4.4.2.2. Fig. 4.26 shows zoomed in plots up to 40 kHz for +5 cm (or LFS) side only. As discussed earlier, due to the scale length of density inhomogeneity, the fluctuations are expected to be dominant in the range of 3-20 kHz. Our density and potential fluctuations and its bicoherence spectra clearly support our expectations. As can be understood, bicoherence spectrum indicates the strength of three mode non-linear interactions.

Here we have used M = 78 records each with 512 points to estimate $b(\omega_1, \omega_2)^2$, resulting in estimation error $1/M \approx 0.012$. The plot of bicoherence, $b(\omega_1, \omega_2)^2$ for I_{is} fluctuations at +5 cm are shown in Fig. 4.26. Fig. 4.26(a), 4.26(d) and 4.26(g) shows bispectrum at +5 cm radial location for intermediate $\bar{L}_c$ case, Fig. 4.26(b), 4.26(e) and 4.26(h) shows bispectrum at +5 cm for large $\bar{L}_c$ case and Fig. 4.26(c), 4.26(f) and 4.26(i) shows bispectrum at +5 cm for small $\bar{L}_c$ case. Many significant interaction can be observed for B_T=220 G and VF=0 A case, but, only a few are present for higher field for intermediate $\bar{L}_c$ case. It can be concluded that for very large $\bar{L}_c$ values shown in Fig. 4.26(b), (e) and (h) or very small $\bar{L}_c$ shown in Fig. 4.26(c), (f) and (i), only few modes are present, subsequently the non-linear interaction among modes reduces and $b(\omega_1, \omega_2)^2$ is quite smaller than 1.

These fluctuations and non-linear interaction among modes can lead to poloidal flow due to fluctuating component of electric field, as addressed in subsequent section [Sec. 4.9.3].

4.9.3 Poloidal flows

Similar to Part-I, the plasma is dominated by the poloidal flows due to the mean and the fluctuating components of the radial electric field. In this Section, we will discuss, their role in establishing the quasi-static equilibrium and controlling the nature of the fluctuations for the simultaneous variation in B_v and B_T.

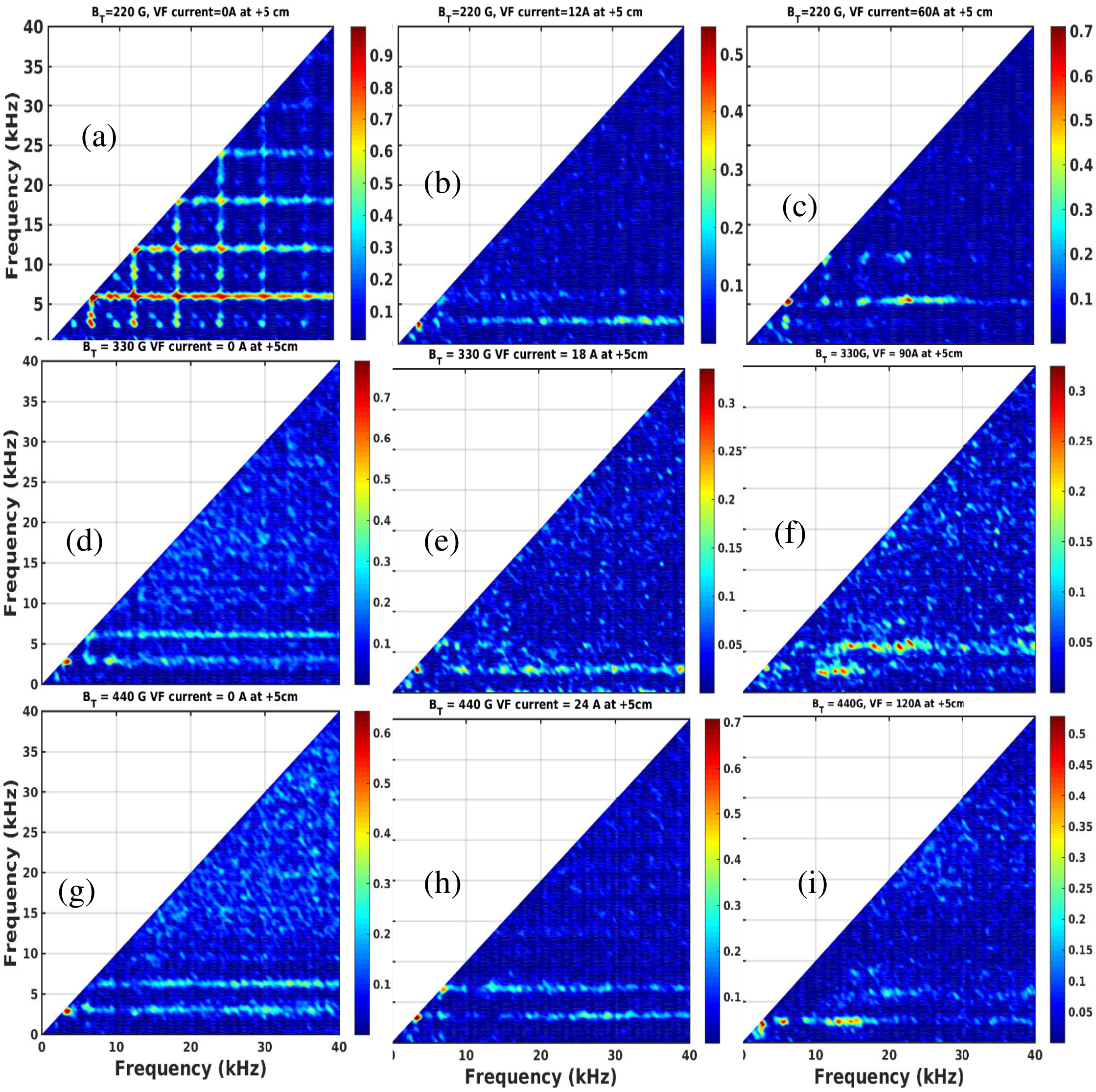

Figure 4.26: Bispectrum of I_{is} fluctuation at +5 cm for (a) 220 G and 0 A, (b) 220 G and 12 A, (c) 220 G and 60 A, (d) 330 G and 0 A, (e) 330 G and 18 A, (f) 330 G and 90 A, (g) 440 G and 0 A, (h) 440 G and 24 A and (i) 440 G and 120 A. Here (a), (d) and (g) represent 0 A , (b), (e) and (h) represent large $\bar{L}_c$ case and (c), (f) and (i) represent small $\bar{L}_c$ case. These plots are zoomed in up to 40 kHz.

4.9.3.1 Mean Electric field driven flow

As discussed in Sec. 4.4.3.1, the radial electric field E_r is estimated from the spatial derivative of the radial profile of plasma potential measured directly using an emissive probe. The electric field is divided by local toroidal magnetic field strength to obtain $E_r \times B$ velocity. To estimate error-bars on $E_r \times B$ velocity, the uncertainty in emissive probe measurement, probe positioning and shot to shot variation have been taken care. The details of the estimation of $E_r \times B$ velocity and error-bars are provided in our previous work. The E_r is due to the potential well created by the hot cathode mounted at the minor axis. This $E_r \times B$ provides poloidal rotation to the plasma shown for three different cases in Fig. 4.27. It can be observed that for intermediate $\bar{L}_c$ and large $\bar{L}_c$ cases shown in Fig. 4.27(a) and Fig. 4.27(b) respectively, the mean flow remains comparable or increases marginally for all B_T values but for small $\bar{L}_c$ case shown in Fig. 4.27(c) the flow reduces on HFS for every value of B_T.

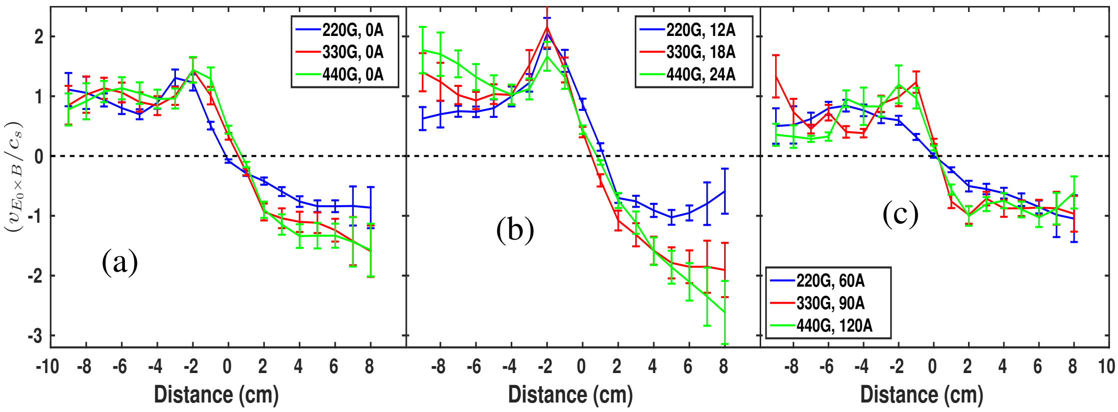

Figure 4.27: Mean Electric field driven poloidal flow normalized to local ion acoustic velocity c_s, $(v_{E_r \times B})/c_s = (1/c_s)(E_r \times B)/B^2 = (1/c_s)(E_r/B)$ for (a) intermediate $\bar{L}_c$ (b) Large $\bar{L}_c$ and (c) small $\bar{L}_c$. This flow is derived from plasma potential profile measured using an emissive probe. The central differencing method is used in the deriving field E_r.

4.9.3.2 Fluctuation driven flow

The mean radial electric field leads to a poloidal flow due to $E_r \times B$ drift as described in Sec. 4.9.3.1. Similarly, a fluctuating radial electric field can also lead to a finite fluctuation induced poloidal flux, depending upon the relative phase between density and potential fluctuations. Fluctuation driven flow is estimated using a radial array of Langmuir Probes described in Sec. 2.3.3, by measuring floating potential fluctuations on first two probes and measuring ion saturation current fluctuation and hence the density fluctuation on the third probe. Then using digital spectral technique to estimate the flux [68], provided in Sec. 4.4.3.2.

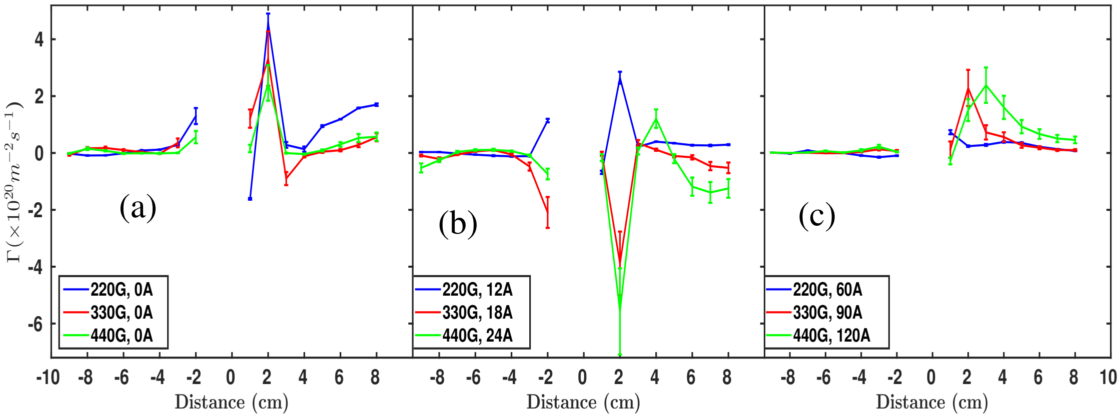

Figure 4.28: Radial profile of fluctuation induced flux, Γ for (a) intermediate $\bar{L}_c$ (b) Large $\bar{L}_c$ and (c) small $\bar{L}_c$. Due to the short nature of wavelengths and the presence of high energy electrons, measurements close to the minor axis are not valid and not shown here.

Fig. 4.28 shows the radial profile of Γ for different $\bar{L}_c$. To estimate the error-bars the uncertainty in density, probe separation uncertainty and shot to shot variation have been taken into account. For all the cases Γ is found to be small on the HFS and significant only on LFS. The comparison of poloidal flow due to fluctuation induced flux is provided in Fig. 4.30.

4.9.3.3 Net Flow

Net flow measurement has been performed using Mach probe described in Sec. 2.3.4, using the method described in Sec. 4.4.3.3, using Eqn. 2.10.

Fig. 4.29 shows the radial profile of net poloidal flow measured using Mach probe for three different $\bar{L}_c$. The error-bars for each case is estimated using the uncertainty in estimating α, area asymmetry between two probe surfaces and shot to shot variation during measurements as described in Sec. 4.4.3.3. The net flow for intermediate $\bar{L}_c$ and large $\bar{L}_c$ cases is more on HFS than on LFS and increases marginally with an increase in B_T. However for small $\bar{L}_c$ case the mean flow and net poloidal flow reduces on HFS, close to the limiter for every B_T, shown in Fig. 4.27(c) and Fig. 4.29(c), however, the net poloidal flow tends to zero but mean flow has non-zero values. It can also be observed from Fig. 4.27(b) and Fig. 4.29(b) that the mean and net flow increases on inboard as well as on outboard with an increase in B_T values. This could be attributed to the slight variation in the ratio of B_v and B_T for very large $\bar{L}_c$. As field lines are nearly closed, a slight

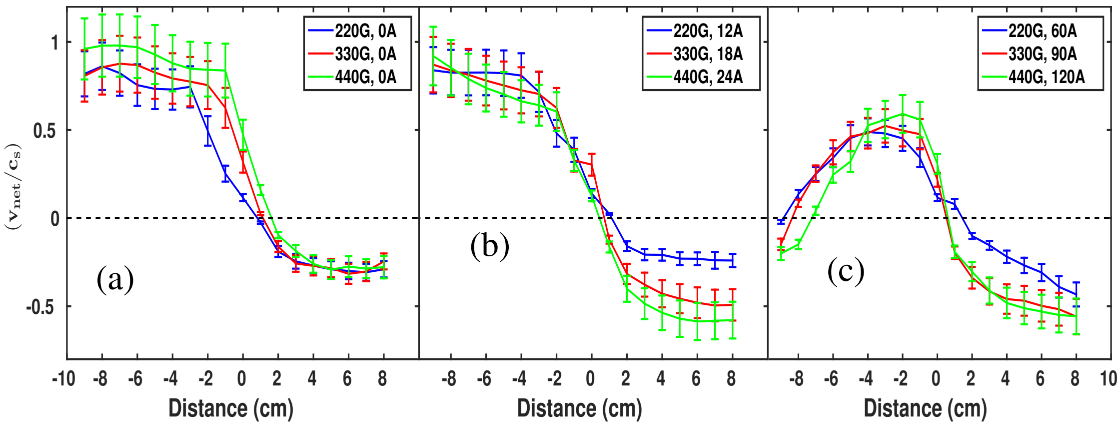

Figure 4.29: Radial profile of net poloidal flow measured using Mach probe for (a) intermediate $\bar{L}_c$ (b) Large $\bar{L}_c$ and (c) small $\bar{L}_c$. The values of velocities are in Mach number as they are normalized with local acoustic speed. The net poloidal flow increases marginally for intermediate $\bar{L}_c$ and large $\bar{L}_c$ case and reduces substantially on HFS for small $\bar{L}_c$.

variation in pitch of the field line significantly alter the toroidal field turns N and hence $\bar{L}_c$. This also can be observed in Fig. 4.28(b), where the direction of Γ changes on outboard side for higher values of B_T and the direction is such that it could increase the net poloidal flow on the outboard side.

4.10 Identification of instabilities

Using the discussion provided in Sec. 4.6.1 in Part. I, we can determine the nature of instabilities for this part as well. As discussed earlier, a comparison between angular diamagnetic velocity ω_D defined as $\omega_D = k_z(T_e/B)(1/L_n)$ and angular velocity due to poloidal flow ω_{pol}, for vertical or poloidal mode number, $m = 1$ is defined as $\omega_{pol} = v_{pol}/r$, where r is the radial distance from the minor axis, as measured at $Z = 0$ plane, indicate the presence of shear driven instabilities. Radial profiles of comparison of ω_D and ω_{pol} for different values of $\bar{L}_c$ are shown in Fig. 4.31. For spatial regions where ω_{pol} greater than ω_D, shear driven instabilities may be expected to dominate [69, 70]. For spatial regions where $\omega_{pol} < \omega_D$, interchange and/or diamagnetic drift related instabilities may be expected to dominate.

Fig. 4.31 indicates that the shear driven instabilities are dominant on few regions of the inboard side except close to the limiter for intermediate $\bar{L}_c$ and large $\bar{L}_c$ values. However,shear effects are not presents on the outboard side for all values

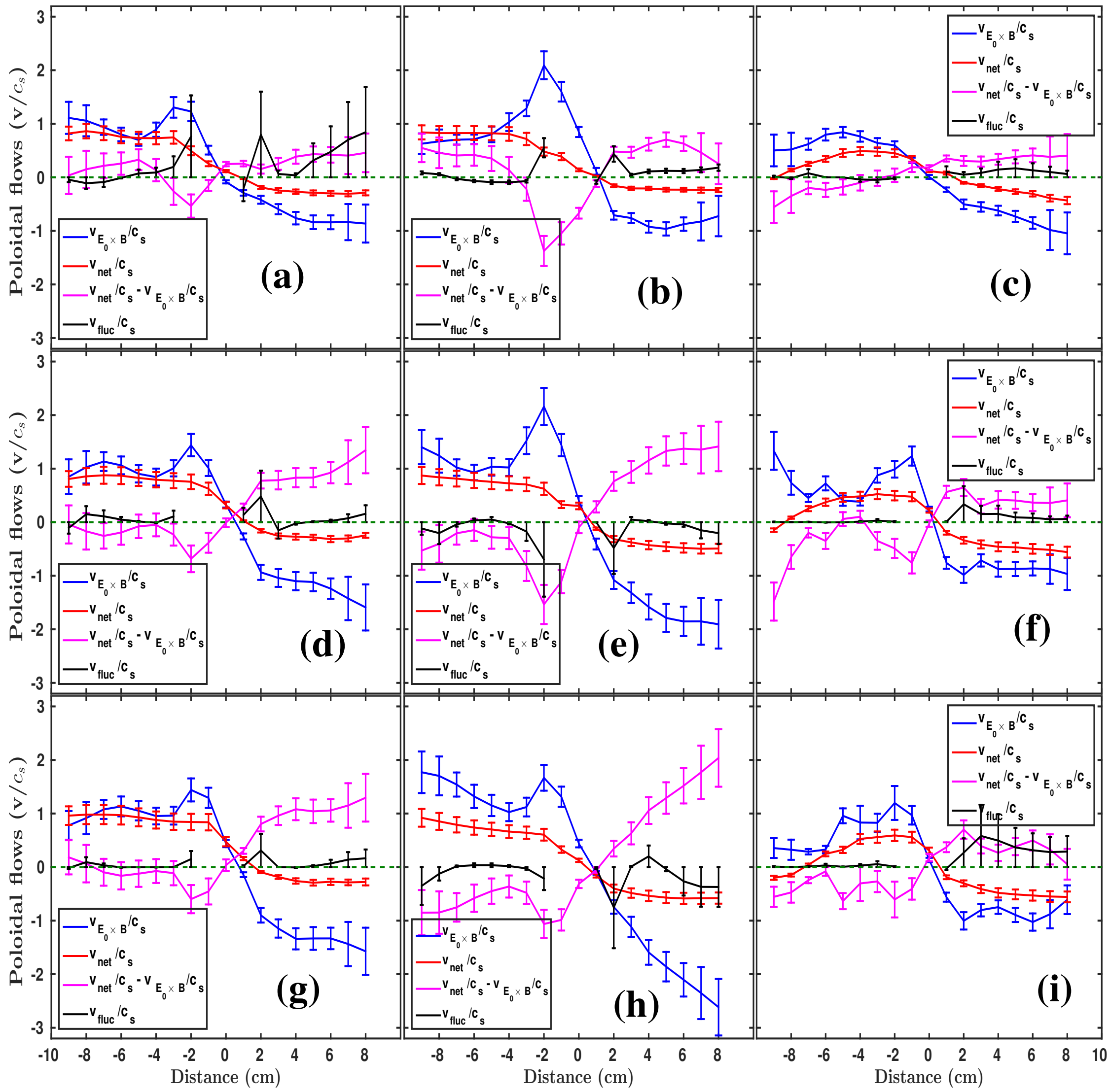

Figure 4.30: Comparison of all the component of Poloidal flows, viz., mean electric field driven flow, fluctuation field driven flow and net poloidal flow for (a) 220 G and 0 A, (b) 220 G and 12 A, (c) 220 G and 60 A, (d) 330 G and 0 A, (e) 330 G and 18 A, (f) 330 G and 90 A, (g) 440 G and 0 A, (h) 440 G and 24 A and (i) 440 G and 120 A. Here (a), (d) and (g) represent 0 A , (b), (e) and (h) represent large $\bar{L}_c$ case and (c), (f) and (i) represent small $\bar{L}_c$ case. Here in all the plots, it can be observed that on HFS there is a significant difference between net flow and mean flow which is unaccountable by fluctuation driven flow, however, on LFS it qualitatively accounted.

of $\bar{L}_c$ and inboard side for small $\bar{L}_c$ values.

The values of $\theta_{n\phi} > 0.5\pi$ on the outboard side for all values of $\bar{L}_c$ as shown in

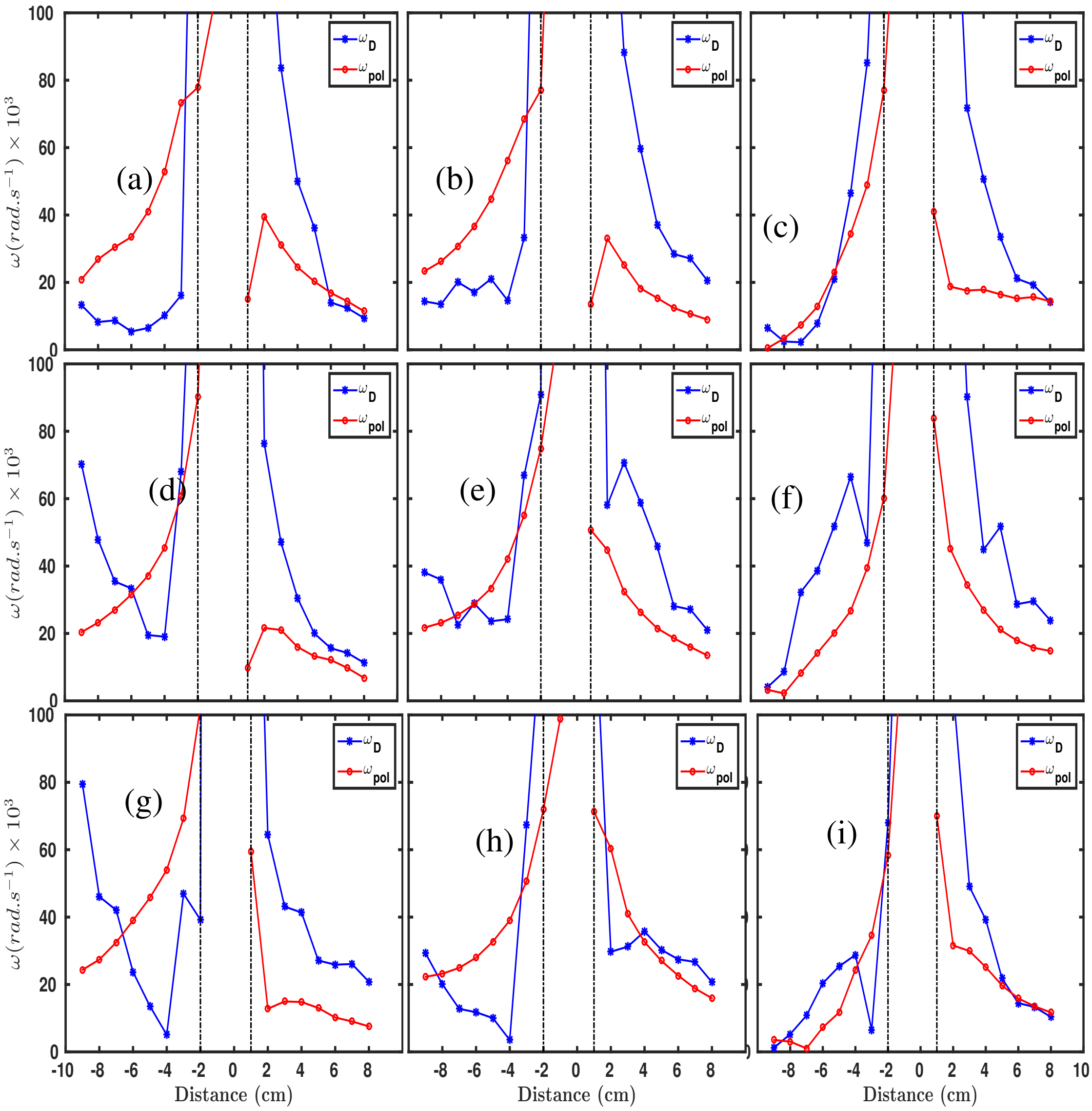

Figure 4.31: Radial comparison of diamagnetic angular velocity ω_D and and angular velocity due to flow ω_{pol} for (a) 220 G and 0 A, (b) 220 G and 12 A, (c) 220 G and 60 A, (d) 330 G and 0 A, (e) 330 G and 18 A, (f) 330 G and 90 A, (g) 440 G and 0 A, (h) 440 G and 24 A and (i) 440 G and 120 A. Here (a), (d) and (g) represent 0 A , (b), (e) and (h) represent large $\bar{L}_c$ case and (c), (f) and (i) represent small $\bar{L}_c$ case. For the cases where $\omega_D \ll \omega_{pol}$, indicate the presence of velocity shear and shear driven instabilities are dominant here and $\omega_D > \omega_{pol}$, implies that shear effects are not dominant here. The region between vertical lines in above plots is populated with high energy electrons, hence the measurements may be erroneous.

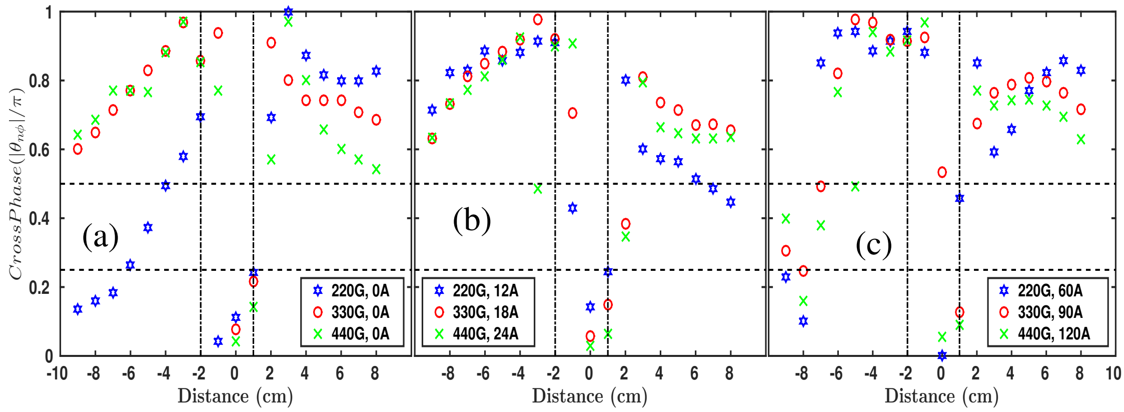

Figure 4.32: Cross phase normalized to π of density and potential fluctuations for (a) intermediate $\bar{L}_c$ (b) Large $\bar{L}_c$ and (c) small $\bar{L}_c$. The region between vertical lines in above plots is populated with high energy electrons, hence the measurements may be erroneous. The horizontal lines shown signifies the different nature of instabilities for different $\theta_{n\phi}$, for example $0 < \theta_{n\phi} < 0.25\pi$ drift-like instabilities dominates, for $0.5 < \theta_{n\phi} < \pi$ flute-like instabilities may be present and intermediate value may indicate drift-interchange case.

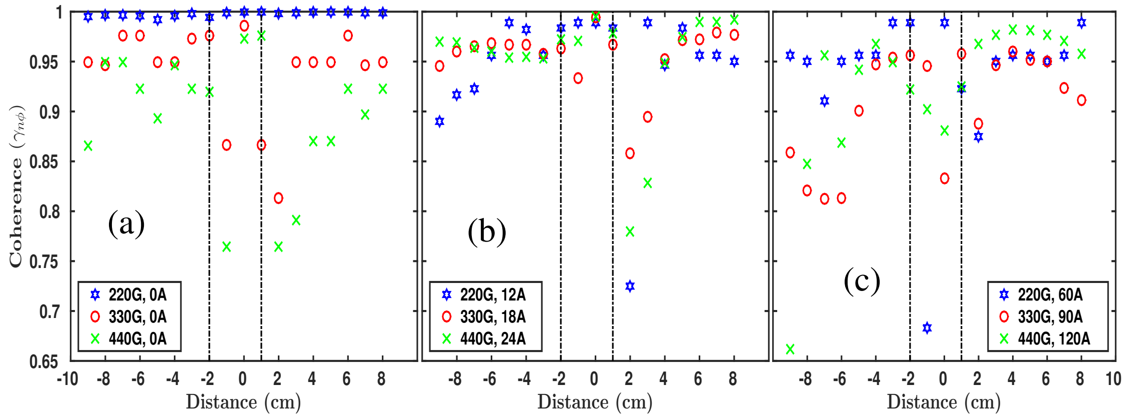

Figure 4.33: Coherence between density and potential for (a) intermediate $\bar{L}_c$ (b) Large $\bar{L}_c$ and (c) small $\bar{L}_c$. Coherence for 220 G and 0 A case is almost 1 for the whole radial profile, but for other values, it ranges from 0.65 to 1. The region between vertical lines in the above plots is populated with high energy electrons, hence the measurements may be erroneous.

Fig. 4.32, indicating that the outboard side is dominated by flute-like instabilities. However on the inboard side, for intermediate and large $\bar{L}_c$ values, $\theta_{n\phi} > 0.5\pi$ except for 220 G, 0 A case shown in Fig. 4.32(a) but for small $\bar{L}_c$ values, $\theta_{n\phi} < 0.5\pi$ for majority of the inboard side. The cross-phase less than 0.5π indicate the presence of drift like modes. All these values of $\theta_{n\phi}$ are accompanied by large coherence as shown in Fig. 4.33.

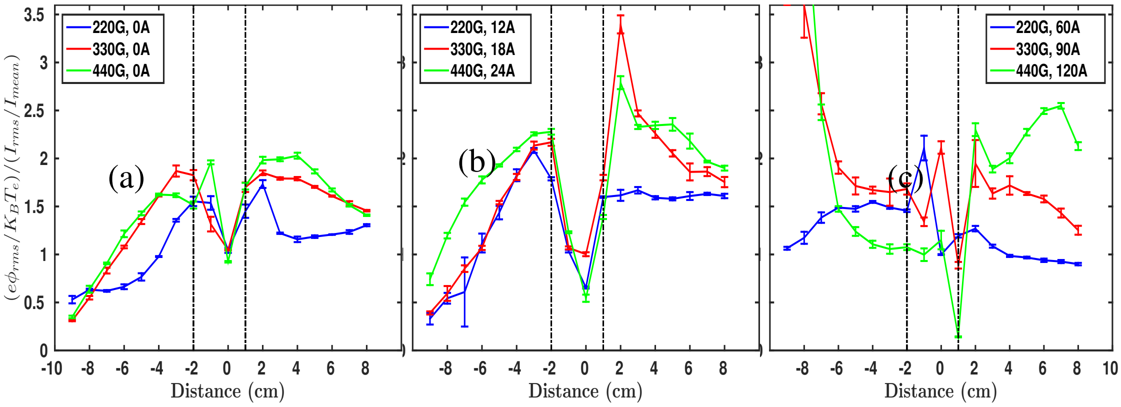

Figure 4.34: Radial profile of ratio of relative potential fluctuations to relative density fluctuations for (a) intermediate $\bar{L}_c$ (b) Large $\bar{L}_c$ and (c) small $\bar{L}_c$. For extreme inboard side for intermediate $\bar{L}_c$ and large $\bar{L}_c$ cases, the value is less than or equal to 1 but for small $\bar{L}_c$ it goes up to 6. For rest of the radial locations, the value is always greater than 1.

As discussed in Sec. 4.6.1 $(e\tilde{\phi}/K_BT_e)/(\tilde{n}/n) < 1$, indicate the presence of drift-like instabilities, $(e\tilde{\phi}/K_BT_e)/(\tilde{n}/n) \geq 1$ corresponds to R-T instability and $(e\tilde{\phi}/K_BT_e)/(\tilde{n}/n) >> 1$ corresponds to shear driven instabilities. Therefore, from Fig. 4.34, it can be observed that the $(e\tilde{\phi}/K_BT_e)/(\tilde{n}/n) \geq 1$ on the outboard side for all values of $\bar{L}_c$. However on the inboard side, close to limiter $(e\tilde{\phi}/K_BT_e)/(\tilde{n}/n) < 1$ for intermediate and large values of $\bar{L}_c$ and $(e\tilde{\phi}/K_BT_e)/(\tilde{n}/n) \geq 1$ for small $\bar{L}_c$ values.

Therefore, it can be concluded that the outboard side is dominated by the presence of R-T instabilities and on the inboard side, shear driven or drift like instabilities may exist.

4.11 Summary of part-II

As discussed in Sec. 4.1, a pathway for electrons along the toroidal field facilitates the reduction in E_z^{res}, which affects the quasi-stationary equilibrium and also controls the nature of instabilities. The time required for electrons to short circuit the E_z^{res} is estimated in Eqn. 1.1 and it can be observed that the shorter the $\bar{L}_c$, faster is the reduction in E_z^{res}. In a simple toroidal device mean parallel connection length $\bar{L}_c$ has been controlled by varying the ratio of the B_v to B_T. We choose three values of $\bar{L}_c$ for which detailed discussion has been performed are the intermediate $\bar{L}_c$ with the inherent opening of field line, large $\bar{L}_c$ and small $\bar{L}_c$.

As discussed earlier, the measurements reported in this work are along the radial direction on $Z = 0$ plane. We assume here that the measurements at $Z = 0$ meaningfully reflect the physics of the addressed problem.

Measured density profile shows that density increases with increase in toroidal field strength for all the three cases. For intermediate $\bar{L}_c$ and large $\bar{L}_c$ cases, densities on HFS are less than that of LFS, which could be attributed to radial plasma loss due to curvature and gradient in B_T. However, for small $\bar{L}_c$ densities on HFS and LFS are comparable, which could be due to an effective short circuit of E_z^{res} due to charge separation.

Relative density and potential fluctuations increase non-monotonically with an increase in B_T for all three cases except for extreme inboard side in case of small $\bar{L}_c$. Relative density fluctuation is found to be greater than 1 for higher fields for the case of intermediate $\bar{L}_c$ and large $\bar{L}_c$. In Sec. 4.10 various instabilities have been identified. It has been confirmed that on LFS the instabilities responsible for fluctuations are mainly R-T along with centrifugal instability for all VF currents. However, on HFS, nature of instabilities changes with variation in $\bar{L}_c$ and also strong poloidal flows present on HFS provides velocity shear, which gives rise to shear driven instabilities. The bispectral analysis also shows the presence of non-linear interaction among modes for 220 G and intermediate $\bar{L}_c$ case and value of $b^2 > 0.9$, but rest of the cases no significant non-linear interaction is present. Coherence measured for all cases shows that for 220 G and intermediate $\bar{L}_c$ case the density and potential fluctuations are coherent for all radial locations, but as VF current increases the coherence decreases and it ranges from 0.65 to 1 at various locations.

The effect of all these instabilities and turbulence can be seen in net poloidal flow, which shows a strong dependence upon $\bar{L}_c$. For intermediate $\bar{L}_c$ case, on HFS the flow increases marginally with the rise in B_T but remains nearly same on LFS. However, for large $\bar{L}_c$ the situation in entirely other way around. For small $\bar{L}_c$ case flow reduces significantly for all values of B_T on HFS. Main observations are as follows

- The electron pathway along B_T facilitates the reduction in E_z^{res} and more effective for shorter values of $\bar{L}_c$, qualitatively consistent with Eqn. 1.1.

- It has been seen that $\bar{L}_c$ strongly affects the mean plasma parameters such as density and plasma potential. Density varies non-monotonically with $\bar{L}_c$ and strong dependence on $\bar{L}_c$ can be seen in plasma potential profiles.

- Nature of fluctuation changes significantly with $\bar{L}_c$, as it can be seen that for large $\bar{L}_c$, few modes are present and for very small $\bar{L}_c$ a broad band or turbulence can be seen, but for some cases where $\bar{L}_c$ is enough to sustain fluctuations, several coherent modes are present with strong non-linear interactions among them.

- Nature of flow also appears to be strongly affected by $\bar{L}_c$. For example, for very large $\bar{L}_c$ the increase in net poloidal flow and mean flow can be observed but for very small $\bar{L}_c$ both flows reduce significantly. Fluctuation driven flow also seems to be affected by $\bar{L}_c$, particularly on LFS.

- Attempt has been made to identify the instabilities for all the values of B_v, it is generally found that while the outboard side is dominated by interchange-like modes, the inboard side is found to be susceptible to shear driven interchange modes, drift-interchange modes and resistive-drift modes.

- Nature of instabilities is strongly dependent on $\bar{L}_c$ and poloidal flows.

- Equilibrium and fluctuation parameters are found to be affected strongly by poloidal flows and as nature of poloidal flows changes with $\bar{L}_c$ and it reflects in these properties.

Part III

Estimation of particle confinement using afterglow method for the hot cathode produced plasma for different values of B_v and B_T in an SMT

In the Part-I and Part-II of the present Chapter, the detailed experimental study has been discussed to understand the role of $\bar{L}_c$ on quasi-stationary equilibrium, flows and fluctuations in an SMT. In the present Part, we will discuss the role of $\bar{L}_c$ on the particle confinement in an SMT.

4.12 Estimation of particle confinement using afterglow method

As we know, estimating energy confinement time (τ) and particle confinement time (τ_C) for a plasma help to understand the balance between sources, sinks and existence of any improved confinement due to plasma collective effects. An SMT provides a simple alternate facility to estimate the particle confinement in a toroidal geometry.

In some of the previous works by Nakao [6] and Muller [7], the role of the external vertical magnetic field on the particle confinement in an ECR plasma has been studied. It has been shown in these works that the particle confinement increases with the increase in the vertical magnetic field as shown in Eqn. 1.5. However, in these works, a zeroth order radial electric field was very weak to generate a poloidal rotation of the plasma.

In the present study of the particle confinement in BETA, we present the effect of variation of $\bar{L}_c$ on the particle confinement in the presence of substantially strong poloidal rotation of the hot cathode produced plasma.

4.12.1 Procedure to obtain particle confinement time using afterglow method

In the afterglow method, as the name suggests, the fall of the plasma density is recorded after the plasma source has been switched off. In the present work, we obtained a time series of the ion saturation current for different VF currents for different values of B_T using a Langmuir probe discussed in Sec. 2.3. As soon as discharge pulse switch off, plasma density and hence the ion saturation current starts falling in the presence of the toroidal and vertical magnetic field. For this purpose, the sampling rate has been increased to 1 MS/s to attain better resolution. To further improve the statistics of the measurements, the final time series is

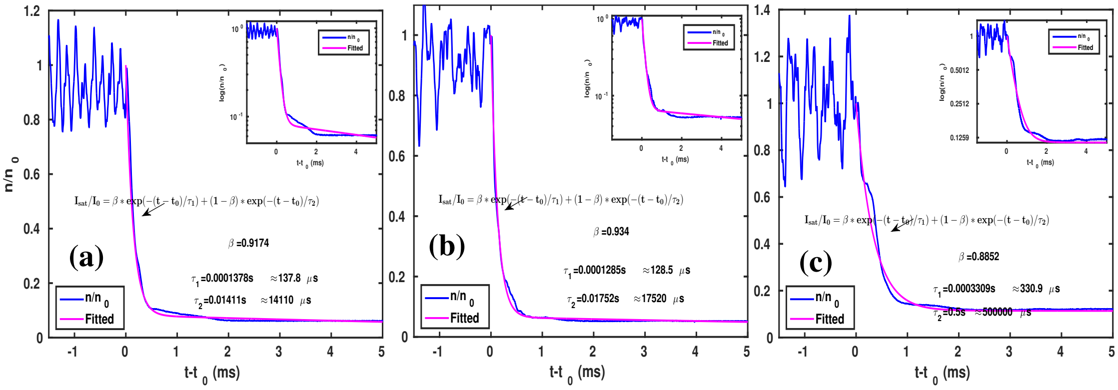

Figure 4.35: The density fall fitted with Eqn. 4.16 to obtain τ_1 and τ_2 for (a) 0 A, (b) 12 A or large $\bar{L}_c$ and (c) 60 A or small $\bar{L}_c$ at r=+5 cm for B_T = 220 G. The fall of density is averaged over 10 shots to obtain current fall of the density. The inset of each plot shows the density fall in the logarithmic scale. It can be observed that the particle confinement increases for an increase in VF coils current or a decrease $\bar{L}_c$.

obtained after averaging over 10 shots taken at the same radial location for similar experimental conditions. The fall of the density in the final time series is fitted with the suitable function to obtain the particle confinement time, τ_C. Following function has been fitted to the density fall:

$$\frac{I_{sat}}{I_0} = \beta \exp(-\frac{t - t_0}{\tau_1}) + (1 - \beta) \exp(-\frac{t - t_0}{\tau_2}) \tag{4.16}$$

where I_{sat} is ion saturation current, I_0 is the ion saturation current at the time t_0 when source is switched off, $0 \leq \beta \leq 1$, τ_1 and τ_2 are fast and slow confinement time respectively.

4.12.2 Experimental observations of particle confinement

Using the procedure discussed in Sec. 4.12.1 to obtain particle confinement, we obtained density fall and particle confinement for different VF currents for different values of B_T. However, let us first discuss the effect of the variation of $\bar{L}_c$ on the particle confinement for a fixed B_T, similar to studies performed in Part-I. The afterglow density fall at r=+5 cm for different VF currents and B_T = 220 G is shown in Fig. 4.35. The inset of each plot shows the fall of the density in the logarithmic scale after the source has been switched off. It can be observed that

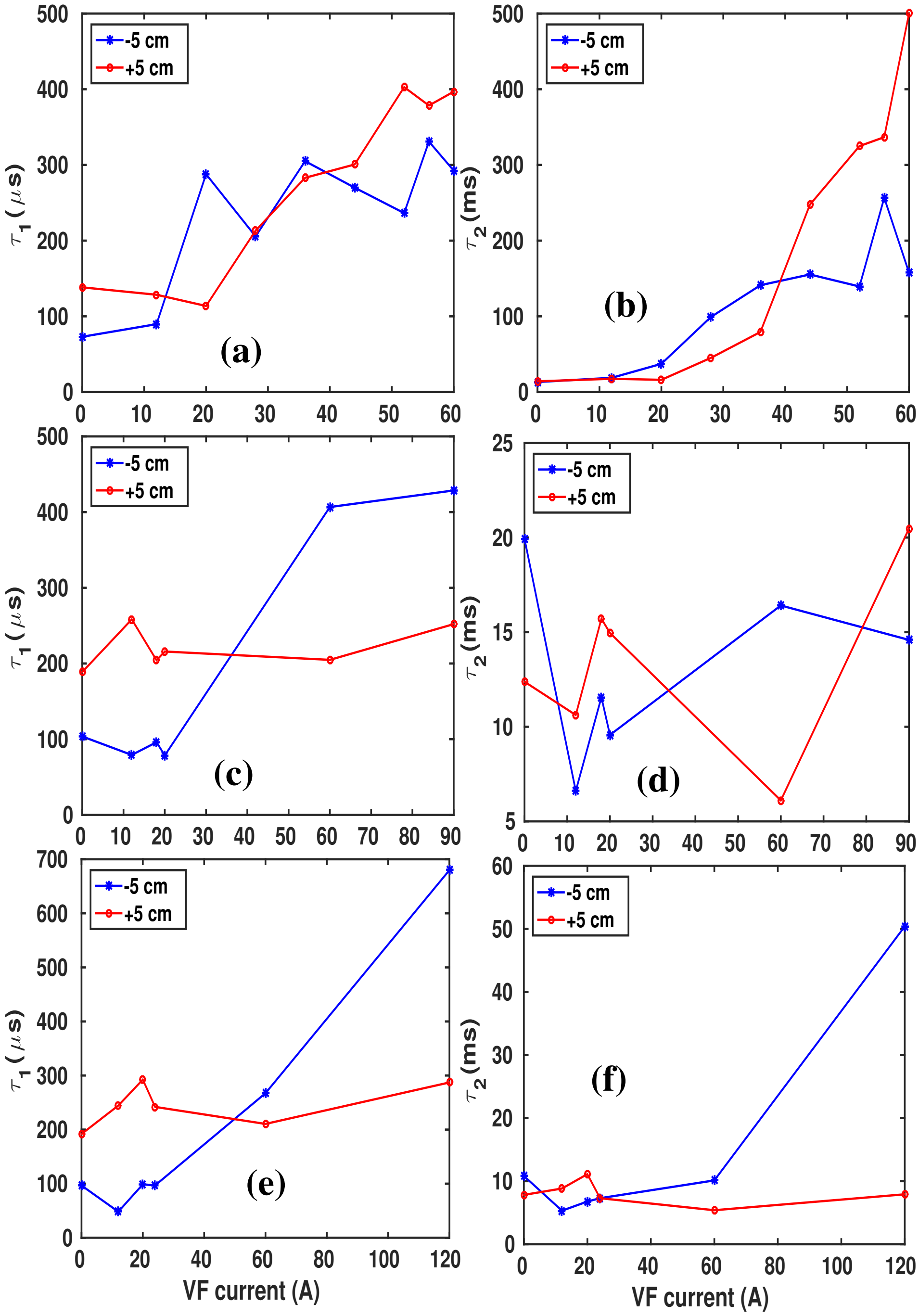

Figure 4.36: The variation of confinement time with VF current for (a) τ_1 for $B_T = 220$ G, (b)τ_2 for $B_T = 220$ G, (c) τ_1 for $B_T = 330$ G, (d) τ_2 for $B_T = 330$ G, (e) τ_1 for $B_T = 440$ G and (f) τ_2 for $B_T = 440$ G. As the VF current is different for each B_T to maintain similar $\bar{L}_c$, therefore, the scale each plot is different.

the particle confinement increases with an increase in VF current or a decrease in $\bar{L}_c$.

Similar studies have been performed for various VF currents for three different B_T values viz, 220 G, 330 G and 440 G, which are discussed in Part-II. The results of which are shown in Fig. 4.36 at r=-5 cm and r=+5 cm. Fig. 4.36, clearly indicate that both τ_1 and τ_2 increase with an increase in VF current or a decrease in $\bar{L}_c$. However, the role of the poloidal flow on the particle confinement has not been investigated in the present Chapter and will be discussed in Chapter-6.

4.12.3 Summary of Part-III

- The particle confinement of the hot cathode produced plasma has been estimated using afterglow method with variation in VF current for different B_T values.

- The fall of the density shows the exponential fall with two different fall time τ_1 and τ_2, which are called as fast and slow confinement time respectively.

- Both τ_1 and τ_2, increases with an increase in VF current or a decrease in $\bar{L}_c$.

- The role of the poloidal flow on the particle confinement will be investigated in Chapter-6.

4.13 Unresolved issues

- On HFS there exists a substantial difference between mean flow and net flow, which is not accounted by fluctuation driven flow alone, however, it qualitatively accounts on LFS, mechanism resolving this discrepancy is still not clear.

- The reason for the reduction of net poloidal flows for shorter $\bar{L}_c$ values is not known yet.

- In the present work, 1-D measurements of plasma profiles have been obtained along radial direction at $Z = 0$ plane, and 2-D measurements would provide further insight and this will be addressed in the future.

- Ideally the nature of plasma profiles and fluctuation should be symmetric with the direction of the vertical field in +Z and -Z direction but the nature of net poloidal flow with the direction of VF current is not found symmetric as shown in Sec. 4.5.0.2, which could be due to misalignment of VF coils.
- The details of the effect of electron temperature fluctuation on the density and potential fluctuations are beyond the scope of the present Thesis.

4.14 Summary

As discussed in Sec. 4.1, the topology of the toroidal field plays an important role in determining the nature of quasi-static equilibrium, fluctuation and flows in a simple magnetized torus. Therefore, a detailed experimental study of the role of toroidal field topology or mean parallel connection length $\bar{L}_c$ on plasma properties has been performed. This study has been divided into two parts: in Part. I, the $\bar{L}_c$ has been varied by varying the external vertical magnetic field, for a fixed value of B_T. It has been observed that the net poloidal flow reduces on the inboard side for shorter values of $\bar{L}_c$, which is accompanied by a broad band in the fluctuation spectrum. These findings are published in **Umesh Kumar et al, Phys. Plasmas, 23, 102301 (2016)**.

In Part. II, the mean parallel connection length has been varied by varying both B_v and B_T simultaneously in three fixed ratios: (i) intermediate $\bar{L}_c$, (ii) large $\bar{L}_c$ and small $\bar{L}_c$. It has been observed that the radial transport of densities reduces for shorter values of $\bar{L}_c$, which is accompanied by a reduction in net poloidal flows on inboard side and presence of a broad band in fluctuation on the outboard side. The manuscript containing the experimental findings is under review (**Umesh Kumar et al, submitted to Phys. Plasmas, May (2018)**).

In Part-III, the particle confinement of the hot cathode produced plasma has been estimated experimentally. The estimate is made using afterglow method for different B_v and B_T values. It has been observed that the particle confinement increases with an increase in VF current or a decrease in $\bar{L}_c$

As discussed in this Chapter, the plasma produced by the hot cathode source has a strong poloidal flow due to the zeroth order radial electric field. Moreover, the region around the minor axis is populated with high energy electrons. Therefore, a new microwave-based, electron cyclotron resonance (ECR) plasma source has been developed, which overcomes above-mentioned issues. The ECR source has been used to produce plasma and various experimental studies have been performed, which would be presented in Chapter. 5

5

Effect of the variation of toroidal field topology on the electron cyclotron resonance produced plasma

5.1 Introduction

As discussed in Chapter. 4, the plasma produced using the hot cathode source has an intrinsic poloidal rotation of the plasma due to the zeroth order radial electric field. Apart from the presence of poloidal flow, the location of the plasma source is different for the hot cathode and the ECR source. Due to which plasma density and electron temperature profiles are quite different, which causes differences in the nature of fluctuations present in both the plasmas as well. Therefore, different level of turbulence and non-linear interaction may lead to generation entirely new kind of plasma modes, details of which are provided in Chapter-7. Moreover, the region around the minor axis is populated with the high energy electrons [9], which alter the plasma properties in that region. Therefore a new microwave based ECR source is developed and used for the plasma production, the details of the source is provided in Sec. 2.2.2.

The ECR plasma sources are considered promising for various plasma studies in several devices. For example, in TORPEX, an ECR based plasma source has been used to study electrostatic turbulence and transport [4], the effect of the vertical magnetic field on particle confinement [7], to study the transition from drift to interchange instabilities [16] etc. In another device, HELIMAK, ECR based plasma source has been used to study the transport and turbulence in an SMT [18]. In BETA, experimental study of a Microwave produced plasma has also been performed [72].

As discussed in Chapter-4, the topology of the toroidal field line can be varied by the application of an external vertical field. In the present experimental study, the toroidal magnetic field has been kept fixed at B_T=750 G at the minor axis. To match the EC resonance condition, required toroidal field should be ~875 G (Sec. 2.2.2), therefore EC resonance occurs at -6 cm inside from the minor axis on the inboard side.

In this Chapter, a detailed study of the variation of an external vertical magnetic field on the plasma properties of an ECR produced plasma will be presented.

5.2 Operating conditions

1. Base pressure $\sim 4 \times 10^{-6}$ torr
2. Filling gas: Argon
3. Working pressure $\sim 1 \times 10^{-4}$ torr
4. Averaged launched power ~ 1 kW
5. B_T at the minor axis ~ 750 G
6. VF current (B_v) ~ 0 A (0 G), 40 A (3.0 G), 160 A (12.0 G) and -160 A (-12.0 G)

5.3 Experimental measurements

For the experimental study discussed in this Chapter, the plasma is produced by launching a Microwave of frequency 2.45 ± 0.1 GHz, from the outboard side. As discussed in Sec. 2.2.2, the averaged launched power is around 1 kW in "O" mode

Plasma parameters	Values
Ion mass	39.95 amu
Toroidal magnetic field (B_T)	0.075 T
Ion Larmor radius (r_{Li})	2.8$\times 10^{-3}$ m
Electron Larmor radius (r_{Le})	1.1$\times 10^{-4}$ m
Electron Debye length (λ_{De})	7.4$\times 10^{-5}$ m
Ion gyration frequency ($\omega_{ci}/2\pi$)	2.7$\times 10^{4}$ s^{-1}
Electron gyration frequency ($\omega_{ce}/2\pi$)	1.9$\times 10^{9}$ s^{-1}
Electron plasma frequency ($\omega_{pe}/2\pi$)	1.0$\times 10^{8}$ s^{-1}
Ion plasma frequency ($\omega_{pi}/2\pi$)	5.0$\times 10^{6}$ s^{-1}
Electron neutral frequency (ν_{en})	7.2$\times 10^{5}$ s^{-1}

Table 5.1: The typical plasma parameters for Argon plasma at $B_T = 750G$. For the calculations mentioned, it is considered that $T_e \sim 3.0$ eV, $T_i \sim 0.1$ eV and $n_0 \approx 10^{16}\ m^{-3}$.

polarization, which implies that the direction of electric field vector is parallel to the toroidal magnetic field.

The measurements of various plasma properties were obtained using the diagnostics discussed in Sec. 2.3. Normally Langmuir probes need to be compensated while used in a time varying field like in capacitive discharges as the plasma potential and T_e part of $I_p - V_p$ also oscillates with the same frequency. Therefore, it provides a higher electron temperature than the actual T_e. However, for Microwave discharge with frequency of 2.45 GHz, this problem does not exist, as with respect to the probe the oscillation is very high and the compensation of Langmuir probes is not needed [42]. Therefore, the diagnostics described in Chapter-2, can be used for the measurements in an ECR plasma without any hassle.

As discussed in Chapter-4, the mean parallel connection length, $\bar{L}_c$ significantly controls the nature of quasi-static equilibrium and fluctuations. An application of external vertical field can further control the value of $\bar{L}_c$. Using the similar approach as in Chapter-4, we have used four different values of the VF current, which provide different values of $\bar{L}_c$. The VF current of 0 A represents the case of the inherent value of $\bar{L}_c$ due to the opening of toroidal field lines without charging the VF coils. The largest value of $\bar{L}_c$ is found for the VF current of 40 A, as field lines are about to close on themselves and similarly, 160 A and -160 A values represent the shorter $\bar{L}_c$ cases [63].

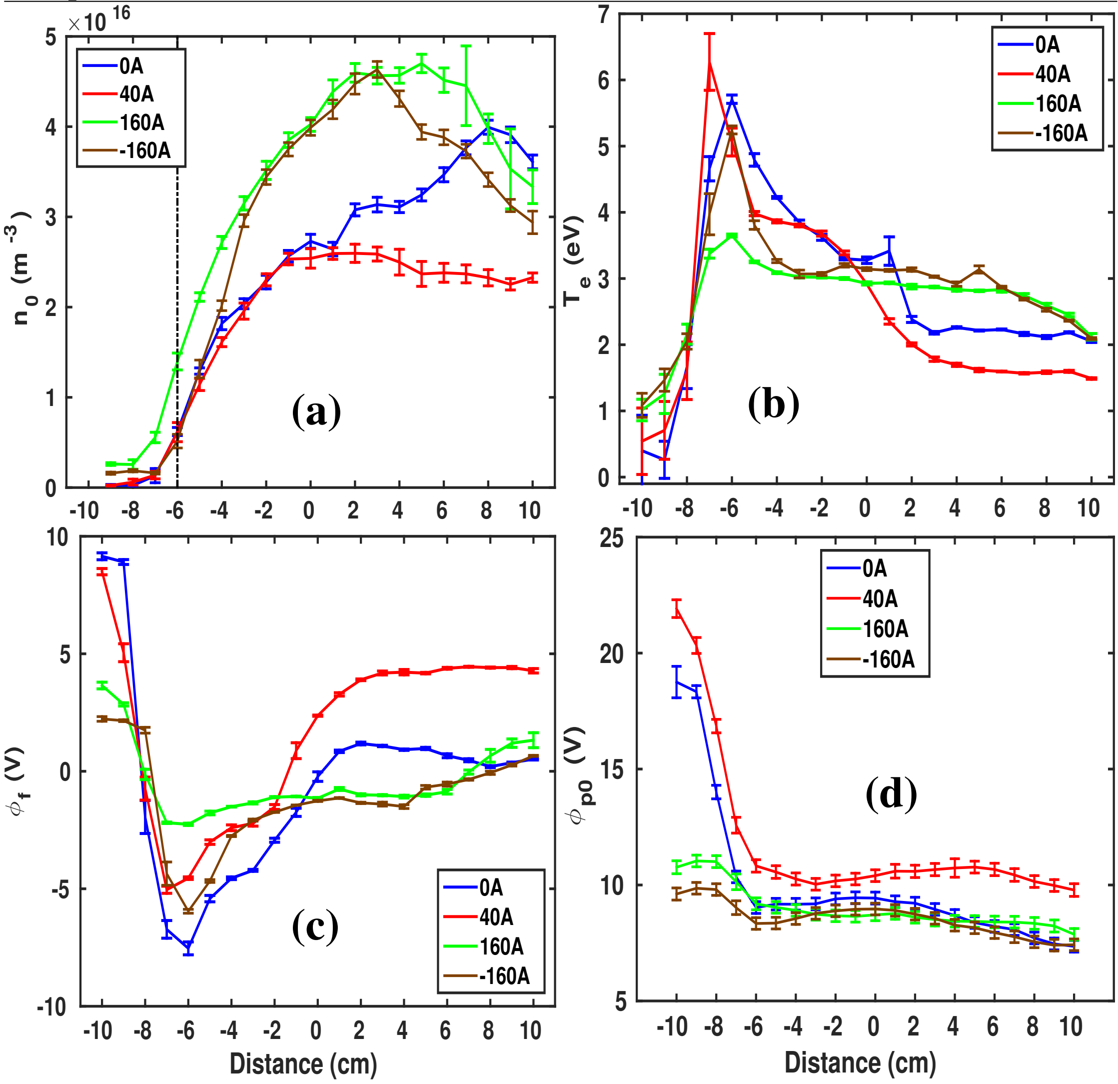

Figure 5.1: Radial profiles of (a) Mean density (b) Mean electron temperature (c) Mean floating potential and (d) Mean plasma potential. Profiles for all the parameter have been shown here for four different values of vertical field coil current. Densities shown here are sheath corrected and error-bars on density measurements are found to be predominantly from uncertainty in ion saturation current and shot-to-shot variations. The vertical line at -6 cm in (a) represents the EC resonance, which coincides with the peak in the electron temperature shown in (b) and dip in floating potential shown in (c).

5.4 Radial plasma profiles

Radial profile of density (n_0), electron temperature (T_e), floating potential (ϕ_f) and plasma potential (ϕ_{p0}) for different values of VF current is shown in Fig. 5.1(a),

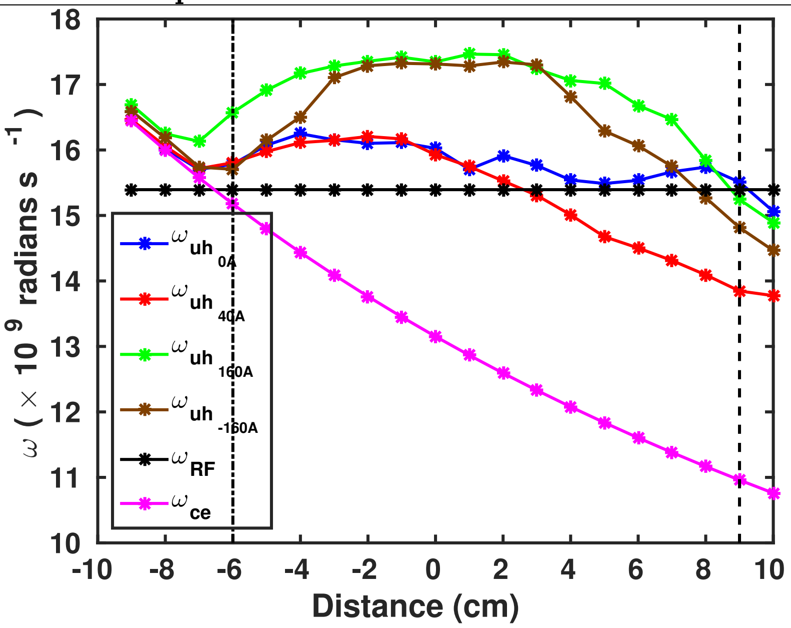

Figure 5.2: Radial profile of the frequency for different VF current shows upper hybrid resonance (UH) location. The frequency of the UH resonance is given as $\omega_{UH}(r) = (\omega_{ce}^2(r) + \omega_{pe}^2(r))^{1/2}$. The primary ionization occurs due to EC resonance at around -6 cm for every VF current, however, secondary ionization occurs due to the resonance of the upper hybrid. The location of the upper hybrid varies for VF current, which governs the density profile. The dash-dot vertical line at -6 cm indicates the EC resonance and dash line at +9 cm indicate the limiter location on the outboard side.

Fig. 5.1(b), Fig. 5.1(c) and Fig. 5.1(d) respectively.

The plasma density has been obtained from the time series of the ion saturation current measured using a Langmuir probe at a fixed bias. The measurements techniques are similar to those which are described in Sec. 4.4.1. The density is shown in Fig. 5.1(a) is sheath corrected using an approach provided by Hutchinson [41]. The details of the estimation of the error-bars on each plasma parameter were also discussed in Sec. 4.4.1.

The primary ionization is caused by the EC resonance of the Microwave and the unspent energy is reflected from the vessel wall and as it is well known [26] it causes a change in the polarization of the Microwave, which results in the upper hybrid (UH) resonance as shown in Fig. 5.2. The frequency of the UH resonance is given as $\omega_{UH}(r) = (\omega_{ce}^2(r)+\omega_{pe}^2(r))^{1/2}$, where ω_{ce} is the electron cyclotron frequency and ω_{pe} is the electron plasma frequency. To estimate ω_{pe}, the electron density is

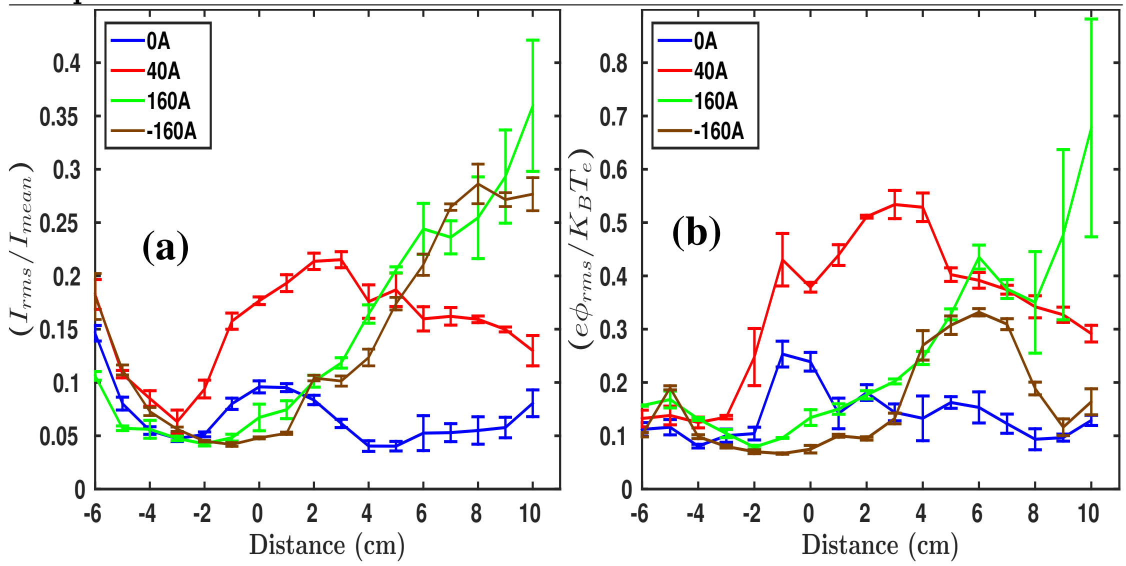

Figure 5.3: Radial profiles of relative fluctuation in (a) ion saturation current (b) floating potential, for different VF current values. As electron temperature values are found to be very small, therefore ion saturation current and floating potential fluctuations are equivalent to density fluctuation and plasma potential fluctuation respectively. The plots have been zoomed for the post-source region i.e, beyond -6 cm as plasma densities are very small for the pre-source region shown in Fig. 5.1(a).

considered almost equal to the plasma density shown in Fig. 5.1(a), under quasi-neutrality condition.

From Fig. 5.1(a), it can be observed that for 0 A or intermediate $\bar{L}_c$ value, the density shows a positive gradient on the outboard side, which could be due to the fact $\omega_{UH} \sim \omega_{RF}$ at more than one location as shown in Fig. 5.2. Similarly for 40 A or large $\bar{L}_c$ value, the location of $\omega_{UH} \approx \omega_{RF}$ close to the minor axis, therefore the density profile for this value is almost flat. However, for 160 A and -160 A or small $\bar{L}_c$ values, the location of $\omega_{UH} \approx \omega_{RF}$ is close to the limiter location on the outboard side, which justifies the presence of a weak negative gradient in the density profile for these values.

The electron temperature profile is shown in Fig. 5.1(b) for different values of VF current or $\bar{L}_c$, indicate that the location of the peak coincides with the location of EC resonance. A gradient in T_e profile can be observed for large and intermediate $\bar{L}_c$ values, however for shorter $\bar{L}_c$ values the gradient becomes weak.

The dip in the floating potential profile shown in Fig. 5.1(c), coincides with the location of the EC resonance and becomes almost flat on the outboard side. The plasma potential profile measured using an emissive probe shown in Fig. 5.1(d) has a very weak gradient for the post-source region (i.e, r>-6 cm) for all values of VF current. This indicates that the zeroth order radial electric field is very small and the poloidal rotation of the plasma expected to be insignificant.

As the density for the pre-source region i.e, r<-6 cm, is around 10 times less than that of bulk plasma, therefore rest of the discussion in the present work deals with the post-source region plasma i.e, r>-6 cm only. Therefore, subsequent radial profiles are zoomed from r=-6 cm.

The radial variations of the relative fluctuation in ion saturation current and floating potential are shown in Fig. 5.3(a) and 5.3(b) respectively. As electron temperature fluctuation (not shown here) are found to very small, therefore, the fluctuation in ion saturation current and floating potential is equivalent to density and plasma potential fluctuation. Fig. 5.3(a) indicates that for the post-source region i.e, beyond -6 cm, the relative fluctuation in density is less than 30% for all VF current, for 0 A case the fluctuation is less than 10%. Similarly, from Fig. 5.3(b), it can be observed that $e\phi_{rms}/K_BT_e < 0.5$ for the radial location beyond -6 cm. It indicates the absence of the velocity shear which is expected as the poloidal flow is very small. In general, fluctuations are known to contribute to the poloidal flow, which further helps in sustaining the mean profiles [3, 38]. However, the fluctuation level are found to be significantly small for all the VF currents. Detailed discussion on the level of fluctuation and poloidal flows presented in Sec. 5.5.1

5.5 Spectral analysis

As discussed previously in Sec. 5.4, there exist weak gradients in n_0 and ϕ_0 for all values of $\bar{L}_c$, which may lead to excitation of various density gradient driven instabilities. These instabilities provide fluctuation in the plasma and these fluctuations can be characterized by different spectral analysis techniques described in the present section.

5.5.1 Power spectrum

As can be expected from the weak gradient in the density may give rise to various cross-field instabilities and the nature of these fluctuations can be characterized by using spectral technique [8, 24]. The auto power spectrum of density and

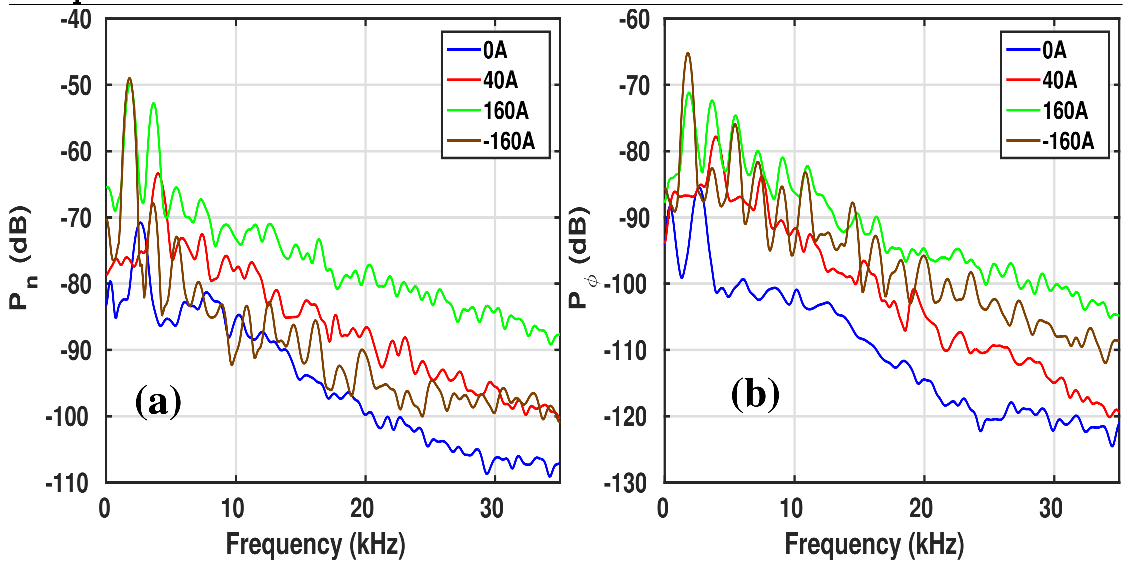

Figure 5.4: The auto power spectrum of (a) density and (b) potential fluctuations, for different VF current values at r=+5 cm on the outboard side. Though the sampling rate for these measurements is 200 kHz, plots are zoomed to 35 kHz for better representation. It can be observed that the nature of fluctuation is similar for both density and potential fluctuation, however, the relative amplitude of fluctuation is different. It can also be observed that for 0 A and 40 A cases i.e, for large and intermediate values of $\bar{L}_c$, there exist a weak mode followed by a turbulent fluctuation. Whereas for small $\bar{L}_c$ values these exist one or two strong coherent modes.

potential fluctuations at r=+5 cm on the outboard side is shown in Fig. 5.4(a) and Fig. 5.4(b) respectively. It can be observed that for large and intermediate values of $\bar{L}_c$ (40 A and 0 A respectively), there exist a weak mode followed by a turbulent background fluctuation. However for 160 A VF current, there exist two strong modes followed by turbulent background fluctuations, the details of which are discussed in Chapter-7. Similarly for -160 A value, there exist a strong mode and few high frequency weaker modes followed by the background fluctuations.

To determine the variation of these modes with time a spectrogram has been plotted for each VF current as shown in Fig. 5.5, which shows the transient nature of modes for 0 A and 40 A VF currents. The details of which are discussed in Sec. 5.7.

We have characterized the quasi-static equilibrium and nature of fluctuations, now we would like to investigate the presence of any poloidal rotation of the plasma either due to mean or fluctuating the radial electric field in subsequent Sec. 5.6.

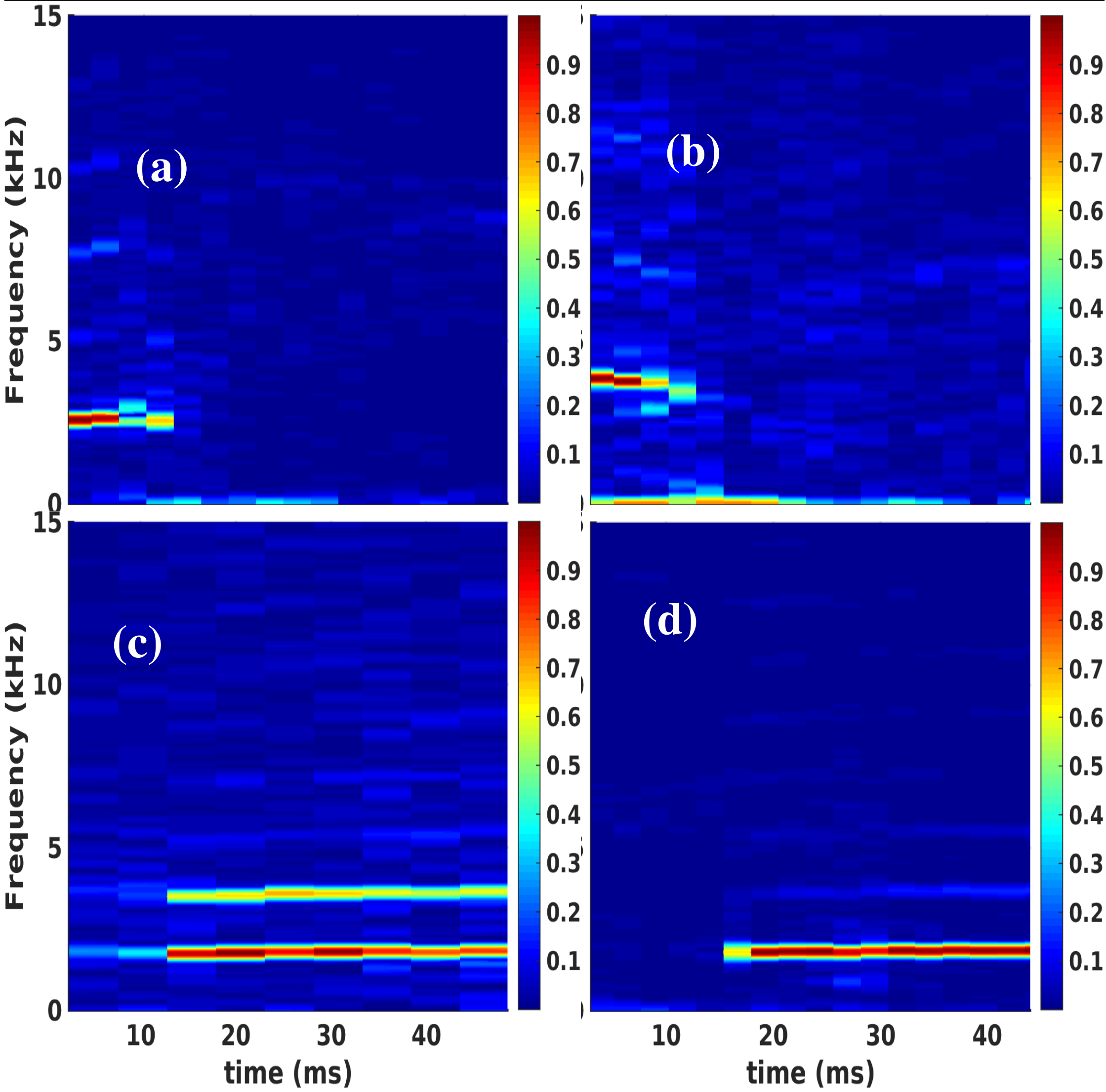

Figure 5.5: The spectrogram of density at r=+5 cm for (a) 0 A, (b) 40 A, (c) 160 A and (d) -160 A. The spectrum is normalized by the amplitude of dominant mode, therefore, the color-bar varies from 0 to 1. Though the sampling rate for these measurements is 200 kHz, plots are zoomed to 15 kHz for better representation. It can be observed that the nature of fluctuations for 0 A and 40 A cases i.e, for large and intermediate values of $\bar{L}_c$, is transient in nature. Whereas for small $\bar{L}_c$ values (160 A and -160 A) it is persistent in time.

5.6 Poloidal flows

As discussed in Chapter-4, the poloidal flow affects the nature of quasi-stationary equilibrium and fluctuations. The poloidal flow can be generated by the presence of mean and fluctuating component of the radial electric field. In this Section, we will try to investigate the presence of poloidal flow and its effect on the plasma properties.

5.6.1 Mean poloidal flow

The poloidal rotation of plasma due to mean zeroth order radial electric field is known as mean poloidal flow. The radial electric field is estimated by taking the spatial derivative of the plasma potential profile shown in Fig. 5.1(d). As discussed earlier, the gradient of plasma potential is very weak and hence mean poloidal flow is expected to be very small. The radial profile of mean poloidal flow for different values of VF current is shown in Fig. 5.6. It can be clearly observed that the maximum value of poloidal flow is around $0.25c_s$ close to the limiter on the outboard side and nearly zero at every other radial location, which could be attributed to the weak gradient in plasma potential.

The error-bars on the mean poloidal flow consist of uncertainty in the estimation of plasma potential and shot to shot variation as described in Sec. 4.4.3.1.

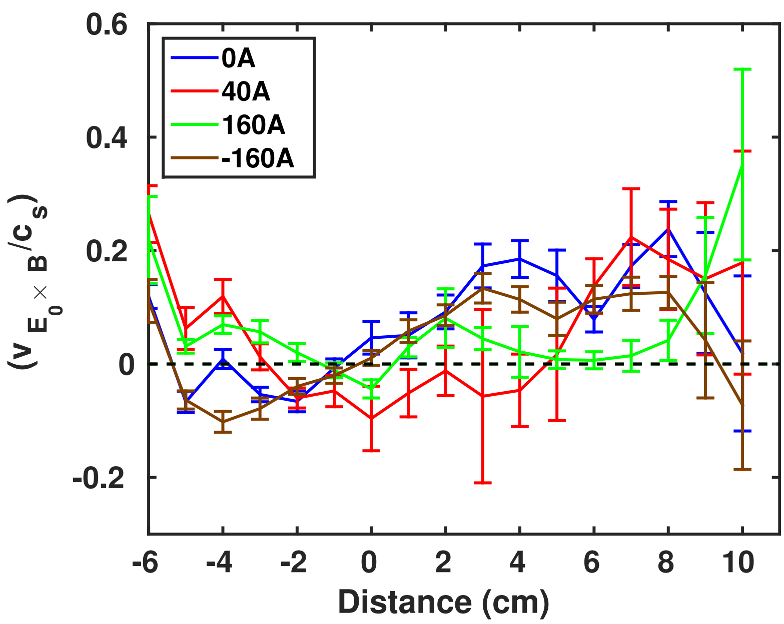

Figure 5.6: Radial profile of mean poloidal flow due to zeroth order radial electric field. The plot is zoomed for post-source region only and horizontal line represents the zero poloidal flow.

5.6.2 Net poloidal flow

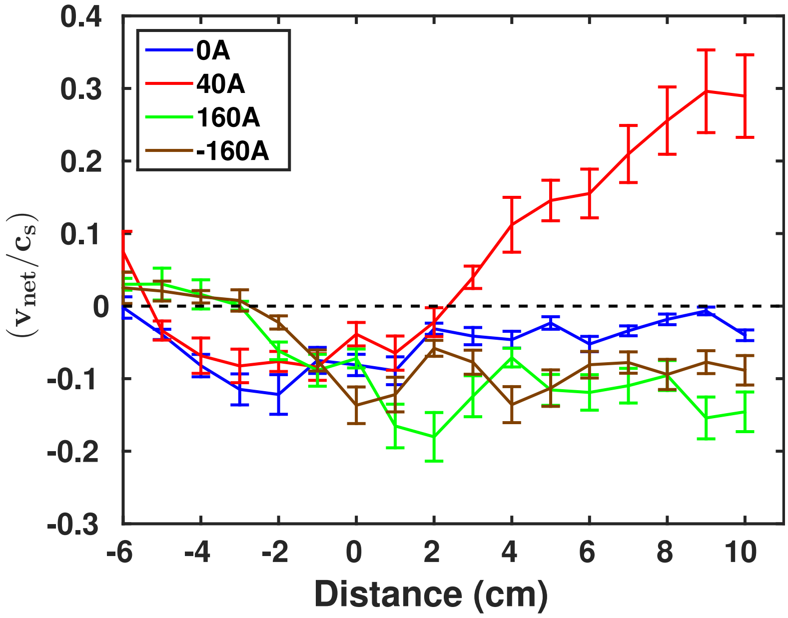

Figure 5.7: Radial profile of Net poloidal flow measured using Mach probe. The plot is zoomed for the post-source region only and horizontal line represents the zero poloidal flow.

In Sec. 5.6.1, the mean poloidal flow is discussed, which is purely due to the radial electric field. However, the fluctuating electric field can also provide a component of the poloidal flow. In this Section, we will discuss the net poloidal flow measured directly using the Mach probe discussed in Sec. 2.3.4. The net poloidal flow is the resultant of all the poloidal flow present in the plasma.

The net poloidal flow obtained using the Mach probe is shown in Fig. 5.7 for different values of VF current. It can be observed that the value of net poloidal flow is significantly small values around $0.1c_s$, except for 40 A VF current case. It can also be noted that there exists a difference between mean and net poloidal flow except for 40 A case. As the level of fluctuations is very small, therefore the fluctuation driven flow cannot account for this difference.

An attempt was made to measure the toroidal flow using the Mach probe and it is found to be below $0.1c_s$, therefore considered negligible.

As shown in Fig. 5.5, the modes observed for 0 A and 40 A VF currents show transient nature on time, the details of which are discussed in Sec. 5.7.

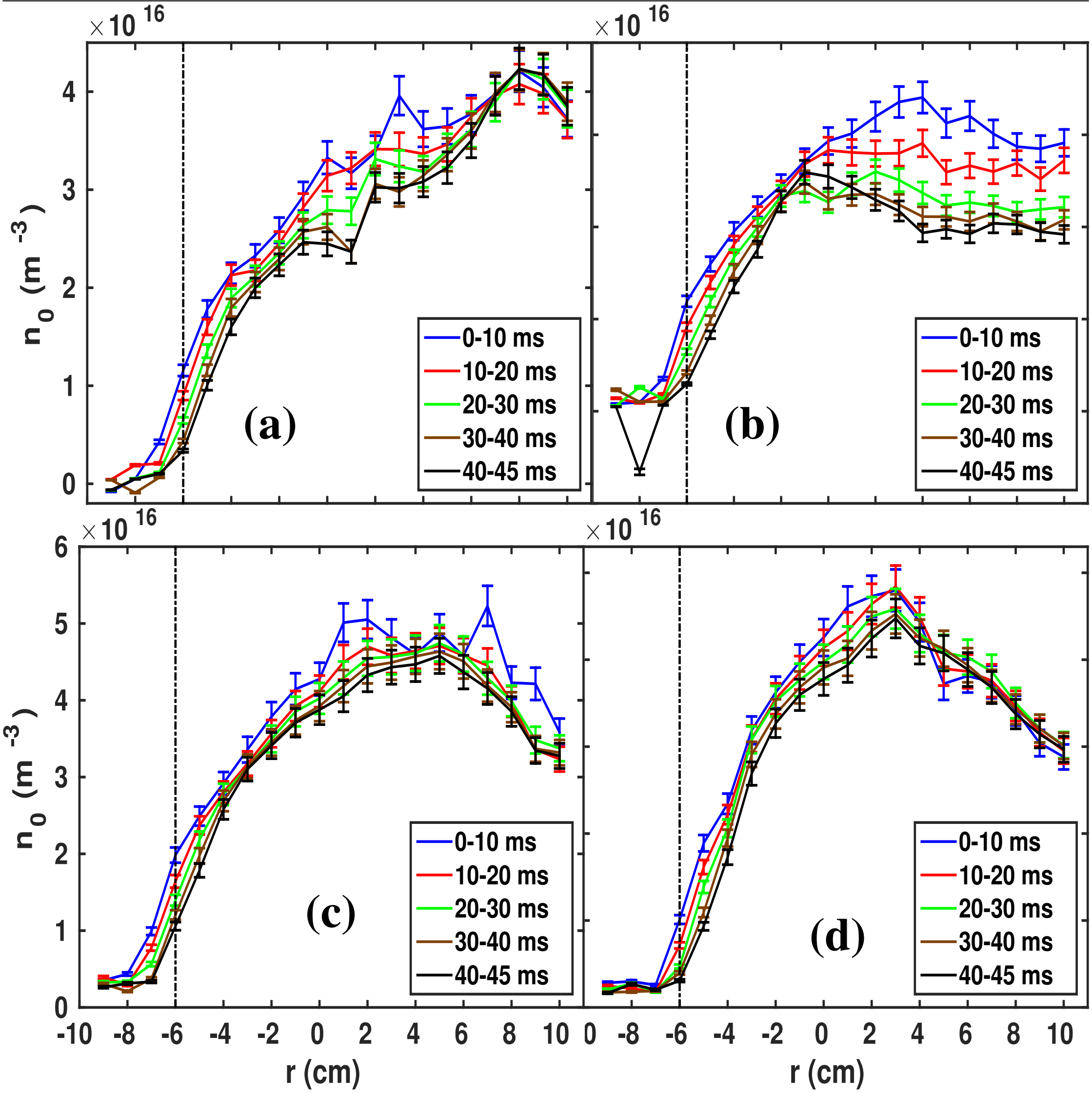

Figure 5.8: Radial profile of density at different plasma duration for (a) 0 A, 40 A, (c) 160 A and (d) -160 A. It can be observed that the nature of density profile varies with time for 0 A and 40 A values, whereas for 160 A and -160 A values, the variation in profile is not significant with time, particularly for the duration beyond 10 ms.

5.7 Transient nature of modes

The spectrogram for density fluctuation shown in Fig. 5.5, for different VF current at r=+5 cm on the outboard side, indicate the presence of transient nature of modes particularly for 0 A and 40 A VF values. Whereas for 160 A and -160 A

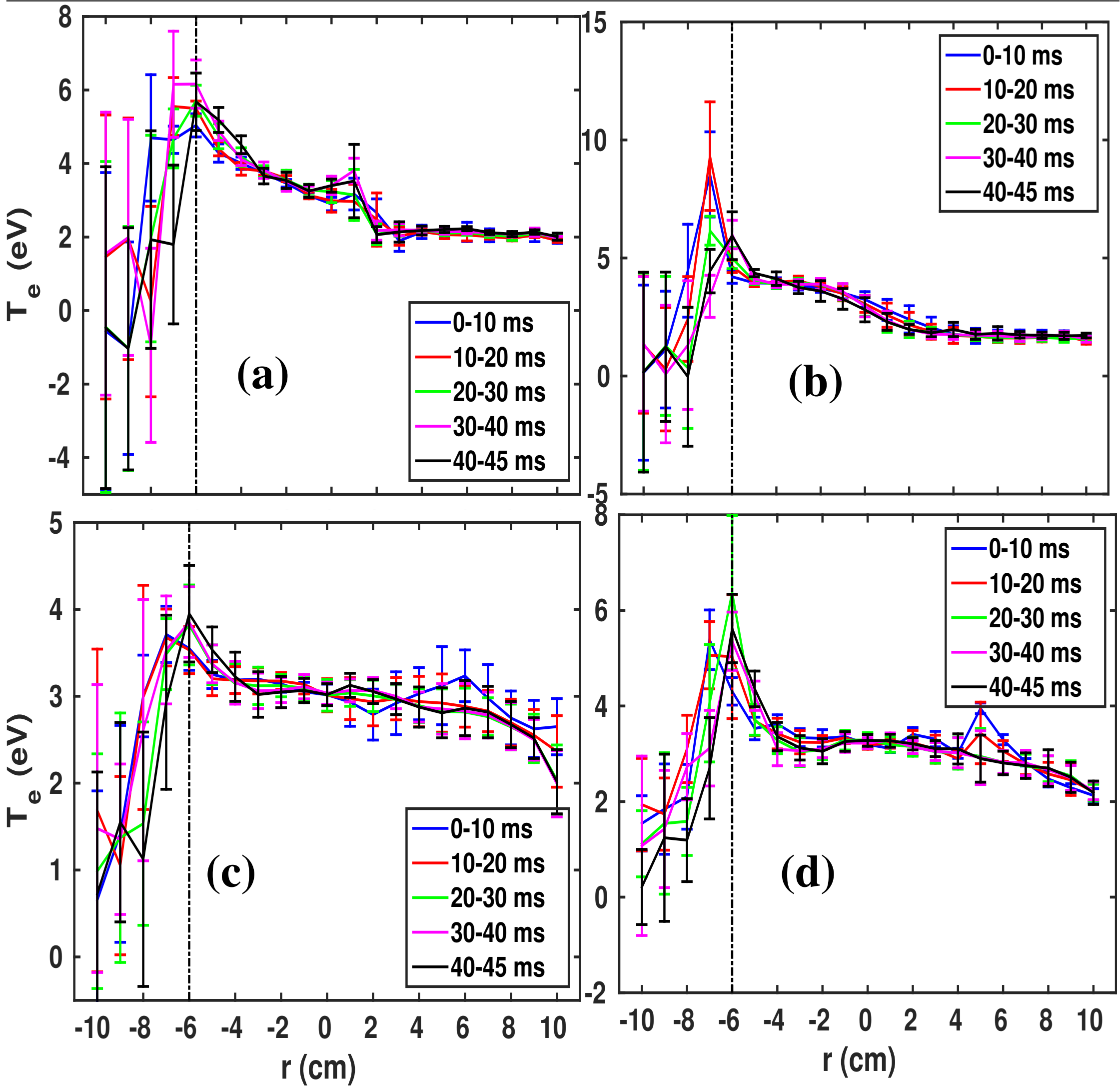

Figure 5.9: Radial profile of electron temperature at different plasma duration for (a) 0 A, 40 A, (c) 160 A and (d) -160 A. It can be observed that the nature of temperature profile does not vary much with time for post source region.

values the modes are continuous after getting excited. The spectrogram, shown in Fig. 5.5 is auto power spectrum of density fluctuation and is normalized by the amplitude of the dominant mode. It can be observed from Fig. 5.5(a) and Fig. 5.5(b) for 0 A and 40 A values respectively, the mode excites as soon as the discharge is struck, however, disappear after 10-15 ms of the plasma duration. Whereas for 160 A and -160 A values the mode (or modes) excites after 15 ms of plasma duration remains continuous till the end of the plasma.

A typical variation of the input power with time is shown in a viewgraph in

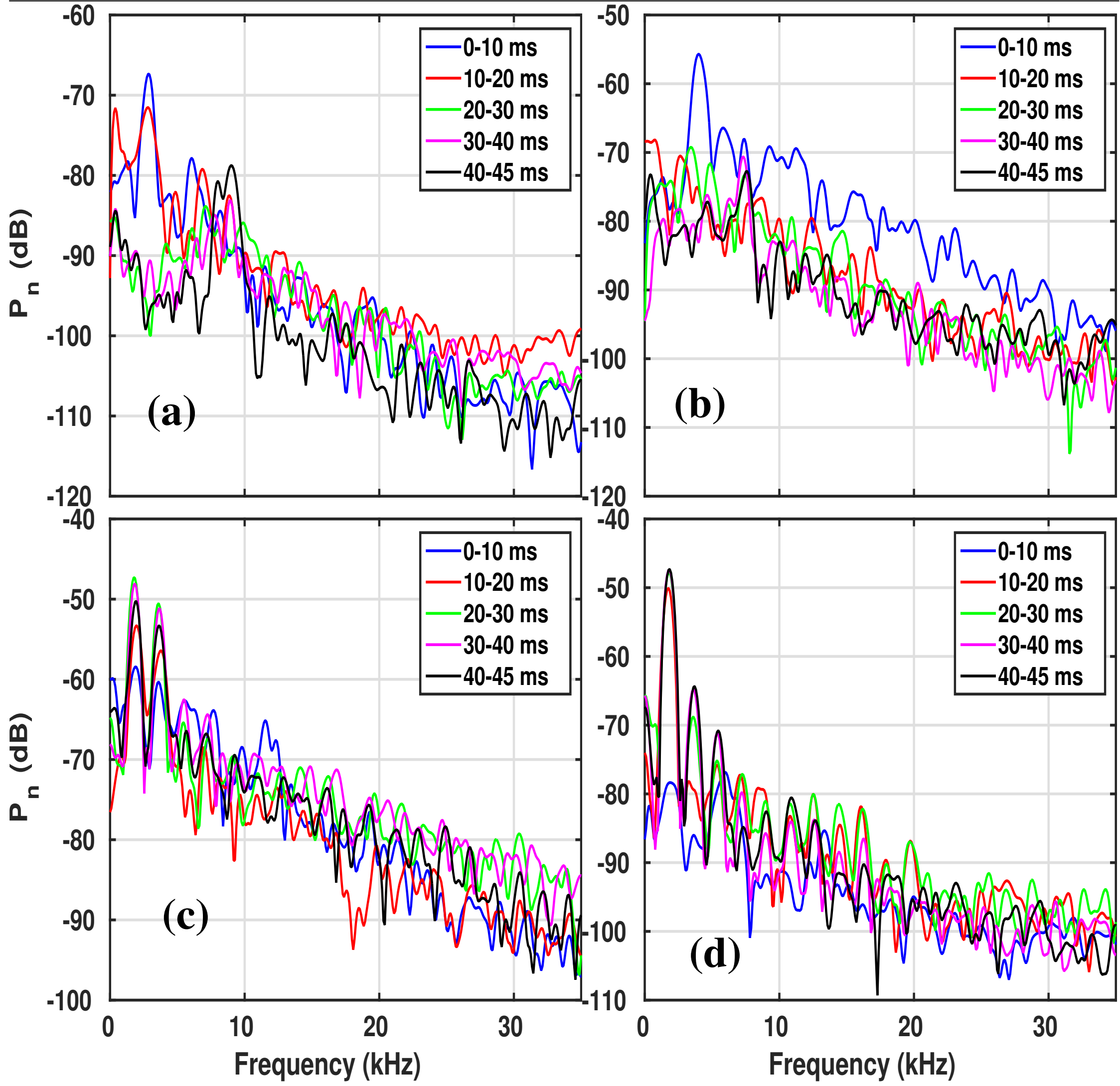

Figure 5.10: Power spectrum of density at r=+5 cm at different plasma duration for (a) 0 A, 40 A, (c) 160 A and (d) -160 A. It can be observed that the modes for 0 A and 40 A VF currents disappear after t> 10 ms.

Fig. 2.7, which shows that the forwarded power (cyan curve) shows a weak decay with time, however, the reflected power (magenta) is almost constant in time. To further determine the cause of this transient nature of modes, the radial profile of density and electron temperature at different times and for various VF current is shown in Fig. 5.8 and Fig. 5.9 respectively. An auto power spectrum of density at different plasma duration for different VF current has been shown in Fig. 5.10, which shows that the modes for 0 A and 40 A VF currents disappear after 10 ms. Time variation of T_e shown in Fig. 5.9, indicate that T_e profile does not

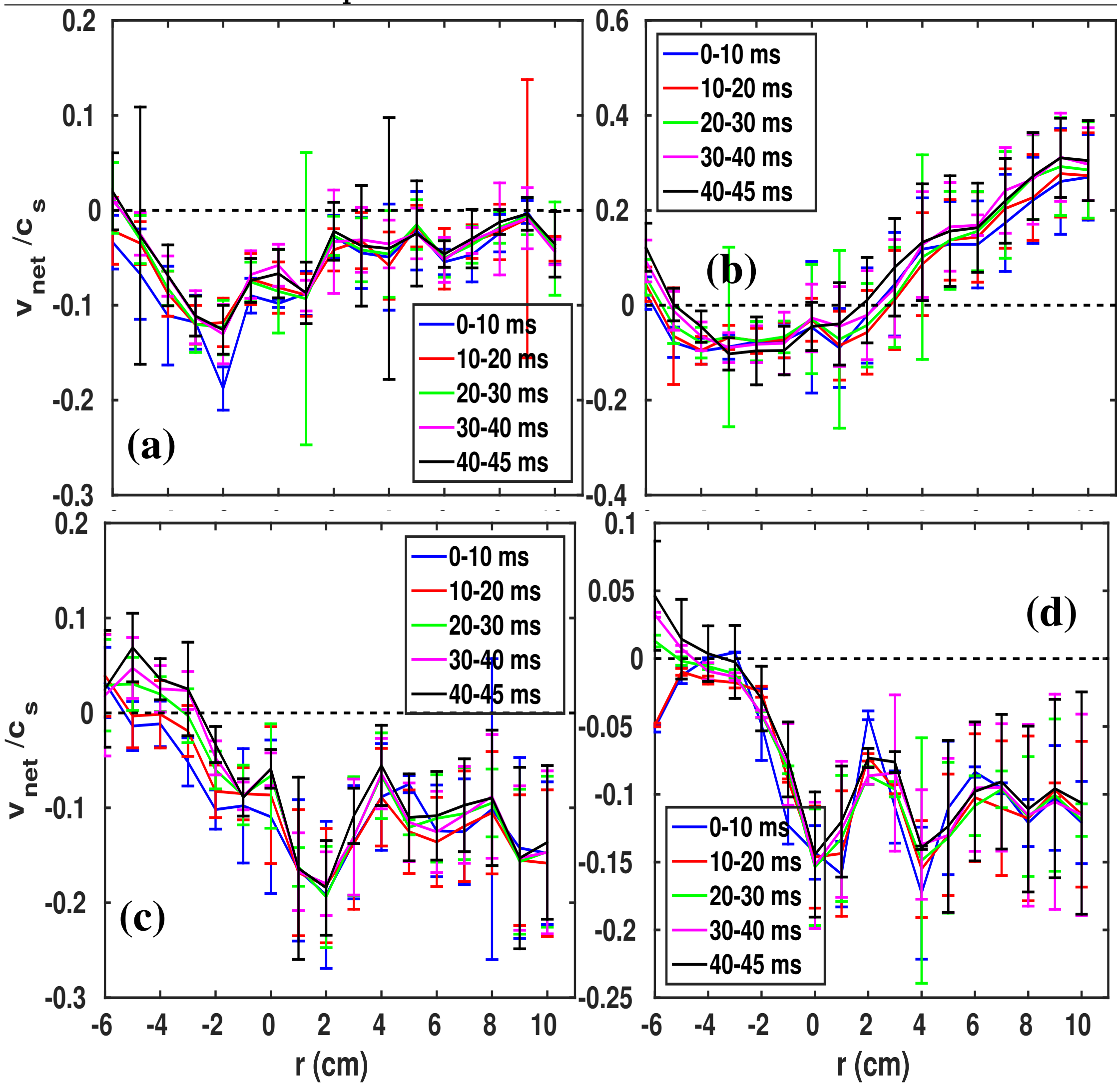

Figure 5.11: Radial profile of net poloidal flow at different plasma duration for (a) 0 A, 40 A, (c) 160 A and (d) -160 A. It can be observed that the nature of poloidal flow profile does not vary much with time for post source region.

vary significantly with time for the post-source region. Whereas density profile is shown in Fig. 5.8 indicate that for 0 A and 40 A VF values, there exist a significant variation of plasma profile with time, however for 160 A and -160 A values, the profile remains almost constant after 10 ms of the plasma duration untill the end of the plasma. Fig. 5.8(a) and Fig. 5.8(b) show that the density gradient becomes weaker with time, that could be the reason for the disappearing of modes after 15 ms for 0 A and 40 A VF currents.

Similarly, the poloidal flow profile for different times for different values of VF current has been shown in Fig. 5.11, which shows that poloidal flow does not vary significantly with time. Therefore, it can be concluded that the profile of plasma density varies with time significantly for 0 A and 40 A VF current and the rest of the plasma parameters like T_e, poloidal flows etc, are almost constant in time. Hence, a possible reason for the transient nature could be the variation in the gradient of the plasma density with time. However, details are not known yet.

We have characterized, mean plasma profiles and fluctuation spectrum for an ECR plasma. In Sec. 5.8, we will try to identify possible instabilities for each observed mode.

5.8 Identification of observed modes

As observed in Sec. 5.4, there exist weak yet finite gradients in plasma density and electron temperature profiles. These gradients may trigger instabilities and excite fluctuations and turbulence in the plasma. As observed in Sec. 5.5, there are few modes which get excited in the plasma and the transient nature of the modes for 0 A and 40 A VF currents have been established in Sec. 5.7. In this Section, we will try to find out the nature of instabilities which excites those modes.

To identify the instabilities, we would like to employ the technique based on the value of cross-phase between density and potential fluctuations estimated simultaneously at a particular radial location. The details of this method are already discussed in Sec. 4.6.

It can be observed from Fig. 5.4, that for all VF currents there exists one dominant mode except for 160 A case, where two dominant modes exist. The cross-phase is shown in Fig. 5.12 for dominant mode only. It can be observed that for each value of VF current the value of $\theta_{n\phi} > 0.5\pi$ on the outboard side, with $\gamma_{n\phi} > 0.8$. It indicates that the observed modes are of flute-like which includes interchange type instabilities.

For the interchange type instabilities, the source of free energy is the gradient in the plasma density. Theoretically speaking in the toroidal devices, the outboard side is known as the bad curvature region as the direction of the density gradient and effective gravity due to curvature are such that Rayleigh Taylor (R-T) instability may dominate. However, for a given density gradient, the R-T mode can only be unstable if following criteria are satisfied [37]:

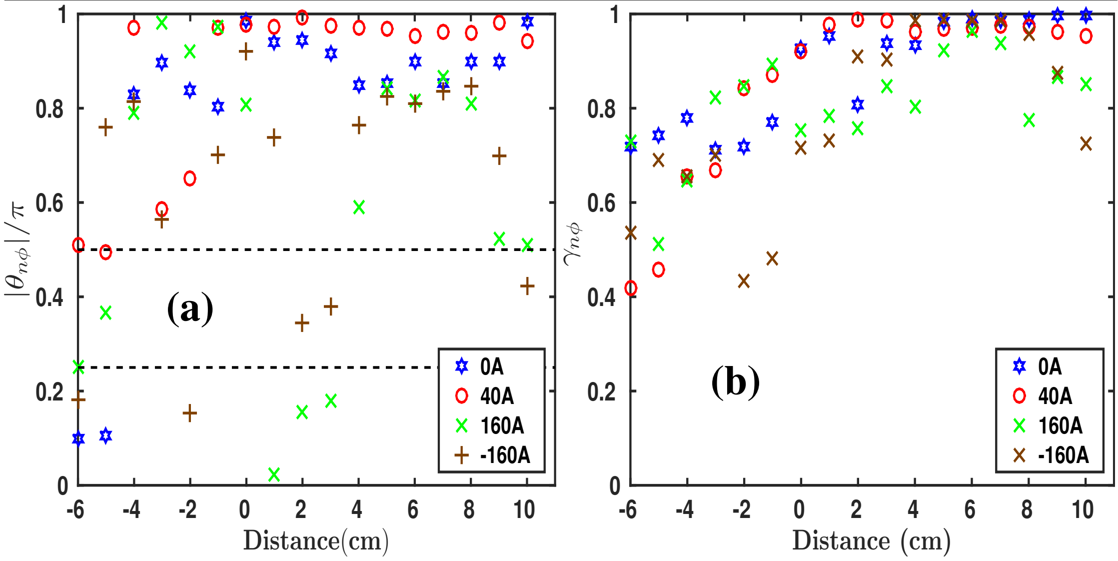

Figure 5.12: Radial profile of (a) cross-phase ($\theta_{n\phi}$) and (b) coherence ($\gamma_{n\phi}$) between density fluctuation and potential fluctuation for different values of VF current. The plot is zoomed for post-source region only and horizontal lines in (a) represent the $\theta_{n\phi} = 0.25\pi$ and $\theta_{n\phi} = 0.5\pi$. It can be observed that the $\gamma_{n\phi} > 0.6$ for majority of the values of radial location and VF currents.

$$\epsilon_n(1 + \eta_e - \epsilon_n) > \frac{k_z^2 a_s^2}{4}[\epsilon_n + \frac{T_i}{T_e} + \frac{v_E a_s}{c_s k_z^2 L_n^3}(\frac{L_n^2}{l_v^2} + \frac{L_n}{L_v})]^2 \tag{5.1}$$

where L_n is the density scale length, L_v velocity scale length, $\epsilon_n = 2L_n/R$, R is the major radius of the torus, k_z is the vertical (or poloidal) wavenumber, v_E is poloidal velocity of the plasma, $a_s = c_s/\omega_i$, c_s is the ion acoustic velocity and ω_i is the ion cyclotron frequency.

Using Eqn. 5.1, for the density gradient and net poloidal flow in the present experimental study, it has been estimated that R-T is stable for every value of VF current. Therefore, the presence of R-T instability has been ruled out.

For 160 A and -160 A, the frequency of the first dominant mode matches with the diamagnetic frequency, $f_{De} = \omega_{De}/(2\pi) = k_B T_e/(2\pi e B_T L_n a)$ and $\theta_{n\phi} \geq 0.5\pi$. Therefore, it can be inferred that these modes have interchange like properties. The details of the second dominant mode for 160 A VF current is provided in Chapter-7.

It can be observed from Fig. 5.1(a) that the density gradient is weak for 40 A VF current, but there exists a finite gradient in electron temperature profile shown in Fig. 5.1(b). The diamagnetic frequency estimated after incorporating both density and temperature scale length i.e, $f_{D_e} = \frac{k_B T_e}{2\pi e B(L_n + L_{T_e})a}$ matches with the frequency of the mode observed at $r = +5$ cm. However from Fig. 5.9(b), it can be observed that the gradient of the electron temperature does not change significantly with time but the observed mode is found to be transient in nature as shown in Fig. 5.5(b). Therefore, it can be inferred that the mode is due to the gradient in electron temperature profile but the reason for the transient nature is not known yet.

Similarly, for 0 A, there exists a very weak transient mode and still could not be identified.

5.9 Summary

The plasma is produced using a newly developed ECR based Microwave source. The frequency of the launched Microwave is around 2.45 GHz, with averaged launched power is around 1 kW, launched in “O” mode. The plasma produced from ECR source has a very weak zeroth order radial electric field and hence the poloidal flow is not significant. In addition, the ECR plasma is free from the high energy electrons which were present in hot cathode produced plasma discussed in Chapter-4.

The value of density increases for the small value of $\bar{L}_c$ and gradient in the density profile is very weak to generate R-T instability on the outboard side. However, a gradient in the electron temperature profile exist for 0 A and 40 A VF values, which gets weaker for 160 A and -160 A i.e, for small value of $\bar{L}_c$.

The transient nature of modes have been observed for 0 A and 40 A VF currents and reason for them is not known yet. The drift-interchange mode has been observed for 160 A and -160 A VF values.

The major findings of the present Chapter are listed as follows:

- A newly developed Microwave based ECR source with a frequency of ∼2.45 GHz, with averaged power of around 1 kW, launched from the outboard side in “O” mode has been used to produce plasma in an SMT, BETA.

- The primary ionization takes place due to EC resonance at r=-6 cm and the unspent energy, reflects from the vessel wall which causes a change in its polarization and a secondary ionization occurs due to the upper hybrid resonance (UHR).

- The radial location of UHR varies with the applied VF current or $\bar{L}_c$, which significantly affects the density profile.
- The equilibrium and fluctuation plasma profiles have been characterized for different values of externally applied vertical magnetic field.
- It has been observed that the magnitude of density increases for widely opened field lines or small values of $\bar{L}_c$, which could be due to effective reduction of E_z^{res} [6].
- The gradient in density profiles for all values of $\bar{L}_c$, found to be weak enough to generate R-T instability on the outboard side. However, it can still generate drift-like modes.
- The transient nature of modes have been observed for 0 A and 40 A VF currents and reason for them is not known yet.

In the present Chapter, we discussed the effect of the toroidal field topology on an ECR produced plasma, in the Chapter-6, we will compare the plasma properties of the hot cathode produced plasma and the ECR produced plasma and will try to investigate the role of poloidal flows on the plasma properties in an SMT.

6

A comparative study to determine the role of the poloidal flow on quasi-static equilibrium, fluctuations and particle confinement in a simple toroidal device

6.1 Introduction

In the Chapter. 4, it has been clearly shown that the zeroth order poloidal flow can affect the nature of quasi-static equilibrium and fluctuation in an SMT. Furthermore, the nature of poloidal flow strongly depends on the topology of the toroidal field line. Therefore, to study the role of the poloidal flow on plasma properties in detail, we need to "switch-off" the poloidal flow. For this very purpose a new ECR plasma source discussed in Chapter. 5 has been developed and it has also been shown that a very weak zeroth order radial electric field and hence weaker poloidal rotation of the plasma exist for ECR plasma as compared to the hot cathode discharge.

Moreover, as discussed in Chapter. 4, the plasma produced by the hot cathode source by the thermionic emission of a 2 mm thick and 20 cm long filament, mounted at the minor axis at one particular toroidal location. The primary energetic electron density emitted from the filament is estimated to be around 1×10^{14} m^{-3}. As the location of both the sources are different, therefore, plasma densities and their profiles are expected to be different for both the sources, for both fast electrons as well as secondary or plasma electrons.

These two sources separately had been used for plasma production in several SMTs. The detailed studies of the equilibrium, fluctuations and flows using Hot cathode produced plasma have been performed in the devices like BLAAMANN [21], THORELLO [23] and BETA [38]. Characterization and studies of the various phenomenon have been performed using the Microwave plasma in the devices like TORPEX [26] and HELIMAK [25]. In ACT-I [32], the plasma produced and characterized by using Hot cathode, Microwave and lower hybrid sources.

We investigate the dependence of plasma properties on the method of the plasma production and on the poloidal flows. Hence, in the current Chapter, we present the comparative study of the plasma produced using two different kinds of sources namely (i) the hot cathode source and (ii) the ECR source, by keeping the toroidal field strength at 750 G at the minor axis and working pressure of 1×10^{-4} torr for both the sources.

6.2 Experimental results

As discussed in Sec. 6.1, a comparative study of plasma properties involving the two above mentioned sources. For this purpose, the experimental conditions like working pressure, toroidal field, vertical field etc, have been kept similar for both kinds of plasma. Therefore, basic experimental parameters such as electron neutral collisions, electron and ion Larmor radii, magnetization etc, are same as listed in Table. 5.2.

In the following Sections, we will compare the plasma properties beginning with the net poloidal flows for both these sources.

6.2.1 A comparison of net poloidal flow

As discussed in Sec 5.6, the net poloidal flow for the ECR plasma is very weak as compared to the plasma produced by the hot cathode, a comparison is shown in Fig. 6.1. It can be observed that the net poloidal flow is very small for ECR produced plasma shown in Fig. 6.1(b) as compared to the hot cathode produced

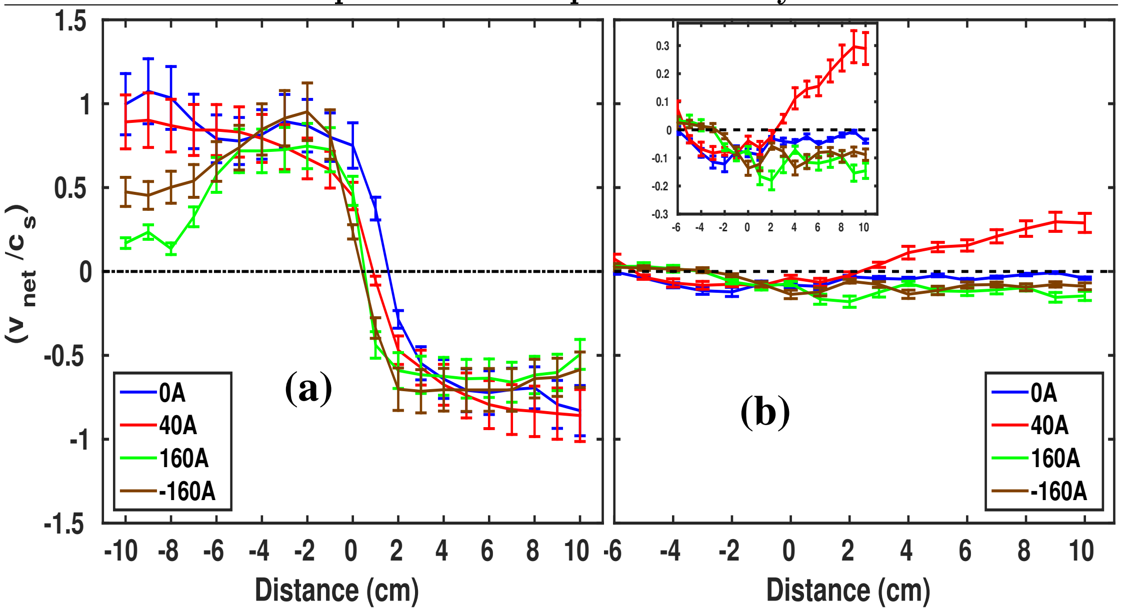

Figure 6.1: A comparison of net poloidal flow for (a) hot cathode and (b) ECR produced plasma for various values of VF current. It can be observed that the net flow for ECR plasma shown in (b) is significantly small as compared to the hot cathode plasma. In (b), the plot has been zoomed for post-source region i.e, beyond -6 cm and y-axis scale has been set same to (a) for comparison purpose, an actual scale has been shown in the inset plot in (b). The horizontal line represents the zero poloidal flow in both the plots.

plasma shown in Fig. 6.1(a) except for VF current of 40 A. For 40 A VF current, a small net poloidal flow can be observed particularly on the outboard side. The toroidal flow measured to be around $0.1c_s$ maximum and hence considered negligible.

The poloidal flow as discussed in Chapter. 4 were found to influence strongly the natures of quasi-static equilibrium and fluctuation. Therefore, let us have a look on the role of the net poloidal flow on quasi-static equilibrium, fluctuations and particle confinement in an SMT.

6.3 Radial profiles of hot cathode produced plasma

Radial profiles of mean plasma parameters for ECR produced plasma are shown in Fig. 5.1. Let us compare those with the hot cathode plasma profiles measured for the same experimental conditions shown in Fig. 6.2. It can be observed that

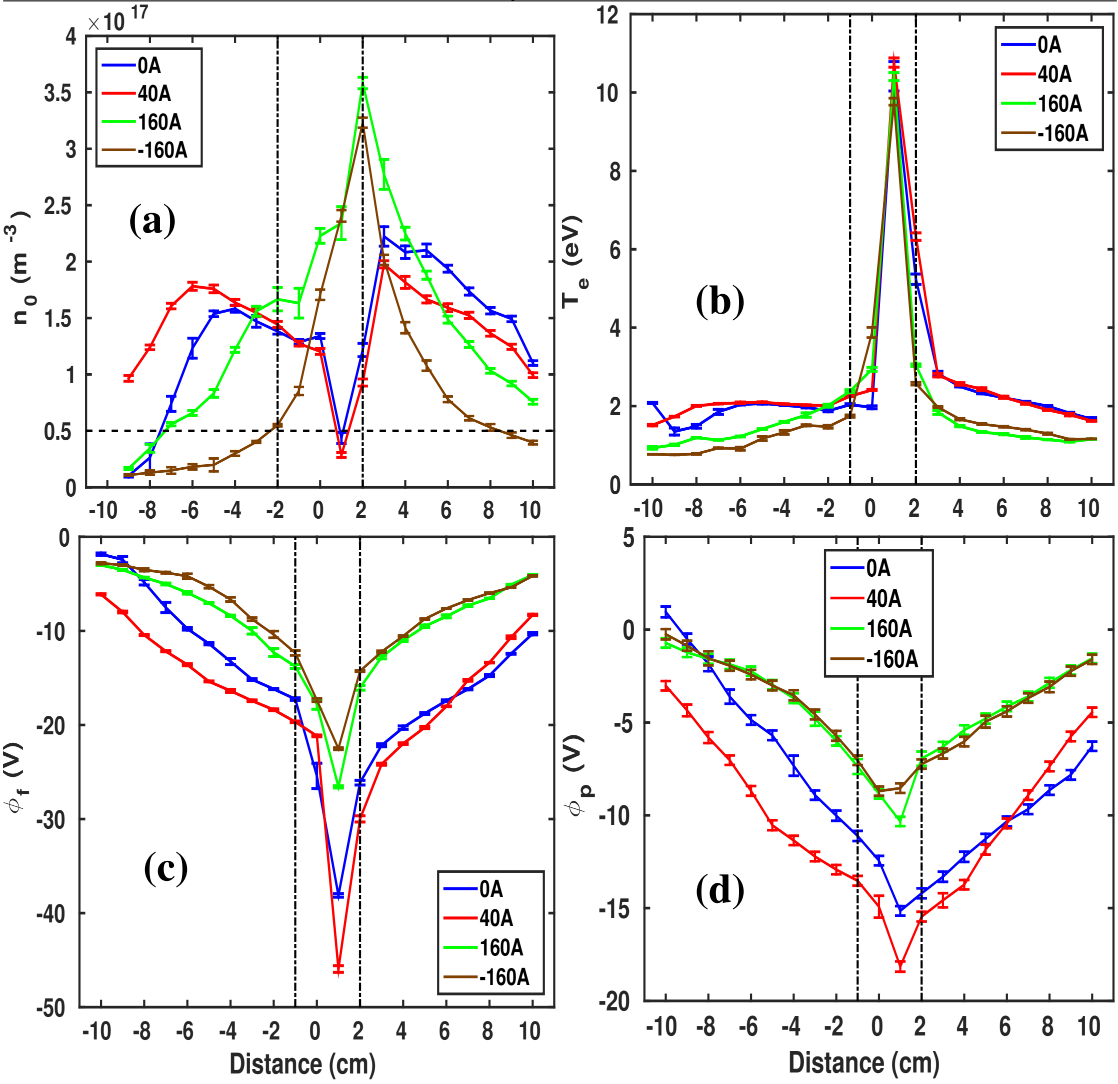

Figure 6.2: Radial mean profiles of (a) plasma density, (b) electron temperature, (c) floating potential and (d) plasma potential for different values of VF current at B_T=750 G. The region between vertical lines represents the region of high energy electrons, emitted from the hot cathode mounted at the minor axis. The horizontal line in (a) represents the maximum plasma density for the ECR produced plasma as shown in Fig. 5.1(a).

the density profile becomes symmetric around the peak for 160 A and -160 A VF current, which could be due to effective reduction of E_z^{res}. However, for 0 A and 40 A, VF currents have relatively higher densities on the outboard side. These results are similar to observations presented in Chapter-4. The peak in the T_e profile and the dip in the ϕ_f and ϕ_p profiles coincide with the location of the cathode location at the minor axis. As discussed in Chapter-4, the region around the minor axis, represented by the vertical lines in Fig. 6.2 is contaminated by the presence of high energy electrons.

On comparing the radial profiles of the hot cathode plasma shown in Fig. 6.2 to the radial profiles of the ECR produced plasma shown in Fig. 5.1 in Chapter-5. One can observe that the maximum plasma density for the ECR plasma is around 5-8 times less than that of the hot cathode plasma density. The horizontal line in Fig. 6.2(a) represents the maximum plasma density for ECR plasma as shown in Fig. 5.1(a). This could be attributed to the fact that the "O" mode polarization is not the most efficient method for exploiting the ECR coupling. There are several issues are at play here

1. For the magnetic field strength used in the experiments ($\sim$ 750 G) the resonance layer is at ~ -6 cm inboard. Since the "O" mode propagates only below the critical density (for $\omega_{pe} < \omega$), this implies that the plasma density on the outboard side can never rise beyond the critical value ($\sim 7 \times 10^{10}$ cm^{-3}). Hence the lower densities.

2. As noted above, the normal polarization that should have been used for ECR coupling is the "X" mode. But this would have required launching the microwave from the inboard side where access of the ports is not possible.

3. It turns out that ECR resonance with the "O" mode is less efficient than the "X" mode on account of the fact that the O-mode does not yield the fundamental cold plasma resonance, as does the X-mode. In fact, this resonance vanishes for cold plasma ($T_e = 0$), whereas the "X" mode resonance survives even for $T_e = 0$. On this count, the "O" mode is weaker and yields lower densities.

However, launching the Microwave in "X" mode from the outboard side will be attempted in the near future.

Moreover, the profile of density is quite different for both the sources. It has been discussed in Chapter-5, the gradient in density profile is relatively weak to excite the R-T like instabilities on the outboard side. However, it can be observed from Fig. 6.2(a), the density gradient is relatively strong for the hot cathode produced plasma as compared to ECR plasma. The nature of instabilities will be discussed in subsequent Section.

On comparing floating potential and plasma potential for both the sources, it is clear that the potential profiles for the hot cathode produced plasma (Fig. 6.2(c) and Fig. 6.2(d)) show a strong gradient and the presence of a zeroth order radial electric field. It may provide a strong poloidal rotation to the plasma, which has been already discussed in Sec. 6.2.1.

It may also be noted that T_e profile for hot cathode source shown in Fig. 6.2(b) has very weak gradient except for close to the minor axis. However, for ECR plasma T_e profile shown in Fig. 5.1(b) indicates the presence of substantial gradient for 0 A and 40 A VF currents, which gets weaker for higher VF currents of 160 A and -160 A.

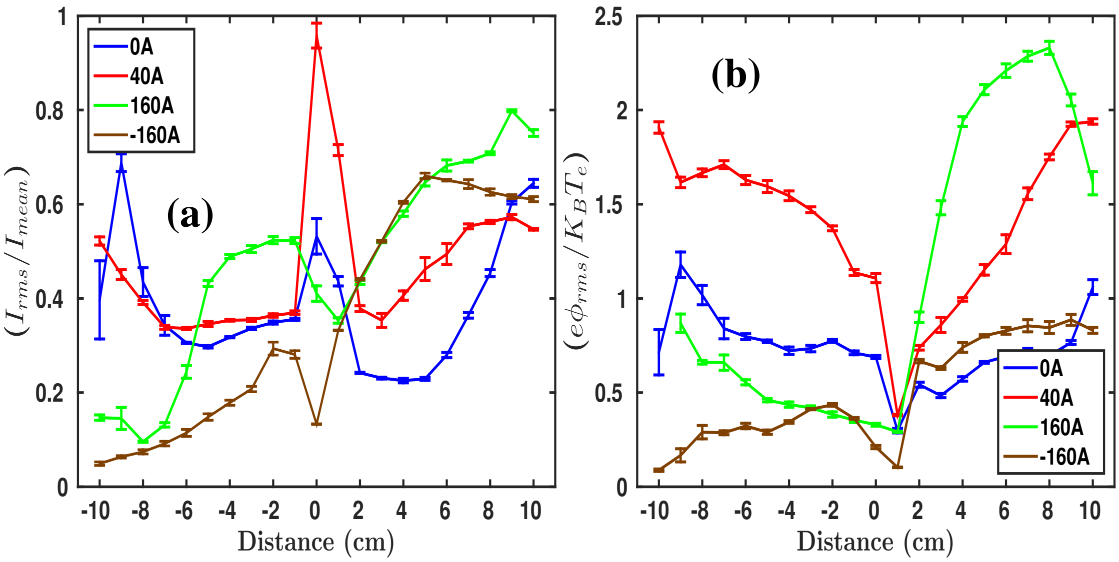

Figure 6.3: Radial profiles of relative fluctuation in (a) ion saturation current or plasma density, (b) floating potential or plasma potential for different values of VF current at B_T=750 G. For negligible fluctuations in T_e, ion saturation current fluctuation is similar to density fluctuation, similarly, plasma potential fluctuation is similar to the floating potential fluctuation.

The relative density and potential fluctuations for hot cathode produced plasma is shown in Fig. 6.3(a) and Fig. 6.3(b) respectively. On comparing with the ECR plasma counterpart shown in Fig. 4.2(a) and Fig. 4.2(b) respectively, it can infer that the relative density and potential fluctuations are less in ECR plasma than that of hot cathode plasma. It is believed that the fluctuation driven poloidal flow can also control the plasma properties. As relative fluctuation levels are quite small, hence the poloidal rotation of the plasma due to fluctuations is negligible, which can be again confirmed by the comparison of net poloidal flows shown in Fig. 6.1.

In this Section, we compared the mean plasma properties and relative fluctuation level for both the sources. In the Sec. 6.4, we will Characterize the nature of fluctuations.

6.4 Spectral analysis

By comparing the plasma mean profiles for both the sources, we found that the nature of plasma profiles are very different for both the sources. Therefore, we expect the nature of fluctuation should also be different for both the sources. Therefore, in the present Section, we will characterize the nature of fluctuations present in both the sources at the same radial location.

6.4.1 Power spectrum

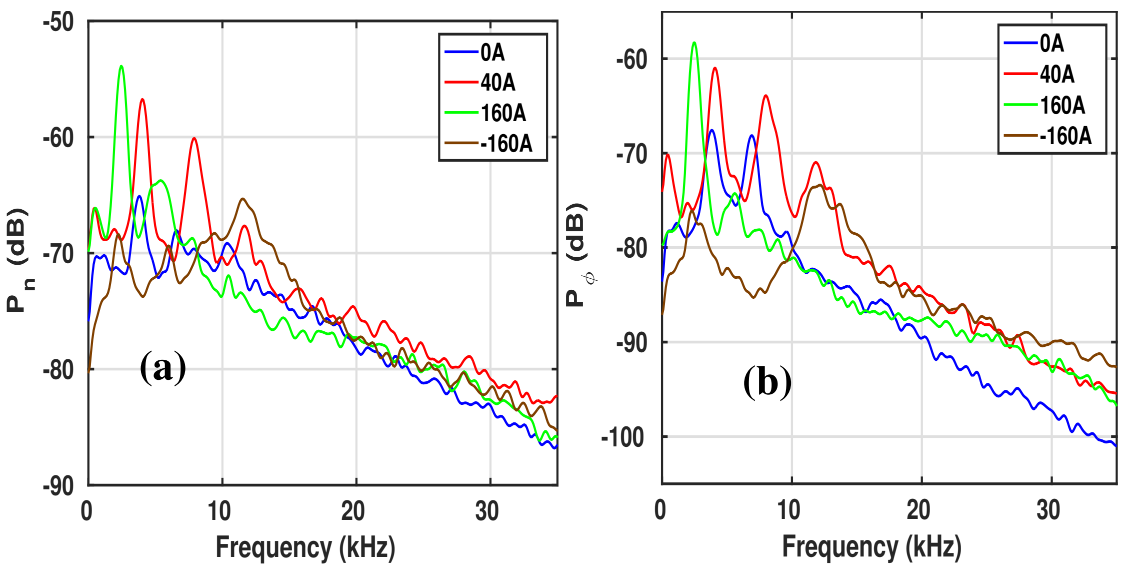

Figure 6.4: Auto power spectrum of (a) density and (b) potential fluctuations, for different VF current for the hot cathode source values at r=+5 cm on the outboard side at B_T=750 G. The sampling rate for these measurements is 200 kHz, plots are zoomed to 35 kHz for better representation. For all VF values, there are one or two modes followed by a turbulent background. The spectrum of potential fluctuation in (b) looks similar to density fluctuation. A turbulent high frequency broadband can be observed for -160 A or widely opened field lines.

The auto power spectrum of density and potential fluctuations shown in Fig. 6.4(a) and Fig. 6.4(b) respectively at r=+5 cm on the outboard side. On comparing with the auto power spectrum of ECR plasma shown in Fig. 5.4 at the same radial location, it can be observed that the frequencies of the modes are different for both the sources. However, it can be noted that for the hot cathode source, the amplitude of the turbulent background is relatively higher than the ECR plasma. It implies that the hot cathode produced plasma is more turbulent than the ECR plasma. Moreover, broadband which is present in hot cathode plasma is absent in the ECR fluctuation spectrum. It has been discussed in Sec. 5.7 that the nature of modes observed for 0 A and 40 A VF currents in ECR plasma are of transient nature. However, in hot cathode produced plasma no transient nature of the modes has been observed. In this Section, we characterized the nature of modes present in the hot cathode plasma and compared the characteristics with the ECR plasma. In Sec. 6.5, we will try to identify the instabilities, responsible for generating these modes.

6.5 Identification of instabilities

As discussed in Chapter-4, when the hot cathode is the plasma source, BETA is dominated by the presence of poloidal flows. In addition to that, there exists a free energy source for instabilities which is the presence of a substantially strong density gradient.

6.5.1 Instabilities on the outboard side

Using the stability criteria given in Eqn. 5.1, unlike the ECR plasma, the hot cathode plasma is vulnerable to R-T instability on the outboard side for every VF current. However, for R-T instability, $\theta_{n\phi} > 0.5\pi$, but for 40 A VF current $\theta_{n\phi} \leq 0.5\pi$ on the outboard side as shown in Fig. 6.5. Whereas for other VF currents, $\theta_{n\phi} > 0.5\pi$, which indicate the presence of R-T instability on the outboard side for those values of VF currents. From Fig. 6.5(a), it can be observed that $\theta_{n\phi} > 0.5\pi$ throughout the radial location for every VF current (except 40 A case on the outboard side). It indicates the presence of flute-like instability at every radial location for every VF current except for the outboard side for 40 A VF current.

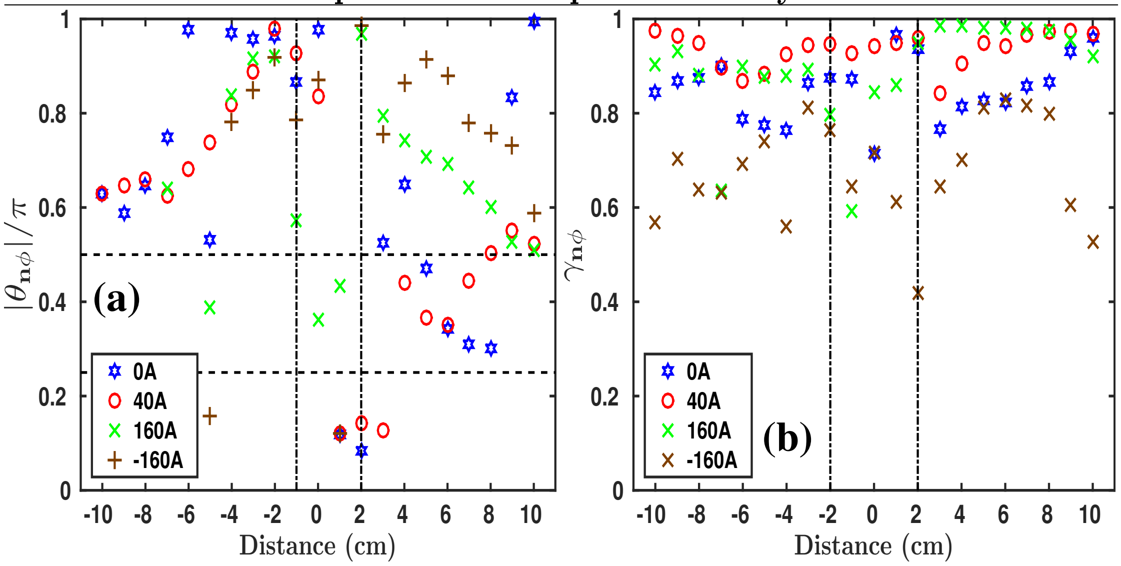

Figure 6.5: Radial profile of (a) cross phase ($\theta_{n\phi}$) and (b) coherence ($\gamma_{n\phi}$) between density fluctuation and potential fluctuation for different VF currents for the hot cathode produced plasma. It may be noted that $\gamma_{n\phi} \geq 0.6$ for most of the values except in the region around the minor axis. It can be observed that for most of VF current values, $\theta_{n\phi} > 0.5\pi$ on the outboard side, which indicate the presence of the flute-like instabilities.

As discussed in Sec. 4.6, a comparison between angular diamagnetic velocity ω_D defined as $\omega_D = k_z(T_e/B)(1/L_n)$ and angular velocity due to poloidal flow ω_{pol}, for vertical or poloidal mode number, m=1 is defined as $\omega_{pol} = v_{pol}/r$ provides insight of the nature of instability [69, 70]. For this purpose a comparison of ω_D and ω_{pol} is shown in Fig. 6.6, which indicate that the shear driven instabilities dominate throughout the radial location for every value of VF current, except for inboard side for 160 A VF current. However, as for ECR plasma, the poloidal rotation of the plasma was not significant, hence, one may not expect shear driven instabilities there.

However Fig. 6.7 indicate that on the outboard side $(e\tilde{\phi}/K_BT_e)/(\tilde{n}/n) \sim 3$ for all VF current except -160 A, which indicate the presence of shear driven instabilities. For -160 A case $(e\tilde{\phi}/K_BT_e)/(\tilde{n}/n) \geq 1$ indicating presence of R-T instability. Therefore, from Fig. 6.5(a), Fig. 6.6 and Fig. 6.7, it can be confirmed that the outboard side is dominated by shear driven R-T instability for 0 A, 40 A and -160 A VF currents and for -160 A, it could be R-T instability (without shear). However, for 40 A, VF current, $\theta_{n\phi} \leq 0.5\pi$, which contradicts the belief and the

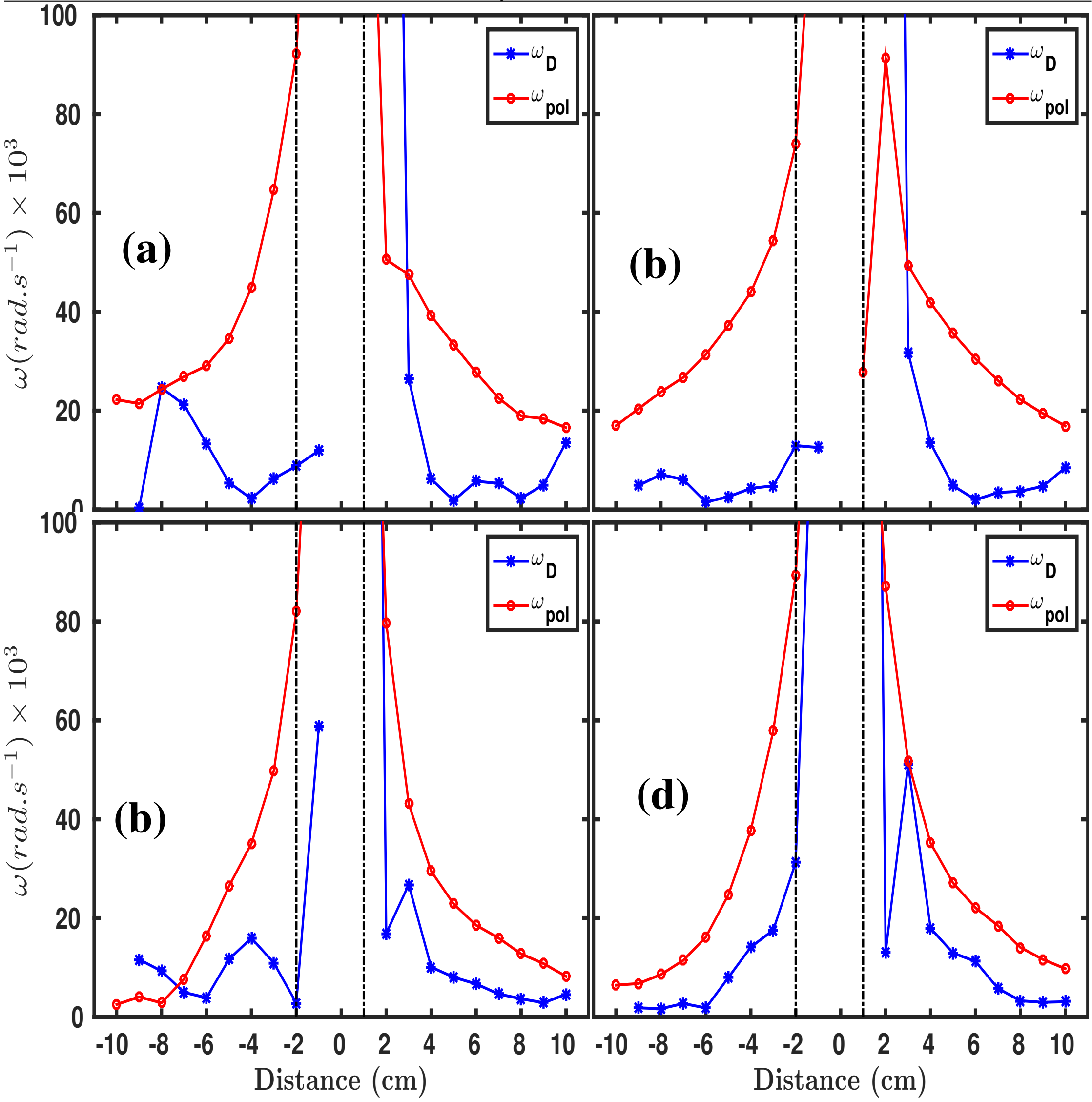

Figure 6.6: Radial comparison of diamagnetic angular velocity ω_D and angular velocity due to flow ω_{pol} for VF current of (a) 0 A (b) 40 A (c) 160 A and (d) -160 A. It indicate that $\omega_D > \omega_{pol}$ throughout the radial locations, which implies that shear effects are dominant here. However for 160 A VF current on the inboard side close to the limiter $\omega_D < \omega_{pol}$ as the poloidal flow is very small. The region between vertical lines in the above plots are populated with high energetic electrons, hence the measurements may be erroneous.

reason for which is not yet clear. The frequency for the shear R-T instability is given in Eqn. 4.15 as a function of ω_{pol}, ω_D and density gradient length scale. As discussed in Chapter-5, R-T instability does not exist for ECR plasma as the gradient in density profile is substantially weak to drive that. It has been observed

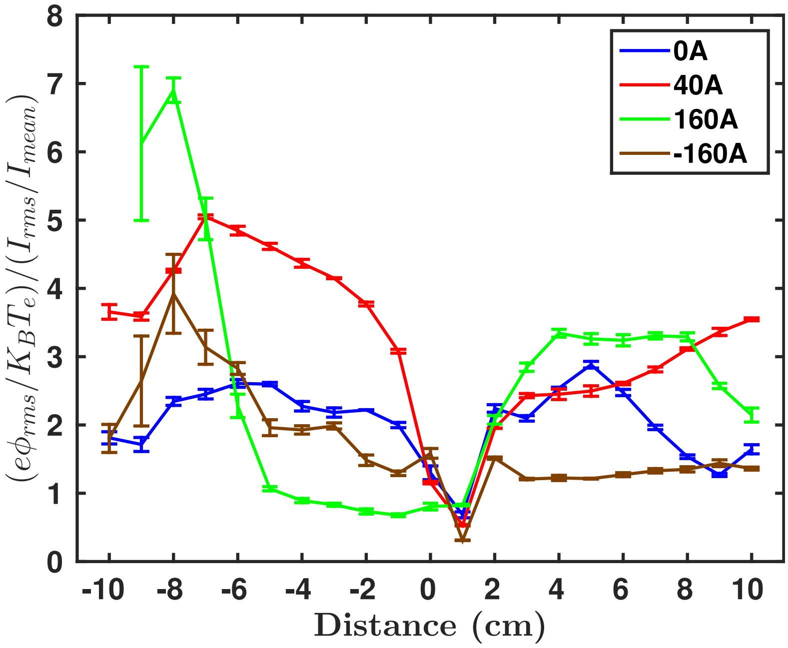

Figure 6.7: Radial profile of ratio of relative potential fluctuations to relative density fluctuations. It can be observed that on the outboard side, the ratio is close to 3 for all VF currents except for -160 A.

that the drift-interchange instability dominates for ECR plasma on the outboard side.

6.5.2 Instabilities on the inboard side

As discussed in Sec. 6.5.1, the outboard side is dominated by the presence of the R-T and shear driven R-T instabilities. As observed in Chapter-4, the presence of poloidal flow brings more flute like towards the inboard side. It can be confirmed by the cross-phase values shown in Fig. 6.5(a), which indicate the flute like nature of observed mode as $\theta_{n\phi} > 0.5\pi$ for all VF currents. Moreover from Fig. 6.6 and Fig. 6.7, it can be observed that shear effects are dominant on the inboard side for all VF currents except for 160 A. As the presence of R-T instability on the inboard side is unlikely, therefore, it confirms the presence of shear driven Kelvin Helmholtz (K-H) instability on the inboard side for all VF current except 160 A.

Till now in the present Chapter, we compared the plasma properties such as mean and fluctuations for two different sources to study the role of poloidal flows on plasma properties. In the Sec. 6.6, we will discuss the effect of poloidal flows on the particle confinement in an SMT.

6.6 Estimation of particle confinement in an SMT using afterglow method

As discussed in Sec. 4.12, an estimate of plasma confinement time helps to understand the balance between sources, sinks and existence of any improved confinement due to plasma collective effects.

In the present study of the particle confinement in BETA, we present a comparative study for two different plasma sources mentioned earlier to study the role of the poloidal rotation on the particle confinement.

6.6.1 Procedure to obtain particle confinement time using afterglow method

As discussed in Sec. 4.12.1, in afterglow method the fall of the plasma density is recorded after the plasma source has been switched off. In the present work, we obtained a time series of the ion saturation current for different VF currents for both the sources using a Langmuir probe discussed in Sec. 2.3. As soon as respective plasma source switch off, plasma density and hence the ion saturation current starts falling in the presence of the toroidal and vertical magnetic field. For this purpose, the sampling rate has been increased to 1 MS/s to attain better resolution. To further improve the statistics of the measurements, the final time series is obtained after averaging over 10 shots taken at the same radial location for similar experimental conditions. The fall of the density in the final time series is fitted with the suitable function to obtain the particle confinement time, τ_C. Following function has been fitted to the density fall in case of the hot cathode produced plasma is provided in Eqn. 4.16.

However, for the density fall in case of ECR plasma does not follow Eqn. 4.16, even for sum of up to 10 exponentials. Therefore, the initial fall of the density for ECR plasma is fitted with the following function:

$$\frac{I_{sat}}{I_0} = 1 - \frac{t - t_0}{\tau_0} \tag{6.1}$$

τ_0 is the confinement time for the linear fall of the ECR plasma. After the initial fall is fitted with Eqn. 6.1, the subsequent fall is fitted with Eqn. 4.16. Therefore, for the ECR plasma density fall, two different functions have been used to fit and estimate three particle confinement times, viz, τ_0, τ_1 and τ_2.

6.6.2 Experimental observations of particle confinement

Using the procedure discussed in Sec. 6.6.1 to obtain particle confinement, we obtained density fall and particle confinement for different VF currents for two different sources. The results obtained are shown in Fig. 6.8 and Fig. 6.9 for 40 A and 160 A VF currents respectively. As discussed in Sec. 5.3 that 40 A VF current represents the case of longest connection length $\bar{L}_c$ and 160 A represents the case of short $\bar{L}_c$. The particle confinement time for the rest of the VF currents is listed in Table. 6.1.

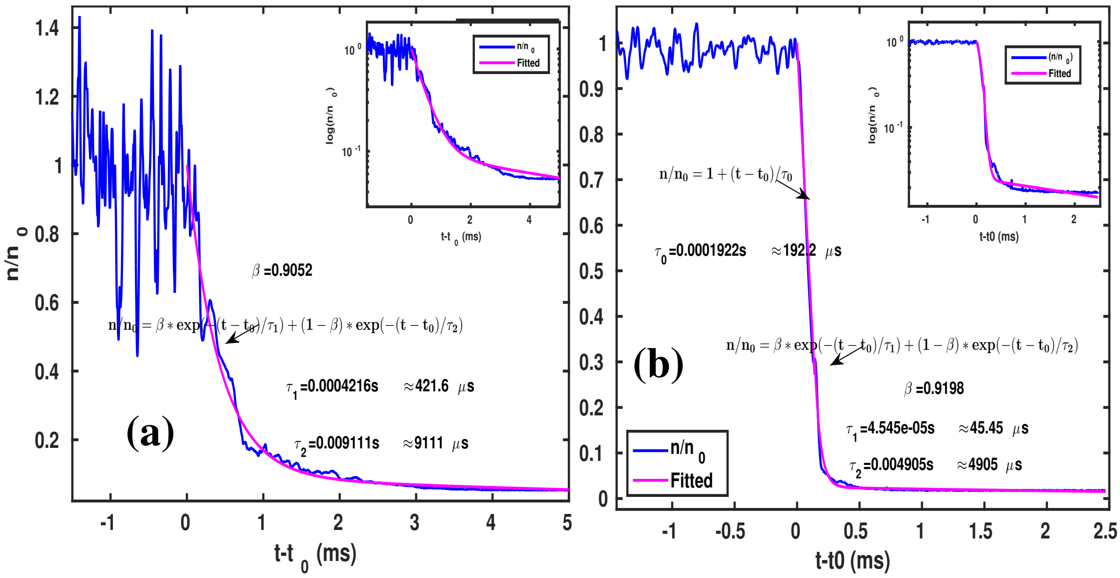

Figure 6.8: Density fall for (a) hot cathode source and (b) ECR source for 40 A or large connection length case. It shows exponential fall for the hot cathode plasma and an initial linear fall for ECR plasma as soon as the source is switched off.

From the Table.6.1, it can be seen that for hot cathode plasma τ_1 increases monotonically with an increase in VF current. Here -160 A implies that field lines are opened up in the other direction. However, for Microwave source for 0 A case, τ_0 is comparable with τ_1 for hot cathode but much less for 40 A case. It could be because for 40 A case, the field lines are almost closed and in the absence of any

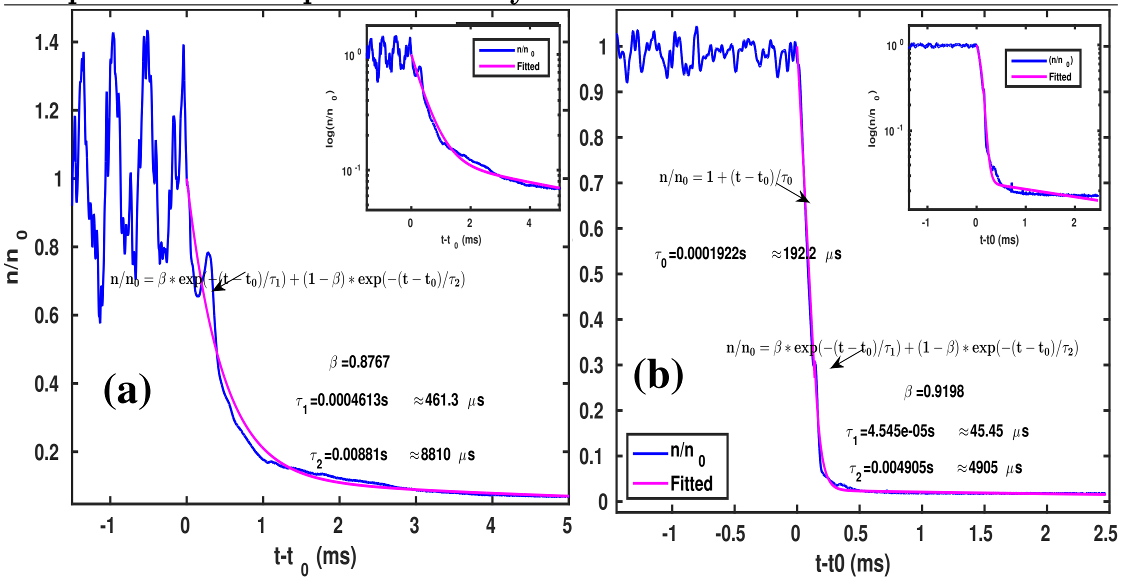

Figure 6.9: Density fall for (a) hot cathode source and (b) ECR source for 60 A or large connection length case. It shows exponential fall for the hot cathode plasma and an initial linear fall for ECR plasma as soon as the source is switched off.

gradient and poloidal flow the Microwave plasma is most vulnerable to $E_z \times B$ loss. However, the hot cathode produced plasma has a strong poloidal flow, which may increase the confinement, therefore even for longest connection length confinement time increases for 40 A VF current. Similarly, for 160 A case, τ_0 for Microwave plasma is much larger than the τ_1 of hot cathode plasma, it could be due to minimization of the E_z due to external B_v as per Nakao's model [6]. Though hot cathode plasma for 160 A case has a poloidal flow but also has a gradient in plasma density, which may cause the loss of the plasma. For -160 A, the field lines are opened up in the opposite direction, therefore the opening of field line is more than that of 160 A case, which may result in loss of majority of electrons to the wall or limiter before setting up the discharge, which may decrease the confinement of the Microwave plasma. However for hot cathode plasma, the electron density is much larger than the Microwave plasma, therefore, it may set up a proper discharge.

As observed, an algebraic like fall for density has been observed for the ECR plasma, which is quite different from the hot cathode produced plasma. Possible causes of the deviation of the fall from exponential behavior could be (i) absence of poloidal flow of the plasma or (b) low values of density and relatively flat density gradient as compared to the hot cathode plasma or both of these. Moreover,

VF (A)	Hot Cathode source β	$\tau_1(ms)$	$\tau_2(ms)$	Microwave Source $\tau_0(ms)$	β	$\tau_1(ms)$	$\tau_2(ms)$
0	0.9433	0.287	19.2	0.214	0.9337	0.021	11.3
40	0.9052	0.422	9.1	0.192	0.9198	0.045	4.9
160	0.8767	0.461	8.8	0.771	0.9380	0.108	3.08
-160	0.8327	0.589	10.1	0.291	0.9456	0.049	7.91

Table 6.1: Table showing the confinement time for Hot cathode and Microwave source for different VF current. The hot cathode source has density gradient and strong poloidal flow but Microwave source have neither of these. The τ_0 is the algebraic fall time for Microwave source and rest of the time scales are due to exponential fall.

a suitable function to fit the fall of the density for ECR plasma is yet to be determined and the possible reason for this algebraic fall needs to be investigated.

6.7 Unresolved issues

- Reason for the existence of broadband for -160 A spectrum is not known yet.
- Nature of mode for 160 A for the hot cathode source could not be determined yet.
- Possible reason for the unusual fall of the density for the ECR plasma is not known yet.
- Mechanism by which poloidal flow of the plasma affects the confinement is not known yet.

6.8 Summary

In the present Chapter, we discussed the results of the hot cathode plasma at 750 G of toroidal field strength and compared with the ECR plasma profiles discussed in Chapter-5 for similar experimental conditions. The major difference between these two plasmas is the presence of a strong zeroth order poloidal flow for the hot cathode produced plasma. We observed that the presence of poloidal flow controls the quasi-static equilibrium and fluctuations in an SMT as discussed in Chapter-4. Apart from the absence of poloidal flows in the ECR plasma, the plasma density of the ECR plasma is around 5-8 times less than of the hot cathode plasma for similar experimental conditions. As discussed in Sec. 6.3, the reason for high density in the hot cathode plasma could be due to the lower ionization rate for "O" mode Microwave.

Moreover, it has also been observed that the gradients in the density profiles, which are free energy sources for various instabilities are weaker as compared to the hot cathode plasma. Due to which, it has been estimated that the outboard side of the hot cathode plasma is dominated by the presence of R-T instability, whereas for the ECR plasma drift-interchange instability is present. The relative fluctuation in density and potential is found to be much less in case of the ECR plasma as compared to the hot cathode plasma. Due to the presence of the poloidal flows, shear effects are dominant for the hot cathode plasma, which is absent in the ECR plasma.

Furthermore, a comparative study of the particle confinement time for both the sources has been performed using the afterglow method to study the effect of the poloidal flow on the confinement in an SMT. It was found that the nature of density fall as soon as respective sources are switched off is quite different for both the sources. The hot cathode shows usual exponential fall of the density with two fall times known as fast and slow confinement time. The confinement time for hot cathode source increases with an increase in the VF current, even for long $\bar{L}_c$, which could be due to the presence of strong poloidal flow. However, for ECR plasma the initial fall of the density is found to follow the algebraic nature and subsequent fall is exponential. The reason for this unusual trend is not known yet. The confinement time for the ECR plasma increases with a decrease in $\bar{L}_c$. This is consistent with the Nakao's model [6] of the reduction of E_z^{res} with an increase in VF current or decrease in $\bar{L}_c$.

The major findings of the present Chapter are listed as follows:

- The plasma produced by the hot cathode source has an inherent zeroth order radial electric field which provides a strong poloidal rotation to the plasma.
- To study the role of poloidal flows on plasma properties, a comparative study has been performed using both the hot cathode plasma source and the ECR source for similar experimental conditions like for the same toroidal and vertical field strength and the same working pressure.

- It has been observed that the density for ECR produced plasma is around 5-8 times less than that of hot cathode produced plasma.

- Moreover, the gradients in the density profiles for the hot cathode source are strong enough to trigger R-T instability on the outboard side, whereas for the ECR plasma, drift-like modes are dominant.

- On comparing the estimation of particle confinement using afterglow method for both the sources, it has been observed that the fall of the density after the source is switched off is exponential for hot cathode source and linear followed by exponential for the ECR plasma.

- The confinement time for both kinds of plasma found to increase with an increase in VF current or with a decrease in $\bar{L}_c$.

- The reason for linear fall for the ECR plasma is not yet clear.

In the Chapter-5 and Chapter-6, the ECR and hot cathode plasmas have been characterized for various VF currents. In the Chapter-7, we will discuss a surprising observation of the GAM-like mode, perhaps the first time in an SMT for the ECR plasma and VF current of 160 A, which was not discussed in Chapter-5.

7

Observation of high frequency Geodesic Acoustic-like Mode in a Simple Toroidal Plasma

7.1 Introduction

In Chapter-5, we discussed the ECR plasma profiles and non-linear interaction may lead to the generation of entirely different fluctuating mode. Moreover, details of the observed mode for VF current of 160 A has not been addressed in Chapter-5. Two modes were observed for the mentioned case and one of them turns out to be a Geodesic Acoustic-like Mode. In the present Chapter, we will discuss the details of the observed GAM-like mode in an SMT observed perhaps the first time. To begin with, let us try to understand what is a Geodesic Acoustic Mode or GAM.

Geodesic Acoustic Modes (GAMs) are pressure oscillations supported by plasma compressibility in a toroidal magnetic geometry where average geodesic curvature provides a restoring force. GAMs exhibit top bottom anti-symmetry in density fluctuations and potential fluctuations are nearly independent of the poloidal angle. GAMs were first predicted as oscillating zonal flows [73] and are believed to regulate turbulence in Tokamaks [11]. GAMs in Tokamak can be driven unstable by non-linear Reynolds Stress [74], parametrically driven by drift waves [75] and linearly driven unstable by suprathermal ions [76, 77]. A GAM can be a continuum mode i.e, the frequency and amplitude of the mode can vary locally [78] or can be a discrete global mode [79] or can be a discrete eigen-mode, embedded in a continuum [80]. GAMs can interact with several background modes as they are large scale low frequency fluctuation. For example, a possible up-shift of GAM frequency due to background plasma fluctuations have also been reported [12].

Let us consider a quasi-neutral plasma in a toroidal curved magnetic field given as $\vec{B} = \frac{B_0 R_0}{R}\hat{\Phi}$ and it is always axis-symmetric i.e, toroidal mode number, $n = 0$, where B_0 is the toroidal field strength at the major radius, R_0. Let us perturb the plasma and the perturbed radial electric field is $\vec{E}_1$, therefore, perturbed velocity is given as $\vec{v}_1 = \vec{E}_1 \times \vec{B}/B^2$. As we know, in a curved magnetic field, plasma is compressible. Therefore

$$\vec{\nabla}.\vec{v}_1 = 2\frac{\vec{E}_1 \times \vec{B}}{RB^2}.\hat{R} \tag{7.1}$$

Now transforming the co-ordinates from the Cylindrical (R, Φ, Z) to the Toroidal (r, θ, ϕ) using the transformation, $R = R_0 + rcos\theta$, $Z = rsin\theta$ and $\Phi = -\phi$ see Fig. 2.1(b), we get

$$\hat{R} = \hat{r}cos\theta - \hat{\theta}sin\theta \tag{7.2}$$

where second term $\hat{\theta}sin\theta$ is called Geodesic term. Considering $\vec{E}_1$ to be purely radial, implies, $m = 0, n = 0$ for electric field as well as for the potential fluctuations (where m and n are poloidal and toroidal mode numbers respectively). Because of the radial nature of electric field fluctuation Eqn. 7.1 modifies as follows:

$$\vec{\nabla}.\vec{v}_1 = 2\frac{E_1}{RB}sin\theta \tag{7.3}$$

As is known, the continuity equation for the perturbed quantities is given as

$$\frac{\partial n_1}{\partial t} + n_0 \nabla.\vec{v}_1 = 0 \tag{7.4}$$

where n_0 is the equilibrium plasma density and n_1 is the perturbed density. Now using Eqn. 7.3 into Eqn. 7.4, we obtain

$$\frac{\partial n_1}{\partial t} = -\frac{2n_0 E_1}{BR}sin\theta \tag{7.5}$$

Eqn. 7.5 implies that n_1 goes as $sin\theta$ or $m = 1$. Now using perturbed equation of state, perturbed pressure is given as $p_1 = \frac{\gamma p_0}{n_0}n_1$, where p_0 is the equilibrium pressure and γ is the adiabatic constant. The equation of motion is given as

$$\rho_0 \frac{\partial v_1}{\partial t} = j_1 \times \vec{B} - \frac{\gamma p_0}{n_0} \nabla n_1 \tag{7.6}$$

where $\rho_0 = m_0 n_0$ is the mass density, $m_0 \approx M_i$ is the reduced mass of the plasma (mass of the ion, M_i) and j_1 is the perturbed current density. Taking the time derivative of Eqn. 7.6 and averaging over θ gives

$$\frac{\partial^2 v_1}{\partial t^2} = -2 \frac{\gamma p_0}{\rho_0 R^2} v_1 = -\omega_0^2 v_1 \tag{7.7}$$

where $\omega_0^2 = 2\frac{c_s^2}{R^2}$ is the frequency of the Geodesic Acoustic Oscillation or Mode (GAM), $c_s^2 = \frac{\gamma p_0}{\rho_0} = \frac{K_B T_e}{M_i}$. is the ion acoustic velocity. The frequency of the GAM mode is given as $f_{GAM} = \frac{\sqrt{2} c_s}{2\pi R}$.

Therefore, one can confirm that GAM can be excited by the pressure fluctuations accompanied by fluctuation in radial electric field in a geodesic curvature.

In this Chapter, we report a simple yet surprising experimental finding, perhaps the first time, of the observation of high frequency Geodesic Acoustic like (GAM-like) mode in a simple toroidal device (SMT), which unlike Tokamak, has no zeroth order toroidal current (q$\rightarrow \infty$, where q is magnetic safety factor).

In our present work, we find a global, discrete frequency mode with $n = 0$, $m = 1$, top bottom symmetry for density fluctuation and n=0, $m \geq 0$ for potential fluctuation, which is driven by the non-linear interaction of a unstable ($m = 0, n = 0$) interchange like mode with itself. The real frequency of the GAM-like mode is found to be $f_{GAM-like} = A f_{GAM}$, where scaling factor $A \sim 3$, $c_s = \sqrt{\bar{T}_e / M_i}$ is the ion acoustic speed, R is the major radius $\bar{T}_e$ is mean electron temperature. As our plasma is collision-less i.e., $\nu_{en}/\omega_{ce} << 1, \nu_{in}/\omega_{ci} < 1$, (where ν_{en}, ν_{in} are electron neutral and ion neutral collision frequency respectively and ω_{ce}, ω_{ci} are gyration frequency of the electron and ion respectively) and measured $k_\phi \simeq 0$, this self excited GAM-like mode is found to be undamped. Furthermore, a single discrete frequency is found, which is independent of the radial location, thus indicating a discrete, global, eigenmode like structure for this high frequency GAM-like mode. This upshift in GAM frequency is shown to be due to interaction of GAM-like mode with background fluctuations [12]. For different ion masses, the experimentally observed frequency of the GAM-like mode is found to scale linearly with $1/\sqrt{M_i}$, where M_i is the ion mass.

7.2 Experimental setup

The GAM-like mode has been observed in BETA for the Microwave plasma described in Chapter-5. As discussed in Chapter-4, the residual E_z can be reduced by the application of an external vertical magnetic B_v field [6], such that the toroidal parallel connection length for electrons is reduced, facilitating further reduction in E_z, which in turn is found to lead to a quasi-stationary equilibrium. The GAM-like characteristics have been observed after applying VF current of 160 A, which provides around 12 G of an external vertical field at the minor axis. For this value of B_v, the field lines are widely open and make around 4 turns before hitting the limiter or wall [63]. The applied vertical magnetic field B_v varies as a function of (R, Z)- weaker function of R as compared to Z, where R and Z are radial and vertical distances respectively in cylinderical coordinates. As it is well known, a non uniform vertical field provides non-uniform helical pitch at a given R surface. This results in a non-zero average geodesic curvature in a current-less toroidal device (geodesic curvature is expected to be zero for helical field with uniform pitch). The working pressure is 1.0×10^{-4} torr of different gases, with the ionization efficiency of almost 1%. As discussed earlier, for this working pressure and toroidal magnetic field, the plasma is found to be collision-less as $\nu_{en}/\omega_{ce} << 1, \nu_{in}/\omega_{ci} < 1$.

To measure the GAM-like characteristics, we mount a pair of two tip Langmuir probes as per the arrangement shown in Fig. 7.1. The two tips in each of the Top Probe (TP) and Bottom Probe (BP) are separated by 4 mm. While the first tip of each probe measures the floating potential fluctuation with respect to the grounded wall, the second tip provides density fluctuation. Plasma center is shifted from the vessel center, as shown in Fig. 7.1, by approximately 3 cm towards the outboard side. Therefore probes TP and BP are mounted at $r = +3$ cm from the vessel major radius R_0. Probes TP and BP can be moved along the equatorial plane. To measure toroidal mode number n, two radial probes R_1 and R_2 are mounted at $Z = 0$ plane at a nearly similar radial location and are separated toroidally by almost 120^o simultaneous measurement of density and potential fluctuation are obtained at two toroidal locations. The tip length for each probe is nearly 4 mm and probe separation is also 4 mm.

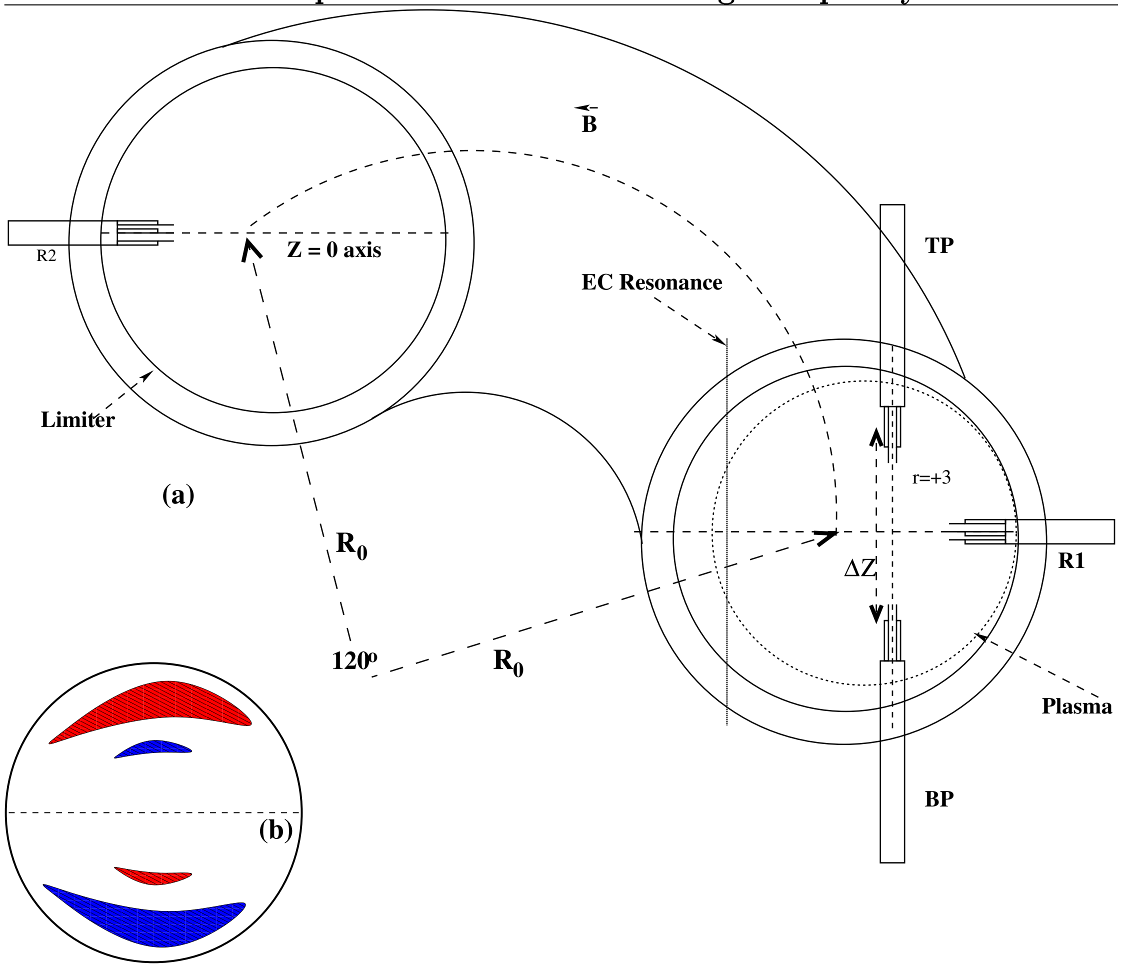

Figure 7.1: (a) A schematic showing BETA device and diagnostics. The probe assembly to measure toroidal and poloidal mode numbers is shown. The ECR region is shown by a vertical line on the inboard side. The plasma region is shown by the dashed circle. The TP and BP are the top and bottom two tips Langmuir probe respectively measuring relative phases in density and potential fluctuations. These TP and BP are movable across Z-axis. The probe assembly R_1 and R_2 are two radial probes mounted at two different toroidal locations supported by a toroidal angle of almost 120^o, to measure toroidal phase for density and potential fluctuation to estimate toroidal mode number "n". (b) A schematic of GAM-like instantaneous density fluctuation in the poloidal cross section of a toroidal device is shown. Here red and blue colors indicate compression and expansion of plasma due to GAM phase velocity respectively.

7.3 Experimental measurements

Using the method discussed in Sec. 7.2, an experimental measurement of GAM-like mode has been performed for Neon, Argon and Krypton plasmas. However, first of all, we will discuss the results for the Argon plasma in detail, followed by the significance of the variation of ion mass on nature on the observed GAM-like mode.

7.4 Argon plasma profiles

The radial profiles of mean density ($\bar{n}_0$) and mean electron temperature ($\bar{T}_e$) are shown in Fig. 7.2(a), with peak density of 5×10^{16} m^{-3} and peak temperature of around 3.5 eV respectively. It can be observed that mean density profile has a weak gradient from r=+1 cm to r = +7 cm, followed by a region of the increased gradient. The mean temperature profile is almost flat from r = -3 cm to r = +7 cm and the peak in the electron temperature lies in the EC resonance at r=-6 cm, shown by vertical lines in Fig. 7.1 and Fig. 7.2. The radial profile of mean plasma potential (shown in Fig. 5.1(d)) is also nearly flat, which implies absence of any significant "equilibrium" radial electric field, $\vec{E}_0$ present. The Mach probe measurements (Fig. 5.7) suggest that the maximum net poloidal flow present is $\sim 0.15c_s$ or less and the net flow in the toroidal direction is well below the noise level of the Mach probe.

The spectrogram of the density fluctuation shown in Fig. 7.3(a), demonstrates that there are two strong frequencies in the density fluctuation corresponding to two discrete modes. The dominant mode is found to be at 1.7 kHz and the second mode is 3.4 kHz. As shown in Fig. 7.2(a) density and temperature profiles have weak gradients on the outboard side. The density and electron temperature length scales are found to be large enough that the plasma is stable to Rayleigh Taylor (R-T) instability [37], which is commonly found in SMTs. As discussed earlier, the equilibrium radial electric field $\vec{E}_0$ is very small and plasma is collision-less. Thus the Simon Hoh (SH) and Modified Simon Hoh (MSH) instabilities are found to be stable as the basic instability condition $\vec{E}_0.\vec{\nabla}\bar{n}_0 > 0$ is not satisfied on the outboard side in our case. The electron diamagnetic drift frequency, $f_{De} = \omega_{De}/(2\pi) = k_B T_e/(2\pi e B L_n a)$, where $L_n = -n_0/\nabla n_0$ is density gradient scale

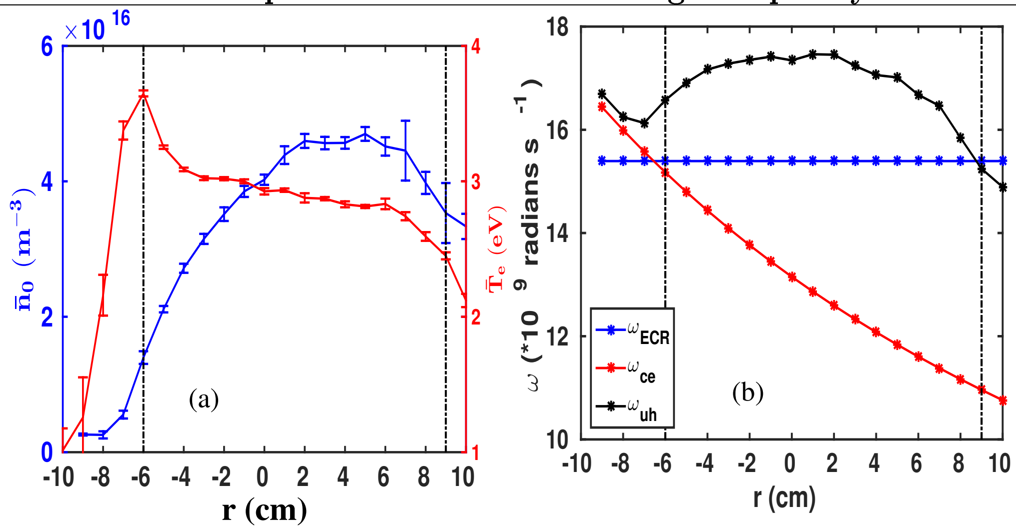

Figure 7.2: (a) The radial profile of mean density ($\bar{n}_0$) and mean electron temperature ($\bar{T}_e$) and (b) the upper hybrid frequency $\omega_{UH}(r) = (\omega_{ce}^2(r)+\omega_{pe}^2(r))^{1/2}$ for VF current of 160 A is shown. The electron gyration frequency and plasma frequency are denoted as $\omega_{ce}(r)$ and $\omega_{pe}(r)$ respectively. The EC resonance is shown by a vertical line in (a), which coincides with the peak in the location of electron temperature. The location of the limiter is shown by a vertical line at +9 cm radial location in both (a) and (b). In (a) the left y-axis shows the radial variation of the density and the right y-axis is for electron temperature. It can be observed that the gradients in $\bar{n}_0$ and $\bar{T}_e$ are weak for the region of +1 cm to +6 cm, then scale length changes beyond +7 cm.

length, measured at r=+7 cm.

For this density and electron temperature, f_{De} is found to be close to 1.7 kHz and cross phase between density fluctuation and potential fluctuation is $\sim \pi$ (Fig. 7.5(a)) which is characteristics of an interchange type mode. Both modes shows characteristics of an interchange like mode except close to the minor axis. Also, the toroidal phase difference for 1.7 kHz peak, shown in Fig. 7.7, is close to zero. Hence we attribute the dominant 1.7 kHz peak to an unstable interchange like mode. However, the exact nature of the driver mode is not known. A bispectrum analysis shown in Fig. 7.4 clearly demonstrates that the 3.4 kHz mode is generated by the non-linear interaction of 1.7 kHz i.e, the interchange like mode with itself. This is corroborated by the spectrogram in Fig. 7.3(a), where 3.4 kHz peak appears as soon as 1.7 kHz build up to its full amplitude. Presence of interaction of 1.7 kHz and 3.4 kHz with low amplitude background fluctuation can be observed in the Fig. 7.4 beyond 20 kHz. This interaction may lead to an upshift in the frequency

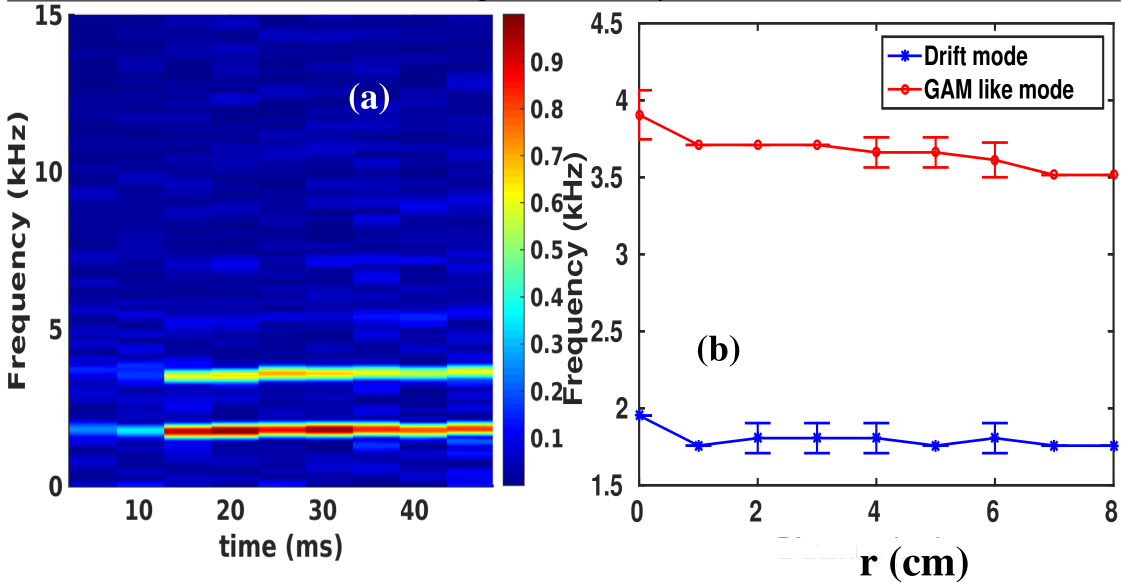

Figure 7.3: (a) Spectrogram of density fluctuation at +5 cm and (b) radial variation of two dominant modes. The color-bar in (a) has maximum value 1, as the spectrogram is normalized by the maximum power of the spectrum. The spectrogram in (a), shows the existence of two dominant modes and it can be clearly observed that second mode is excited after the first mode has reached its peak. The sampling frequency for these measurement is 200 kS/s but the plot is zoomed up to 15 kHz for better presentation. The radial variation of mode frequencies in (b) is shown from minor axis to the edge of the limiter on the outboard side. It clearly shows that mode frequencies are nearly constant radially. The error-bars are due to multiple shots taken at one radial location. For some radial distances, the error-bar on frequency is smaller than the marker size of the plot and hence are not visible.

of the GAM-like mode [12]. Also, the real frequency measured at various radial locations shown in Fig. 7.3(b) indicates that the frequencies are nearly constant throughout the radial locations, which demonstrates that the modes are global, discrete modes.

Let us now try to find the poloidal and toroidal mode numbers to determine GAM-like characteristics.

7.5 Determination of GAM-like characteristics

To confirm that the nature of 1.7 kHz peak is interchange like, the poloidal and toroidal phase difference were measured using the probe assembly shown in Fig. 7.1

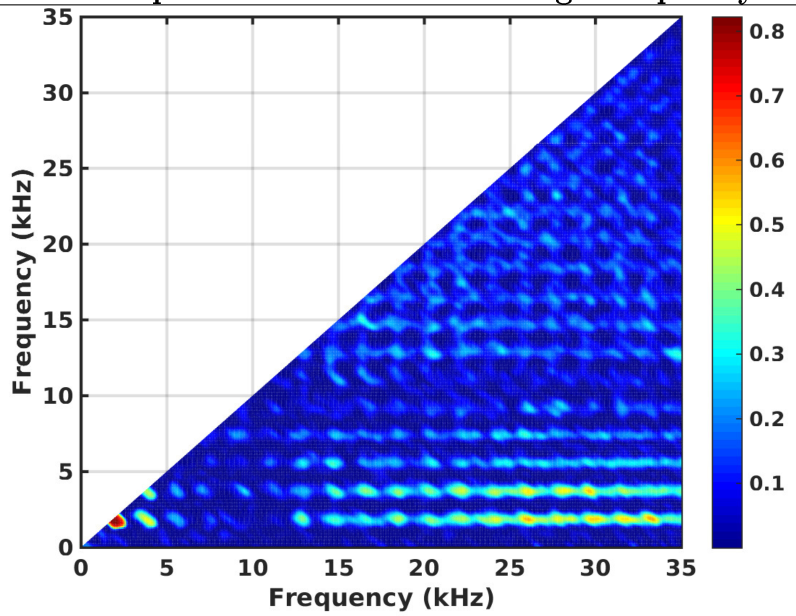

Figure 7.4: Bispectrum for density at r=+5 cm, the peak value of the bispectrum is around 0.8 for the interaction of the 1.7 kHz mode with itself. It implies that the 3.4 kHz peak is due to the self non-linear interaction of the 1.7 kHz. The sampling frequency is 200 kS/s for these measurements but the plot is zoomed up to 35 kHz to have a better look on the interaction. Presence of low amplitude background fluctuations is visible for frequencies beyond 20 kHz.

and the results are presented in Fig. 7.6 and Fig. 7.7. The poloidal variation of phase difference with vertical probe separation ΔZ, for density fluctuation of 1.7 kHz mode (blue curve) is shown in Fig. 7.6(a). The maximum phase difference is found to be approximately 0.3π and coherence is more than 0.8 for all values of ΔZ. Similarly, the toroidal phase difference measured using R1 and R2 probe tips for 1.7 kHz mode (blue curve) for density fluctuation, as shown in Fig. 7.7(a), indicates that the phase difference is well below 0.2π with coherence close to 1. To determine the toroidal mode number, the wavelength from measured phase difference and probe separation Δx i.e, $\lambda_{tor} = \Delta\theta/\Delta x$ is obtained. Estimated λ_{tor} is found to be such that $\lambda_{tor} >> 2\pi R_0$, suggesting toroidal mode number, $n \sim 0$. Similarly, poloidal phase measured experimentally confirms that the poloidal mode number m for 1.7 kHz is m$\sim$ 0. Similarly for 1.7 kHz potential fluctuation, poloidal phase difference (blue curve) shown in Fig. 7.6(b) varies from zero to 0.6π. The toroidal phase difference shown in Fig. 7.7(b), indicates phase difference is well below 0.2π. Therefore, like density fluctuation, potential fluctuation also shows

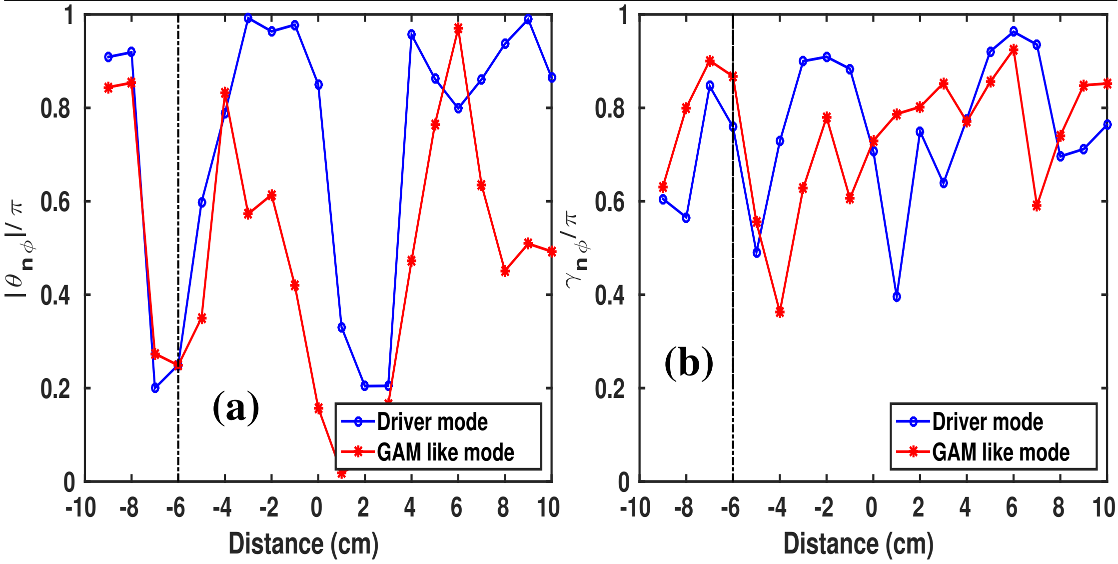

Figure 7.5: Radial profile of (a) cross phase and (b) coherence between density fluctuations measured simultaneously using radial array of probes. Both modes shows characteristics of an interchange like mode except close to the minor axis.

$m = n = 0$ symmetry for 1.7 kHz mode as can be expected for a interchange like mode.

Let us characterize the 3.4 kHz GAM-like mode. The measured poloidal phase difference for density fluctuation shown in Fig. 7.6(a). Phase difference obtained is more than 0.8π for $\Delta Z \geq 10$ cm, with coherence is close to 1 except at $\Delta Z = 2$ cm and $\Delta Z = 10$ cm. Similarly, toroidal phase difference (red curve) shown in Fig. 7.7(a) is close to 0.2π throughout the radial location. It implies density fluctuation shows m=1 for $\Delta Z > 10$ cm, n=0 symmetry. Similarly, the poloidal phase difference of potential fluctuation presented in Fig. 7.6(b) shows that the phase difference is close to 0.3π, but increases to 0.7π for $\Delta Z = 16$ cm, with coherence above 0.6. Toroidal phase difference for 3.4 kHz presented in Fig. 7.7(b), shows that the phase difference is $\sim 0.3\pi$ or less, except at r=5 cm, which is accompanied by low coherence value. Therefore, 3.4 kHz potential fluctuation shows $m \geq 0$, n=0 symmetry. Thus the 3.4 kHz frequency mode, density fluctuation shows the strong GAM-like characteristics but potential fluctuations show weak GAM-like characteristics.

Radial spectrum of $k_r(r)$ measured at $z = 0$ plane shown in Fig. 7.8 indicates that $< k_r\rho_s >_{(r,f)} \sim 1.5$ for 15 kHz $< f <$ 30 kHz background fluctuation in our experiments (See Fig. 7.4). (Here $\rho_s = (M_i\bar{T}_e)^{1/2}/(eB_T)$, M_i is the ion mass and B_T

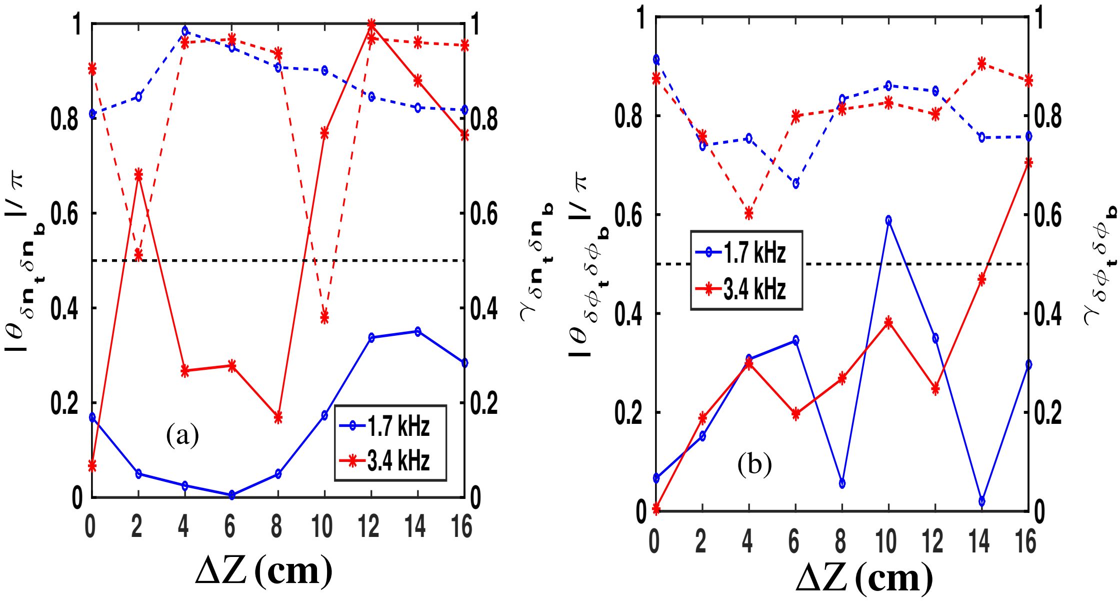

Figure 7.6: Variation of the poloidal phase and coherence for (a) density fluctuation and (b) potential fluctuation using vertical probe assembly with separation ΔZ as shown in Fig. 7.1. The coherence (γ) for each plot is shown on the right y-axis (same color dashed curves), data points with lower coherence i.e, $\gamma \leq 0.5$, may not reliable, shown by horizontal. The phase for density fluctuation for 3.4 kHz is $\sim 0.8\pi$ or more beyond $\Delta Z \geq 10cm$, with $\gamma > 0.8$ and for potential phase varied from 0.2π to 0.7π in the same region. For 1.7 kHz peak for 1.7 kHz, the maximum phase is 0.25π and for potential is 0.6π.

is toroidal field strength). We propose that the experimentally observed up-shift in frequency of the GAM-like mode may be shown to be meaningful if an empirical formula is supposed, namely $f_{GAM-like} = f_{GAM}(1 + \alpha|k_r\rho_s|^2)$. The mathematical form of this empirical formula is motivated by earlier studies [12] where a similar up-shift is proposed due to coupling of a mode to background turbulence, though in the context of Tokamaks. In this empirical formula, the only unknown quantity is α and which is obtained by substituting in values of $f_{GAM-like}$(experimental), f_{GAM}(theoretical) and $< k_r\rho_s >$ (experimental). The resulting value of $\alpha \sim 0.5$. This is an empirical fitting and detailed theoretical explanation is called for.

To further confirm the acoustic like nature of the mode, experiments were repeated for Neon and Krypton plasmas and the results are as follows.

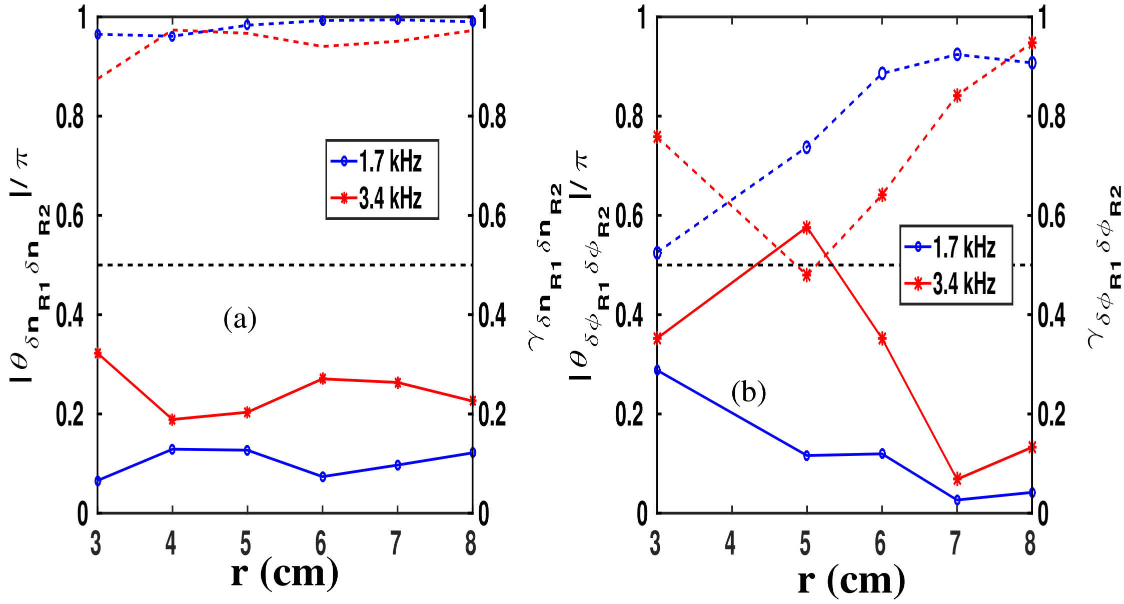

Figure 7.7: Variation of the toroidal phase and coherence for (a) density fluctuations and (b) potential fluctuations measured using radial probe assembly as a function of radial distance, r. The coherence (γ) for each plot is shown on the right y-axis, (same color dashed curves), the horizontal dashed line represents $\gamma = 0.5$. The toroidal phase for density fluctuation for 3.4 kHz is $\sim 0.2\pi$ or less for $\gamma > 0.9$ and for potential phase varies from 0.1π to 0.6π in the same radial region. The phase for potential fluctuation is around 0.7π, at r=+5 cm, however the coherence at this point is $\gamma \leq 0.5$. For 1.7 kHz peak, the maximum phase for density fluctuations is 0.15π and for potential fluctuations is 0.3π.

7.6 Variation of frequency of the GAM-like mode with the ion mass

Mean profiles of plasma density, electron temperature as well as fluctuation for different ion masses have been obtained. The spectrogram of density fluctuation measured at r=+5 cm is shown in Fig. 7.9 for Neon, Argon and Krypton plasmas. In all the three cases, two dominant modes are found, a low frequency interchange mode and a high frequency GAM-like mode. It can be observed that the frequency of two modes varies with the mass of the gas. As discussed in the Manuscript, the GAM-like mode is generated by the non-linear interaction of the dominant mode (identified as drift interchange mode) with itself.

To establish GAM-like properties of the second dominant mode, the toroidal

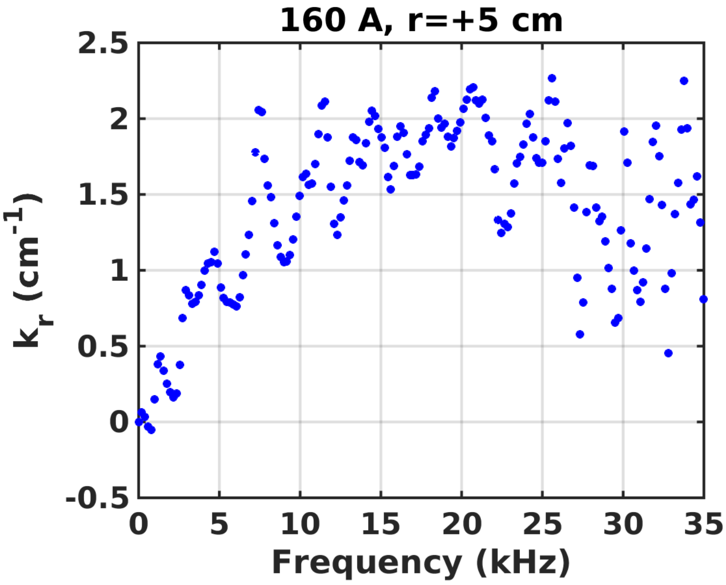

Figure 7.8: Variation of radial wavenumber k_r with the frequency at $r = +5$ cm for Argon gas. It can be observed that $< k_r\rho_s >_{(r,f)} \sim 1.5$ for 15 kHz $< f <$ 30 kHz background fluctuation in our experiments.

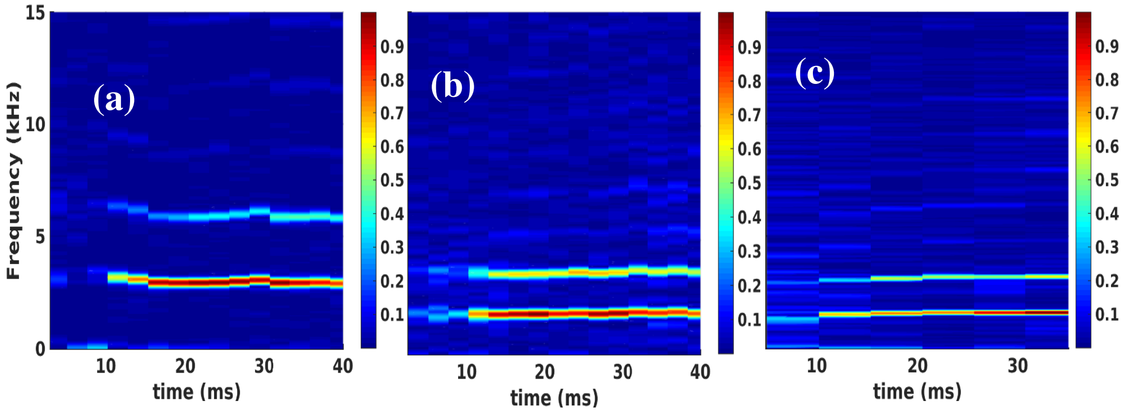

Figure 7.9: A spectrogram of density fluctuations for (a) Neon plasma ($M_i = 20$ amu), (b) Argon plasma ($M_i = 40$ amu) and (c) Krypton plasma ($M_i = 82$ amu) at r=+5 cm. It can be observed that the similar modes exist for all three different gases, however, frequencies vary with the ion mass. The sampling frequency is around 400 kHz, the plots are zoomed to 15 kHz for better representation.

and poloidal mode numbers are measured for Neon and Krypton plasmas using the Top-Bottom probes assembly shown in Fig. 7.1. From Fig. 7.10 it can be observed that a strong GAM-like property exists for density fluctuations for different masses. However, for the potential fluctuations, the GAM-like nature becomes weaker with

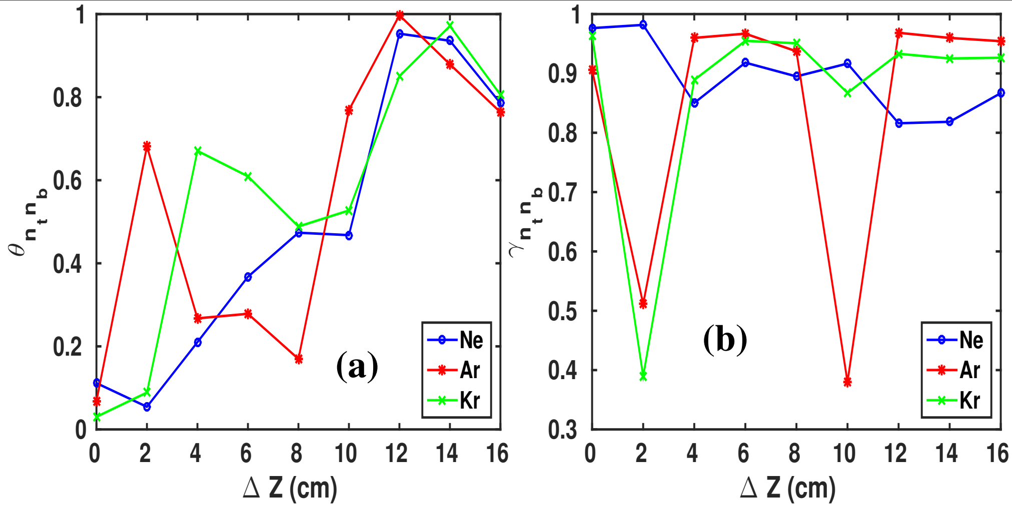

Figure 7.10: Variation of the poloidal (a) phase and (b) coherence of the GAM-like mode of density fluctuations with the vertical separation of the top-bottom probes. The poloidal phase of the density fluctuation is close to π for $\Delta Z > 10$ cm for every species of the gas. It demonstrate that there exist a strong GAM-like property for density fluctuation.

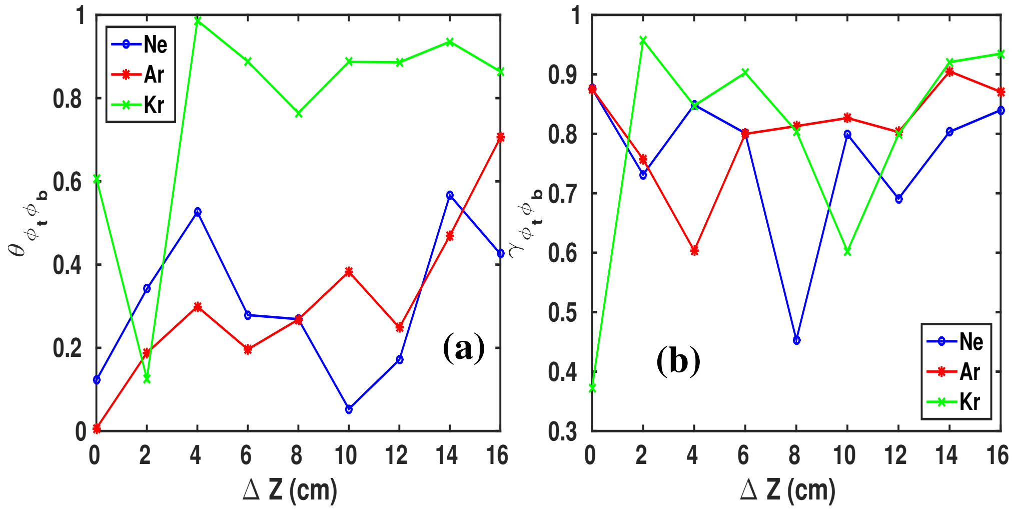

Figure 7.11: Variation of the poloidal (a) phase and (b) coherence of the GAM-like mode of potential fluctuations with the vertical separation of the top-bottom probes. The poloidal phase of the potential fluctuation increases with an increase in the ion mass. It indicates that there exists a weak GAM-like property for potential fluctuation, which gets weaker with an increase in the ion mass.

an increase in the ion mass. The toroidal mode number is found to be close to zero for both density fluctuation as well as for potential fluctuation for all the cases.

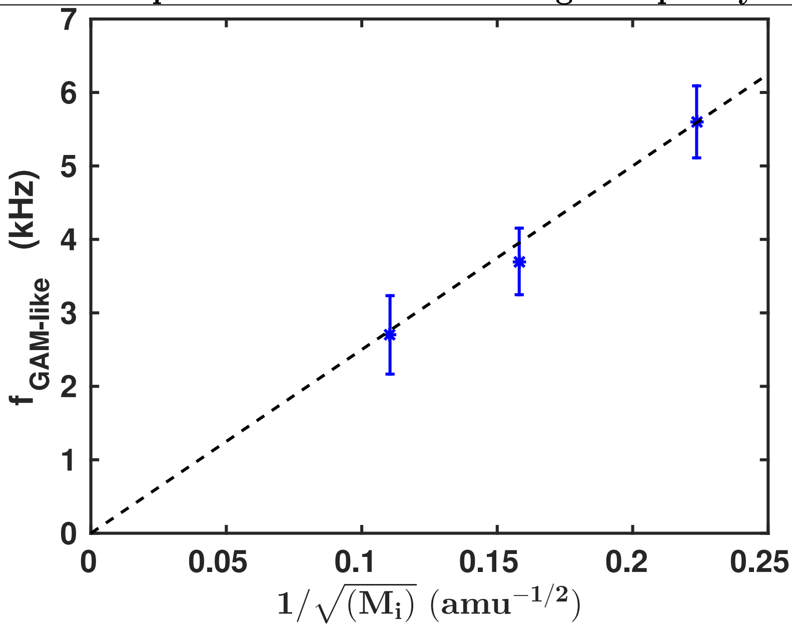

Figure 7.12: Variation of the frequency of the GAM-like mode with ion mass. The error-bars are the resultant of the frequency resolution and shot to shot variation in the frequency and a dashed black line has been added to aid the view. The fitted line has been extrapolated to origin to confirm that no intercept exists for the curve. Thus demonstrating that the frequency of the GAM-like mode, $f_{GAM-like} \propto 1/\sqrt{M_i}$, thus confirming the Acoustic-like nature of the mode.

As shown in Fig 7.12, the observed frequency of the GAM-like mode is found to scale linearly as $1/\sqrt{M_i}$, where M_i is the ion mass, which further strengthens our findings.

7.7 Summary

In summary, we present the first experimental observation of the existence of a high frequency GAM-like mode [12] in a simple toroidal plasma. The frequency of the observed GAM-like mode for Argon plasma is almost three times that of theoretical GAM frequency for an SMT. In our finding, we observe that an unstable $(m = 0, n = 0)$ finite frequency interchange like mode driven unstable by weak equilibrium gradient instability, non-linearly couples with itself to drive the high frequency GAM-like mode [75]. While the density fluctuation shows strong GAM-like signatures, the potential fluctuations exhibit a weak GAM-like symmetry. Measured frequency of the GAM-like mode is found to be independent of the plasma radius, thus demonstrating the global, discrete nature of the mode, while the frequency upshift may be attributed to the interaction of GAM-like mode with background fluctuations. For three different ion masses, the observed frequency of the GAM-like mode is found to scale linearly with $1/\sqrt{M_i}$.

In the Chapter-8, we will conclude our findings of the present Thesis along with some of the future works.

8

Conclusions and future scope

8.1 Conclusions

Magnetically confined plasmas in toroidal devices gained significant importance in the last few decades due to their potential to achieve controlled thermonuclear fusion. However, despite several decades of research, cross-field instabilities and transport still pose challenges. However, due to a complex scheme of magnetic field limits the study of individual instabilities. A simple magnetized toroidal device provides an alternative facility to carry out these studies which are particularly important for Edge/SOL region of the Tokamak. As discussed in Chapter-1, that an SMT serves two purposes: First, it offers a simple and well-diagnosable testbed in which study of the basic physics of plasma instabilities and the associated transport of particles and energy becomes possible. Second, by virtue of its dimensionless parameters and magnetic geometry, it provides a simplified setting in which one may explore one of the most important topics in fusion research namely, the physics of turbulent transport in the edge region of magnetically confined fusion devices such as Tokamaks. Understanding edge-SOL physics in Tokamaks is an important issue because particles and heat transport across the edge region of these machines largely govern the fusion power output of the entire device.

The topology of the toroidal field serves two purposes in a toroidal device, (i) it provides a pathway along the field line to minimize the residual vertical electric field, E_z^{res} created due to the charge separation due to curvature and gradient drift. (ii) determines the minimum parallel wavenumber as provided in Eqn. 1.2, thus controls the nature of instabilities or fluctuation. Therefore, it implies that by the variation of toroidal field topology one can control the nature of quasi-stationary equilibrium [21], transport [4, 18] and confinement in an SMT [6, 7]. Secondly, by the controlled variation of the topology one can control the minimum parallel wavenumber, which further controls the nature of instabilities. It means by simply varying the topology, nature of instabilities can be varied from drift-like to interchange like [16, 25]. The transition to the turbulence regime, characterized as low and high confinements can also be controlled by varying the toroidal field topology [27].

Therefore, the present Thesis demonstrates the strong influence the vertical field and the consequent topology of the toroidal field on the quasi-stationary equilibrium and confinement.

In a magnetized toroidal device, the topology of the toroidal field plays a crucial role in producing and confining a plasma. A proper understanding of the magnetic flux surfaces and error fields or offset in toroidal field often help in improving the performance of the fusion device. In Chapter-3, a novel yet effective method has been discussed to determine the topology of the toroidal field. This technique involves the use of a tiny plasma beam-let generated from a tiny filament and a regular camera. This method also helps us to determine the inherent vertical offset in the toroidal field line even without applying any vertical magnetic field. Moreover, by the application of a particular value of the external vertical field for a fixed toroidal field, we can nearly close the toroidal field or can widely open it in either direction. Furthermore, the alignment of two Langmuir tips using the tiny plasma beam-let is demonstrated, which is an essential method to determine the minimum parallel wavenumber $k_{||}^{min}$. To determine the possible reason of offset in the toroidal field line, a 3-D numerical simulation was performed using EEFI code. The actual co-ordinates of all 16 TF coils (given in Appendix. A) were measured using an electronic co-ordinate displacement machine and these co-ordinates were used as input to the EEFI code to simulate the toroidal field in BETA. Numerical simulation clearly shows that no offset in the toroidal field exist, therefore, it has been concluded that the offset observed during the experiment could be due to the presence of uncompensated lead in the TF coils. The major findings of the **Chapter-3** are listed as follows:

- The topology of the toroidal field is experimentally determined using a simple yet effective method, by using a tiny plasma beam-let and a regular camera.
- An inherent offset in the toroidal field is observed, even without charging the VF coils and the inherent offset is determined to be around 1 G for B_T =220 G.
- It has been demonstrated that the topology of the toroidal field or $\bar{L}_c$ can be varied from very long ($N \sim 180$) to very small ($N \sim 4$) connection length by varying the VF current.
- To determine the minimum parallel wavenumber $k_{||}^{min} = \frac{2\pi}{\bar{L}_c}$, Langmuir probes mounted at the different toroidal location, aligned to the same toroidal field line by using the tiny plasma beam-let.
- $k_{||}^{min}$ has been determined experimentally for different VF currents and found to be in the agreement with the theoretical values.
- Further to determine the cause of the opening of the toroidal field line, the co-ordinates of TF coils is measured using ECDS equipment and these co-ordinates are used as input for performing a numerical simulation using EFFI code.
- The results of numerical simulation confirm that the misalignment of TF coils cannot result in opening up of a toroidal field line. Therefore, the observed opening is attributed to the presence of uncompensated leads in the TF coils.

As discussed in Chapter-3, the topology of the toroidal field can be controlled by the application of an external vertical field applied using one pair of VF coils. It has also been discussed that for some particular value of VF current the field line is nearly closed and traverse a very long path before hitting the limiter or the wall, known to have longest mean parallel connection length $\bar{L}_c$. Similarly, for some VF current value, the toroidal field line is widely opened and hence has a shorter value of $\bar{L}_c$. In the Chapter-4, it has been demonstrated that controlling the topology does further control the nature of quasi-static equilibrium, fluctuation and poloidal flows. Chapter-4 has been divided into three parts, in Part-I, the magnitude of the external vertical field is varied for fixed toroidal field strength.

The VF current has been varied gradually to study the effect of $\bar{L}_c$ on the plasma properties. Interestingly, for nearly closed field lines, which are characterized by large values of $\bar{L}_c$, it is found that flute like coherent modes are observed to be dominant and is accompanied by large poloidal flows. For small values of $\bar{L}_c$, the mean density on the high field side is seen to increase and the net poloidal flow reduces while turbulent broadband in the fluctuation spectrum is observed. Upon a gradual variation of $\bar{L}_c$ from large to small values, continuous changes in mean plasma potential and density profiles, fluctuation, and poloidal flows demonstrate that in a simple toroidal device there exists a strong relationship between $\bar{L}_c$, flows, and fluctuations. The net flow measured is found independent of the direction of $\bar{L}_c$, but an asymmetry in the magnitude of the flow is found.

In the Part-II, both B_T and B_v are varied simultaneously in three fixed ratios, namely large $\bar{L}_c$, intermediate $\bar{L}_c$ and small $\bar{L}_c$. As known, E_z^{res} can be reduced by the application of B_v. Thus the plasma properties may be expected to depend strongly on reducing or minimizing this residual vertical electric field. Hence $\bar{L}_c$ can be expected to strongly influence both the quasi-static equilibrium and fluctuations in a simple magnetized torus. It has been observed that the loss of plasma density on the outboard side reduces for shorter $\bar{L}_c$. As $\bar{L}_c$ also determines the minimum parallel wavenumber, $k_{||}^{min}$, the nature of fluctuations changes significantly with $\bar{L}_c$. For example, it is shown that for large $\bar{L}_c$ values, there are only a few dominant modes followed by turbulent fluctuations, whereas for shorter $\bar{L}_c$ values, there exist broadband for the turbulent fluctuation. As the nature of equilibrium and fluctuation varies with $\bar{L}_c$, the profile of poloidal flows also shows a strong dependence on $\bar{L}_c$, particularly for shorter $\bar{L}_c$, where net poloidal flow reduces significantly on the inboard side. Experiments for a given $\bar{L}_c$ (small, intermediate and large) performed for three different ratios of (B_v, B_T) pairs clearly demonstrate the role of $\bar{L}_c$ in the confinement and stability of the plasma in an SMT.

In the Part-III, the particle confinement is estimated experimentally for various VF currents for three different toroidal magnetic fields. It has been observed that the particle confinement increases with an increase in the VF current or with a decrease in $\bar{L}_c$.

The major findings of the **Chapter-4** are listed as follows:

- It has been seen that $\bar{L}_c$ strongly affects the mean plasma parameters such as density, electron temperature, plasma potential and floating potentials.

Density varies non-monotonically with $\bar{L}_c$ and strong dependence on $\bar{L}_c$ can be seen in plasma potential profiles.

- Nature of fluctuation changes significantly with $\bar{L}_c$, as it can be seen that for large $\bar{L}_c$, few modes are present and for very small $\bar{L}_c$ a broad band or turbulence can be seen, but for some cases where $\bar{L}_c$ is enough to sustain fluctuations, several coherent modes are present with strong non-linear interactions among them.

- Nature of flow also appears to be strongly affected by $\bar{L}_c$. For example, for very large $\bar{L}_c$ the increase in net poloidal flow and mean flow can be observed but for very small $\bar{L}_c$ both flows reduce significantly. Fluctuation driven flow also seems to be affected by $\bar{L}_c$, particularly on LFS.

- Equilibrium and fluctuation parameters are found to be affected strongly by poloidal flows and as nature of poloidal flows changes with $\bar{L}_c$ and it reflects in these properties.

- Poloidal flows generate velocity shear which can be confirmed by comparing angular velocity of poloidal flows to diamagnetic velocity.

- The electron pathway along B_T facilitates the reduction in E_z^{res} and more effective for shorter values of $\bar{L}_c$, qualitatively consistent with Eqn. 1.1.

- It has been seen that $\bar{L}_c$ strongly affects the mean plasma parameters such as density and plasma potential. Density varies non-monotonically with $\bar{L}_c$ and strong dependence on $\bar{L}_c$ can be seen in plasma potential profiles.

- Nature of fluctuation changes significantly with $\bar{L}_c$, as it can be seen that for large $\bar{L}_c$, few modes are present and for very small $\bar{L}_c$ a broad band or turbulence can be seen, but for some cases where $\bar{L}_c$ is enough to sustain fluctuations, several coherent modes are present with strong non-linear interactions among them.

- Nature of flow also appears to be strongly affected by $\bar{L}_c$. For example, for very large $\bar{L}_c$ the increase in net poloidal flow and mean flow can be observed but for very small $\bar{L}_c$ both flows reduce significantly. Fluctuation driven flow also seems to be affected by $\bar{L}_c$, particularly on LFS.

- Attempt has been made to identify the instabilities for all the values of B_v, it is generally found that while the outboard side is dominated by interchange-like modes, the inboard side is found to be susceptible to shear driven interchange modes, drift-interchange modes and resistive-drift modes.

- Nature of instabilities is strongly dependent on $\bar{L}_c$ and poloidal flows.

- Equilibrium and fluctuation parameters are found to be affected strongly by poloidal flows and as nature of poloidal flows changes with $\bar{L}_c$ and it reflects in these properties.

- The particle confinement of the hot cathode produced plasma has been estimated using afterglow method with variation in VF current for different B_T values.

- The fall of the density shows the exponential fall with two different fall time τ_1 and τ_2, which are called as fast and slow confinement time respectively.

- Both τ_1 and τ_2, increases with an increase in VF current or a decrease in $\bar{L}_c$.

The experimental study performed in Chapter-5 provides an insight into the variation of toroidal field topology for an ECR produced plasma. As discussed in Chapter-4, the plasma produced by the hot cathode source has a zeroth order radial electric field due to a bias of the filament with respect to the vessel wall. The radial electric field provides a strong poloidal rotation to the plasma, which further controls the nature of the plasma properties. Moreover, the region around the minor axis is contaminated by the presence of high energy electrons. Therefore, to study the effect of poloidal flows on the plasma properties and avoid the problem of high energy electrons a Microwave based ECR plasma source has been developed and used for plasma production. The frequency of the launched Microwave is around 2.45 GHz, with averaged launched power is around 1 kW, launched in "O" mode. The plasma produced from ECR source has a very weak zeroth order radial electric field and hence the poloidal flow is not significant. The topology of the toroidal field is varied by the application of the vertical magnetic field for a fixed toroidal field strength of 750 G at the minor axis.

As expected, the value of density increases for the small value of $\bar{L}_c$ could be due to the reduction of E_z^{res}. Moreover, the gradient in the density profile is very weak to generate R-T instability on the outboard side. However, a gradient in the electron temperature profile exist for 0 A and 40 A VF values, which gets weaker for 160 A and -160 A i.e, for a small value of $\bar{L}_c$. The transient nature of modes have been observed for 0 A and 40 A VF currents and reason for them is not known yet. The drift-interchange mode has been observed for 160 A and -160 A VF values.

The major findings of the **Chapter-5** are listed as follows:

- A newly developed Microwave based ECR source with a frequency of ~2.45 GHz, with averaged power of around 1 kW, launched from the outboard side in "O" mode has been used to produce plasma in an SMT, BETA.

- The primary ionization takes place due to EC resonance at r=-6 cm and the unspent energy, reflects from the vessel wall which causes the change in its polarization and a secondary ionization occurs due to the upper hybrid resonance (UHR).

- The radial location of UHR varies with the applied VF current or $\bar{L}_c$, which significantly affects the density profile.

- The equilibrium and fluctuation plasma profiles have been characterized for different values of externally applied vertical magnetic field.

- It has been observed that the magnitude of density increases for widely opened field lines or small values of $\bar{L}_c$, which could be due to effective reduction of E_z^{res} [6].

- The gradient in density profiles for all values of $\bar{L}_c$ found to be weak enough to generate R-T instability on the outboard side. However, it can still generate drift-like modes.

- The transient nature of modes have been observed for 0 A and 40 A VF currents and reason for them is not known yet.

A comparative study to determine the role of poloidal flows on quasi-static equilibrium, fluctuation and the particle confinement in an SMT has been discussed in Chapter-6. To achieve this, two different plasma sources namely, the hot cathode source and the ECR plasma source have been used. The experimental conditions like working pressure, the toroidal field strength, the vertical field strength etc., have been kept the same for both kinds of plasmas. Apart from the absence of poloidal flows in the ECR plasma, the plasma density of the ECR plasma is around 5-8 times less than of the hot cathode plasma for similar experimental conditions. This could be attributed to the fact that the “O” mode polarization is not the most efficient method for exploiting the ECR coupling.

Moreover, it has also been observed that the gradients in the density profiles, which are free energy sources for various instabilities are weaker as compared to the hot cathode plasma. Due to which, it has been estimated that the outboard side of the hot cathode plasma is dominated by the presence of R-T instability, whereas for the ECR plasma drift-interchange instability is present. The relative fluctuation in density and potential is found to be much less in case of the ECR plasma as compared to the hot cathode plasma. Due to the presence of the poloidal flows, shear effects are dominant for the hot cathode plasma, which is absent in the ECR plasma.

Furthermore, a comparative study of the particle confinement time for both the sources has been performed using the afterglow method to study the effect of the poloidal flow on the confinement in an SMT. It was found that the nature of density fall as soon as respective sources are switched off is quite different for both the sources. The hot cathode plasma shows usual exponential fall of the density with two fall times known as fast and slow confinement time. The confinement time for hot cathode source increases with an increase in the VF current. However, for ECR plasma the initial fall of the density is found to follow the algebraic nature and subsequent fall is exponential. The reason for this unusual trend is not known yet. The confinement time for the ECR plasma increases with a decrease in $\bar{L}_c$. This is consistent with the Nakao's model [6] of the reduction of E_z^{res} with an increase in VF current or decrease in $\bar{L}_c$.

The major findings of the **Chapter-6** are listed as follows:

- The plasma produced by the hot cathode source has an inherent zeroth order radial electric field which provides a strong poloidal rotation to the plasma.

- To study the role of poloidal flows on plasma properties, a comparative study has been performed using both the hot cathode plasma source and the ECR source for similar experimental conditions like for the same toroidal and vertical field strength and the same working pressure.

- It has been observed that the density for ECR produced plasma is around 5-8 times less than that of hot cathode produced plasma.
- Moreover, the gradients in the density profiles for the hot cathode source are strong enough to trigger R-T instability on the outboard side, whereas for the ECR plasma, drift-like modes are dominant.
- On comparing the estimation of particle confinement using afterglow method for both the sources, it has been observed that the fall of the density after the source is switched off is exponential for hot cathode source and linear followed by exponential for the ECR plasma.
- The confinement time for both kinds of plasma found to increase with an increase in VF current or with a decrease in $\bar{L}_c$.
- The reason for linear fall for the ECR plasma is not yet clear.

In Chapter-7, using ECR plasma and external B_v, we reported, a simple yet surprising experimental finding, perhaps the first time, of the observation of high frequency, discrete and global Geodesic Acoustic like (GAM-like) mode in a simple magnetized torus (SMT), which unlike Tokamak, has no zeroth order toroidal current (q$\rightarrow \infty$, where q is the magnetic safety factor).

The frequency of the observed GAM-like mode for Argon plasma is almost three times that of theoretical GAM frequency for an SMT. In our finding, we observe that an unstable (m=0, n=0) drift-interchange mode driven unstable by weak equilibrium gradient instability, non-linearly couples with itself to drive the high frequency GAM-like mode. While the density fluctuation shows strong GAM-like signatures, the potential fluctuations exhibit a weak GAM-like symmetry. Measured frequency of the GAM-like mode is found to be independent of the plasma radius, thus demonstrating the global, discrete nature of the mode, while the frequency upshift may be attributed to the interaction of GAM-like mode with background fluctuations. For three different ion masses, the observed frequency of the GAM-like mode is found to scale linearly with $1/\sqrt{M_i}$.
The major findings of the **Chapter-7** are listed as follows:

- A high frequency, global, discrete GAM-like mode has been observed, perhaps the first time in an SMT.

- The mode is generated due to the non-linear interaction of the drift-interchange mode with itself.

- The frequency of the observed mode is around three times than the theoretical frequency of the GAM mode.

- The density fluctuation shows strong GAM-like characteristics as $m = 0, n = 0$, however, potential fluctuation shows weak GAM-like properties with $m \geq 0, n = 0$.

- The frequency of the observed mode is found to scale linearly with $1/\sqrt{M_i}$, which confirms the Acoustic nature of the observed mode.

In summary, determination of magnetic field topology by a novel yet effective method, varying the topology to further control the nature of quasi-static equilibrium, fluctuation, flow and confinement in a simple magnetized torus has been demonstrated. The topology of the toroidal field has been varied by the controlled variation of the toroidal field and the vertical magnetic field. It has been demonstrated that the plasma properties strongly depends on the topology of the toroidal field. Furthermore, to study the role of poloidal flows on the plasma properties in detail, a new Microwave based ECR plasma source has been developed. A comparative study of both the sources demonstrates that in the absence of the poloidal flow strongly affects the plasma properties and confinement in an SMT. Moreover, a surprising observation of the high frequency, discrete, global GAM-like mode has been reported perhaps the first time.

8.2 Unresolved issues throughout the Thesis

Though in the present Thesis, several problems have been attempted successfully, despite that few unsolved issues still persist, which are listed below:

- On the inboard side of the hot cathode produced plasma, there exists a substantial difference between mean flow and net flow, which is not accounted by fluctuation driven flow alone, however, it qualitatively accounts on LFS, mechanism resolving this discrepancy is still not clear.

- The reason for the reduction of net poloidal flows for shorter $\bar{L}_c$ values is not known yet.

- In the present work, 1-D measurements of plasma profiles have been obtained along radial direction at $Z = 0$ plane, and 2-D measurements would provide further insight and this will be addressed in the future.

- Ideally the nature of plasma profiles and fluctuation should be symmetric with the direction of the vertical field in +Z and -Z direction but the nature of net poloidal flow with the direction of VF current is not found symmetric as shown in Sec. 4.5.0.2, which could be due to misalignment of VF coils.

- The reason for low plasma density in the ECR region as compared to the outboard side plasma density is not known yet.

- The reason for the existence of the transient nature of modes for relatively large values of $\bar{L}_c$ for the ECR plasma and its effect on plasma properties is not known yet.

- Possible reason for the unusual linear fall of the density for the afterglow, for the ECR plasma, is not known yet.

- The details of the effect of electron temperature fluctuation on the density and potential fluctuations are beyond the scope of the present Thesis.

8.3 Scope of the future work

Based on the unresolved issues mentioned in Sec. 8.2, there are some of the future works are as follows:

- A possible mechanism needs to be investigated to account the difference between net poloidal flow and mean poloidal flow for the hot cathode produced plasma.

- All the experimental studies reported in the present Thesis have been performed at $Z = 0$ plane assuming the slab-like geometry of the plasma. Therefore a 2-D measurement of plasma profiles is required for both the sources to get a complete picture of plasma properties.
- As discussed in Chapter-2, the estimate of coupled power to the plasma for Microwave source is not available. The detailed measurement will be performed in the future by using suitable detectors.
- To determine the possible reason for the linear density fall for the afterglow in the ECR produced plasma.
- To launch Microwave in "X" mode from the outboard side to make an effort for higher ionization due to Microwave and higher density.
- Majority of the measurements are performed for the Argon gas only, therefore to study the variation of plasma properties with variation in topology for different ion masses needs to be investigated.
- The effect of electron temperature fluctuation on the plasma properties is to be investigated.

However, apart from these works, there is a scope for various new and interesting physics issues, which can be investigated. Some of them are listed as follow.

- In the present Thesis work, both the sources have been used independently of each other. However, using both the sources in tandem may provide better control over the gradient in the plasma profile. This can help us to control the nature of instabilities and hence the nature of fluctuation, which will further help in establishing a quasi-static equilibrium in an SMT.
- As we all know, Reynolds stress, a component of the total stress tensor plays an important role in sustaining the poloidal flow due to turbulence. To determine, Reynolds stress, we need to measure the electric field fluctuations in both poloidal as well as in the radial direction simultaneously at a particular position in the space. Therefore a specialized diagnostic needs to be developed to achieve this. The measurement of the Reynolds stress for various

mean parallel connection lengths, $\bar{L}_c$ and for both the sources may provide an insight into the turbulence in toroidal devices.

- A 3-D Numerical simulation for BETA and comparison with the experimental results will help us in better understanding the nature of instabilities, flows, fluctuation and confinement.

- To study phenomenon related to the plasma current in an SMT, we need to induce an "external" q-profile in the plasma. This involves mounting a toroidal copper conductor at the minor axis of BETA. Passing a substantial current through this copper conductor may provide a rotational transform in the plasma, which would help us in understanding the nature of instabilities in the presence of the plasma current in an SMT.

A

Co-ordinates of TF and VF coils

In the Chapter-3, the topology of the toroidal field has been determined experimentally and an inherent offset (B_{off}) in the toroidal field is observed without even charging the VF coils. Due to this inherent offset field lines do not close on themselves. To further determine the reason for B_{off}, a 3-D numerical simulation has been performed using an EFFI code. As discussed in Sec. 3.5, the EFFI code calculates the electromagnetic field and vector potential in coil systems of arbitrary geometry. The coils are made from the circular arc and/or straight segments of rectangular cross-section conductor. EFFI can also calculate magnetic flux lines, magnetic force, and inductance. The methods used for the calculations are based on a combination of analytical and numerical integration of the Biot-Savart law for a volume distribution of current. These methods yield accurate field values inside and outside the conductor [62].

It has also been discussed in Sec. 3.5 that the simulation requires actual coordinates of TF and VF coils as an input to generate 3-D magnetic field mapping. These coordinates are measured using a metrology instrument named as electronics co-ordinates displacement sensor (ECDS). The principle of working of ECDS is the measurement of distance with a modulated microwave or infrared carrier signal, generated by a small solid-state emitter within the instrument optical path, and reflected by a prism reflector or the object under survey. The modulation pattern in the returning signal is read and interpreted by the on-board computer in the total station. The distance is determined by emitting and receiving multiple frequencies and determining the integer number of wavelengths to the target for each frequency. In short, given the co-ordinate of the instrument position and bearing

TF Coil	Coordinates at TF Midplane			Coordinates at TF Outer Leg Top			Coordinates at TF Outer Leg Bottom		
	X(mm)	Y(mm)	Z(mm)	X(mm)	Y(mm)	Z(mm)	X(mm)	Y(mm)	Z(mm)
TF 1									
point 1	670.1831624482	-436.8085734735	0	670.1588673064	-436.7927385095	300	670.9539048781	-437.3109240549	-300
point 2	648.4013111673	-422.6117092149	0	648.3770160254	-422.595874251	300	649.1720535972	-423.1140597964	-300
point 3	657.5304196122	-409.2081773873	0	654.3440800378	-407.2251874436	300	657.7324843121	-409.3339305465	-300
TF 2									
point 1	784.5881742383	-149.4439777355	0.814	784.6097856938	-149.4480941649	300.814	784.7217723268	-149.4694247539	-299.186
point 2	759.0473632015	-144.5791065569	0.814	759.068974657	-144.5832229863	300.814	759.18096129	-144.6045535753	-299.186
point 3	762.776531722	-128.8031182821	0.814	762.8849962128	-128.8214336918	300.814	763.9706271619	-129.0047542919	-299.186
TF 3									
point 1	781.3173081606	172.9535120477	-0.21	781.3173081606	172.9535120477	299.79	781.3173081606	172.9535120477	-300.21
point 2	755.9318257035	167.3341454982	-0.21	755.9318257035	167.3341454982	299.79	755.9318257035	167.3341454982	-300.21
point 3	752.2629338861	183.1232362704	-0.21	752.6175773592	183.2095670699	299.79	752.6175773592	183.2095670699	-300.21
TF 4									
point 1	653.0199527056	476.3038255865	0.642	653.0199527056	476.3038255865	300.642	653.0199527056	476.3038255865	-299.358
point 2	632.0139537568	460.9823371418	0.642	632.0139537568	460.9823371418	300.642	632.0139537568	460.9823371418	-299.358
point 3	622.2245669363	474.1127937537	0.642	617.5634704322	470.561205464	300.642	617.5634704322	470.561205464	-299.358
TF 5									
point 1	434.3158110052	677.6631516667	-0.006	434.3217465222	677.6724128566	299.994	434.0443959989	677.2396627125	-300.006
point 2	420.2864070994	655.7730665584	-0.006	420.2923426165	655.7823277483	299.994	420.0149920931	655.3495776042	-300.006
point 3	406.9804591023	665.2701703804	-0.006	406.7153602692	664.8368268576	299.994	407.0321220638	665.354621185	-300.006
TF 6									
point 1	145.8214505723	792.0657906273	0.649	145.8218126921	792.0677575714	300.649	145.8933313386	792.4562290417	-299.351
point 2	141.1138940927	766.4955166359	0.649	141.1142562125	766.4974835801	300.649	141.185774859	766.8859550503	-299.351
point 3	124.9091444071	768.5010507732	0.649	125.128613688	769.8513312014	300.649	124.739408662	767.456754945	-299.351
TF 7									
point 1	-167.6443313965	788.0485230236	-0.339	-167.6358002278	788.0084204157	299.661	-167.5538177774	787.6230441348	-300.339
point 2	-162.2343219805	762.6176009381	-0.339	-162.2257908118	762.5774983302	299.661	-162.1438083614	762.1921220493	-300.339
point 3	-178.0015732881	758.3598755254	-0.339	-177.9631837939	758.1963204988	299.661	-178.0193969819	758.4358117878	-300.339
TF 8									
point 1	-453.0096631043	666.991563934	0.506	-453.0141578888	666.9981818576	300.506	-453.4175647959	667.5921404986	-299.494
point 2	-438.4016135428	645.483312308	0.506	-438.4061083273	645.4899302315	300.506	-438.8095152344	646.0838888726	-299.494
point 3	-451.801634822	636.1392518916	0.506	-452.1426914802	636.6194615915	300.506	-452.6771486884	637.3719803571	-299.494
TF 9									
point 1	-675.6603628395	443.5153609196	1.044	-675.7264055464	443.5587125154	301.044	-675.8869144037	443.664073356	-298.956
point 2	-653.9247884134	429.2477470908	1.044	-653.9908311203	429.2910986867	301.044	-654.1513399776	429.3964595272	-298.956
point 3	-662.8798001133	415.5335749585	1.044	-660.1718650338	413.8360757374	301.044	-660.9937351925	414.3512741869	-298.956
TF 10									
point 1	-792.8704077275	156.5870709064	-0.226	-792.8704077275	156.5870709064	299.774	-792.8704077275	156.5870709064	-300.226
point 2	-767.3630912085	151.5495314277	-0.226	-767.3630912085	151.5495314277	299.774	-767.3630912085	151.5495314277	-300.226
point 3	-773.6099282195	136.0213089527	-0.226	-771.7612861393	135.6962682489	299.774	-772.824969382	135.8832922021	-300.226
TF 11									
point 1	-790.7119461077	-165.0342276122	-0.078	-790.5053970343	-164.9911175176	299.922	-791.4314416953	-165.1843978469	-300.078
point 2	-765.2604015119	-159.7220832534	-0.078	-765.0538524385	-159.6789731588	299.922	-765.9798970995	-159.8722534882	-300.078
point 3	-760.2414091401	-175.3604329508	-0.078	-761.5276351272	-175.6571191655	299.922	-761.16028119	-175.5723837845	-300.078
TF 12									
point 1	-670.2882207255	-448.9984429612	-0.21	-670.3413934765	-449.0340611947	299.79	-670.5740242618	-449.1898909664	-300.21
point 2	-648.6867906628	-434.528535593	-0.21	-648.7399634137	-434.5641538265	299.79	-648.972594199	-434.7199835982	-300.21
point 3	-640.7358442169	-448.9164410441	-0.21	-640.239535769	-448.5687142482	299.79	-640.8070964198	-448.9663622177	-300.21
TF 13									
point 1	-447.3910233595	-669.4313936307	-1.617	-447.3782434418	-669.412271034	298.383	-447.2071036747	-669.1561945218	-301.617
point 2	-432.9441598969	-647.8145451996	-1.617	-432.9313799792	-647.7954226029	298.383	-432.760240212	-647.5393460907	-301.617
point 3	-418.714428318	-655.8396286771	-1.617	-418.8376579644	-656.0326453972	298.383	-419.2218761636	-656.6344529873	-301.617
TF 14									
point 1	-156.7208164838	-785.0026940824	0.424	-156.7170966614	-784.9840617739	300.424	-156.7705446359	-785.2517786281	-299.576
point 2	-151.630533198	-759.5058508254	0.424	-151.6268133756	-759.4872185169	300.424	-151.6802613501	-759.7549353711	-299.576
point 3	-135.8382782329	-763.3093431701	0.424	-135.7252697672	-762.6743202676	300.424	-135.936569317	-763.8616654155	-299.576
TF 15									
point 1	159.0876552963	-782.4091113307	0.6	159.1000090036	-782.4698681074	300.6	159.2193617563	-783.0568569663	-299.4
point 2	153.9070683642	-756.9304630338	0.6	153.9194220715	-756.9912198105	300.6	154.0387748243	-757.5782086693	-299.4
point 3	169.8957891183	-754.3229035372	0.6	169.5881736759	-752.957117046	300.6	170.0113646345	-754.8360490332	-299.4
TF 16									
point 1	447.0910751042	-662.9396059267	-0.368	447.0910751042	-662.9396059267	299.632	447.1117631001	-662.9702817612	-300.368
point 2	432.5535644706	-641.383614078	-0.368	432.5535644706	-641.383614078	299.632	432.5742524665	-641.4142899126	-300.368
point 3	446.3077359389	-632.784707851	-0.368	446.3077359389	-632.784707851	299.632	0	0	-300.368

Table A.1: The coordinates of all 16 TF coils in Cartesian coordinates measured using ECDS system. All the measurements are performed with respect to a imaginary reference frame described during the measurement. Point-1 represents the point on the outer leg of the TF coil whose normal is parallel to the major radius, point-2 and point-3 represent points whose normals are 90^o and 270^o respectively.

of a backward station, the coordinates of any other point can be computed. The angular accuracy of ECDS varies from 1" to 20", an instrumental error is ±10 mm to ±2 mm and error due to the length of the measurement varies from ±10 mm to ±2 mm per kilometer.

The actual data obtained using ECDS measurement are shown in Table. A.1 and Table. A.2 for 16 TF coils and 2 VF coils respectively.

Vertical Field coils co-ordinates			
Coil			
VF coil(Top)	**X(mm)**	**Y(mm)**	**Z(mm)**
point 1	**798.8571260278**	**-827.2407703894**	**598.5**
point 2	**813.1727983645**	**813.1727983645**	**592**
point3	**-813.1727983645**	**813.1727983645**	**593**
point4	**-827.2407703894**	**-798.8571260278**	**595**
VF coil(Bottom)			
point 1	**1050.577276289**	**-467.7471395372**	**635**
point 2	**-1050.577276289**	**467.7471395372**	**604**
point3	**-393.3231648245**	**-1080.6465139038**	**625**

Table A.2: The co-ordinates of 2 VF coils in Cartesian coordinates measured at various points using ECDS system.

All the measurements for both TF and VF coils have been performed with respect to an imaginary reference frame described during the measurement. The coordinate measurement of each TF coil is performed at three different points which are at the center, top and bottom on the outer leg of the TF coil. These points are represented as Midplane, Top and Bottom in Table. A.1. Similarly for VF coils, 3 or 4 different points have been chosen on each VF coil for coordinate measurement. The difference between two points is 45^o for 4 points and 60^o for three points measurements.

Bibliography

[1] K. Rypdal, A. Fredriksen, O. M. Olsen, and K. G. Hellblom. *Phsics of Plasmas*, 4:1468, 1997.

[2] S. Yoshikawa, W. Harries, and R. M. Sinclair. *Phys. Fluids.*, 06:1506, 1963.

[3] Sangeeta Mahajan, R. Singh, and K. Avinash. *Phys. Plasmas*, 4:2612, 1997.

[4] A. Fasoli, B. Labit, M. McGrath, S. H. Mueller, G. Plyushchev, M. Podesta, and F. M. Poli. *Phys. Plasmas*, 13:055902, 2006.

[5] P. K. Sharma and D. Bora. *Plasma Phys. Controlled Fusion*, 37:1003, 1995.

[6] S. Nakao, K. Ogura, Y. Terumichi, and S. Tanaka. *Phys. Lett. A*, 96A:405, 1983.

[7] S. H. Muller, A Fasoli, B. Labit, M. McGrath, M. Podesta, and F. M. Poli. *Phys. Rev. Lett.*, 93:16, 2004.

[8] T. S. Goud, R. Ganesh, Y. C. Saxena, D. Raju, K. Sathyanarayana, K. K. Mohandas, and C. Chavda. *Phys. Plasmas*, 19:032307, 2012.

[9] T. S. Goud, R. Ganesh, K. Sathyanarayana, D. Raju, K. K. Mohandas, C. Chavda, Aruna M. Thakar, and N. C. Patel. *Journal of Physics*, 208: 012029, 2010.

[10] Niels Winsor, John L. Johnson, and John M. Dawson. *Phys. Fluids*, 11:2448, 1968.

[11] T. S. Hahm, M. A. Beer, Z. Lin, G. W. Hammett, W. W. Lee, and W. M. Tang. *Physics of Plasmas*, 6:922, 1999.

[12] Robert Hager and Klaus Hallatschek. *Phys. Rev. Lett.*, 108:035004, 2012.

[13] Paolo Ricci and B. N. Rogers. *Phys. Rev. Lett.*, 104:145001, 2010.

[14] C. Riccardi and A. Fredriksen. *Phys. Plasmas*, 8:199, 2001.

[15] L. Federspiel, B. Labit, P. Ricci, A. Fasoli, I. Furno, and C. Theiler. *Phys. Plasmas*, 16:092501, 2009.

[16] F. M. Poli, P. Ricci, A. Fasoli, and M. Podesta. *Phys. Plasmas*, 15:032104, 2008.

[17] F. M. Poli, M. Podesta, and A. Fasoli. *Rev. Sci. Instrum*, 80:053501, 2009.

[18] B. Li, B. N. Rogers, and K. W. Gentle. *Phys. Plasmas*, 16:082510, 2009.

[19] T. S. Goud. Ph.D. thesis, Institute for Plasma Research, Gandhinagar, 2012.

[20] R. Singh, S. Mahajan, and K. Avinash. *Phys. Rev. Lett.*, 77:1504, 1996.

[21] K. Rypdal, E. Gronvoll, F. Oynes, A. Fredriksen, R. J. Armstrong, and J. Trulsen. *Plasma Phys. Controlled Fusion*, 36:1099, 1994.

[22] K. Rypdal, O.E. Garcia, and J. V. Paulsen. *Phys. Rev. Lett.*, 79:1857, 1997.

[23] C. Riccardi, D. Xuantong, M. Salierno, L. Gamberale, and M. Fontanesi. *Phys. Plasmas*, 4:3749, 1997.

[24] J. M. Beall, Y. C. Kim, and E. J. Powers. *J. Appl. Phys.*, 52:3933, 1982.

[25] Jean C. Perez and W. Horton. *Phys. Plasmas*, 13:032101, 2006.

[26] M. Podesta, A. Fasoli, B. Labit, S. H. Muller, and F. M. Poli. *Plasma Phys. Control. Fusion*, 47:1989, 2005.

[27] Paolo Ricci, B. N. Rogers, and S. Brunner. *Phys. Rev Lett*, 100:225002, 2008.

[28] S. H. Muller, A Fasoli, B. Labit, M. McGrath, O. Pisaturo, M. Podesta, and F. M. Poli. *Phys. Plasmas.*, 12:090906, 2005.

[29] M. Podesta, A. Fasoli, B. Labit, I. Furno, P. Ricci, F. M. Poli, A. Diallo, S. H. Muller, and C. Theiler. *Phys. Rev. Lett.*, 101:045001, 2008.

[30] S. Nishi, T. Sakabe, M. Uchida, H. Tanaka, and T. Maekawa. *Plasma Phys. Control. Fusion*, 52:065011, 2010.

[31] S. Nishi, T. Sakabe, M. Uchida, H. Tanaka, and T. Maekawa. *Plasma Phys. Control. Fusion*, 52:125004, 2010.

[32] K. L. Wong, M. Ono, and G. A. Wurden. *Review of Scientific Instruments*, 53:409, 1982.

[33] D. Bora. *Phys. Lett. A*, 139:308, 1989.

[34] G. Prasad, D. Bora, and Y. C. Saxena. *Geophysical Research Letters*, 19:241, 1992.

[35] A. K. Singh, R. Kaur, S. K. Mattoo, and A.Hirose. *Phys. Plasmas*, 11:328, 2004.

[36] R. Kaur, A. K. Singh, and S. K. Mattoo. *Phys. Plasmas*, 4:2955, 1997.

[37] Sangeeta Mahajan. Ph.D. thesis, Institute for Plasma Research, Gandhinagar, 1997.

[38] T. S. Goud, R. Ganesh, Y. C. Saxena, D. Raju, K. Sathyanarayana, K. K. Mohandas, and C. Chavda. *Phys. Plasmas*, 18:042310, 2011.

[39] T. S. Goud, R. Ganesh, Y. C. Saxena, and D. Raju. *Phys. Plasmas*, 19: 072306, 2012.

[40] T. S. Goud, R. Ganesh, Y. C. Saxena, and D. Raju. *Phys. Plasmas*, 20: 072308, 2013.

[41] I. H. Hutchinson. *Principle of Plasma Diagnostics*. Cambridge University Press, Reading, Massachusetts, second edition, 1987.

[42] Michael A. Lieberman and Allan J. Litchtenberg. *Principle of Plasma Diagnostics and Material Processing*. Wiley Interscience, John Wiley and Sons Publication, USA, second edition, 2005.

[43] J. A. Tagle, P. C. Stangeby, and S. K. Erents. *Plasma Phys. Controlled Fusion*, 29:297, 1987.

[44] C. Theiler, I. furno, A. Kuenlin, Ph. Marmillod, and A. Fasoli. *Review of Scientific Instruments*, 82:013504, 2011.

[45] P. C. Stangeby. *Physics of fluids*, 27:1063, 1984.

[46] I. H. Hutchinson. *Physics of Fluids*, 30:3777, 1987.

[47] I. H. Hutchinson. *Phys. Rev. A*, 37:4358, 1988.

[48] L. Patacchini and I. H. Hutchinson. *Phys. Rev. E*, 80:036403, 2009.

[49] Kenichi Nagaoka, Atsushi Okamoto, Shinji Yoshimura, and Masayoshi Y. Tanaka. *J. Phys. Soc. Jpn.*, 70:131, 2001.

[50] J. P. Sheehan and N. Hershkowitz. *Plasma Source Sci. Technol.*, 20:063001, 2011.

[51] Robert F. Kemp and J. M. Sellen Jr. *Rev Sci Instrm*, 37:455, 1966.

[52] W. Bradley, S. Thompson, and Y Aranda Gonzalvo. *Plasma Source Sci. Technol.*, 10:490, 2001.

[53] R. J. Colchin, F. S. B. Anderson, R. F. Gandy A. C. England, J. H. Harris, M. A. Henderson, D. L. Hillis, R. R. Kindsfather, D. K. Lee, D. L. Million, M. Murakami, G. H. Neilson, M. J. Saltmarsh, and C. M. Simpson. *Rev. Sci. Instr.*, 60:2680, 1989.

[54] H. Hailer, J. Massig, F. Schuler, K. Scworer, and H. Zwicker, editors. *Proceedings of the 14th European Conference on Control Fusion and Plasma Physics, Madrid*, volume 11 D part 1, p. 423, 1987.

[55] R. Jaenicke, E. Ascasibar, P. Grigull, I. Lakicevic, A. Weller, M. Zippe, H. Hailer, and K. Schworer. *Nucl. Fusion*, 33:687, 1993.

[56] M. G. Shats, D. L. Rudakov, B. D. Blackwell, L. E. Sharp, and O. I. Fedyanin. *Rev. Sci. Instr.*, 66:1163, 1995.

[57] T. S. Pedersen, J. P. Kremer, R. G. Lefrancois, Q. Marksteiner, N. Pomphrey, W. Reiersen, F. Dahlgren, and X. Sarasola. *Fusion Sci. Technol*, 50:372, 2006.

[58] F. Piras, J. M. Moret, J. X. Rossel, and TCV team. *Fusion Eng. Des.*, 85: 739, 2010.

[59] N. Mahdizadeh, F. Greiner, T. Happel, A. Kendl, M. Ramisch, B. D. Scott, and U. Stroth. *Plasma Phys. Controlled Fusion*, 49:1005, 2007.

[60] S. Marsen, M. Endler, M. Otte, and F. Wagner. *Plasma Phys. Controlled Fusion*, 51:085005, 2009.

[61] F. M. Poli, S. Brunner, A. Diallo, A. Fasoli, I. Furno, B. Labit, S. H. Muller, G. Plyushchev, and M. Podesta. *Phys. Plasmas*, 13:102104, 2006.

[62] S. J. Sackett. EFFI: A code for calculating the electromagnetic field, force, and inductance in coil systems of arbitrary geometry. Technical report, March 1978.

[63] Shekar G. Thatipamula, Umesh K. Shukla, R. Ganesh, Y. C. Saxena, and D. Raju. *Rev. Sci. Instrum.*, 86:033504, 2015.

[64] M. Kamitsuma, Sin-Li Chen, and Jen-Shih Chang. *J. Phys. D: Appl. Phys*, 10:1065, 1976.

[65] P. C. Stangeby. *Plasma Phys. Controlled Fusion*, 37:1031, 1995.

[66] Young C. Kim and Edward J. Powers. *IEEE Transaction on Plasma Science*, PS-7:No.2, 1979.

[67] Y. Nagashima, S. I. Itoh, M. Yagi, K. Itoh, A. Fujisawa, K. Hoshino, K. Shinohara, K. Uehara, Y. Kusama, A. Ejiri, and Y. Takase. *Rev Sci. Instrm*, 77: 045110, 2006.

[68] E. J. Powers. *Nuclear fusion*, 14:5, 1974.

[69] D. Jassby. *Phys. Fluids*, 15:1590, 1972.

[70] F. W. Perkins and D. Jassby. *Phys. Fluids*, 14:102, 1971.

[71] F. Brochard, E. Gravier, M. Salierno, and G. Bonhomme. *Phys. Plasmas*, 12: 062104, 2005.

[72] P. K. Sharma, J. P. Singh, and D. Bora. *Plasma Phys. Controlled Fusion*, 39: 1669, 1997.

[73] Niels Winsor, John L. Johnson, and John M. Dawson. *Phys. Fluids*, 11:2448, 1968.

[74] K. Itoh, K. Hallatschek, and S. Itoh. *Plasmas Phys. Controlled Fusion*, 47: 451, 2005.

[75] N. Chakrabarti, R. Singh, P. K. Kaw, and P. N. Guzdar. *Physics of Plasmas*, 14:052308, 2007.

[76] R. Nazikian, G. Y. Fu, M. E. Austin, H. L. Berk, R. V. Budny, N. N. Gorelenkov, W. W. Heidbrink, C.T. Holcomb, G. J. Kramer, G. R. McKee, M. A. Makowski, W. M. Solomon, M. Shafer, E. J. Strait, and M. A. Van Zeeland. *Phys. Rev. Lett.*, 101:185001, 2008.

[77] G. Y. Fu. *Phys. Rev. Lett.*, 101:185002, 2008.

[78] T. Ido, Y. Miura, K. Kamiya, Y. Hamada, K. Hoshino, A. Fujisawa, K. Itoh, S. Itoh, A. Nishizawa, and H. Ogawa. *Plasma Physics and Controlled Fusion*, 48:S41, 2006.

[79] A.V. Melnikov, L.G. Eliseev, S.V. Perfilov, S.E. Lysenko, R.V. Shurygin, V.N. Zenin, S.A. Grashin, L.I. Krupnik, A.S. Kozachek, R.Yu. Solomatin, A.G. Elfimov, A.I. Smolyakov, M.V. Ufimtsev, and The HIBP Team. *Nuclear Fusion*, 55:063001, 2015.

[80] G. Wang, W. A. Peebles, T. L. Rhodes, M. E. Austin, Z. Yan, G. R. McKee, R. J. La Haye, K. H. Burrell, E. J. Doyle, J. C. Hillesheimand M. J. Lanctot, R. Nazikian, C. C. Petty, L. Schmitz, S. Smith, E. J. Strait, M. Van Zeeland, and L. Zeng. *Phys. Plasmas*, 20:092501, 2013.